UNIVERSIDAD COMPLUTENSE DE MADRID
FACULTAD DE CIENCIAS QUIMICAS

TESIS DOCTORAL

Polímeros de coordinación conmutables de hierro(II) para aplicaciones multifuncionales

Switchable iron(II) coordination polymers for multifunctional applications

MEMORIA PARA OPTAR AL GRADO DE DOCTOR

PRESENTADA POR

Esther Resines Urien

Director

José Sánchez Costa

Madrid

UNIVERSIDAD COMPLUTENSE DE MADRID
FACULTAD DE CIENCIAS QUÍMICAS

TESIS DOCTORAL

Polímeros de coordinación conmutables de hierro(II) para aplicaciones multifuncionales

Switchable iron(II) coordination polymers for multifunctional applications

MEMORIA PARA OPTAR AL GRADO DE DOCTORA

PRESENTADA POR

Esther Resines Urien

DIRECTOR

Jose Sánchez Costa

INDEX

INDEX **3**

AGRADECIMIENTOS **5**

ABSTRACT **7**

RESUMEN **11**

1. INTRODUCTION **15**

1.1. Spin crossover phenomenon 16

1.1.1. Cooperativity 17

1.1.2. External stimuli: Temperature 18

1.1.3. External stimuli: guest molecules 23

1.1.4. External stimuli: Pressure 32

1.1.5. External stimuli: Light 33

1.1.6. Spin crossover composites 35

1.2. Electrical conductivity in coordination polymers 38

1.3. Objectives 40

2. REVERSIBLE ELECTRO-OPTICAL ACETONITRILE SENSOR IN A NON-POROUS COORDINATION POLYMER **41**

2.1. Synthesis of compound $1{\cdot}2CH_3CN$ 42

2.1.1. Synthesis of $_\infty\{[Fe(H_2O)_2(CH_3CN)_2(pyrazine)](BF_4)_2{\cdot}2CH_3CN\}$ ($1{\cdot}2CH_3CN$) and $_\infty\{[Fe(H_2O)_2(CH_3CN)_2(pyrazine)](BF_4)_2\}$ (1) 42

2.2. Results and Discussion 43

2.2.1. Structural study 43

2.2.2. Physico-chemical study 45

2.2.3. Magnetic studies 48

2.2.4. Electric transport measurements 49

2.3. Conclusions 52

3. TUNABLE COLOR AND PROTON CONDUCTIVITY VIA LATTICE ACCOMMODATION OF SMALL MOLECULES **55**

3.1. Synthesis of compound 1·pyrrole 57

3.1.1. Synthesis of ∞{[Fe(H2O)2(CH3CN)2(pyrazine)](BF4)2·pyrrole} (1·pyrrole) 57
3.2. Results and Discussion.... 57
3.2.1. Physico-chemical study 57
3.2.2. Electric transport measurements 62
3.3. Conclusions 65
4. COVALENT POST-SYNTHETIC MODIFICATION BY VOLATILE ORGANIC COMPOUNDS 67
4.1. Synthesis of compounds 1-4 71
4.1.1. Synthesis of compounds 1-4.... 71
4.1.2. Synthesis of compounds 1@PMMA-4@PMMA.... 72
4.1.3. Synthesis of compounds 1@PDMS-4@PDMS.... 72
4.2. Results and Discussion.... 73
4.2.1. Physico-chemical study 73
4.2.2. Magnetic studies.... 76
4.2.3. Sensing applications.... 77
4.2.4. Implementation in organic matrixes 79
4.2.5. Reversibility.... 82
4.3. Conclusions 83
5. SUNLIGHT-INDUCED SPIN TRANSITION AS A PASSIVE METHOD TO REDUCE TEMPERATURE FLUCTUATIONS IN BUILDINGS.... 85
5.1. Synthesis of compounds 1-4 88
5.1.1. Synthesis of compounds 1-3.... 88
5.1.2. Synthesis of compounds 1@PMMA-3@PMMA.... 88
5.2. Results and Discussion.... 89
5.2.1. Physico-chemical study 89
5.2.2. Temperature fluctuation studies.... 93
5.3. Conclusions 98
CONCLUSIONS.... 99
REFERENCES.... 101
ANNEX A.... 113
ANNEX B.... 123
ANNEX C.... 125
ANNEX D.... 129
ANNEX E. PHYSICAL TECHNIQUES.... 137
ANNEX F. PUBLISHED ARTICLES AND PATENTS.... 139

AGRADECIMIENTOS

En primer lugar, me gustaría agradecer a mi familia y amigos, que han sido una parte fundamental de esta Tesis doctoral, ya que sin su apoyo no habría conseguido llegar tan lejos.

Quiero dar las gracias de manera especial a mi director de tesis Jose Sánchez Costa por haberme incluido en su grupo de investigación, haberme abierto el camino de la investigación y por todo lo que me ha enseñado.

También dar las gracias al Instituto IMDEA Nanociencia y la Universidad Complutense de Madrid, así como a todas las instalaciones que han prestado su ayuda en esta tesis, como los Servicios Interdepartamentales de Investigación (Universidad Autónoma de Madrid) y al Sincrotrón de ALBA.

Por último, me gustaría agradecer al Ministerio de Ciencia e Innovación y la Comunidad de Madrid, por la financiación de esta Tesis doctoral a través de los proyectos C AIRE PID2019-111479GB-I00 y PEJD-2017-PRE/IND-4037.

ABSTRACT

Switchable iron(II) coordination polymers for multifunctional applications

INTRODUCTION

In recent years, interest in coordination polymers (CPs) has grown rapidly with the demand for new materials that exhibit improved properties, are more cost-effective or can combine several desired properties. This particular development has been driven by crystal engineering, which entails the self-assembly of organic ligands and metal ions with specific functionality and directionality. This enables the design and synthesis of new molecules with targeted properties. Accordingly, a wide variety of CPs with potential applications in catalysis,[1] gas sorption,[2] luminescence,[3] drug delivery,[4] sensing,[5] magnetism[6] and anion exchange[7] have been reported. Among them, the family of spin crossover materials (SCO) and coordination polymers exhibiting electrical properties has garnered considerable attention.

The SCO effect occurs when the metal ion in coordination compounds undergoes a reversible and reproducible spin transition between the low spin (LS) and high spin (HS) electronic states, under the influence of external stimuli, such as temperature, pressure, light, magnetic field and the absorption/desorption of guest molecules.[8,9]

The field of conductive CPs is also increasing exponentially, as electronic devices are crucial to technological development. CPs and MOFs offer a unique opportunity for tailoring electrical properties through chemical design by rational choice of ligands and metals or by post-synthetic modification techniques.[10,11] Their versatility, tunability and diversity of structures provide remarkable possibilities for a variety of applications.

OBJECTIVES

The objective of this Thesis is the synthesis and characterization of multifunctional switching non-porous iron(II) coordination polymers. The employed materials can be mainly classified into two areas: conductive coordination polymers and spin crossover materials. The potential applications of these materials as either molecular sensors for hazardous volatile organic molecules or as passive temperature fluctuation controllers has been studied.

RESULTS

The following results have been obtained in the different chapters:

In Chapter 2, a new 1D non-porous acting as porous crystalline coordination polymer has been synthetized. As the temperature is increased, the non-coordinated acetonitrile molecules are

desorbed, and sharp magneto-structural transitions, such as a color change from yellow to orange, can be found. Additionally, the transport measurements reveal that the polymer is insulating at low temperatures, but the structural changes result in an abrupt high-current peak near RT. Strikingly, the initial yellow color, structure and electrical properties are restored by exposing the empty orange crystals to acetonitrile. Consequently, this CP could provide a flexible platform for the development of an acetonitrile sensor, offering a wide range of readout options such as optical, magnetic, and electrical transport measurements.

In Chapter 3, the mechanism of conduction of the coordination polymer synthetized in Chapter 2 is revealed to be of protonic origin, through a conduction path formed by the non-coordinated acetonitrile molecules. The proton conductivity occurs at low relative humidity levels (RH < 40%). The proton transport was also studied under higher humidity and upon exposure to pyrrole, which leads to a change of color from yellow to green. The proton conductivity properties are modified in both cases, suggesting that they are determined by the nature of the uncoordinated guest molecules. Thus, this material may be useful for the development of switchable proton conductors and capacitive sensors with a distinct optical response to diverse small molecules and able to work at low relative humidity levels.

In Chapter 4, new CPs have been obtained by means of a gas-solid covalent post-synthetic modification between the SCO coordination polymer $[Fe(NH_2trz)_3](OTs)_2$ and three volatile organic compounds: formaldehyde, benzaldehyde and acetone. This method can be applied to the synthesis of new compounds and can be used to develop materials that are impossible to produce by conventional synthetic routes. Furthermore, this could be an innovative way to create sensors for contaminants that contain a carbonyl group. In this case, only exposure to formaldehyde leads to a color change from pink to white at RT. This behavior can also be replicated when the CP is embedded in PMMA and PDMS.

In Chapter 5, three different coordination polymers have been synthetized and embedded in PMMA: one that exhibits a spin transition in the RT region (leading to a color change from pink to white), one pink and another white. These composites were employed in three different experiments to simulate temperature fluctuations in a room, where a different behavior is observed when comparing the composite displaying SCO with the pink reference. This highlights that the heat generated by the Sun can trigger a spin transition, which leads to reduced temperature fluctuations in both heating and cooling. Remarkably, this finding opens up the possibility of using these materials in the passive thermal control of buildings, particularly in regions where temperatures are warm during the day and cold at night.

CONCLUSIONS

In this Thesis non-porous coordination polymers of diverse nature have been synthesized, including conducting and spin crossover coordination compounds, which present several interesting physico-chemical properties that could lead to potential multifunctional applications in diverse fields, like sensing and as passive thermoregulators.

REFERENCES

1. J. P. Zhang, P. Q. Liao, H. L. Zhou, R. B. Lin, X. M. Chen, *Chem. Soc. Rev.* **2014**, *43*, 5789–5814.

2. B. Xiao, P. J. Byrne, P. S. Wheatley, D. S. Wragg, X. Zhao, A. J. Fletcher, K. M. Thomas, L. Peters, J. S. O. Evans, J. E. Warren, W. Zhou, R. E. Morris, *Nat. Chem*. **2009**, *1*, 289–294.

3. A. Gamonal, C. Sun, A. Lorenzo Mariano, E. Fernandez-Bartolome, E. SanVicente, B. Vlaisavljevich, J. Castells, C. Marti-Gastaldo, R. Poloni, R. Wannemacher, J. Cabanillas-Gonzalez, J. Sanchez Costa, *J. Phys. Chem. Lett*. **2020**, *11*, 3362–3368.

4. I. Imaz, M. Rubio-Martínez, L. García-Fernández, F. García, D. Ruiz-Molina, J. Hernando, V. Puntes, D. Maspoch, *Chem. Commun*. **2010**, *46*, 4737–4739.

5. S. Rodríguez-Jimenez, H. L. C. Feltham, S. Brooker, *Angew. Chemie - Int. Ed*. **2016**, *55*, 15067–15071.

6. O. Roubeau, *Chem. - A Eur. J*. **2012**, *18*, 15230–15244.

7. J. H. Askew, H. J. Shepherd, *Dalt. Trans*. **2020**, *49*, 2966–2971.

8. P. Gütlich, A. B. Gaspar, Y. Garcia, *Beilstein J. Org. Chem*. **2013**, *9*, 342–391.

9. K. Senthil Kumar, M. Ruben, *Coord. Chem. Rev*. **2017**, *346*, 176–205.

10. H. N. Wang, X. Meng, L. Z. Dong, Y. Chen, S. L. Li, Y. Q. Lan, *J. Mater. Chem. A*. **2019**, *7*, 24059–24091.

11. V. Rubio-Giménez, S. Tatay, C. Martí-Gastaldo, *Chem. Soc. Rev*. **2020**, *49*, 5601–5638.

RESUMEN

Polímeros de coordinación conmutables de hierro(II) para aplicaciones multifuncionales

INTRODUCCIÓN

En los últimos años, el interés por los polímeros de coordinación (CPs por sus siglas en inglés) ha crecido rápidamente con la demanda de nuevos materiales que presenten mejores propiedades, sean más rentables o puedan combinar varias propiedades deseadas. Este desarrollo ha sido impulsado por la ingeniería cristalina, que implica el autoensamblaje de ligandos orgánicos e iones metálicos con una funcionalidad y direccionalidad específicas. Esto permite el diseño y la síntesis de nuevas moléculas con propiedades específicas. En consecuencia, se ha publicado una amplia variedad de CPs con aplicaciones potenciales en catálisis,[1] absorción de gases,[2] luminiscencia,[3] administración de fármacos,[4] detección de moléculas,[5] magnetismo[6] e intercambio aniónico.[7] Entre ellos, la familia de materiales de transición de espín (SCO por sus siglas en inglés) y los polímeros de coordinación que presentan propiedades eléctricas han recibido una atención considerable.

El efecto SCO se produce cuando el ion metálico de los compuestos de coordinación experimenta una transición de espín reversible y reproducible entre los estados electrónicos de bajo espín (LS) y de alto espín (HS), bajo la influencia de estímulos externos, como la temperatura, la presión, la luz, el campo magnético y la absorción/desorción de moléculas huésped.[8,9]

El campo de los CPs conductores también está aumentando exponencialmente, ya que los dispositivos electrónicos son cruciales para el desarrollo tecnológico. Los CPs y las redes metalo-orgánicas ofrecen una oportunidad única para adaptar las propiedades eléctricas a través del diseño químico mediante la elección racional de ligandos y metales o mediante técnicas de modificación post-sintética.[10,11] Su versatilidad y diversidad de estructuras ofrecen notables posibilidades para desarrollar una gran variedad de aplicaciones.

OBJETIVOS

El objetivo de esta Tesis es la síntesis y caracterización de polímeros de coordinación de hierro(II) multifuncionales conmutables y no porosos. Los materiales empleados pueden clasificarse principalmente en dos áreas: polímeros de coordinación conductores y materiales de transición de espín. Se han estudiado las posibles aplicaciones de estos materiales como sensores moleculares de moléculas orgánicas volátiles tóxicas o como controladores pasivos de fluctuaciones de temperatura.

RESULTADOS

En los diferentes capítulos se han obtenido los siguientes resultados:

En el capítulo 2, se ha sintetizado un nuevo polímero de coordinación cristalino 1D no poroso que actúa como poroso. Al aumentar la temperatura, las moléculas de acetonitrilo no coordinadas se desorben, lo que va acompañado de transiciones magneto-estructurales bruscas, como el cambio de color de amarillo a naranja. Además, las mediciones de transporte eléctrico revelan que el polímero es aislante a bajas temperaturas, pero los cambios estructurales dan lugar a un pico abrupto de alta corriente cerca de RT. Sorprendentemente, el color amarillo inicial, la estructura y las propiedades eléctricas se restauran al exponer los cristales vacíos de color naranja al acetonitrilo. En consecuencia, este CP podría proporcionar una plataforma flexible para el desarrollo de un sensor de acetonitrilo, ofreciendo una amplia gama de opciones de detección, tales como mediciones de transporte óptico, magnético y eléctrico.

En el capítulo 3, se revela que el mecanismo de conducción del polímero de coordinación sintetizado en el capítulo 2 es de origen protónico, a través de una vía de conducción formada por las moléculas de acetonitrilo no coordinadas. La conductividad protónica se produce a niveles bajos de humedad relativa (RH < 40%). También se ha estudiado el transporte de protones bajo una mayor humedad y al exponerlo a pirrol, lo que provoca un cambio de color de amarillo a verde. Las propiedades de conductividad protónica se modifican en ambos casos, lo que sugiere que están determinadas por la naturaleza de las moléculas huésped no coordinadas. Así, este material puede ser útil para el desarrollo de conductores de protones conmutables y sensores capacitivos con una respuesta óptica distinta a diversas moléculas pequeñas y capaz de trabajar a niveles de humedad relativa bajos.

En el capítulo 4, se han obtenido nuevos CPs mediante una modificación covalente post-sintética entre el polímero de coordinación de transición de espín $[Fe(NH_2trz)_3](OTs)_2$ y tres compuestos orgánicos volátiles: formaldehído, benzaldehído y acetona. Este método puede aplicarse a la síntesis de nuevos compuestos y puede utilizarse para desarrollar materiales imposibles de producir por las rutas sintéticas convencionales. Además, podría ser una forma innovadora de crear sensores para contaminantes que contengan un grupo carbonilo en su estructura. En este caso, sólo la exposición al formaldehído provoca un cambio de color de rosa a blanco a temperatura ambiente. Este comportamiento también puede reproducirse cuando el CP se embebe en PMMA y PDMS.

En el Capítulo 5, se han sintetizado tres polímeros de coordinación diferentes y se han embebido en PMMA: uno que presenta una transición de espín en la región RT (que conduce a un cambio de color de rosa a blanco), otro de color rosa y otro blanco. Estos compuestos se emplearon en tres experimentos diferentes para simular fluctuaciones de temperatura en una habitación, donde se observa un comportamiento diferente al comparar el compuesto que muestra SCO con la referencia rosa. Esto pone de manifiesto que el calor generado por el sol puede desencadenar una transición de espín, lo que lleva a reducir las fluctuaciones de temperatura tanto en el calentamiento como en el enfriamiento. Este hallazgo abre la posibilidad de utilizar estos materiales en el control térmico pasivo de los edificios, sobre todo en regiones donde las temperaturas son cálidas durante el día y frías por la noche.

CONCLUSIONES

En esta Tesis se han sintetizado polímeros de coordinación no porosos de diversa naturaleza, incluyendo compuestos de coordinación conductores y con transición de espín, que presentan varias propiedades físico-químicas interesantes que podrían dar lugar a potenciales aplicaciones multifuncionales en diversos campos, como la detección de moléculas y como termorreguladores pasivos.

REFERENCIAS

1. J. P. Zhang, P. Q. Liao, H. L. Zhou, R. B. Lin, X. M. Chen, *Chem. Soc. Rev.* **2014**, *43*, 5789–5814.

2. B. Xiao, P. J. Byrne, P. S. Wheatley, D. S. Wragg, X. Zhao, A. J. Fletcher, K. M. Thomas, L. Peters, J. S. O. Evans, J. E. Warren, W. Zhou, R. E. Morris, *Nat. Chem*. **2009**, *1*, 289–294.

3. A. Gamonal, C. Sun, A. Lorenzo Mariano, E. Fernandez-Bartolome, E. SanVicente, B. Vlaisavljevich, J. Castells, C. Marti-Gastaldo, R. Poloni, R. Wannemacher, J. Cabanillas-Gonzalez, J. Sanchez Costa, *J. Phys. Chem. Lett*. **2020**, *11*, 3362–3368.

4. I. Imaz, M. Rubio-Martínez, L. García-Fernández, F. García, D. Ruiz-Molina, J. Hernando, V. Puntes, D. Maspoch, *Chem. Commun*. **2010**, *46*, 4737–4739.

5. S. Rodríguez-Jimenez, H. L. C. Feltham, S. Brooker, *Angew. Chemie - Int. Ed*. **2016**, *55*, 15067–15071.

6. O. Roubeau, *Chem. - A Eur. J*. **2012**, *18*, 15230–15244.

7. J. H. Askew, H. J. Shepherd, *Dalt. Trans*. **2020**, *49*, 2966–2971.

8. P. Gütlich, A. B. Gaspar, Y. Garcia, *Beilstein J. Org. Chem*. **2013**, *9*, 342–391.

9. K. Senthil Kumar, M. Ruben, *Coord. Chem. Rev*. **2017**, *346*, 176–205.

10. H. N. Wang, X. Meng, L. Z. Dong, Y. Chen, S. L. Li, Y. Q. Lan, *J. Mater. Chem. A*. **2019**, *7*, 24059–24091.

11. V. Rubio-Giménez, S. Tatay, C. Martí-Gastaldo, *Chem. Soc. Rev*. **2020**, *49*, 5601–5638.

1. INTRODUCTION

Among the many studies conducted in inorganic and coordination chemistry over the past 50 years, research on coordination polymers (CPs) occupies a prominent place. The IUPAC defined a coordination polymer as "a coordination compound with repeating coordination entities extending in 1, 2, or 3 dimensions", where a coordination compound is "any compound that contains a coordination entity. A coordination entity is an ion or neutral molecule that is composed of a central atom, usually that of a metal, to which is attached a surrounding array of atoms or groups of atoms, each of which is called ligands".[1] That is to say that CPs are built from metal centers, linked through organic ligands via coordination bonds, extending from one to three dimensions (Figure 1).

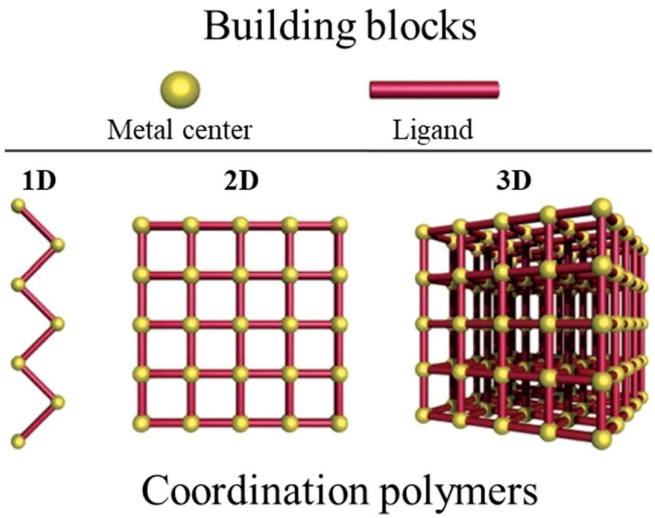

Figure 1. General scheme of coordination polymers. Reprinted with permission from ref 2. Copyright 2011 Metal-Organic Frameworks with Additional Flexible Substituents – Modulating Responsiveness, Gas Sorption Selectivity & Network Topologies.[2]

Interest in CPs increased in the early 1990s, as Hoskins, Robson and coworkers[3] proposed an approach to develop CPs with specific structures. This development was fueled by the increasing importance of crystal engineering which entails the auto-assembly of the organic ligands (with suitable functional groups) and metal ions with a specific directionality and functionality. It involves the study and understanding of intermolecular interactions in a crystalline structure, in order to design and produce new molecules with specific applications. This has been extensively employed for the synthesis of CPs, since the control and modification of synthetic factors such as the metal salt, ligand, solvent and temperature conditions can result in coordination compounds with the intended shape, dimensionality and application. Consequently, a great number of CPs has been documented with potential applications in anion exchange,[4] gas sorption,[5] drug delivery,[6] luminescence,[7] magnetism,[8] sensing[9] and catalysis.[10] An indication of the increasing interest in this

field is the number of publications, that have grown from 83858 hits by the end of 2010 to over 165530, based on a recent SciFinder^n search (as of November 8th, 2021).

A significant proportion of these publications involve porous 3D CPs, generally referred to as metal–organic frameworks (MOFs), a term introduced by Yaghi in 1995.[11] Nevertheless, increasing attention has been recently devoted to the systematical study of the potential properties of CPs of lower dimensions. Because of their greater structural simplicity in comparison to MOFs, 1D CPs are typically easier to synthesize and the resultant structure can be tailored more precisely to produce structures with potential applications by properly selecting the constituent metal centers and ligands. One-dimensional coordination polymers are being studied as materials with unique magnetic, electrical, mechanical, and optical properties, and they have been used as molecular-based ferromagnets, synthetic metallic conductors, non-linear optical materials and ferroelectric materials. A particularly interesting group of coordination polymers, due to their distinctive properties and potential applications, are those that display spin crossover.

1.1. SPIN CROSSOVER PHENOMENON

The spin crossover (SCO) phenomenon is a unique research topic, which lies in the field of magnetochemistry, and is historically and essentially linked to the progress of coordination chemistry.[12] Transition-metal ion coordination compounds can, under specific conditions, display a switching phenomenon, in which the metal ion undergoes a measurable, reversible and reproducible spin transition between the high spin (HS) and low spin (LS) states, in response to certain external stimuli, such as temperature, pressure, light, magnetic field and the absorption/desorption of guest molecules (Figure 2).[13,14] This phenomenon is known as spin crossover or spin transition.[13,15] The change in the electronic configurations of these SCO centers leads to a change in the physical and chemical properties of the complex, mainly in magnetism, color and structure.[13,15] As a result SCO compounds have become very attractive because of their potential applications, that include molecular switches,[13] sensors,[14] thermal display devices,[16] high-density memory units,[17] building blocks for molecular electronics and spintronics,[18] mechanical actuators,[19] contrast agent for magnetic resonance imaging (MRI),[20] and luminescent and plasmonic devices.[21]

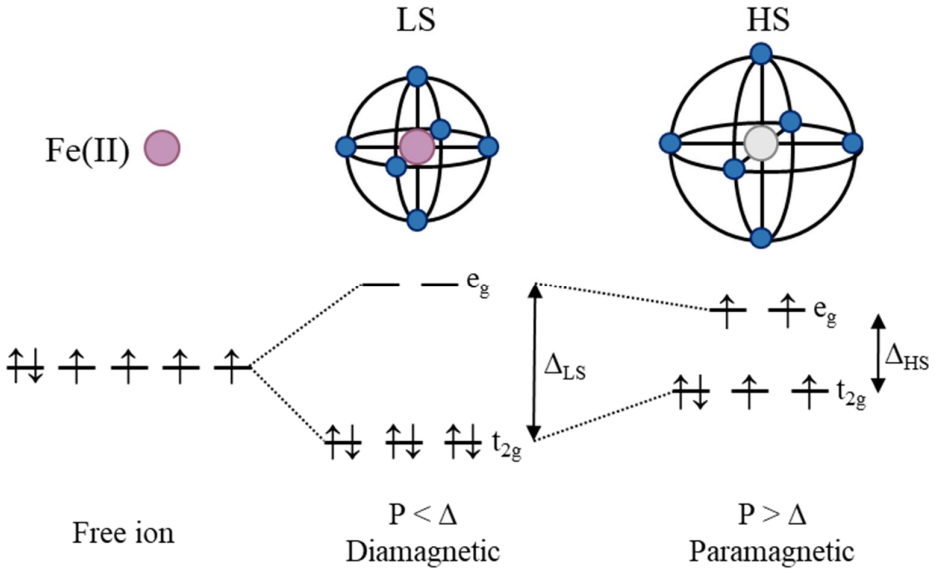

Figure 2. Schematic representation of the partial degeneracy splitting of the 3d orbitals due to the presence of the octahedral ligand field for the LS (left) and HS (right) states.

Usually, this LS-HS transition takes place in octahedral metal complexes with a d^4–d^7 electronic configuration[12] but it can also take place in tetrahedral complexes.[22,23] As a rule, these coordination complexes can have either a HS or LS configuration, in accordance to the splitting of the *d* orbitals in the e_g and t_{2g} levels.[15,24] The adopted state is dictated by whether the ligand field strength is weaker or stronger than the spin pairing energy.[13] When the energy gap between the e_g and t_{2g} levels (ligand field strength, Δ) is less than the interelectronic repulsion energy (P), the *d* electrons follow Hund's first rule and the metal complex adopts the high spin state.[15] On the other hand, if Δ is larger than P, the electrons occupy the orbitals of lower energy, t_{2g}, and the metal complex adopts the low spin state. The majority of complexes can be located in one of these two categories, however, in the unique region where Δ and P are similar, is where the spin crossover family appears.[15,24] This phenomenon takes place mostly with Fe(II),[8,25] but also with Cr(II),[26,27] Mn(II),[28,29] Mn(III),[30,31] Fe(III),[32,33] Ni(II),[34] Co(II)[35–37] and Co(III)[38] complexes.

The SCO phenomenon can be described as an intra-ionic electron transfer, in which the electrons shift between the e_g and t_{2g} orbitals, in the case of octahedral complexes.[15] The population of the e_g orbital takes place simultaneously with an increase in the metal to ligand bond distances, because of the antibonding character of these orbitals.[15] When only the t_{2g} level is occupied, an opposite effect occurs due to the electron back-donation between the metal ion and the vacant π^*orbitals of the ligands, which results in a shortening of the bond distances. The average variation in metal to ligand bond length depends on the metal ion, and is about 0.2 Å for Fe(II), 0.15 Å for Fe(III) and 0.10 Å for Co(II), for example.[15] It is noteworthy that there can also be remarkable changes in bond angles. Therefore, the spin transition leads to a significant change of molecular shape and size.

In addition, significant changes in all properties that depend on the distribution of the 3*d* valence electrons result from LS-HS conversions, in particular optical, vibrational, magnetic and structural properties.[12–14,39] Changes in dielectric constants,[40] electrical resistance,[41] refractive index,[42] luminescence,[43] nonlinear optical[44] and mechanical properties[19] have also been reported. These molecular changes allow the screening of SCO, using a variety of physical methods, mostly magnetic susceptibility measurements, optical vibrational and Mössbauer spectroscopy, crystal-structure determination and heat-capacity.[13]

1.1.1. Cooperativity

SCO can occur both in solution and in the solid state. In liquids there are virtually no interactions between molecules and as a result, the transition curves are gradual.[45] Even though the SCO phenomenon is purely molecular at its source, the macroscopic expression in the solid state is the direct consequence of the cooperative interaction of the SCO molecules.[15] Cooperativity is defined as the extent and speed at which the spin state change propagates throughout the solid. It has an elastic origin that leads to long-range interactions, since it arises from the change in volume of the spin crossover molecules. Generally, the spin transition characteristics indicate the strength of the interactions between the spin centers.[12] When these interactions are weak, the cooperativity is poor, and the spin transition is gradual. On the other hand, when there are strong interactions, the cooperativity is high and thus the more rapidly the magnetic, optical, dielectric and structural properties change.[25] In some occasions, these dramatic changes are coupled with a certain memory effect, which translates into a hysteretic behavior, which confers a bistable character to the material.[15,25] Bistability is an exciting property that has stimulated much interest, and is linked to memory and sensory capabilities, which could potentially be useful for the elaboration of molecular devices.

The diversity of interactions is responsible for the existence of several types of spin crossover behavior, as shown in Figure 3.[45] These curves can be gradual (Figure 3a), when there is barely any cooperativity, like in the liquid state. Depending on the strength of the interactions and cooperativity,

they may also be abrupt (Figure 3b), exhibit hysteresis (Figure 3c) or steps (Figure 3d), or they can be incomplete at high or low temperatures (Figure 3e). In a SCO research, the study of these curves is of great significance since they provide information on the existence of cooperativity, and the presence of hysteresis is a requirement for bistability.

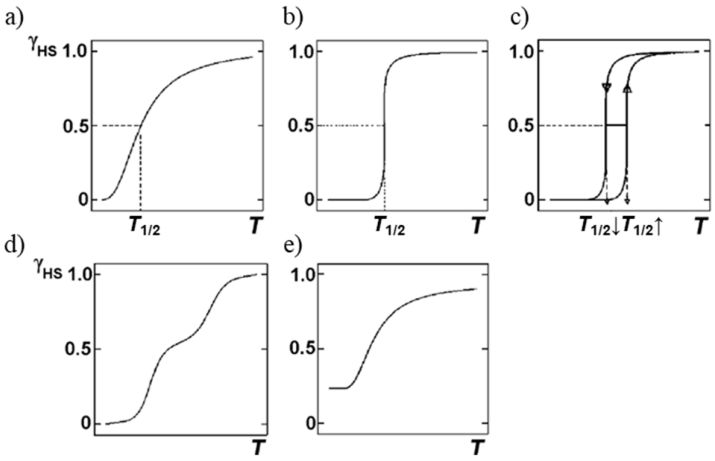

Figure 3. Schematic representation of the types of SCO: a) gradual; b) abrupt; c) with hysteresis; d) with steps; e) incomplete. The graphs represent the fraction of molecules in the HS state (γ_{HS}) *vs*. the temperature. Reprinted with permission from ref 45. Copyright 2001 Spin Transition Phenomena (Magnetism: Molecules to Materials IV).[45]

To enhance cooperativity two methods have been developed: the supramolecular and the polymeric approaches.[25] The first one, aims to increase intermolecular interactions between SCO molecules (mainly hydrogen bonding and π-π interactions are used).[25,46] On the contrary, in the latter, coordination bonds replace partially or totally the intermolecular interactions between SCO centers, thus leading to the formation of spin crossover coordination polymers.[25] Here, cooperative spin transitions can be observed when the bridging ligands are rigid enough. In either case, the higher the number and strength of the interactions between the SCO centers, the more abrupt the transition is.

Regardless of the shape of the curve, SCO can be triggered by different external stimuli, mainly the application of temperature or pressure, light irradiation or exposure to guest molecules. The effect of these on the spin transition will be explored in the following sections.

1.1.2. External stimuli: Temperature

The first documented case of thermal spin crossover in the literature was reported about ninety years ago. Around 1930, Szegö *et al*. synthesized a number of iron(III) tris(ditiocarbamate) complexes[47] and discovered that some of them presented an anomalous change in the magnetic moment, from a value of one unpaired electron at low temperatures, to that corresponding of five unpaired electrons at room temperature. Around the same time, Pauling and coworkers reported a similar abnormal magnetic behavior in ferrihemoprotein hydroxides.[48] About twenty years passed between these publications and the moment when the basis of the ligand field theory was firmly established. It was around this time when Griffith and Orgel proposed a spin state equilibrium to justify these unusual properties.[49] Later on, Martin, White *et al*. published the first theoretical analysis of the magnetic behavior in tris(dithiocarbamate)iron(III) complexes.[50]

In 1964 Baker and Bobonich documented an iron(II) coordination compound with an unusual temperature-dependent cooperative behavior, the $[Fe(phen)_2(NCX)_2]$ (X= S, Se; phen = 1,10-

phenanthroline) complexes, representing the first reported iron(II) SCO systems.[51] Nevertheless, they did not connect these findings with a spin transition between the S = 0 and S = 2 spin states. It was not until three years later when König and Madeja conclusively established the nature of the spin transition for these iron(II) complexes from extensive Mössbauer spectroscopic and magnetic studies.[52] During the 1970s, the number of SCO compounds quickly rose, in particular those with iron(II),[8,12,13,25] but also with other 3*d* transition elements such as cobalt(II),[35–37] cobalt(III),[38] chromium(II),[26,27] manganese(II),[28,29] manganese(III),[30,31] and nickel(II).[34] Since then, the interest in this field has increased significantly, as well as the number of published articles and reviews.[14,15] Now that the fundamental aspects have been understood, the current focus of the SCO research is mainly on the synthesis of new molecular functional materials, where the SCO properties can be combined with other chemical or physical properties in a synergetic manner. The development of sensing and memory devices is the primary objective of this research.

Out of all the possible external stimuli capable of inducing SCO, temperature is the most common. For a thermally induced spin transition to take place, the energy difference between the HS and LS states must be of the same order of magnitude of the thermal energy (k_BT), as depicted in Figure 4.[13–15,24,53] A temperature increase favors the HS state, while decreasing the temperature benefits the LS state.[13] This is an entropic effect, which occurs at a temperature where the higher configurational and vibrational entropy of the HS state, overcome the enthalpy of the stronger M–L bonds in the LS state.[12,24,54]

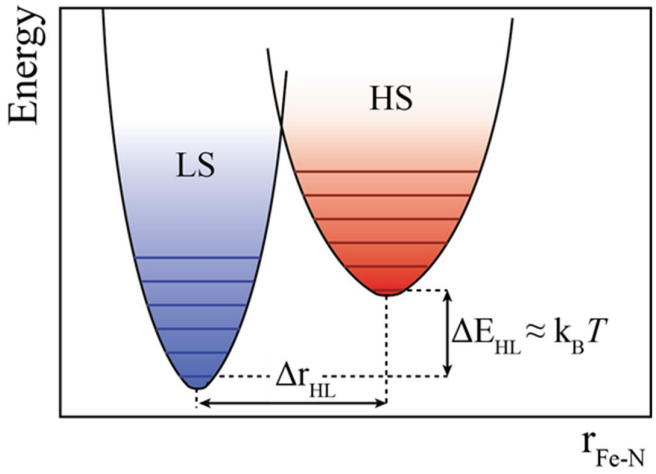

Figure 4. The condition to fulfil in order to observe thermal spin crossover is $\Delta E_{HL} \approx k_BT$.[13] Increasing the temperature favors the HS state, decreasing it favors the LS state.

Thermal SCO occurs almost exclusively with 3*d* metal ion coordination complexes. It nearly never happens for 4*d* and 5*d* metal compounds on the basis of ligand field theory, since the ligand field strength increases significantly going down in the same group in the periodic table (by 50% from 3*d* to 4*d* and from 4*d* to 5*d*). This results in a ligand field strength generally much higher than the spin pairing energy. Therefore, practically all 4*d* and 5*d* transition metal complexes present LS behavior.[13]

Thermal spin crossover is most common in hexacoordinate iron(II),[55] iron(III)[32,56] and cobalt(II)[57] molecular complexes, but various different types of compounds can also present SCO,[58–61] including organometallic compounds,[58,59] metal–metal bonded species,[59,60] and even inorganic salts.[61] Iron(II) is the most widely used metal center, since SCO occurs predominantly for hexacoordinate complexes with an $[Fe^{II}N_6]$ donor atom set.[8,13] Some examples have been reported with other donor-atom sets like $[FeN_4O_2]$[62,63], $[FeN_4S_2]$,[64] $[FeS_6]$[65] and $[FeP_4Cl_2]$.[66] Furthermore, $[FeN_6]$ complexes are used more often in SCO research, because they display the largest structural differences between their

low and high spin states,[12,13,67] and this metal/ligand combination generally affords the most cooperative spin transitions.[12]

A particularly interesting family of ligands used for the synthesis of 1D SCO iron(II) coordination polymers is the family of triazoles.[8] Triazoles, as well as tetrazoles, are recognized for producing an appropriate ligand field strength for the appearance of SCO.[68] These materials, with the general formula $[Fe(Rtrz)_3](A)_x \cdot yH_2O$ (Rtrz = 4- substituted-1,2,4-triazole, and A = anion), have been the focus of many studies, both in early stages and more recently. In fact, they have enabled the design of the first prototypes of optical devices,[69] the development of SCO nanoparticles,[70] supramolecular gels,[71] thin films,[72] dendrimers,[73] and liquid crystals,[74] as well as the electrical addressing of SCO.[75] These $[Fe(Rtrz)_3](A)_x$ polymers usually present a thermochromic effect, where the spin transition is accompanied by a color change, from purple to white, since the *d–d* transition between the HS and LS states is in the range of 520 nm and 800 nm.[8]

The polymeric nature of $[Fe(Rtrz)_3](A)_x$ complexes makes it difficult to obtain single crystals suitable for single crystal X-ray diffraction, and are generally isolated as microcrystalline powders. Hence, their structure was first suggested[76] via a combination of X-ray absorption, powder diffraction, modelling and comparison with structures of linear trinuclear compounds with the same triple N^1,N^2-triazole bridges. The general structure was proposed to be that of linear chains of Fe(II) centers bridged by three triazole ligands (through the N^1 and N^2 donor atoms) and spaced by 3.6–3.7 Å, depending on the spin state and, therefore, on the temperature. Every metal ion, except the terminal ones, present an octahedral $[FeN_6]$ coordination sphere. As a result, these Fe(II) ions exhibit appropriate coordination characteristics for SCO to occur. The coordination environment of terminal Fe(II) is completed with solvent molecules (water or alcohols) or N^1-monodonating triazoles, and thus these metal centers are generally in the HS state and do not undergo SCO, as is the case in trinuclear compounds.[77] The counterions were believed to be distributed between the coordination chains, interacting via hydrogen bonds, or other supramolecular interactions, with the ligands, either the 4-substituent or the triazole ring. The first single crystal structure of one of these systems was reported by Guionneau *et al.* in 2011, for a single crystal of $[Fe(NH_2trz)_3](NO_3)_2 \cdot 2H_2O$ (Figure 5).[78] This structure confirmed the polymeric one-dimensional nature of these materials, with the metal centers bridged via three triazole ligands. The chains are connected through hydrogen bonds between the amino substituent groups, the lattice nitrate ions and water molecules.

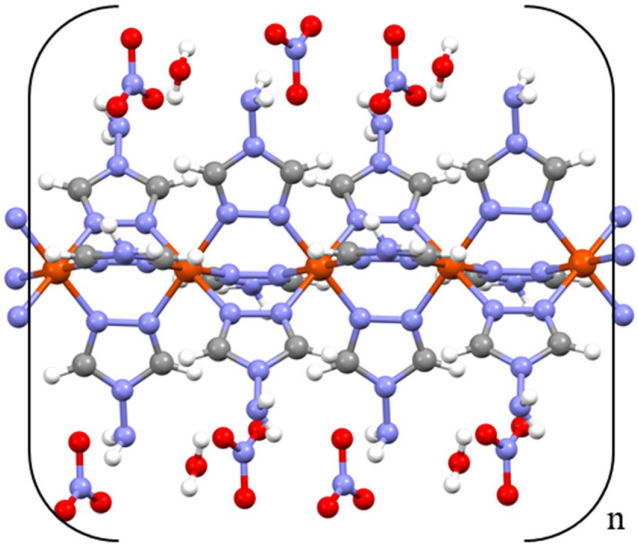

Figure 5. Crystallographic structure of $[Fe(NH_2trz)_3](NO_3)_2 \cdot 2H_2O$.

A major advantage of these polymers, which accounts for their popularity in this field, is their chemical flexibility, while retaining the 1D coordination chains. In comparison to other 1D SCO compounds, what really makes the triazole-based systems unique is the short, rigid and very stable N^1-N^2 bond in triazole bridges.[8] For one thing, this bond provides an efficient means of spreading the volume variation of the coordination sphere upon SCO, as compared to flexible ligands, thereby enhancing cooperativity. In addition, the capability of modifying the 4-position on the triazole ring allows for a diversity of materials with the same 1D structure. Furthermore, the shape and position of the spin transition curve can be tailored by both the nature of the 4-substituent and/or the selection of the counterion. Thanks to their polymeric nature, it is also possible to combine either two different triazole ligands, like NH_2trz and Htrz, or two different anions, such as NO_3^- and BF_4^-.[16]

The 4-substituted triazoles can coordinate in a monodentate fashion, but usually adopt the 1,2-bridging mode. Since the bridged metal centers are thereby separated by approximately 3.7 Å, triple bridges are generally created to minimize the electrostatic repulsion between the two Fe(II). The formation of the triple bridge places the iron centers on a trigonal axis with angles similar to 125.26°, which is nearly the angle of a regular five-membered ring (126°). Thus, the formation of these bonds generates barely any tension, explaining its stability. These bonds are prone to form and spread in one dimension, leading to the formation of coordination chains, although steric hindrance of bulky 4-substitutents can destabilize these triple bridges, preventing the formation of extended chains. Another attractive aspect is that the synthesis of these materials is quite simple, as it merely involves the reaction of a solution of an iron hydrate salt with the solution of the target triazole ligand in a ratio of 1:3 or higher. Generally, these compounds are obtained as hydrates, and these water molecules play a crucial role in the SCO, even though the release of water does not necessarily prevent the existence of a spin transition.[8]

So far, the amount of employed 4-substituents remains limited, although the large number of different types suggests that nearly any chemical functionality can be inserted in these materials, by merely designing a suitable reaction route. Although the one-dimensional structure is maintained in this family of materials, variations in the 4-substituent in the triazole ligand can result in dramatic modifications in the spin transition, which is one of the appeals of these polymers. A comparative example is shown in Figure 6, where six different SCO polymers with the same counterion, BF_4^-, have been represented. As can be observed, the position and hysteresis of the curves varies significantly even after small changes in the ligand. The substitution of a trz (trz = triazolate) for a Htrz (Htrz = 4-H-triazole) results in a considerable decrease of the spin crossover temperature ($T_{1/2}$: defined as the temperature for which there are the same proportion of HS and LS molecules) and a diminution of the hysteresis by half (defined by $T_{1/2}\downarrow$ and $T_{1/2}\uparrow$). In the case of fartrz (fartrz = 4-formamidotriazole), no hysteresis is observed, while this effect is present in all other cases. The transition temperature decreases in the following order: $(Htrz)_2(trz)$ > Htrz > fartrz > NH_2trz > tba > mxetrz, (NH_2trz = 4-amino-1,2,4-triazole; mxetrz = 4-methoxyethyltriazole; tba = 4-benzamidotriazole) so the R-substitution alters the SCO in an unpredictable manner. While $(Htrz)_2(trz)$ and Htrz present a really abrupt behavior, this behavior is more gradual in tba, NH_2trz, and especially in fartrz, signifying that the shape of the transition curve can also be altered by modifications in the ligand, since the shape of these curves strongly depends on the intermolecular interactions.

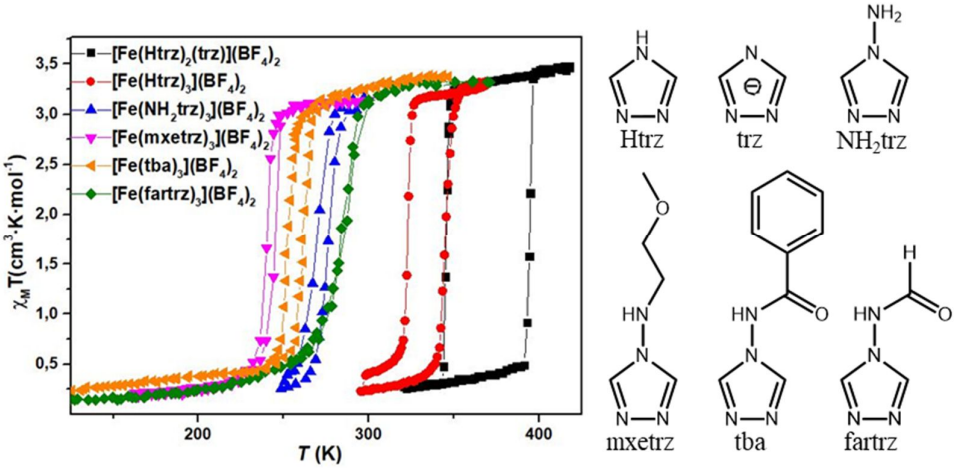

Figure 6. Magnetic behavior of $[Fe(Htrz)_2(trz)](BF_4)_2$,[79] $[Fe(Htrz)_3](BF_4)_2$,[79] $[Fe(NH_2trz)_3](BF_4)_2$,[80] $[Fe(mxetrz)_3](BF_4)_2$,[81] $[Fe(tba)_3](BF_4)_2$[82] and $[Fe(fartrz)_3](BF_4)_2$.[83] Graphs were obtained from their respective publications using the GetData Graph Digitizer software.

Modifications of the counterion can also be enough to alter the spin transition, even the abruptness, since it is extremely sensitive to small changes in the ligand field strength, like the ones resulting from a variation in the intermolecular interactions with the anion. The transition temperature generally increases with the anion size, for a family with the same 4-substituent.[8] This effect is particularly well documented for spherical anions, where an almost linear relationship of the SCO temperature with the anion volume has been observed. An example of this is represented in Figure 7 for the NH_2trz ligand. Changing the counterion can also result in a hysteresis loss.

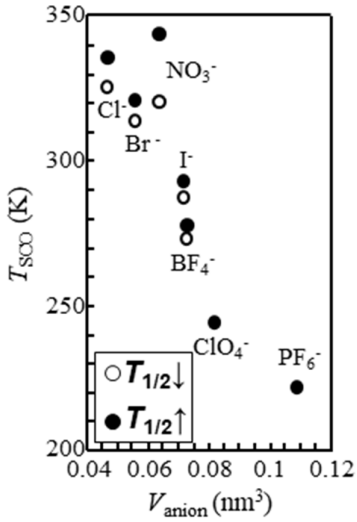

Figure 7. Variation of the SCO temperature for the $[Fe(NH_2trz)_3](A)_2$ family as a function of the volume of the spherical anion A. Reprinted with permission from ref 8. Copyright 2012 Chemistry - A European Journal.[8]

Although this is a particularly interesting family of materials, all attempts to date to obtain a 3D SCO structure with this coordination mode with a triazole ligand have been unsuccessful. However, Li *et al.* reported three MOF polymorphs with the chemical formula $[Fe_2(H_{0.67}bdt)_3]\cdot xH_2O$ (H_2bdt = 5,50-(1,4-phenylene)bis(1H-tetrazole); x =4 for 1, 13 for 2,or 15 for 3) where the Fe(II) ions are

triply-bridged by tetrazole ligands, with an octahedral coordination environment of [FeN_6] (Figure 8a).[84] In 1 and 3, there is a single crystallographically independent Fe(II), which according to the bond lengths, is in the HS and LS state, respectively. In complex 2, there are two Fe(II) centers, one with HS and the other with LS bond lengths. Interestingly, when single crystal X-ray diffraction is measured at 100 K, the HS Fe(II) undergoes a significant bond contraction, coupled with a color change from red to black; indicating the presence of a spin transition. Only this complex displays SCO, proving the importance of solvent molecules in this phenomenon.

The spin state of these materials was evaluated by temperature-dependent magnetic susceptibility measurements (Figure 8b). The $\chi_M T$ value of 1 remains roughly constant (~4.14 $cm^3 \cdot K \cdot mol^{-1}$) until 50 K where a sharp decrease is observed, because of zero-field splitting of the S = 2 ground state of the Fe(II) ion. For 2, a case of mixed spins at room temperature is found. The $\chi_M T$ values decrease gradually from 4.02 $cm^3 \cdot K \cdot mol^{-1}$ at 300 K to 2.01 $cm^3 \cdot K \cdot mol^{-1}$ at 30 K (where the zero-field splitting starts). In this partial spin transition, only 25% of the Fe(II) centers experience SCO, and no thermal hysteresis is found in the subsequent warming process. The $\chi_M T$ value of 3 at room temperature is just 1.26 $cm^3 \cdot K \cdot mol^{-1}$, indicating that the HS:LS population is approximately 1:2, in contrast with the X-ray diffraction measurements that suggest only one LS Fe(II). Upon cooling down, the $\chi_M T$ value constantly decreases to that of a diamagnetic LS.

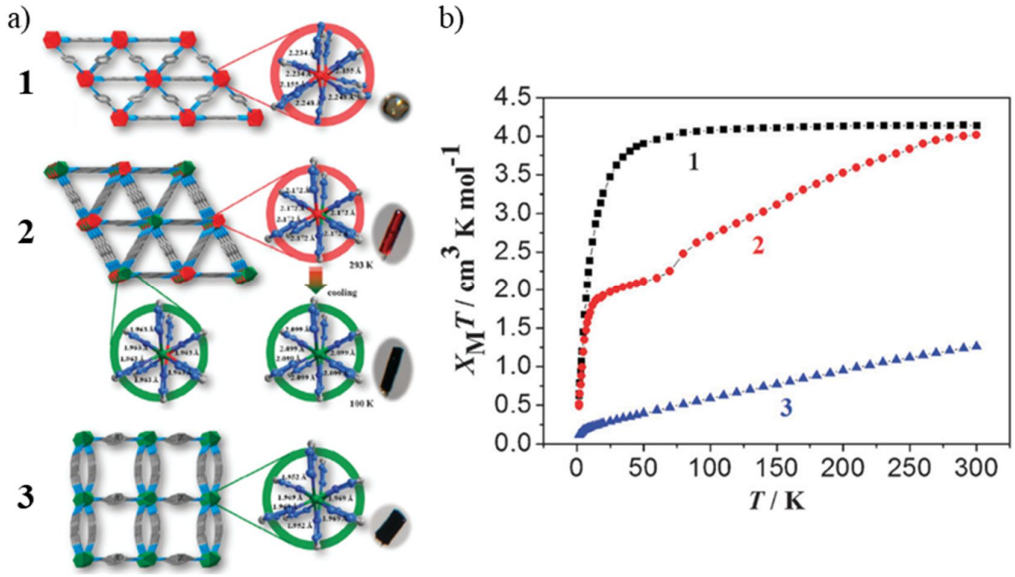

Figure 8. a) Representation of the geometry of complexes 1, 2 and 3. The circles highlight the different Fe(II) spin states, while the inserted pictures show the color changes of the single crystals. Color code: HS Fe in red, LS Fe in green, N in blue, C in grey, H omitted. b) Temperature-dependent $\chi_M T$ plots for polymorphs 1, 2 and 3. Reprinted with permission from ref 84. Copyright 2012 Chemical Communications.[84]

1.1.3. External stimuli: guest molecules

The critical role of solvent molecules on the SCO behavior has been well known from the very first studies.[15] The complex [$Fe(pic)_3$]$Cl_2 \cdot$Solv (where pic = 2-aminomethylpryridine) is one of the first reported examples that demonstrates this influence.[85] The spin state properties of this material are highly dependent on the nature of the solvent molecule: EtOH ($T_{1/2}$ = 121 K) < MeOH ($T_{1/2}$ = 150 K) < $2H_2O$ ($T_{1/2}\downarrow$ = 204 K, $T_{1/2}\uparrow$ = 295 K). Even though solvent molecules do not interact directly with the SCO centers, small variations in the solvent can wield a dramatic influence in the SCO behavior. This prompted the study of absorption/desorption of guest molecules (gas or solvent) in

these functional materials, where the physical properties change as a result of the variations in the environment of the metal centers. The inclusion of a molecule in a SCO material may result in the stabilization of the HS or LS state, or have no impact at all (Figure 9). The subsequent outcome depends on the chemical nature and size of the guest molecules.[13] Hence, this ability allows for the design of gas and solvent sensing devices based on SCO materials.[14,86–89]

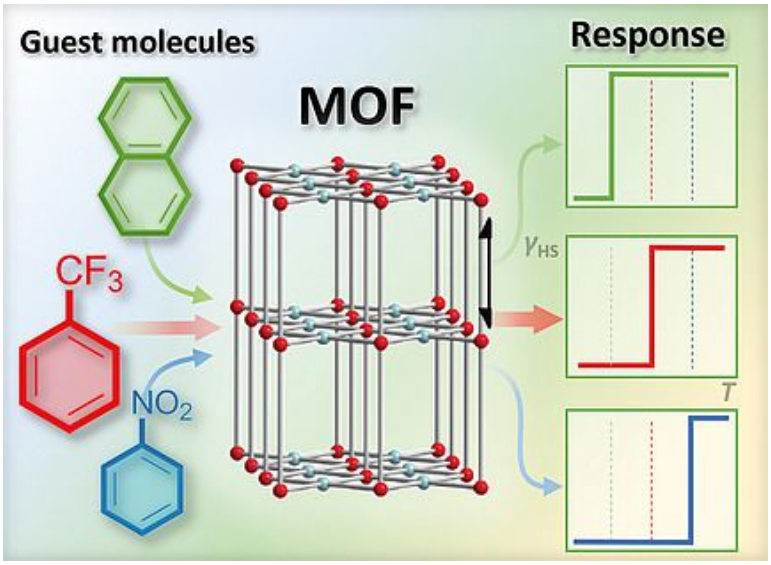

Figure 9. Scheme of the variation in the SCO properties upon guest molecules adsorption. Reprinted with permission from ref 90. Copyright 2020 European Journal of Inorganic Chemistry.[90]

In both the home and workplace environment, harmful chemical substances may be found. Therefore, the detection of such compounds with low-cost technology is an exciting research topic nowadays. An interesting approach could be the use of a SCO material, in which an analyte could trigger the HS-LS transition, ideally at room temperature, resulting in a change in the physical properties of the complex (magnetism,[12–15] luminescence,[43] conductivity,[41] etc.) including a color change that could be easily detected by the naked-eye.[13] The ability to adjust the spin transition relies on the chemical nature and size of the guest molecule.[91] The first work on the control of the SCO properties in the solid state by solvent molecules was published by Kepert *et al.* in 2002, on the coordination polymer $[Fe(azpy)_2(NCS)_2]$ (azpy = trans-4,4'-azopyridine).[92] At temperatures below 150 K, the adsorption of different guest molecules leads to the stabilization of the low spin state. However, these low temperatures are an obvious limitation. From that point, the effect of guest molecules on SCO has attracted increasing attention.[87,93,94] This uptake of guest molecules has been explored in both porous SCO materials[95,96] and in several non-porous SCO molecular materials, as will be explored over the next sections.[9,97] In the first case, solvent molecules are lodged in the pores or cavities of the material. Interactions between these molecules and the host can be of different types, like hydrogen bonds, π-π stacking and other weak interactions.[98] The guest molecules trapped in the synthetic process can be eliminated by heating and through exchange with another molecule. Surprisingly, non-porous materials can also experience absorption/desorption or exchange of guest molecules through a process of reorganization of the crystal lattice, which may entail either breakage or formation of bonds or other structural reassembly.[99,100]

In addition to the absorption of guest molecules into the material taking place through the formation of weak non-covalent interactions (like Van der Waals interactions or hydrogen bonds), it can also cause a reaction in the ligand, such as a redox reaction, the formation of covalent bonds, a chemical modification of the ligand or even a ligand exchange.

1.1.3.1. Guest-induced spin crossover by non-covalent interactions

In this case, the driving force for reversible SCO is the shift in host–guest intermolecular interactions upon uptake and desorption of small guest molecules.[86] It should be noted that the solvent absorption/desorption does not change the first coordination sphere of the metal center. The nature of these intermolecular interactions can be different, from weak Van der Waals forces to the formation of hydrogen bonds.[87] One of the most typical guests, whose impact in the SCO properties in the solid state is widely recognized, are water molecules. Usually, crystallization water molecules stabilize the LS state and when the material is dehydrated and the water molecules are released, the HS state is stabilized. This LS state stabilization of the hydrate complex derives from the hydrogen bonding between water molecules and the SCO material.[101] Therefore, a reversible SCO can be prompted by cycles of hydration and dehydration at a constant temperature.[102] Interestingly, water is capable of stabilizing the LS state in solution, as well as in the solid state.[86]

Generally, the modification of the SCO is achieved by the use of solvent molecules (like H_2O, MeOH, aromatic molecules, etc.) as they can infiltrate the cavities, or the non-porous structure, which leads to structural changes in the material.[103,104] On the other hand, adsorbed gas molecules (H_2, N_2, CO_2, etc.) do not interact significantly with the host material, therefore barely influencing the SCO behavior. As a matter of fact, modification of the magnetic properties via gas adsorption has rarely been reported in SCO materials. An exception was reported by Vitórica-Yrezábal and coworkers, where the SCO properties of a coordination polymer were modified upon CO_2 absorption.[105] This polymer, $[Fe(btzx)_3](ClO_4)_2$ (btzx = 1,4-bis(tetrazol-1-ylmethyl)benzene), is comprised of linear chains formed by $[Fe(btzx)_3]^{2+}$ units. This polymer exhibits a spin transition with transition temperatures: $T_{1/2}\downarrow$ = 200 K and $T_{1/2}\uparrow$ = 204 K (Figure 10). Upon CO_2 absorption, the spin transition shifts to higher temperatures ($T_{1/2}\downarrow$ = 209 K), and the hysteresis decreases slightly to 3 K. Therefore, CO_2 physisorption stabilizes the LS state. The gas adsorption isotherms show a preferential adsorption of CO_2 over N_2 and, as it was to be expected, the presence of N_2 does not affect the SCO behavior.

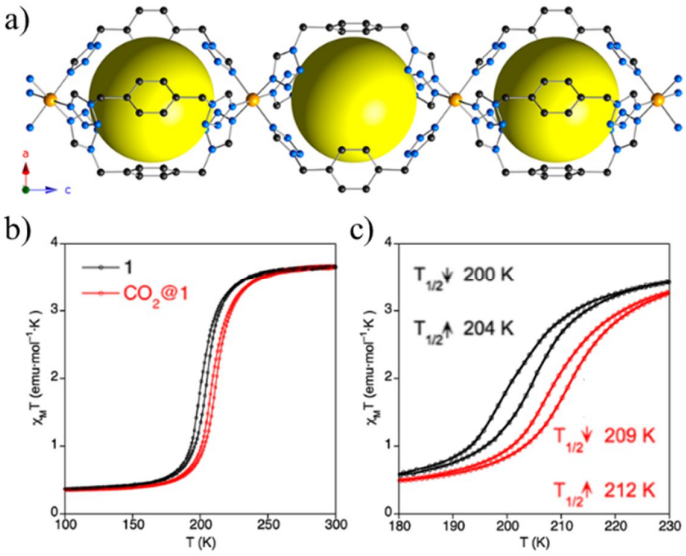

Figure 10. a) Crystal structure viewed along the *b* axis. The ClO_4^- anions and hydrogen atoms have been removed for clarity. Color code: Fe in orange, N in blue, C in black, H omitted. The yellow spheres (diameter of 9 Å) represent the empty space of the internal voids. b) Temperature dependence of $\chi_M T$ for $[Fe(btzx)_3](ClO_4)_2$ (1, black, as-synthesized) and loaded with CO_2 (CO_2@1, red). c) Detailed view of the spin transition region. Reprinted with permission from ref 105. Copyright 2013 Journal of the American Chemical Society.[105]

As previously explained, the adsorption of molecules can also take place in non-porous coordination polymers that behave as porous materials. An example of this was reported by Sánchez Costa *et al.* Here, a non-porous material capable of accommodating guest molecules was described.[106] The non-porous complex $[Fe(bpp)(H_2L)](ClO_4)_2 \cdot 1.5C_3H_6O$ (bpp = 2,6-bis(pyrazol- 3-yl)pyridine; H_2L = 2,6-bis(5-(2-methoxyphenyl)pyrazol-3-yl)pyridine) hosts crystallization acetone molecules. This complex is capable of releasing one-third of the acetone molecules (Figure 11), leading to $[Fe(bpp)(H_2L)](ClO_4)_2 \cdot C_3H_6O$, by heating to 375 K and keeping it under a dry N_2 flow for 2 h, or by heating for 2h at 390 K. This process results in a space group transformation, a change of color from dark red to orange and a spin transition from LS to HS. This compound can revert to the original material when acetone is reabsorbed. After the exposure, the original crystalline structure and the dark-red color is recovered. Similarly, $[Fe(bpp)(H_2L)](ClO_4)_2 \cdot C_3H_6O$ may substitute acetone by MeOH and H_2O to form $[Fe(bpp)(H_2L)](ClO_4)_2 \cdot 1.25MeOH \cdot 0.5H_2O$, which also involves a spin transition and the restoration of a dark-red color. Exposition of this complex to acetone results in a reversion to the original compound. The magnetic behavior measurements show that until nearly 300 K $[Fe(bpp)(H_2L)](ClO_4)_2 \cdot 1.5C_3H_6O$ presents a LS state. When the temperature is increased, the $\chi_M T$ value rises slowly because of a progressive transition from LS to HS. At 375 K, the $\chi_M T$ product rises abruptly until saturation at a value corresponding to the HS state. From this heating process, the compound loses 1/3 of the acetone molecules, transforming to $[Fe(bpp)(H_2L)](ClO_4)_2 \cdot C_3H_6O$, for which the SCO cycle presents the following temperatures: $T_{1/2}\downarrow$ = 235 K and $T_{1/2}\uparrow$ = 240 K. When the sample is exposed to acetone and measured it turns diamagnetic at room temperature again.

Methanol absorption was also studied by magnetic measurements, which show that at room temperature this compound presents a LS state. When heated, the $\chi_M T$ value rises gradually until 350 K, where the increase becomes more pronounced, indicating a LS to HS transition. This behavior is caused by a desolvation process, and after this, the magnetic behavior displayed by the complex is different. As the temperature decreases, the $\chi_M T$ value drops to almost zero at about 200 K, due to a spin transition process. Upon heating, the magnetic curve overlaps with the cooling behavior and not with the initial one.

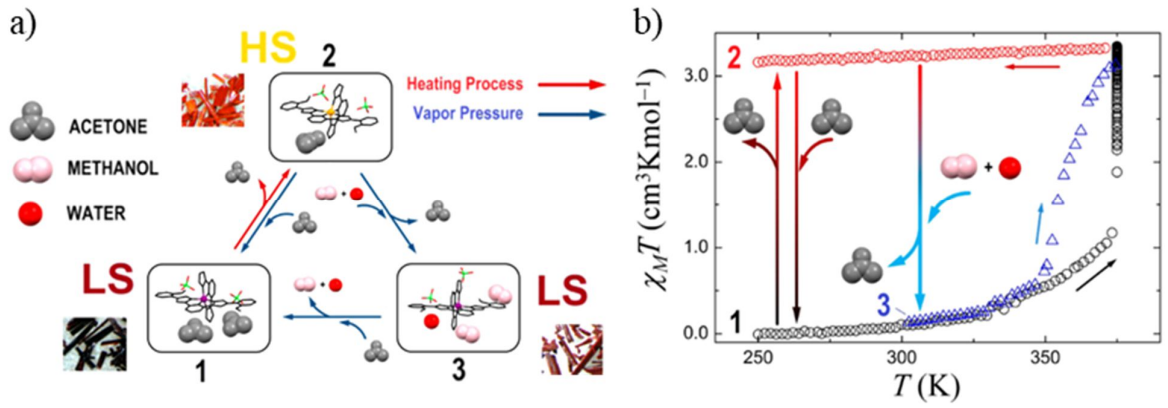

Figure 11. a) Representation of the molecular structure of 1−3 emphasizing the full conversion cycle undergone by these three species through subsequent absorption, desorption, or exchange of small molecules. Color code: HS Fe in orange, LS Fe in pink, N in blue, C in grey, O in red, Cl in green, H omitted. Pictures of the corresponding single crystals are also shown. b) Plots of $\chi_M T$ *vs*. *T* for 1 upon warming and concomitant desorption of acetone (black circles), for resulting compound 2 upon cooling (red circles) and for 3 (blue triangles) upon warming and concomitant depletion of MeOH + H_2O. The crystal-to-crystal transformations are shown with vertical arrows positioned, for clarity, at arbitrary temperatures. Reprinted with permission from ref 106. Copyright 2014 Journal of the American Chemical Society.[106]

Porous materials include 3D Hofmann-type systems with general formula $[Fe(pz)M(CN)_4]$ (pz = pyrazine; M = Ni^{2+}, Pd^{2+}, Pt^{2+}), where the spin transition properties can undergo considerable perturbations upon exposure to a guest, and may, in certain cases, exhibit room temperature sensitivity.[98] Kepert and coworkers reported a detailed guest-dependent study on $[Fe^{II}(pz)Ni^{II}(CN)_4]\cdot x$Guest (where Guest = methanol, ethanol, acetone, acetonitrile and toluene).[104] This material presents a synergistic relationship between SCO and guest-exchange, resulting in guest-induced modifications of the SCO properties. The general structure of this family consists of 2D $FeNi(CN)_4$ layers connected through the Fe(II) ions by pyrazine bridges, resulting in a $[FeN_6]$ octahedral coordination sphere (Figure 12a). The Fe-N bond distances at 150 K and 300 K are characteristic of LS and HS Fe(II) centers, respectively. The conversion between these two states is also accompanied by a change of color from pink (LS) to yellow (HS) (Figure 12b). The SCO behavior of $[Fe(pz)Ni(CN)_4]\cdot 2H_2O$ shows the conversion between the HS and LS states ($T_{1/2}\downarrow$ = 270 K and $T_{1/2}\uparrow$ = 278 K). The total desorption, to produce $[Fe(pz)Ni(CN)_4]$, induces a symmetry change from an orthorhombic to a tetragonal cell, with a dynamic rotation of the pyrazine ligands. In this case, the spin transition is significantly sharper and has a wider hysteresis with $T_{1/2}\downarrow$ = 287 K and $T_{1/2}\uparrow$ = 307 K (Figure 12c).

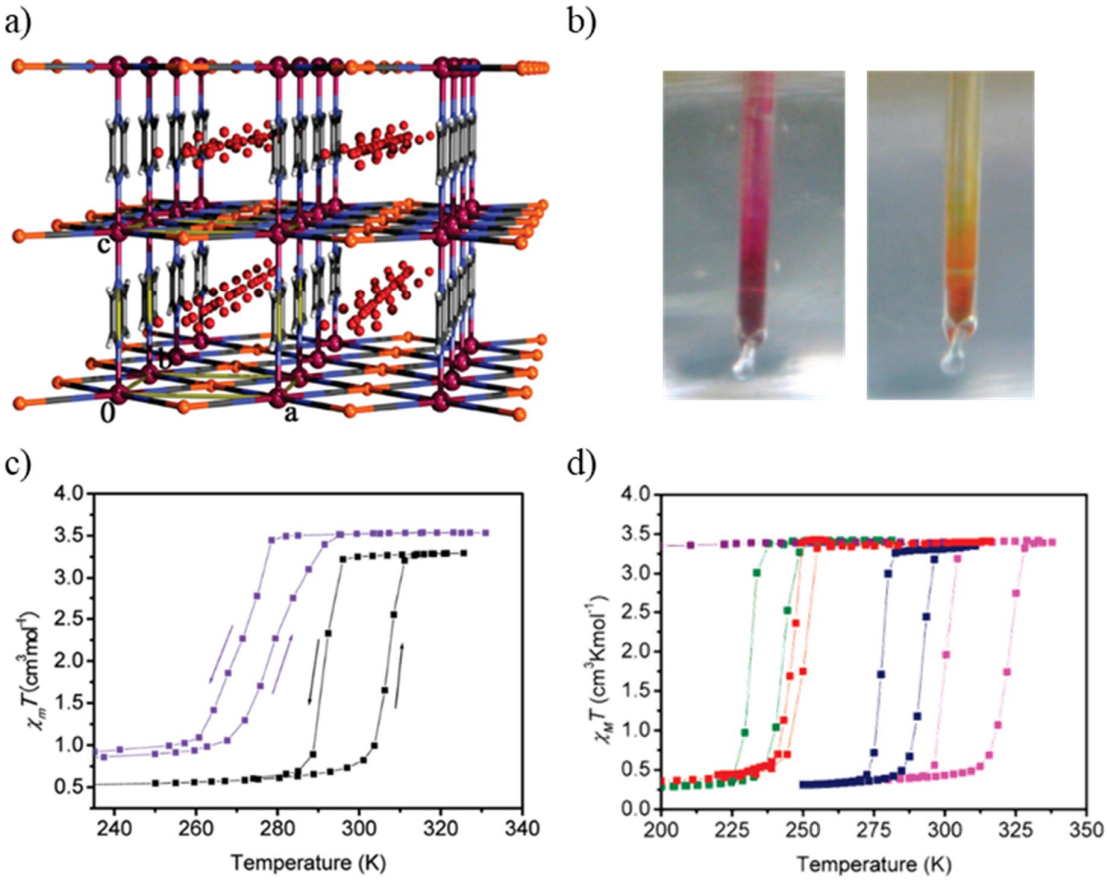

Figure 12. a) Structure of $1\cdot 2H_2O$. The 1D channels are filled with disordered water molecules (red). Color code: Fe in pink, Ni in orange, N in blue, C in grey, H in white. b) Color change induced by SCO from LS (pink) to HS (yellow). Temperature dependence of $\chi_M T$ for c) $1\cdot 2H_2O$ (violet) and 1 (black) and d) 1·0.6Toluene (purple), 1·1.2Acetone (green), 1·1.5EtOH (red), 1·1.8MeOH (blue), and 1·1.0Acetonitrile (pink). Reprinted with permission from ref 104. Copyright 2009 Journal of the American Chemical Society.[104]

Adsorption isotherms revealed that the maximum uptake into the pores, which occurs at low pressures, amounted to 1.8, 1.5, and 1.2 guest molecules per formula unit for methanol, ethanol, and acetone, respectively. The adsorption lessens as the size of the molecule increases, as is expected, and this stoichiometry is in good agreement with those established by thermogravimetric analysis. Temperature-dependent magnetic measurements were carried out for $[Fe^{II}(pz)Ni^{II}(CN)_4]\cdot xGuest$, demonstrating the strong dependence of the guest in the SCO properties, both in the transition temperatures and hysteresis widths (Figure 12d). The adsorption of these molecules leads to a number of remarkable behaviors in which the spin transition fluctuates within a 100 K window or is completely extinguished. This can be linked with strong host-guest interactions. For these six molecules, a correlation between the solvent size and the SCO temperature can be established, with the larger guests stabilizing the HS state, resulting in lower transition temperatures, or even suppression of the SCO. An exception is the increase of the SCO temperature with the exposure to acetonitrile, which the authors attributed to an internal compressive effect derived from interactions between the pyrazine π-cloud and the acetonitrile. Despite this, there is no obvious correlation between the guest size and the SCO hysteresis width, which differs significantly for each molecule. In every case, guest adsorption was fully reversible, with guest desorption yielding $[Fe^{II}(pz)Ni^{II}(CN)_4]$.

1.1.3.2. Guest-induced spin crossover by a redox process in the ligand

As previously explained, the combination of the coordination ligands defines the force field strength, which must be well-tuned for SCO to occur. Thus, the chemical modification of one ligand can also result in a spin transition. Therefore, the spin state of the metal center can also be modified by a redox reaction in a non-innocent redox-active ligand.[107] The ligand reduction can take place either in solution (with transitions reported at room temperature)[108] or in the solid-state (described at lower temperatures).[109] It is important to mention that numerous ligands possess extended π-systems with heteroatoms, which are potential redox-active systems. However, in many of these cases, the inclusion of a non-innocent redox ligand results in a change of the oxidation state of the metal center. Nevertheless, some cases have been described where the oxidation state of the cation remains the same. An example of this was reported by Zuo *et al*. in 2017, where they presented a 3D $\{[Fe(dca)][TTF(py)_4]\cdot ClO_4\cdot CH_2Cl_2\cdot 2CH_3OH]\}_n$ (dca = dicyanamide; $TTF(py)_4$ = tetra(4-pyridyl)tetrathiafulvalene) complex, that changes its magnetic and structural properties upon doping with I_2, because of a chemical oxidation of the organic $TTF(py)_4$ ligand (Figure 13).[110] The initial compound presents a $\chi_M T$ value consistent with a HS Fe(II) ion at room temperature. The $\chi_M T$ value steadily decreases between 175 K and 78 K upon cooling, and then presents a wide plateau, indicative of an incomplete spin transition. Then the $\chi_M T$ value decreases abruptly because of weak antiferromagnetic interactions between the metal centers and/or zero-field splitting. When the temperature is increased, no hysteresis is observed. The measured bond lengths and angles of the $TTF(py)_4$ ligand in the crystalline structure are similar to the reported ones for the neutral molecule.

The I_2-doped compound was prepared by submerging the crystals in a solution of iodine in cyclohexane. In this case, the $TTF(py)_4$ central C=C bond is longer than the one of the neutral molecule, clearly confirming that the TTF is in its radical cationic state. This was supported by XPS measurements, which also indicate that iron is entirely in the 2+ oxidation state, both in the initial compound and the I_2-doped one. The magnetic studies reveal that the doped complex suffers a gradual and incomplete spin transition similar to that of its parent structure, however the shape of the curve varies substantially (Figure 13). An additional consequence of tuning the SCO by redox-state in electroactive MOFs is the potential for modulating the conducting properties of the material.[111] Here, the electrical conductivity at room temperature of the I_2-doped compound increases by 2 orders of magnitude in respect to that of the initial compound.

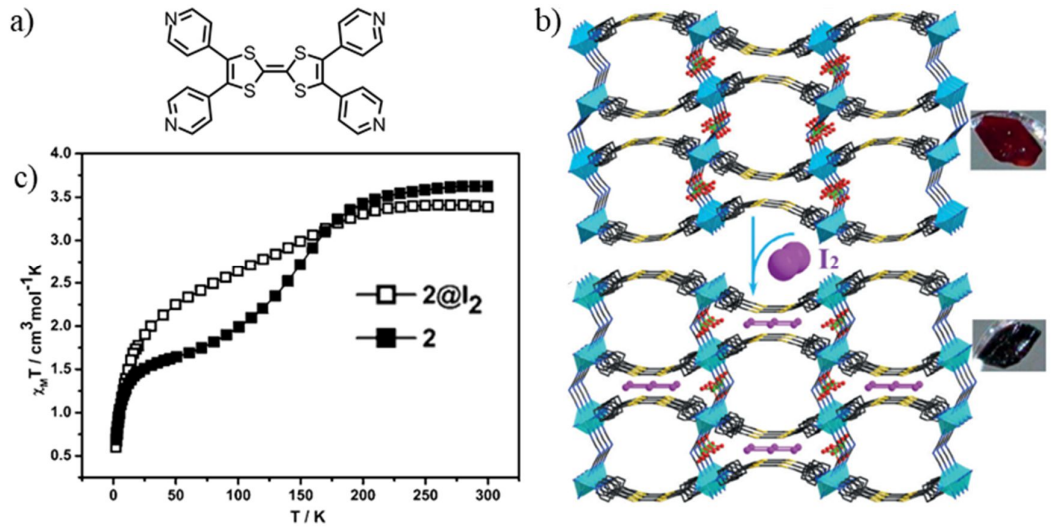

Figure 13. a) $TTF(py)_4$ ligand. b) View of 3D network for 2 and $2@I_2$. Insets show the photographs of the corresponding crystals. Color code: Fe in blue octahedra, N in blue, C in grey, S in yellow, Cl in green, I in purple, O in red, H omitted. c) Magnetic properties of 2 and $2@I_2$ as plots of $\chi_M T$ *vs*. *T*. Reprinted with permission from ref 110. Copyright 2017 Angewandte Chemie International Edition.[110]

1.1.3.3. Guest-induced spin crossover by ligand exchange

The delicate balance of energies necessary for SCO in metal complexes is achieved by a suitable combination of coordination ligands. Thus, the substitution of one ligand for another can result in a modification of the spin transition (or the appearance or disappearance of the SCO). This mechanism involves a ligand replacement in the direct coordination sphere of the metal center and is, therefore, directly responsible for the ligand field strength.[112]

Ligand exchange can occur spontaneously when a solid sample is dissolved, in which case counterions or solvent molecules may replace certain labile ligands (mainly monodentate ligands). This exchange is typically described as a complex equilibrium in solution, which is to be prevented, since that makes control difficult. Nevertheless, when controlled, the ligand substitution constitutes an elegant method for triggering the spin transition and switching the magnetic properties of solutions at room temperature. Ligand exchange is not limited to reactions in solution but may as well take place in the solid state. An example of this is a non-porous 2D SCO coordination polymer reported by Real *et al*., $\{Fe(3\text{-}CNpy)_2(MeOH)_{2/3}[Au(CN)_2]_2\}$ (3-CNpy = 3-cyanopyridine) that upon desorption of MeOH turns into a triple interpenetrated 3D microporous SCO framework with the *NbO* structure type, $\{Fe(3\text{-}CNpy)_2[Au(CN)_2]_2\}$. The concerted coordination and uncoordination of the terminal cyanide group is also involved. This exchange directly involves the coordination sites or iron(II) (Figure 14). The transformation is reversible and the coordination sites are able to selectively recognize MeOH. Furthermore, the transformation results in dramatic structural effects, particularly on the porosity of the networks. The magnetic susceptibility measurements show that upon desorption of MeOH, the hysteresis width decreases slightly.

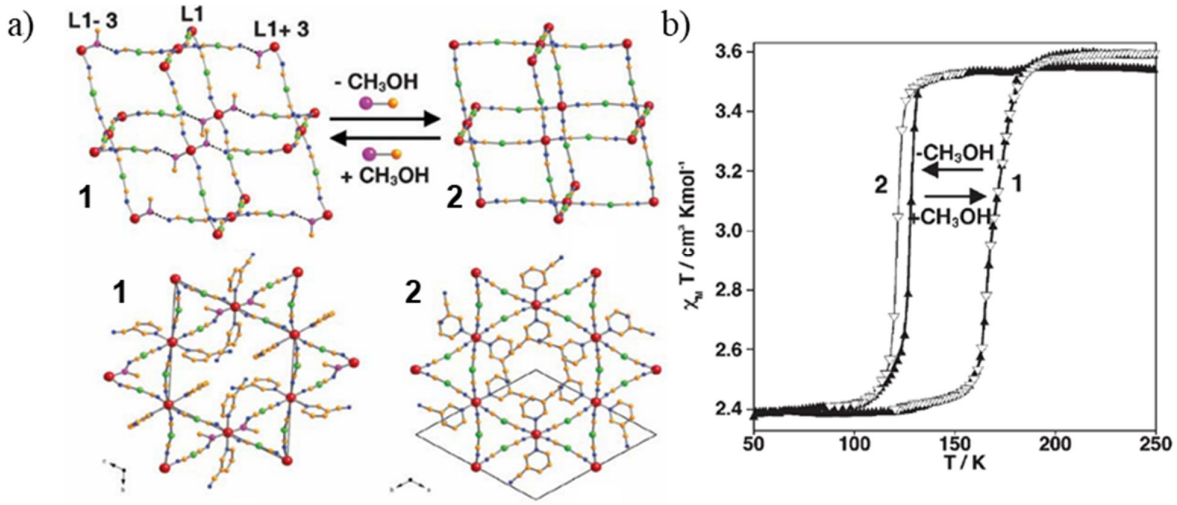

Figure 14. a) Structural modifications during the ligand substitution from 1 to 2. Top: perspective view of three layers interconnected via hydrogen bonds represented as dotted lines (1) and condensation of the three layers to form 2. Bottom: two perspective views of the coordination polymers 1 and 2 along the [001] and [100] directions, respectively. Color code: Fe in red, Au in green, N in blue, C in orange, O in red, H omitted. b) Magnetic susceptibility measurements for 1 and 2. Reprinted with permission from ref 99. Copyright 2006 Chemical Communications.[99]

1.1.3.4. Guest-induced SCO by chemical modification of the ligand

In recent years, this strategy has gained interest as a way to incorporate functionality without altering the initial structure and it can also be a useful approach to synthesize new SCO materials. Guest molecules can either form a covalent bond with the ligand,[113] or provoke a chemical reaction in it,[114] resulting on a direct modification of the ligand field strength. As mentioned above, the directionality and strength of the bonds and intermolecular interactions helps propagate the spin transition throughout the material.[115] Therefore, changing these pathways can alter the shape of the spin transition curve and whether it is direct or step-wise.[116] The first example of a chemical modification on the ligand after exposure to a guest molecule was reported by Kepert *et al.*[114] Here, they presented a 3D spin crossover Hofmann-type framework, $[Fe(bipytz)(Au(CN)_2)_2]$ (bipytz = 3,6-bis(4-pyridyl)-1,2,4,5-tetrazine), with a complete spin transition ($T_{1/2}\downarrow$=273 K, $T_{1/2}\uparrow$=277 K) and a 4 K thermal hysteresis. Exposure of this compound to an excess of 2,5-norbonadiene in a sealed vessel while heating results in a Diels-Alder reaction in the bipytz ligand, transforming it to bipydz (bipydz = 3,6-bis(4-pyridyl)-1,2-diazine). This is accompanied by a color change from purple to yellow, a shift of the spin transition to lower temperatures and a loss of the hysteretic behavior (Figure 15).

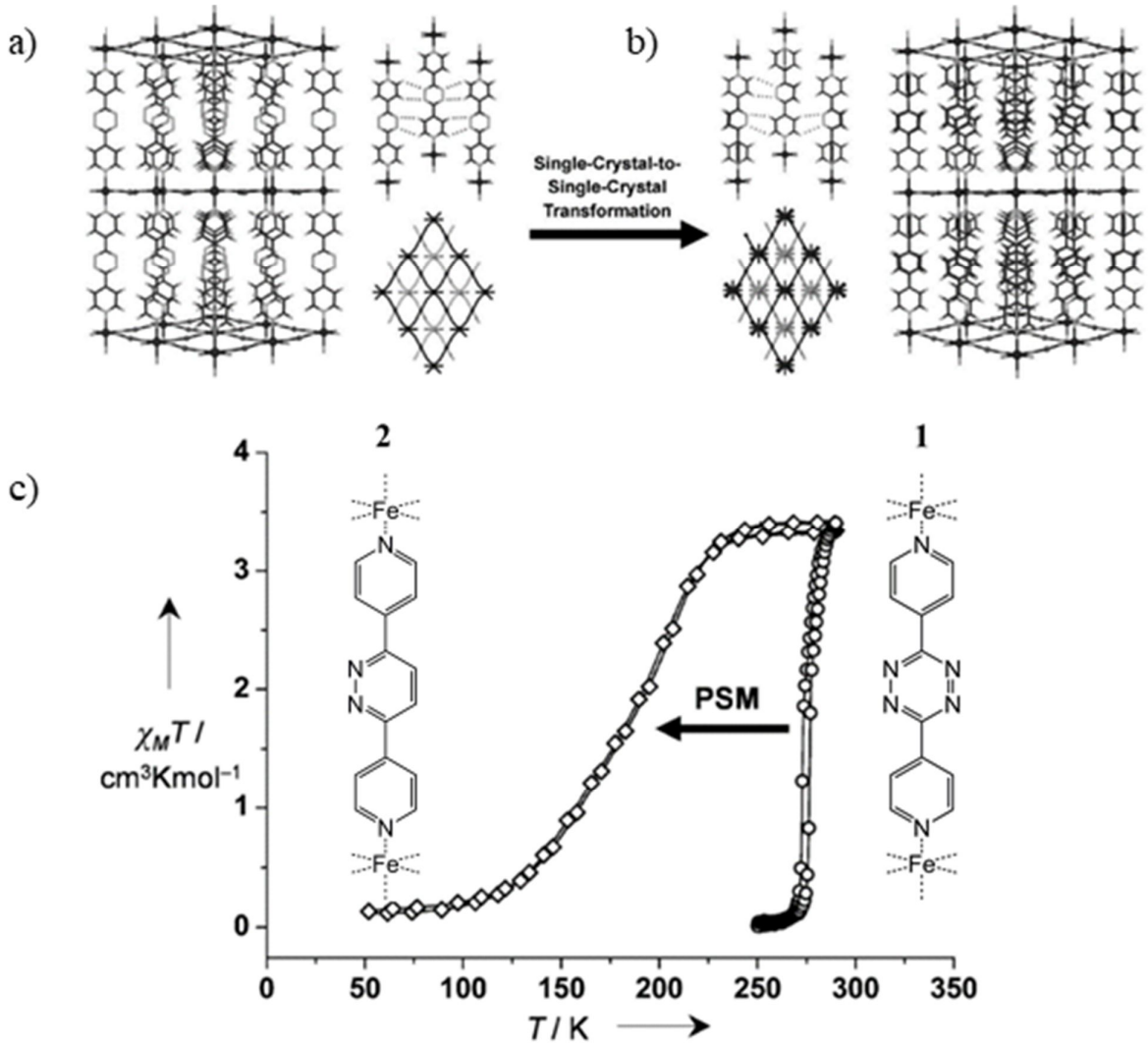

Figure 15. a) Structural representations of 1 and b) corresponding structural representations of 2. c) Magnetic susceptibility data for 1 (○) and post-synthetically modified 2 (◊). Reprinted with permission from ref 114. Copyright 2014 Angewandte Chemie International Edition.[114]

This has also been achieved by means of a reaction in solution. An example of this was reported by Tao and coworkers, where they reported a covalent reaction between the amino group of the $[Fe(C_2H_4N_4)_3](ClO_4)_2$ (FeL; $C_2H_4N_4$ = 4-NH_2-1,2,4-triazole) coordination polymer, and the carbonylic groups of 1- pyrenecarboxaldehyde (PCA) and Rhodamine B (RhB) (Figure 16).[113] According to the elemental analyses, 14.67% and 9.67% of 4-amino-1,2,4-triazoles on FeL reacted with PCA and RhB, respectively. FeL displays an incomplete, single-step spin transition, with $T_{1/2}\downarrow$ = 189 K and $T_{1/2}\uparrow$ = 197 K. The spin transitions for FeL-PCA and FeL-RhB, present a similar behavior to that of FeL, but with remarkable differences in the transition temperatures and hysteresis width (Figure 16b). The transition temperatures of FeL-PCA ($T_{1/2}\downarrow$ = 220 K and $T_{1/2}\uparrow$ = 230 K) and FeL-RhB ($T_{1/2}\downarrow$ = 252 K and $T_{1/2}\uparrow$ = 263 K) are higher than those of FeL, which may result from ligand-field strength changes and intra- and inter-chain interactions, induced by the graft of fluorophores. Furthermore, fluorimetric and magnetic studies at variable temperature reveal synergetic effects between the spin transition and fluorescence in both compounds.

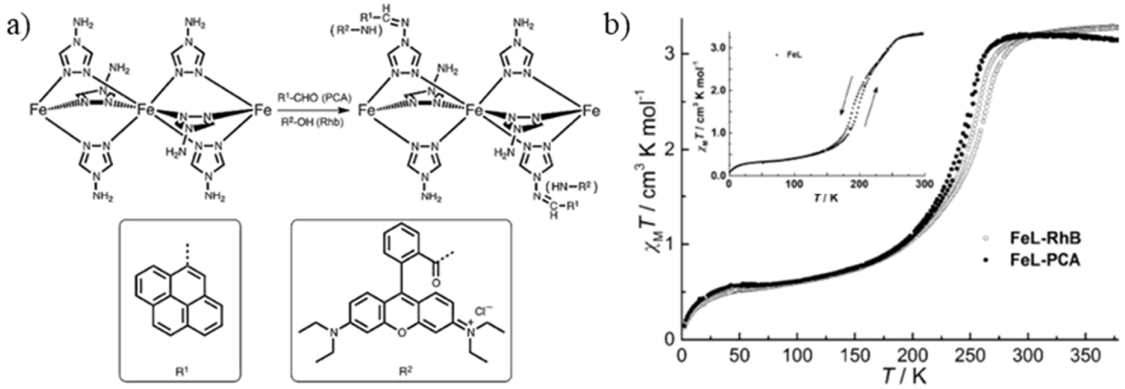

Figure 16. a) Scheme of the CPSM. b) Magnetic measurements for FeL-RhB and FeL-PCA and Inset: FeL. Reprinted with permission from ref 113. Copyright 2015 Angewandte Chemie International Edition.[113]

1.1.4. External stimuli: Pressure

Spin transition compounds can also respond to the application of external pressure as a stimulus.[24] This effect continues to be studied less in comparison to thermal- and light-induced SCO, mostly due to the experimental challenges of operating under variable temperature and pressure at the same time.[117] The use of pressure reduces the metal–ligand distances of SCO molecules and enhances the ligand field strength at the metal center. Thus, it is expected that application of pressure, irrespective of its source (mechanical or chemical), stabilizes the LS state and may also induce a transition from the HS to the LS state,[13,24,118] although exceptional cases have also been published where the HS state is stabilized under pressure.[119] The effect of pressure was corroborated experimentally by Ewald and coworkers on solutions of iron(III) complexes.[120] Since the main effect of the pressure is stabilizing the LS state, with increasing pressure the transition curves generally shift to higher temperatures and they also become slightly less abrupt and the hysteresis width decreases.[13,15,25,121] Li *et al.*[122] explored this effect in a 3D iron(II) coordination polymer $Fe(NCS)_2(TINM)\cdot 1/2TINM$ (TINM = tetrakis(isonicotinoxymethyl)methane) with twofold interpenetrated topology.

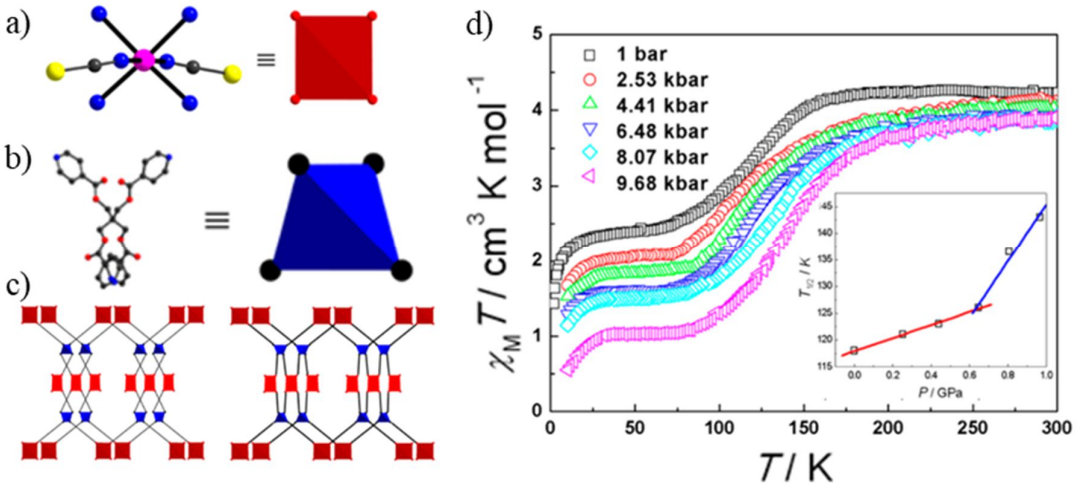

Figure 17. a) Square and b) tetrahedral building blocks that construct the c) 3D structure. Color code: Fe in pink, N in blue, C in black, S in yellow, O in red, H omitted. d) Magnetic behavior *vs*. *T* at different pressures (inset: SCO temperature *vs*. pressure). Reprinted with permission from ref 122. Copyright 2018 Crystal Growth and Design.[122]

At ambient pressure and temperature, the value of $\chi_M T$ is 4.22 $cm^3 \cdot K \cdot mol^{-1}$, mildly higher than the usual for Fe(II) in the HS state, that could be attributed to unstable solvent molecules and spin orbital coupling of iron centers. When cooling this value is maintained virtually constant until 170 K, and then drops gradually to 2.26 $cm^3 \cdot K \cdot mol^{-1}$ until 60 K, where it remains stable down to 17.5 K. This value indicates an incomplete spin transition. Below 17.5 K, there is a strong decrease of $\chi_M T$, that can be associated with zero-field splitting of the remaining HS-Fe(II) centers. When heating up, no hysteresis is observed. As is generally the case, the value of $\chi_M T$ gradually decreases as the external pressure is increased (Figure 17), while $T_{1/2}$ rises to higher temperatures (inset of Figure 17).

The change of the spin crossover properties, like the critical transition temperature, the shape and position of the curves and the width of the hysteresis, that results from the application of pressure, leads to potential practical applications as a pressure sensor.[13]

1.1.5. External stimuli: Light

Given the possibility of potential technological applications, light is a particularly useful way to "communicate" with a specific molecular system.[15] Therefore, the possibility of controlling the spin state with light prompted the idea that SCO compounds could be useful as optical switches in memory devices. In this regard, the most remarkable result in the SCO field is undoubtedly the discovery of the LIESST effect, where the photoconversion of the metal center to the HS state is feasible when the LS material is irradiated with the typical wavelength for the *d–d* absorption bands.[45,123] It was first observed by McGarvey and Lawthers in 1982 in solutions at relatively high temperatures,[124] although the resulting states induced by light were short-lived. It was two years later when this remarkable photophysical phenomenon was reported for the first time in the solid state by Decurtins *et al.*[125] in a single crystal of $[Fe(ptz)_6](BF_4)_2$ (ptz = 1-propyltetrazole). Another example of the LIESST effect was reported by Zhang *et al.* in a 1D iron(II) coordination polymer, $\{Fe(DPIP)_2(NCSe)_2\}_n \cdot 4DMF$ (DPIP = N,N′-dipyridin-4-ylisophthalamide) (Figure 18).[126]

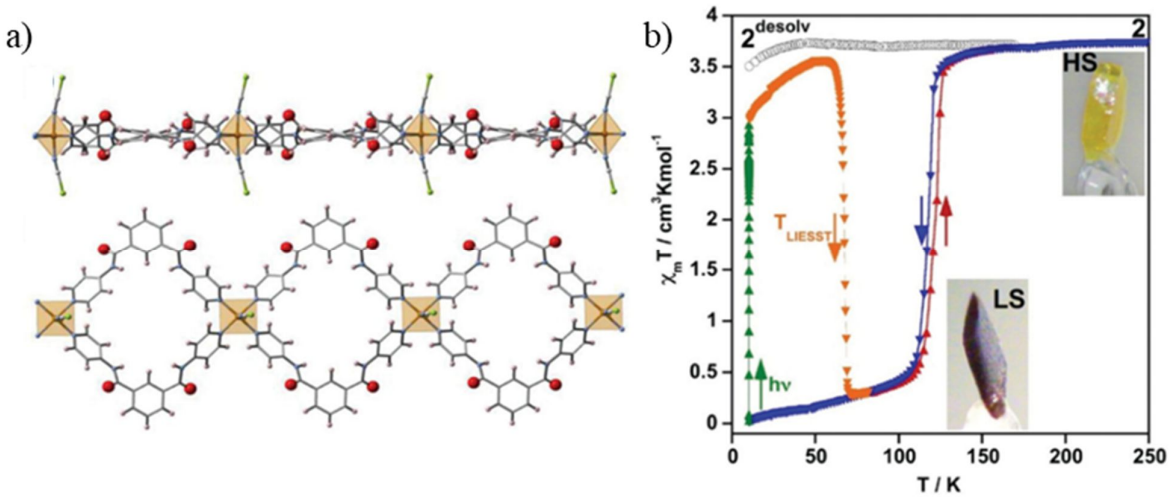

Figure 18. a) Side and top views of the 1D chain structure. Color code: Fe in orange, N in blue, C in grey, Se in green, O in red, H omitted. b) Magnetic and photomagnetic properties of 2. Inset: pictures of a single crystal in the HS state (yellow) and LS state (dark red-violet). Reprinted with permission from ref 126. Copyright 2019 Dalton Transactions.[126]

The equatorial positions of the metal center are occupied by two independent DPIP ligands that serve as bridges linking the Fe(II) centers, thereby generating a 1D chain in the form of a loop. This

compound exhibits strong thermochromism (from dark red-violet to yellow) associated with a spin transition centered at 120.5 K (5 K hysteresis), and complete LIESST effect at low temperatures. The photogeneration of the metastable HS state is achieved in under an hour at 10 K by irradiating with red light (λ = 633 nm). As the temperature is further increased, the $\chi_M T$ value decreases abruptly, signifying a relaxation from the metastable HS to the LS state.

Although the LIESST effect was a very relevant breakthrough, in most SCO compounds it is still produced at temperatures below that of liquid nitrogen. Thus, Zarembowitch *et al.* developed an alternative approach to induce photoconversion of spin states at room temperature, the ligand-driven light-induced spin changes (LD-LISC).[127,128] This strategy consists in the synthesis of complexes with ligands that are isomerically stable and can suffer photoinduced modifications, which leads to a change in the ligand field and could, therefore, trigger the spin transition at high temperatures.[13,15] The LD-LISC phenomenon was reported for the first time for $[Fe(stpy)_4(NCBPh_3)_2]$ (stpy =4-styrylpyridine) where the cis–trans photoisomerization of a C=C integrated in stpy (Figure 19a) was exploited.[127–129] In the temperature range where the two isomers are present, the photoisomerization of the ligand leads directly to a SCO transition. When the ligand presents the trans configuration, the compound displays an abrupt transition at 190 K, whilst the cis derivative maintains the HS state upon cooling down (Figure 19b).[129]

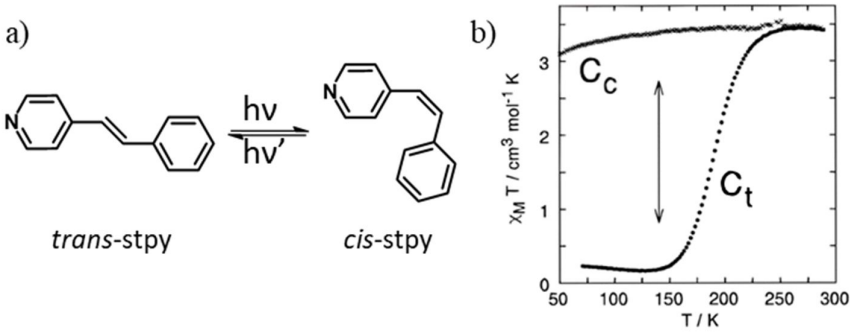

Figure 19. a) cis–trans photoisomerization of stpy. b) Temperature dependence of $\chi_M T$ for the C_t and C_c forms of $[Fe(stpy)_4(NCBPh_3)_2]$. At 140 K, photoinduced C_c-C_t conversion results in a HS to LS transition. Reprinted with permission from ref 129. Copyright 1996 Inorganic Chemistry.[129]

The operating temperature and excitation wavelengths can be altered by modifying the composition of the compound. For example, Nishihara and coworkers[130] studied the effect of similar ligands on LD-LISC. For that, the *Z*-to-*E* photoisomerization was studied in a family of Fe(II) coordination polymers (Figure 20) coordinated to (*Z*)-2,6- di(1H-pyrazol-1-yl)-4-styrylpyridine ligands (*Z*-H) and its derivatives *Z*-CN and *Z*-NO_2 (substituted by cyano and nitro groups in the 4-position, respectively). The samples *Z*-H, *Z*-CN, *Z*-NO_2, and *Z*-NO_2·acetone were irradiated with visible light (λ > 420 nm) for several days until considerable color changes were observed. Temperature-dependent magnetic measurements were conducted for the original samples and their respective photoirradiated samples. *Z*-CN presents a $\chi_M T$ value characteristic of the HS state in the whole temperature range. Upon irradiation a decrease in the magnetization value is found, as well as the appearance of a gradual thermal SCO. *Z*-H displays a behavior similar to *Z*-CN, for both the initial sample and the irradiated one. *Z*-NO_2 shows a gradual hysteretic thermal spin crossover *ca.* 150 K. In this case, the magnetization value increases after light irradiation, with the thermal SCO being very similar to the previous irradiated samples. *Z*-NO_2·acetone presents thermal SCO around room temperature. Photoisomerization from *Z* to *E*, increases the $\chi_M T$ values, similarly to *Z*-NO_2, and shows the greatest modification in $\chi_M T$ at room temperature out of the four samples.

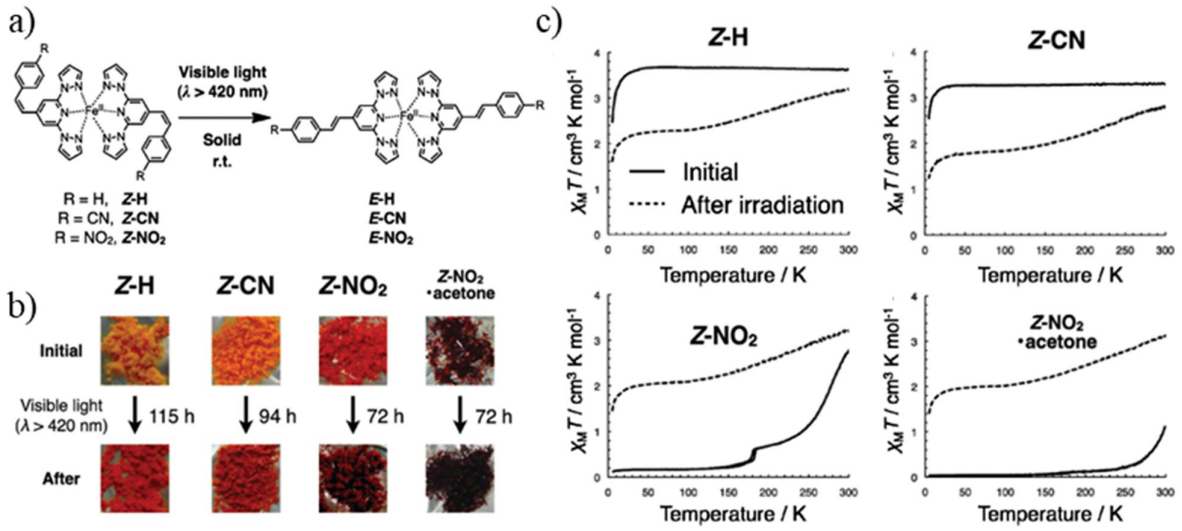

Figure 20. a) Photoisomerization from *Z* to *E*. b) Color changes of the samples upon irradiation. c) Temperature dependence of $\chi_M T$ for *Z*-H, *Z*-CN, *Z*-NO_2, and *Z*-NO_2·acetone before and after irradiation. Reprinted with permission from ref 130. Copyright 2012 Inorganic Chemistry.[130]

1.1.6. Spin crossover composites

Generally, powdered materials are not easily implemented in devices. Therefore, in order to exploit the properties of CPs, extensive research has been conducted with the aim of embedding them in matrixes, leading to the formation of polymeric composites. These materials consist on multi-phase compounds in which one or more of the phases is a polymer.[131] In most cases, the matrix employed is an organic polymer. By combining these components, the initial physical properties vary from those of the individual components. Frequently, the major target driving the development of these materials in various fields such as automotive, aerospace and construction is the alteration of the thermal and mechanical properties, but also to afford the opportunity of creating a wide array of original physical properties.[132]

Within the scope of transition metal ion SCO complexes, polymeric composites have been developed for several reasons.[131] In early years, the embedding of SCO complexes was conducted to enable some physical characterizations that were not feasible employing microcrystalline powder samples or liquid solutions. For this purpose, SCO composites were manufactured through the use of simple methods such as drop casting or spin coating. Over the last twenty years, the research on SCO compounds has been largely oriented to the search for potential technological applications. Consequently, the necessity to integrate devices and process SCO materials in different shapes and sizes (from the nanometer to the macroscopic scale) has also grown considerably. This juncture has prompted significant research into the embedding of SCO materials and nanomaterials[70] into malleable and processable polymer matrixes by progressively more refined methods, for the development of SCO composites exhibiting a synergy between the properties of the polymer matrix and the SCO compound. This can enable the development of SCO materials for applications such as actuators, sensors and energy harvesters.[133,134] Embedding SCO complexes in polymeric matrixes is a straightforward, yet compelling and generic method for achieving processable SCO materials, relevant for their various applications and integration into devices. Besides facilitating the implementation of these materials, the appropriate selection of the matrix and concentration of the SCO compound can be used to tune the spin transition.

One example of a potential application that is being explored, is the use of SCO materials as molecular actuators, which involves the use of switchable materials capable of translating thermal,

electrical, optical or chemical stimuli into useful mechanical work. In fact, the reversible change of volume of molecular SCO switches has been successfully explored to develop mechanical actuators,[135] for integration into microelectromechanical systems[136] and in "artificial muscles."[137] In addition, improved compatibility with current technology would be achieved by the use of electrical stimuli to trigger the spin transition. However, bulk SCO solids are characterized by rather low electrical permittivity and conductivity values. Improved electrical properties can be obtained by synthesizing hybrid materials containing both SCO materials and electroactive bricks. An example of this was reported by Bousseksou *et al.*, where they synthetized a novel and versatile SCO-ferroelectric polymer nanocomposite, with the objective of acquiring new electromechanical properties (Figure 21).[133] To this end, they combined $[Fe\{(Htrz)_2(trz)\}_{0.9}(NH_2\text{-}trz)_{0.3}](BF_4)_{1.1}$ spin crossover particles with poly(vinylidene fluoride-co-trifluoro-ethylene), P(VDF-TrFE), and poly(vinylidene fluoride) (PVDF) (30–70% mol) to form a macroscopic, freestanding, and flexible nanocomposite. The composite exhibits an electro–mechanical synergy between the two constituents, and is highly attractive for its easy and versatile processing. Notably, this results in the concomitant macroscopic thermal expansion and electrical discharge peaks at the spin transition. Moreover, both strain and permittivity changes (which also displays an important hysteresis) accompany the spin transition, providing clear evidence of a strong electromechanical coupling between the components of the composite. These findings afford a novel pathway for the development of molecular SCO materials as actuators in artificial muscles and generators in thermal energy harvesting devices.

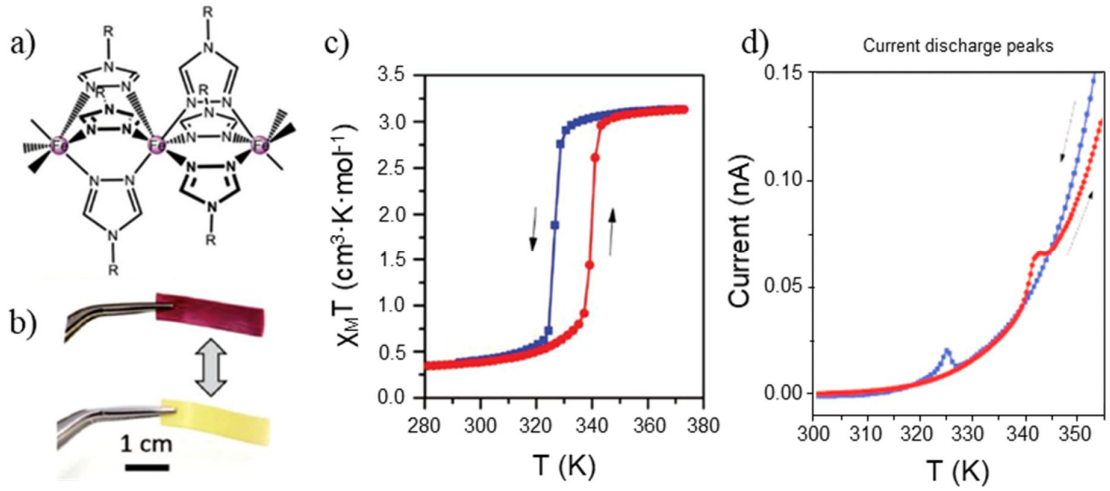

Figure 21. a) Scheme of the SCO complex. b) Photographs of the flexible, freestanding film in the LS (violet) and HS (yellow) states. c) Variable-temperature magnetic susceptibility. d) Short-circuit current under zero applied bias on heating and cooling of the P(VDF-TrFE)/SCO composite. Reprinted with permission from ref 133. Copyright 2018 Advanced Materials.[133]

The color changes linked to SCO is of great technological interest for the use of these CPs as sensors. This trend includes the use of devices such as optical digital cameras, computer screens and microscopes for colorimetric detection.[138] Therefore, the synergy between the SCO and thermochromism can be monitored through the use of a photographic digital camera, thereby enabling a straightforward method for temperature detection. To this end, Capitán Vallvey and coworkers[80] developed several optical sensors by using different matrixes of different polarity, where different amounts of the SCO material $[Fe(NH_2\text{-}trz)_3](BF_4)_2$ were embedded (Figure 22). Images of the sensors were recorded with a digital camera. The images are analyzed by numeric representation of color through RGB, since it has a better correlation as it maintains the greatest difference in histogram values. Among the various types of matrixes employed, the best results were

obtained by embedding the SCO material in polyurethane hydrogel D6 and PMMA, which present an excellent time response, on the scale of seconds. This composite is therefore a suitable candidate for possible applications as a temperature sensor, avoiding uncertainty in the temperature range from 10 °C to −24 °C. Thus, the operational range would go from −20 to 25 °C. This analytical range can be refined by incorporating different SCO materials, and the appropriate selection of matrixes. Temperature quantification can be easily conducted, even by the naked eye, based on the color change response of the composite to each temperature. Furthermore, uniform sensing films can be fabricated in a one-step using screen-printing techniques.

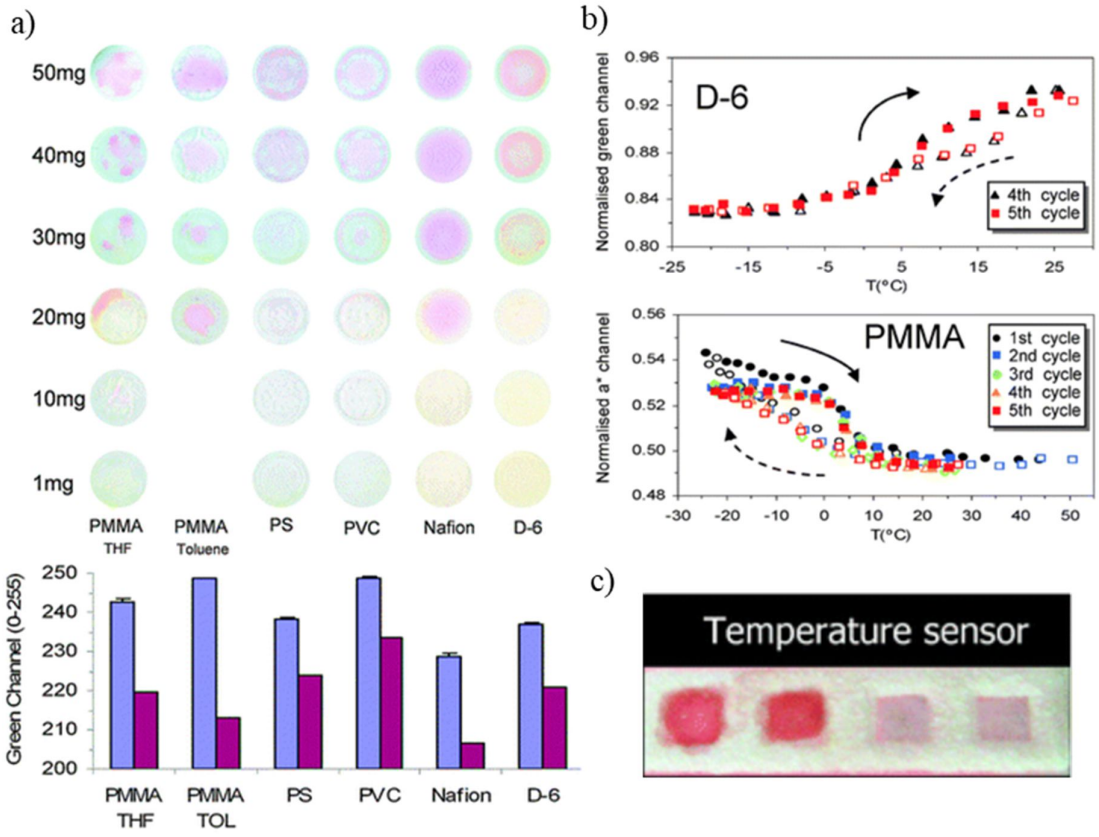

Figure 22. a) Optical sensors by different polymeric matrixes. Sensor colors are all related to exposure at −25 °C. Differences in green channel values between white (high temperature) and pink/violet (low temperature) for each tested sensor. b) Thermochromism induced by thermal variation in D6-PMMA sensors. c) Example of a temperature sensor built by a screen-printing technique. Reprinted with permission from ref 80. Copyright 2013 Chemical Communications.[80]

In summary, the presence of spin transition in a material is very interesting as it offers the possibility of using it in a wide variety of applications, due to the spin state change upon external stimuli, but it is not the only attractive property for the development of new functional materials. Another particularly exciting one, considering the current technological progress, is the presence of electrical conductivity, especially if combined with some other physico-chemical property for the development of multifunctional materials.

1.2. ELECTRICAL CONDUCTIVITY IN COORDINATION POLYMERS

Nowadays, a very interesting property in order to develop applications is the presence of conductivity in a material, since electronic devices are shaping the world as we know it. The enormous technological progress in the past 50 years has mainly been based on the gradual miniaturization of these devices and their components to develop more complex and potent platforms. Generally, metal chalcogenides have been used for this purpose. Nevertheless, they have a major design limitation because of the shortage of suitable inorganic anions.[139] Consequently, the field of electronics is undergoing a drastic transformation from a materials viewpoint, due to the shift from purely inorganic, organic, and silicon-based materials to hybrid organic–inorganic materials. Thus, coordination polymers and metal–organic frameworks are gaining increasing interest in the world of electronics, in order to develop more sophisticated and potent electronic devices that can enhance current properties and provide new ones.[139] MOFs and CPs provide a great opportunity for tuning the electric properties through chemical design by the rational choice of the building units or by post-synthetic modification methods.[139,140] For this purpose, a nearly endless variety of ligands and metal ion combinations is available, which allows for a simple production of tailor-made materials. In addition, the connectivity between them may also be modified, and, for MOFs, functional guests can also be embedded in the pores. Their versatility and diversity of crystalline structures provide tunable properties and offer significant possibilities for various applications.[140] For example, the association of electrical conductivity with porosity or spin transition can yield unparalleled technological opportunities for their inclusion in functional devices.[139]

However, CPs and MOFs are generally insulating and display very low electric conductivity, due to the fact that they are frequently built from hard metal ions and O- or N-donor redox-inactive ligands which are unable to supply effective charge transport routes.[140] Several design approaches have been devised to improve their conductivity, such as post-synthetic modification of the metal or the organic ligand, or inserting guest molecules into pores.[140] In recent years, and with the help of these strategies, impressive progress has been achieved in this regard, and numerous reports on conductive CP and MOFs have been published.[141] In certain cases, the use of these materials for fuel cells and as electrodes in electrochemical devices has been successfully explored.[142]

One of the most prominent examples of a conductive coordination polymer was reported by Zhu *et al.*[143] that described highly crystalline 2D nanosheets of a copper coordination polymer, Cu-BHT (BHT= benzenehexathiol), with formula $[Cu_3(C_6S_6)]_n$. Morphology and structure characterization show that each Cu center coordinates to four S in a square-planar manner. Each BHT is connected to six different BHTs via the shared Cu atoms, resulting in a dense topological structure with sixfold symmetry (Figure 23a). The electrical conductivities of Cu-BHT nanosheets with various thicknesses (15–500 nm) were measured and it was revealed that all films display high electrical conductivities spanning from 750 to 1580 $S \cdot cm^{-1}$ at RT, that are not related to the size of the film. The latter value (1580 $S \cdot cm^{-1}$) is the greatest conductivity value ever recorded for a CPs. On the other hand, a slight dependence of the conductivity with the temperature was found. In addition, this material exhibits a non-linear correlation between the logarithm of the conductivity and the reciprocal of the temperature (Figure 23b), which is typically seen in conducting coordination polymers. The activation energy (E_a) steadily increases with the temperature and fluctuates between 0.12 meV at 40K to 2.06 meV at 300 K, which is exceptionally narrow, particularly in the low temperature range. Interestingly, this material could be used as a transparent electrode, since it also presents good transmittance in the visible region and small sheet resistances.

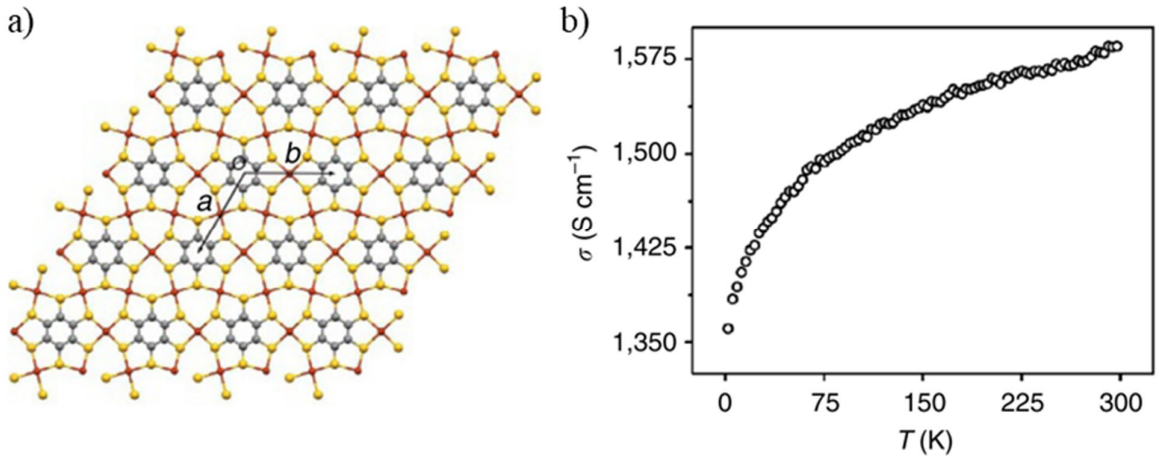

Figure 23. a) Two-dimensional lattice of $[Cu_3(C_6S_6)]_n$. Color code: Cu in red, C in blue and S in yellow. b) Electrical conductivity of a 150-nm film as a function of the temperature. Reprinted with permission from ref 143. Copyright 2015 Nature Communications.[143]

As mentioned above, the conductive properties of coordination polymers can be combined with others, to develop certain applications. For example, the presence of electric conductivity may be of interest in the development of sensing devices. In this way, the presence of an analyte that causes a change in the electrical current of the material, would allow for the development of sensors that, unlike vapochromic ones, do not need to be constantly monitored to detect the change. Even better, a material that upon the inclusion of a guest molecule, displays a change in both the conductance and its optical properties (whether that change is due to a spin transition or not) would constitute a very elegant sensing device. Although the electrical properties of SCO materials have been studied, research on these properties in combination with vapochromism has not been widely explored. Besides SCO materials, other coordination polymers have been explored in this regard, with the change in the optical properties being primarily in their luminescence.

An example of this was reported by Kato and coworkers[144] in the form of two luminescent and highly conductive Pt(II) coordination complexes [PtCl(tpypy)]Cl and $[PtCl(tpypyH)]Cl_2$ (1 and 1·HCl, respectively; tpypy = 2,2':6',2''-terpyridine-4',4'''-pyridine). The transformation between the two is reversible by exposure to humid HCl gas and drying with temperature (Figure 24a). Both complexes show a strong relative humidity (RH)-dependent proton conductivity. A remarkably high conductivity value ($\sigma = 6.8 \cdot 10^{-3}$ S·cm^{-1}) was measured for 1·HCl at 95% RH at 298 K, which is similar to that of the well-known proton conductor, Nafion 117 (~0.1 S cm^{-1}). Conversely, the conductivity diminishes substantially when the RH is reduced to 0%, suggesting that 1·HCl possesses an electron insulating nature. The activation energies of $1 \cdot 2H_2O$ and $1 \cdot HCl \cdot 6H_2O$ were calculated at 0.30 and 0.19 eV at 95% RH, respectively, which are fairly small values and suggest a conduction mechanism of proton hopping through the hydrogen bond network. In addition, the luminescence of 1·HCl also switches when the relative humidity is changed, from orange (0% RH) to red (23% RH) and lastly to bright orange (95% RH) (Figure 24b), which indicates the presence of two vapor-induced structural transformations. In addition, the excitation and emission spectra of $1 \cdot H_2O$ change when exposed to MeOH vapor, whereas in the case of $1 \cdot HCl \cdot 2H_2O$, different vapochromic behaviors are observed in response to various hydrophilic vapors including, MeOH and EtOH. This represents the first highly proton-conducting and switchable vapochromic material regulated by HCl adsorption/desorption and can thus be used to monitor the proton conducting state by the color and luminescence of the material.

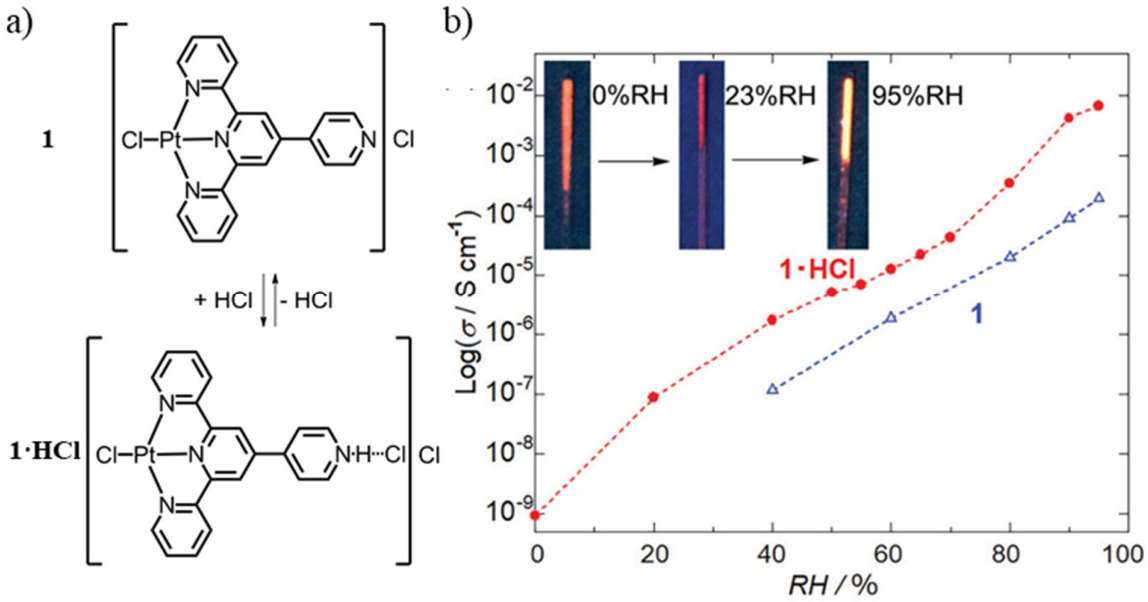

Figure 24. a) Molecular structures and reversible HCl addition and removal between 1 and 1·HCl. b) Log(σ/S·cm^{-1}) vs. RH profiles at 298 K for 1·HCl and 1. Insets: Luminescence images of 1·HCl in 0% (left), 23% (center), and 95% (right) RH. Reprinted with permission from ref 144. Copyright 2019 Journal of Materials Chemistry C.[144]

1.3. OBJECTIVES

This Doctoral Thesis studies the development of several non-porous iron(II) coordination polymers for different multifunctional applications, mainly as sensors and as controllers of temperature fluctuations under solar irradiation. Hence, every chapter in this Thesis begins by detailing the synthesis of these materials. Thereafter, in order to implement the synthesized complexes in technological areas, a study of the optical, thermal, structural and magnetic properties of the materials has been conducted, both before and after being subjected to external stimuli, such as temperature and the adsorption of small volatile molecules. In addition, Chapters 2 and 3 include the electrical characterization of the materials, to enable their use as electro-optical sensors for small guest molecules. Chapter 4 explores the spin transition properties resulting from a covalent post-synthetic modification of the organic ligand in a coordination polymer. Finally, in Chapter 5 the combination of the coordination polymers with organic matrixes is studied, including the variation of the spin transition properties arising from this combination, and their application as thermal-fluctuations controllers.

2. REVERSIBLE ELECTRO-OPTICAL ACETONITRILE SENSOR IN A NON-POROUS COORDINATION POLYMER

The rise in emissions of volatile organic compounds (VOCs) and their consequent impact on the quality of air and water has emerged as one of the main ecological concerns of our time.[145] VOCs emissions can originate from various diffuse and point sources, such as industrial discharges, agricultural runoff, solvent use, water treatment, and accidental spills, while contributions also come from natural sources.[146,147] In addition, controlling VOCs emissions is particularly difficult as they can also be emitted from the manufacture and use of numerous ordinary domestic products.[146,147] It has been established that some VOCs are highly toxic or carcinogenic and can cause both short- and long-term damage to human health (from sensory irritation to behavioral, neurotoxic, hepatoxic and genotoxic effects, according to the World Health Organization)[148] as well as on the environment.[147] As a result, several major environmental safety institutions have defined guides to reduce human exposure to VOCs.

One of these VOCs is acetonitrile (Figure 25), which is mainly used as an organic solvent in extraction processes, and is also widely employed in textile dyeing, as a metal cleaner and for battery applications.[149–151] Exposure to acetonitrile generally occurs via inhalation and dermal contact in workplaces where acetonitrile is manufactured or employed, given its high volatility. The European Chemicals Agency (ECHA) suggests a time-weighted average concentration of 40 ppm of acetonitrile as the maximum exposure limit for a 40-hour workweek.[149,150] Toxicology studies have shown evidence that large levels of acetonitrile may potentially cause neurotoxicity, nausea, impaired motor activity, shallow and irregular respiration and, in extreme cases, death.[149,150]

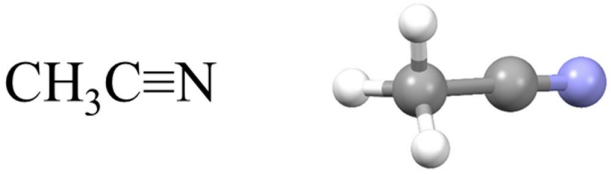

Figure 25. Chemdraw and Mercury representations of an acetonitrile molecule.

Highly sensitive analytical techniques are currently employed for the accurate quantification of VOCs. The two main groups of instruments that have been used for VOCs identification and quantification are gas or liquid chromatography and mass spectrometry.[152–154] Gas chromatography analysis of VOCs typically employs flame-ionization detection or electron-capture detection[153] and it is the most frequently used analytical technique for acetonitrile detection.[155] Nevertheless, all these techniques come with some drawbacks, such as high cost, lack of portability, lower throughput, complex and time consuming pre-treatment steps and require highly qualified operators.[147,156]

To exploit more cost-effective alternatives, the emergence of porous materials such as MOFs[157] and Covalent Organic Frameworks (COFs)[158] has yielded commendable results. These materials have rapidly arisen as a kind of functional materials with potential applications in catalysis, magnetism, electrical conductivity, luminescence, gas storage and enantioselective separations, drug delivery, biomedical properties, optoelectronics, and sensing.[9,156,159,160] They have been extensively used as sensing materials due to tunable pore dimensions and specific functional sites[100,161] and numerous studies have been published on the applications of MOFs for VOCs sensing specifically.[147] These materials are excellent candidates for sensing applications since certain MOFs exhibit interesting dynamic behavior that can be triggered by external stimuli, such as adsorption and desorption of guest molecules.[100,147,162] These perturbations can modify the MOF physical properties, thus opening the possibility to their application as switches and molecular sensors.[9,100,147,162]

Recently, increasing attention has been given to materials where, in the absence of pores, such exchange could still occur through a process of diffusion throughout the crystal lattice,[163] such as non-porous coordination polymers. This process may lead to a variation of the macroscopic properties of these materials, which in turn could produce an easy-to-measure response, in agrement with the definition of chemosensor.[106] Specifically, these chemosensors could display easily detectable changes in almost any physicochemical property, such as the luminescent emission,[156,160] the electrical conductivity,[9,147] the magnetic behavior[100] and a color change.[9,100] While it is rather common for a color change to occur upon insertion of small molecules,[164,165] it is far less frequent for a change in the electrical current to happen, although some examples have been reported in recent years.[147,166–169]

Here, a novel non-porous crystalline 1D Fe(II) coordination polymer $_\infty${$[Fe(H_2O)_2(CH_3CN)_2(pyrazine)](BF_4)_2 \cdot 2CH_3CN$} (**1**·2$CH_3CN$), acting as porous material that hosts acetonitrile is presented.[170] The crystalline structure was determined, and the physical changes that occur when the crystals are heated were characterized by several techniques, including optical reflectivity, infrared spectroscopy, differential scanning calorimetry, elemental analysis, thermogravimetric analysis and powder X-ray diffraction. In addition, in collaboration with Dr. Enrique Burzurí the electric transport through the crystals was measured as a function of the temperature.

2.1. SYNTHESIS OF COMPOUND 1·2CH_3CN

All chemicals and reagents used in this thesis were purchased from commercial suppliers and used as received.

2.1.1. Synthesis of $_\infty${$[Fe(H_2O)_2(CH_3CN)_2(pyrazine)](BF_4)_2 \cdot 2CH_3CN$} (1·2$CH_3CN$) and $_\infty${$[Fe(H_2O)_2(CH_3CN)_2(pyrazine)](BF_4)_2$} (1)

Synthesis of compound **1**·2CH_3CN was carried out at room temperature. A solution of iron(II) tetrafluoroborate hexahydrate (0.64 mmol, 216 mg) in 2.5 mL of acetonitrile was added drop by drop to a solution of pyrazine (1.2 mmol, 96.1 mg) in 2.5 mL of acetonitrile. The resulting solution was stirred for 15 minutes and filtered, affording a yellow solution. After one day, needle-shaped yellow crystals appeared (58%, 190 mg).

Anal. calcd (%) for **1**·2$CH_3CN \cdot 0.6H_2O$: C 27.69, H 4.10, N 16.14; found C 27.85, H 3.72, N 15.77. FTIR **1**·2CH_3CN (cm^{-1}): ν = 3481 (w; ν(OH)), 2309 (w; ν(C≡N)), 2281 (w; ν(C≡N)), 1642 (m; ν(CC)), 1488 (w), 1423 (s; δ(CH)), 1366 (w), 1289 (w), 1058 (s), 1002 (s, ν(BF4)), 817 (s; δ(ring)), 766 (m; δ(CCN)), 589 (w), 518 (w), 466 (m).

1·2CH_3CN powder was heated in the Linkam T95 system controller at 50°C for 5 hours to eliminate the uncoordinated acetonitrile (**1**). In the case of a single crystal, acetonitrile is eliminated after 2 minutes.

Anal calcd (%) for **1**·0.6H_2O: C 21.91, H 3.49, N 12.77; found C 21.73, H 3.31, N 12.6. FTIR **1** (cm^{-1}): ν = 3481 (w; ν(OH)), 2306 (w; ν(C≡N)), 2277 (w; ν(C≡N)), 1641 (m; ν(CC)), 1490 (w), 1423 (s; δ(CH)), 1369 (w), 1288 (w), 1059 (s), 998 (s, ν(BF4)), 815 (s; δ(ring)), 573 (w), 518 (w), 455 (m).

Reversibility could be attained in two ways. The first one consists on adding a few drops of acetonitrile to the **1** powder and drying it using filter paper. In the case of a single crystal, only one drop of acetonitrile is necessary.

Reversibility was also achieved by exposing the **1** crystals or powder to an acetonitrile atmosphere. For exposing the materials to various volatile organic compounds at saturated vapor pressure in a reactor, a protocol was followed all throughout this doctoral Thesis. For this purpose, a screw vial for chromatography (diameter 12 mm, height 32 mm) displaying 10 mg of **1**·2CH_3CN was placed in a clear glass vial (diameter 27 mm, height 55 mm) containing 0.1 ml of pyrrole. The glass vial was sealed and kept at room temperature overnight to allow the gas-solid reaction between the VOC and **1**·2CH_3CN (Figure 26).

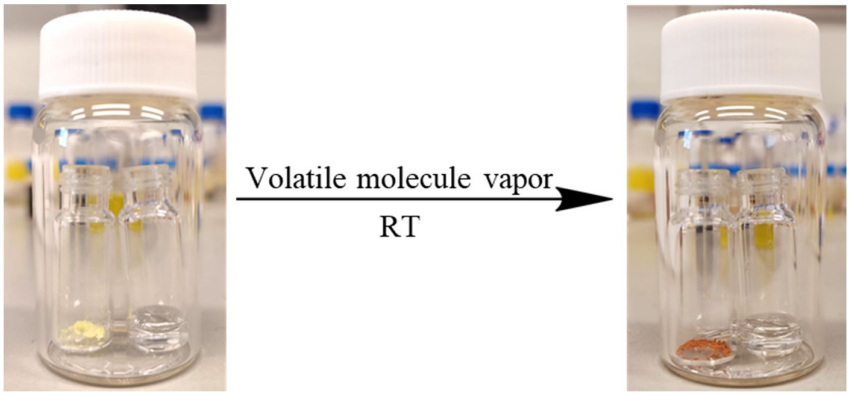

Figure 26. Exposition of **1**·2CH_3CN to acetonitrile vapor following the reported protocol.

Anal calcd (%) for **1**·2CH_3CN·0.35H_2O (after exposure to acetonitrile): C 27.93, H 4.04, N 16.28; found C 28.26, H 3.76, N 15.95.

2.2. RESULTS AND DISCUSSION

2.2.1. Structural study

The **1**·2CH_3CN coordination polymer crystallized in the orthorhombic space group *Cmca* (Annex A1). In this structure there is one crystallographically independent iron(II), which is coordinated octahedrically with two H_2O molecules, two acetonitriles (CH_3CN) and two pyrazines. Pyrazine acts as a bridging ligand between two neighboring irons, resulting in the formation of 1D polymeric chains along the *a* axis (Figure 27). The distance between Fe-N(pyrazine) is 2.225 Å, and Fe-N(CH_3CN), 2.163 Å (Annex A2). These distances are characteristic of high spin (HS) iron(II).[106,171]

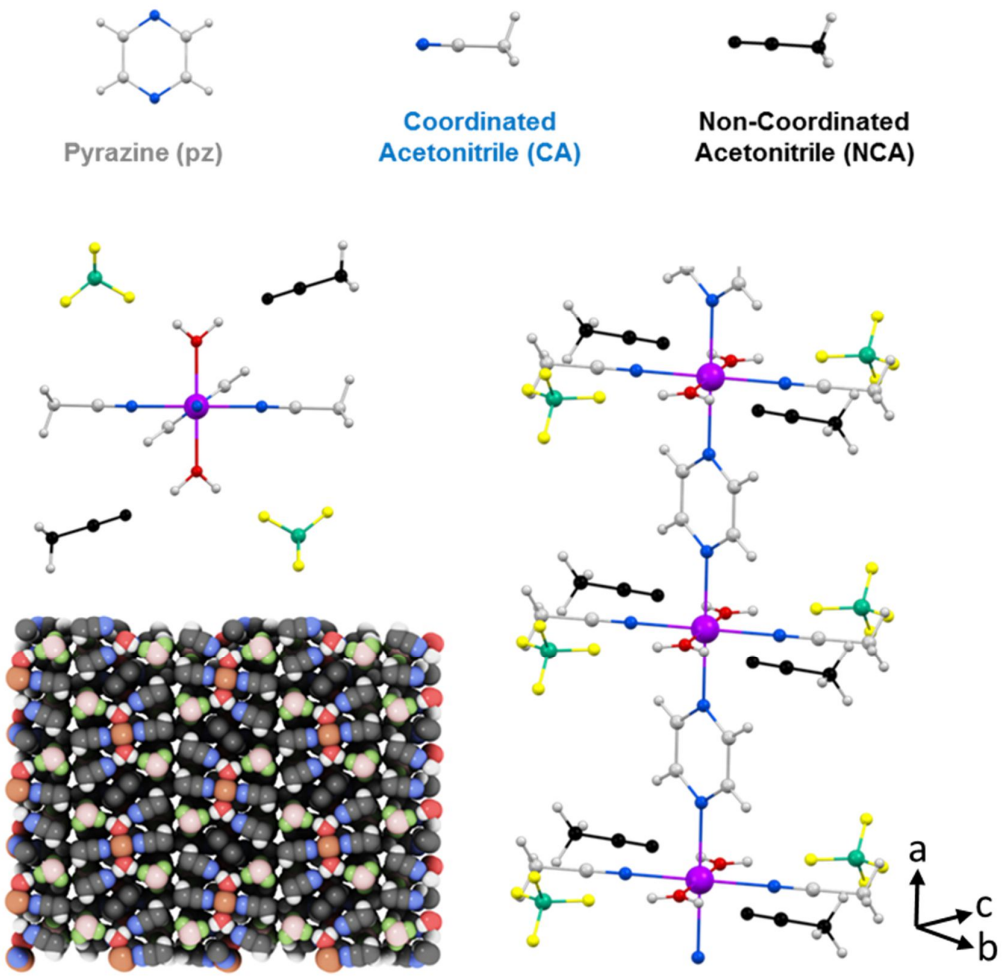

Figure 27. Crystal structure of **1**·2CH_3CN, where Fe is represented in purple, C in grey, N in blue, O in red, B in green, F in yellow, H in white and the uncoordinated acetonitrile in black.

There is no direct inter-chain interaction although they interact via the BF_4^- counterion, which forms a hydrogen bond with a water molecule of one chain, with F-H (H_2O) bond lengths of 1.795 Å (F-O: 2.655 Å), and a Van der Waals interaction with a coordinated acetonitrile of the adjacent chain, with F-H (CH_3CN) of 2.270 Å (F-C: 3.066 Å). These interactions occur along the *b* axis, but there is no interaction along the *c* axis. The interstitial acetonitrile forms a hydrogen bond with the water molecule, with an O-H distance of 1.862 Å (O-N: 2.744 Å), and a BF_4^- counterion, with a distance F-H of 2.667 Å (F-C: 3.193 Å).

To measure the porosity of a material, generally adsorption isotherms are employed.[100,172] However, this procedure involves the prior degassing of the material, by vacuum and/or the application of temperature. In the case of **1**·2CH_3CN, this results in a loss of the non-coordinated acetonitrile molecules in the structure, and is therefore not a suitable option. Nevertheless, several close-related works[173,174] justify the absence of pores by showing the structure in the spacefill mode (covalent ratii), where the presence of any pores, if present, should be visible. Here, the view of the **1**·2CH_3CN coordination polymer illustrates that the polymer is tightly packed, with no visible pores or voids in the structure, as shown in Annex A3. Furthermore, the porosity can be calculated the use of the PLATON software. This procedure was followed for **1**·2CH_3CN, and there are no residual voids accessible by the solvent, irrespective of whether it is calculated with the CALC VOID or SQUEEZE functions, when the default Van der Waals radius was used (1.2 Å).[175] In addition, there

are multiple reports of molecule exchange in non-porous coordination polymers, where the exchange takes place through a process of diffusion throughout the crystal lattice.[100,106,162] This same type of process is proposed to be what occurs in **1**·2CH_3CN.

2.2.2. Physico-chemical study

Figure 28a shows the optical reflectivity (OR) of a **1**·2CH_3CN crystal measured while heating it from 288 K up to 373 K. Initially, the OR remains constant and no change in the color of the crystal is observed. Interestingly, the OR sharply increases at around 305 K and the **1**·2CH_3CN crystal changes color to a brighter shade of yellow, as seen in Annex A4. The OR remains approximately constant from 306 K up to 316 K and thereafter gradually decreases as the color of the crystal changes from yellow to orange (see Figure 28b and Annex A5). At 355 K, the **1**·2CH_3CN crystal is completely orange and the OR stabilizes to a constant value. Upon cooling down the sample back to room temperature no change in color was observed, suggesting that the change in the optical reflectivity is not temperature reversible.

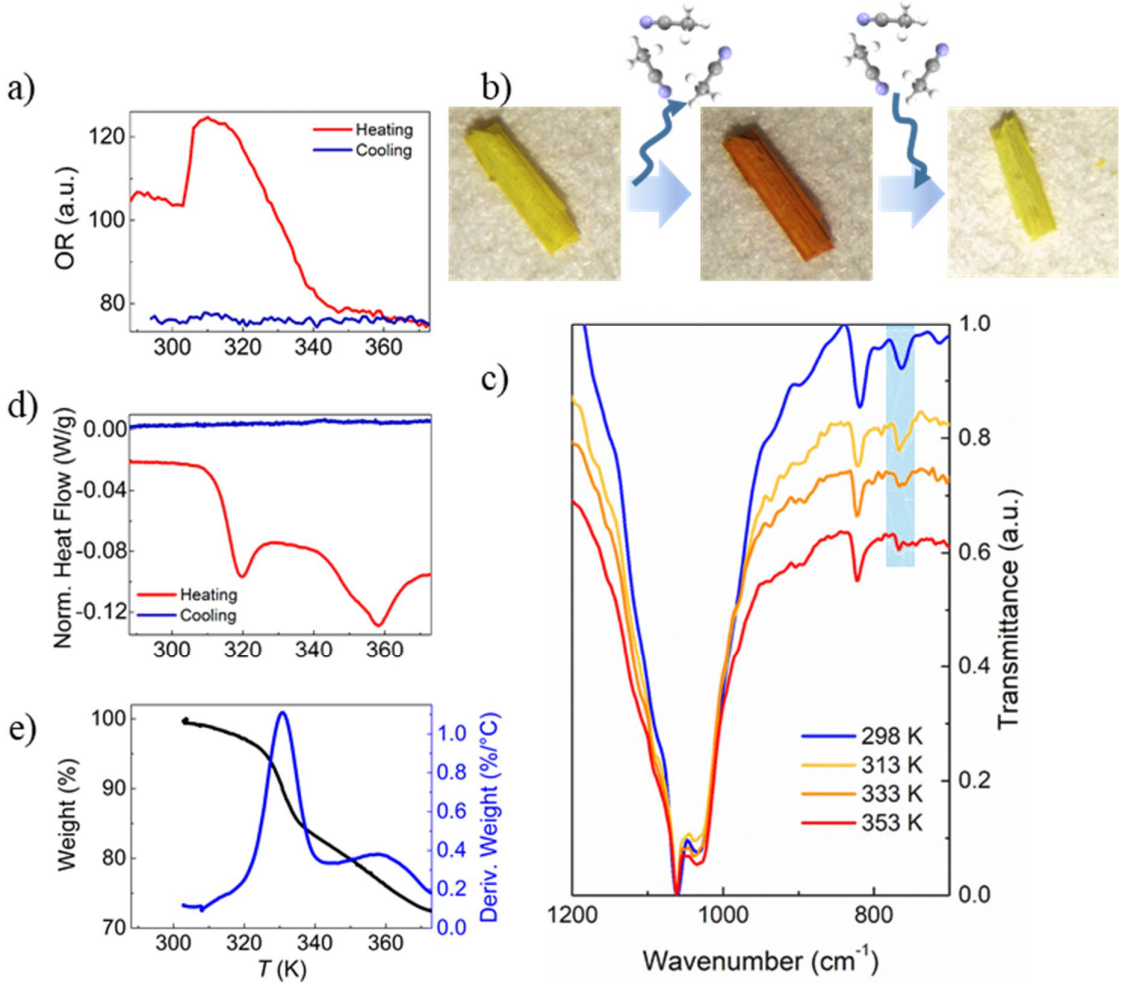

Figure 28. a) **1**·2CH_3CN optical reflectivity measurement between 288 K and 373 K. b) Optical image of a **1**·2CH_3CN crystal at room temperature (yellow), after heating and subsequent loss of acetonitrile molecules (**1**, orange) and after exposition to acetonitrile (yellow). c) **1**·2CH_3CN infrared spectra at different temperatures. d) DSC measurements on a **1**·2CH_3CN crystal between 288 K and 373 K. e) TGA curve measured between 303 K and 373 K (black line). The blue line represents the derivative weight.

The infrared spectrum of **1**·2CH_3CN is measured in the same range of temperatures to determine whether the changes in the OR are related to structural changes in the molecules. The low energies spectrum is shown in Figure 28c. See Annex A6 to Annex A9 for the full energy scale spectrum. The room temperature spectrum shows the bands associated to the different constituents of the polymer: acetonitrile, coordinated water molecules, pyrazine and the broad band of the BF_4^- anions at 1002 cm^{-1}.

Interestingly, a gradual disappearance of the band at 766 cm^{-1} is clearly observed as the temperature increases (Figure 28c, signaled in a blue background). The vanishing band can be assigned to the C≡N bend overtone[176,177] that is present in the uncoordinated acetonitrile of the **1**·2CH_3CN. Its disappearance therefore suggests that acetonitrile desolvation from the crystal occurs as the temperature increases. On the other hand, the structural integrity of the crystal is conserved, which is an indication that the acetonitrile groups coordinated to the Fe(II) remain in the structure. To further prove this, the **1**·2CH_3CN IR spectra was compared with that of the analogue $_\infty$\{[Fe(CH_3CN)$_4$(pyrazine)](ClO_4)$_2$\} with similar structure.[171] The difference is that no uncoordinated acetonitrile molecules are present in its lattice. The band at 766 cm^{-1} does not appear in the spectrum at any temperature (Annex A10). Therefore, the presence and vanishing of the bands in **1**·2CH_3CN can be unambiguously assigned to the desorption of uncoordinated acetonitrile with increasing temperature. The process is not temperature reversible and the IR bands do not reappear when cooling down to room temperature, in agreement with the OR measurements (Annex A9). These results are consistent with the loss of these non-coordinated acetonitrile molecules in the structure.

To further explore the reversibility of the optical and structural transitions induced by the loss of acetonitrile in the crystal, a drop of acetonitrile is added to the "dry" orange crystal at room temperature after one temperature cycle. The drop is thereafter let dry in ambient conditions to eliminate any non-reabsorbed acetonitrile from the surface. Strikingly, color and optical reflectivity returns back to the initial yellowish characteristic as seen in Figure 28b and Annex A5. In addition, the absorption band at 766 cm^{-1} reappears in the IR spectrum (Annex A11). The initial properties are also recovered when **1** is exposed to acetonitrile via vapor diffusion.

While the structural integrity of the single crystal is mostly maintained, all attempts to solve the structure of **1** and after acetonitrile reabsorption by single crystal X-ray diffraction, even in the ALBA synchrotron, have been unsuccessful. Consequently, powder X-ray diffraction (PXRD) measurements of the three phases were performed to determine the unit cell parameters (Figure 29 and Annex A12). The PXRD studies were carried out for the three phases by adjusting the following parameters to be capable of obtaining the best conditions: i) the grinding process and ii) the speed of measurement. The grinding process, which is important for the homogenization of the sample provoked a slight color change in **1**·2CH_3CN (from yellow to orange-yellow) and also, resulted in the appearance of more diffraction peaks than those expected from the pattern simulated from the single crystal X-ray diffraction data. This evidence is in agreement with the formation of novel independent crystalline phases either by an internal rearranging of the polymer or by the loss of acetonitrile during the milling. To rectify this problem, the data acquisition was made from powder without the milling process. The result is plotted in Figure 29. The pattern is in good fit with that obtained by the simulated single-crystal diffractogram. To confirm this agreement, the unit-cell parameters were calculated from these peaks by using HighScore Plus[178] as refinement software, obtaining an excellent match with the single-crystal values (Annex A12).

Sample **1**·2CH_3CN was then heated for 5 hours at 50°C to ensure that the interstitial acetonitrile was completely desorbed from the material. Then the acquisition was performed (see Figure 29). The first observation is that the collected spectrum is different than previously collected for **1**·2CH_3CN. The appearance of new peaks suggests a new crystalline phase associated with the evacuation of acetonitrile molecules. In addition, the lattice parameters from this pattern are smaller than in the initial **1**·2CH_3CN (Annex A12). This is in agreement with the decrease of volume

predicted by Density Functional Theory (DFT) calculations (Annex A13 and Annex A14) and with the decrease of the macroscopic size of the crystals (see Annex A16). The DFT calculations show that after removal of interstitial CH_3CN molecules, the *a*, *b*, and *c* lattice parameters are shortened by 0.8 %, 1.8 % and 5.5%, respectively. The predicted final structure without acetonitrile molecules is shown in Annex A15. This prediction is in good agreement with the experimental decrease in crystal size observed above the transition, as seen in Annex A16. The projected density of states computed for both the ferromagnetic and antiferromagnetic orderings along the 1D chains and shown in Annex A13 and Annex A14 for **1**·2CH_3CN shows, in both cases, a large gap (~3 eV) which is negligibly affected by removal of acetonitrile, consistent with states located far from the conduction and valence bands.

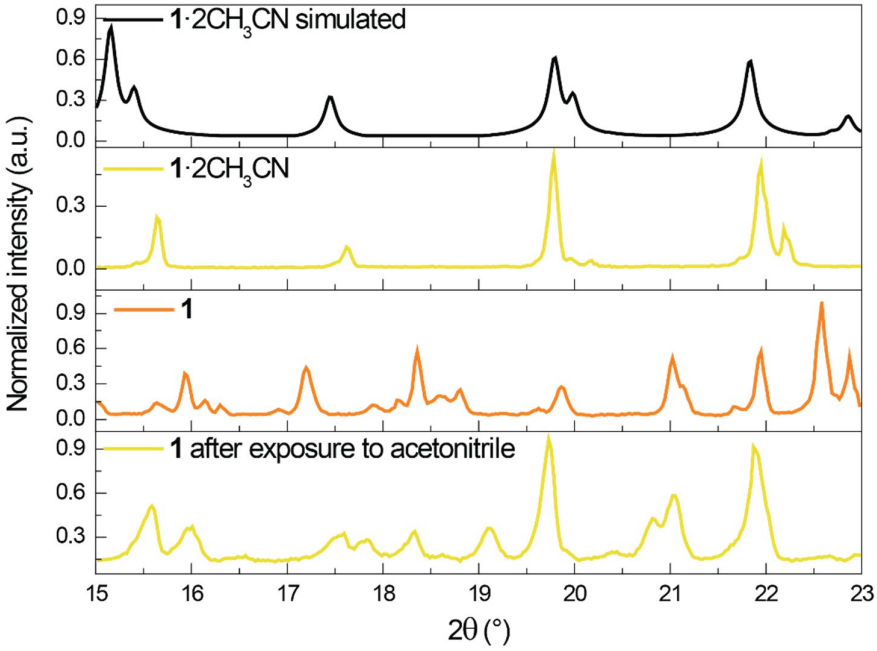

Figure 29. Powder X-ray diffraction patterns: simulated from the CIF file, **1**·2CH_3CN, **1** and **1** after exposure to acetonitrile.

Finally, with the aim of recovering the initial phase, the polycrystalline sample **1** was exposed to a saturated atmosphere of acetonitrile vapors for 10 hours. After confirmation of a pure phase by both, FTIR and naked-eye visible color change (from orange to yellow), the material was measured. The acquired pattern reflects almost pure **1**·2CH_3CN phase (see Annex A12). This study was complemented by elemental analyses of the three phases. The result shows a good agreement in between the calculated and the estimated mass after evacuation and reinsertion of the host acetonitrile molecules (see section 2.1.1).

Further proof of the structural origin behind the color and OR transitions is provided by the differential scanning calorimetry (DSC) measured between 288 K and 373 K. Two clear endothermic peaks, *i.e.* the crystal is absorbing energy, can be observed during the heating process (Figure 28d). The first one is centered around 315 K and is consistent with the first change in the optical reflectivity. The second peak is centered at 358 K and occurs at the same temperature as the OR becomes lowest and constant and the crystal has completely changed from yellow to orange (see Figure 28a and Annex A5). The endothermic nature of the peaks is indicative of a crystalline phase transition involving breaking of molecular bonds or the melting/evaporation of molecular species present in the crystal. No peaks, either endothermic or exothermic, were observed when cooling the sample from 373 K back to 288 K, as was also observed in the OR. Interestingly, both structural

transitions are also translated into magnetic anomalies in the magnetic susceptibility at the same temperatures (see section 2.2.3).

To complete the structural characterization, the thermogravimetric analysis (TGA) of **1**·2CH_3CN was measured between room temperature and 873 K (see Figure 28e and Annex A17). A first weight loss starts at around 315 K (first transition in OR and DSC) and finishes at 345 K (the OR becomes constant). The total weight loss in this temperature range is 15.73 % and approximately fits with the loss of two acetonitrile molecules (16.08 %) per unit formula. This confirms that only the uncoordinated acetonitrile molecules evaporate from the structure at this temperature.

2.2.3. Magnetic studies

The magnetic susceptibility (χ_M) was measured in a set of **1**·2CH_3CN crystals between 10 K and 380 K. The $\chi_M T$ product is represented in Figure 30. The saturation value remains constant at 3.04 $cm^3 \cdot K \cdot mol^{-1}$ from 25 K up to 310 K. This value is characteristic of non-interacting high-spin iron(II) ions.[106,171] A small kink in the slope can be observed at 312 K (signaled with a blue arrow) and thereafter $\chi_M T$ decreases to 3.02 $cm^3 \cdot K \cdot mol^{-1}$. The transition temperature matches with the first structural, optical and calorimetric transitions observed in the **1**·2CH_3CN crystal. According to Curie's law for a paramagnetic material, a change in $\chi_M T$ could be induced by a change in the spin value (S) or a change in the g factor. Here, a high-spin to low-spin switch would have a more dramatic consequence in $\chi_M T$. The most probable scenario is therefore a change in g due to a structural change around the iron, as suggested by the DSC measurements and the DFT calculations.

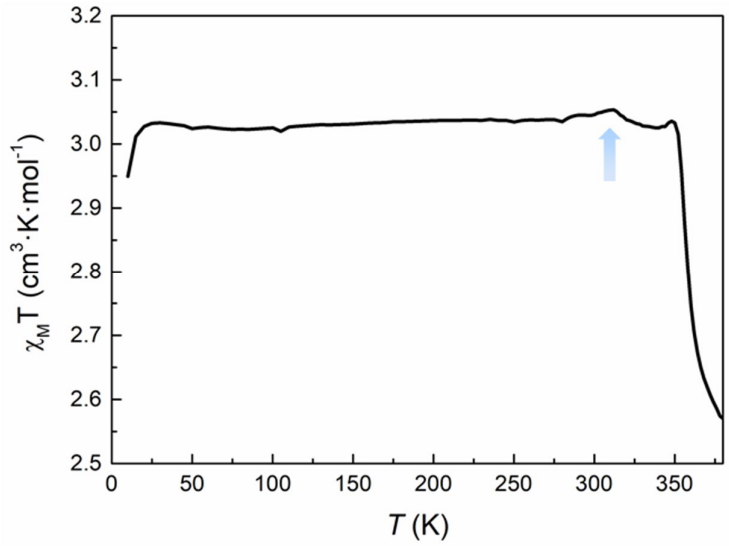

Figure 30. $\chi_M T$ measured as a function of the temperature in a set of **1**·2CH_3CN crystals. A small kink and a large drop in $\chi_M T$ are observed at 310 K and 350 K respectively.

After the first transition, an abrupt change in the slope shows up at 350 K; the second transition temperature. The $\chi_M T$ value decreases down to 2.57 $cm^3 \cdot K \cdot mol^{-1}$ at the highest measured temperature. Note that the limitations in the set-up do not allow measuring above this temperature and therefore it is difficult to determine whether $\chi_M T$ continues dropping to zero or stabilizes at a finite value. A sharp drop of $\chi_M T$ in this kind of materials is typically associated to a spin crossover transition to a low-spin state ($S = 0$).[171] However, this transition typically occurs while decreasing the temperature and the bond lengths around the Fe ions decrease. In **1**·2CH_3CN crystals, such decrease in the bond length could be induced by the structural distortions caused by the release of acetonitrile, as suggested by DFT calculation (see Annex A15).

In the low temperature region, the value of $\chi_M T$ remains approximately constant down to 25 K. The sharp drop in $\chi_M T$ below 25 K may be indicative of antiferromagnetic correlations in the chains or the depopulation of excited magnetic levels.

2.2.4. Electric transport measurements

The effect of the structural transitions in the electronic properties of **1**·2CH_3CN was studied in the same range of temperatures. Figure 31a shows the current (I) measured across a single **1**·2CH_3CN crystal in nitrogen atmosphere at a fixed voltage (V = 1 V) while ramping up the temperature from 288 K to 373 K (red curve) and consecutively down to the initial temperature (blue curve). Additional measurements on different crystals reproducing the same transport features can be found in Annex A18. Initially the crystal behaves almost as an insulator with current levels below 10^{-11} A, in agreement with the large band gap (~3 eV) computed by DFT for this polymer (see Annex A13 and Annex A14). As the temperature is increased, a sharp increment of the current of about two orders of magnitude can be observed at 306 K followed by a softer decay back to low current levels. At higher temperatures, a second wider high-current peak appears between 343 K and 353 K. Note that the order of magnitude and position of the peaks in temperature is roughly reproducible in all the measured crystals (see Annex A18).

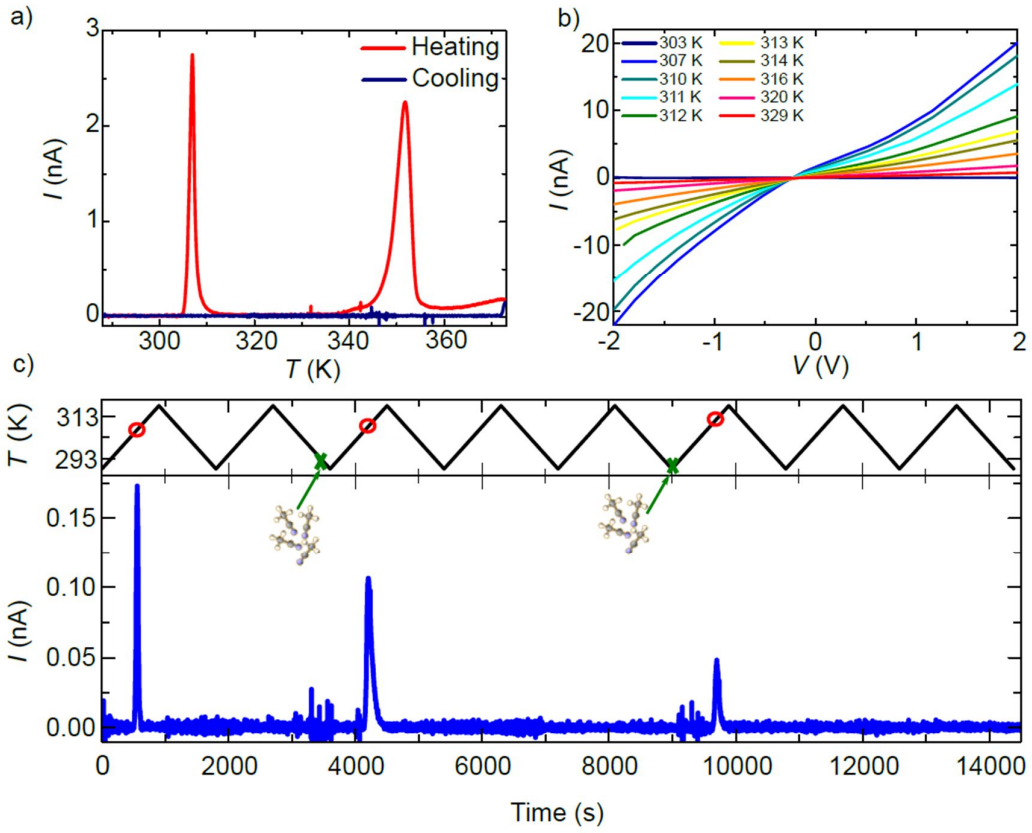

Figure 31. a) Electrical current *vs.* temperature measured in a single **1**·2CH_3CN crystal. Two sharp high-conductance peaks appear centered at 306 K and 353 K while increasing T. The peaks do not show up when the temperature is ramped down to the initial value. b) Current-voltage IV measurements at different temperatures around the first conductance peak. c) Proof-of-concept sensor of acetonitrile. A resonance in the current appears at a specific temperature (red circles) only in those temperature cycles where the **1**·2CH_3CN crystal is exposed to acetonitrile (green crosses).

Figure 31b shows the current-voltage *IV* characteristics measured at different temperatures around the first peak in conductance. The current follows the same dependence in temperature observed in Figure 31a. The shape evolves from an insulating-like material to a clear non-linear dependence with bias, indicating the presence of Schottky barriers at the interface between electrodes and material or between grain boundaries in the material. Interestingly, the current levels after the transition temperature remain higher than before the transition (dark blue curve at 303 K in Figure 31b).

A careful comparison with the structural, optical and magnetic characterization of crystalline **1**·2CH_3CN shows that the high-current peaks match in temperature with the two respective anomalies in the OR, the calorimetric and the magnetic response. The sharp change in the conducting properties of the crystal is therefore unequivocally connected to the structural transitions undergone by the **1**·2CH_3CN crystal at around 306 K and 353 K. None of the current peaks is present when the temperature is ramped back down to 288 K (blue curve in Figure 31a) and do not appear if the temperature is ramped up again, as it is also observed in the optical reflectivity and DSC. Strikingly, the two high-conductance peaks reappear in the charge transport measurement at identical temperatures after the **1**·2CH_3CN crystal is exposed to acetonitrile (vapor or liquid), as seen in Figure 31c and Annex A19. For this, a 10 µl droplet of acetonitrile is deposited in ambient conditions with a micro pipette at approximately 4 cm distance from the "dried" crystal. The changes in the conductance are therefore reversible upon acetonitrile absorption-desorption in the **1**·2CH_3CN lattice. A simple conductance measurement can in principle be used as method to detect ambient acetonitrile. A proof-of-concept of such sensor is shown in Figure 31c. The current is measured across a single **1**·2CH_3CN crystal while cycling the temperature between 288 K and 318 K, *i.e.* around the first peak in conductance. A peak in the current shows up at roughly the same temperature (red circles) in those cycles where the crystal is exposed to acetonitrile vapor (green crosses), whereas it is absent in the rest of the cycles. That is, the emission of acetonitrile is detected only if previously the acetonitrile molecules have been previously inserted in the crystal. Furthermore, the immersion of acetonitrile in the crystal is also immediately sensed by the conductance through the crystal. This is seen as a distinct noise in the current before the high conductance peaks in Figure 31c. A second example is shown in Annex A20.

The origin of the sharp change in conductance is intriguing since MOFs and coordination polymers are typically insulators or bad conductors[179,180] except for a few remarkable cases.[141,174,181–183] A possible explanation for the first high-conductance peak can be connected to the structural change and the augmented mobility of the interstitial acetonitrile in the **1**·2CH_3CN crystals, proved by IR spectroscopy and DSC measurements. Reordering of small molecules in porous materials is known to induce structural changes in the chain-like architecture that in turn may induce transitions in the magnetic behavior[184] and possibly the charge transport properties. On the other hand, the rapid drop in current under increasing temperature after the transition seems to rule out static changes in the electronic structure of the polymer, like a change in the band gap. This scenario is in agreement with the DFT calculations that show a sizeable change in the structure of the polymer after removal of the acetonitrile molecules, but a negligible change in the band gap, consistent with weakly interacting molecules (see Annex A13 and Annex A14).

An alternative but related explanation for dynamic changes in the conductance has been proposed for porous silicon and metal oxides detectors exposed to acetonitrile[185–187] and other polar solvents with high dielectric constants. The rise in current is not related to static changes in the bandgap. Instead, it can be explained in terms of dynamic changes in the dielectric constant of the material after infiltration of the acetonitrile that in turn modifies the charge distribution in the material. The consecutive rapid decrease of the conductance can be explained in this case as a dynamic capacitive effect over time or by the fast evaporation of acetonitrile due to its low vapor pressure. This effect has also been observed in MOFs[188–190] and CNT-polymer hybrid materials.[180] The fast evaporation

is clearly observed in Annex A21 where the release of acetonitrile gas can be seen as blurriness in the image. To check this scenario the complex AC admittance across a crystal was measured while heating it. The real and imaginary components of the complex current $I^* = I' + jI''$ measured with an AC voltage excitation are proportional to the conductance *(G)* and susceptance *(B)* of the complex admittance (*Y*).

$$Y^* = G + jB \qquad (1)$$

A clear peak in the real conductance and the imaginary susceptance can be observed at around 303 K (Figure 32).

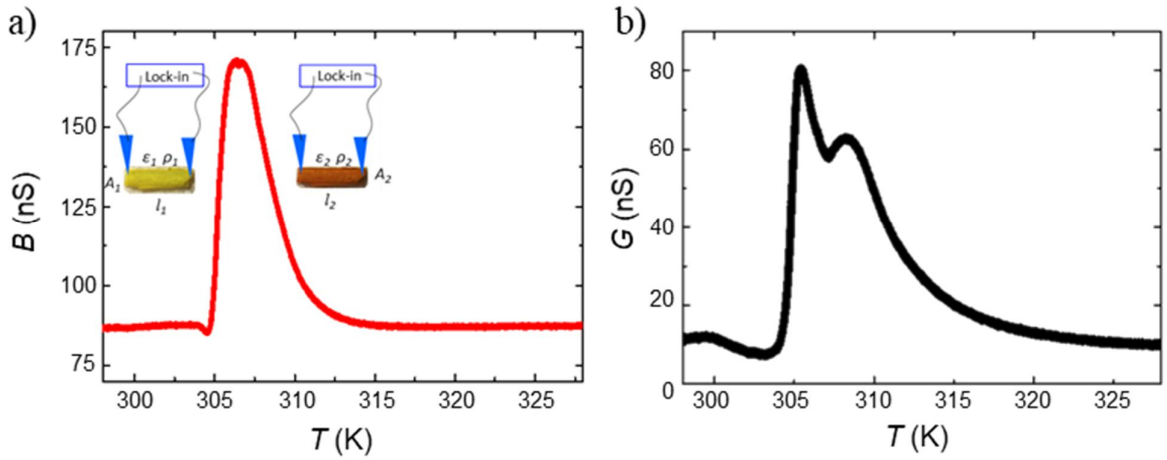

Figure 32. (a) *B* measured as a function of the temperature with an AC excitation V_{AC} = 100 mV and f = 510 kHz. b) *G* measured as a function of the temperature with an AC excitation V_{AC} = 100 mV and f = 510 kHz.

Interestingly, as observed in DC measurements, a sharp peak sets on at around T = 305 K, for both *G* and *B*. Thereafter it decays back to the initial values with a softer dependence with *T*. The excitation frequency during the whole measurement is kept constant. In a real system with the geometry of this device, the more realistic model would be through a combination of resistances and capacitors in parallel and/or perpendicular configuration to account for the material, the contacts, the probes and cables, etc. The expressions for *G* and *B* involve in this case a more elaborated combination of *R* and *C* depending on the specific configuration. In this case, an RC circuit in series is modeled.[191]

$$G = \frac{R\omega^2C^2}{1+(\omega RC)^2} \qquad (2) \qquad ; \qquad B = \frac{\omega C}{1+(\omega RC)^2} \qquad (3)$$

(where $\omega = 2\pi f$, $B = j\omega C$, a capacitor and *R* a resistor). Therefore, according to Eqs.(2) and (3), the change in *B* and *G* can only be attributed to variations of *R* and/or *C* in the crystal while warming up. Figure 33 and Annex A22a show *B* calculated as a function of *C* by using Eq. (3). The experimental peak observed at $T \approx 305$ K in the measurements can be therefore qualitatively explained by a continuous increment of *C* with temperature when the acetonitrile is released.

However, a continuous increment of *C* cannot explain the maximum in *G* observed in the measurements. According to Eq.(2), *G* would increase with *C* and saturate at *1/R* (see Annex A22b). The drop in *G* could be associated either to a side-by-side increment in *R* or a subsequent drop in *C* back to lower values. Figure 33 shows *G* and *B* calculated using Eqs.(2) and (3) under increasing *R* and *C*. Both curves are in good qualitative agreement with the experimental findings.

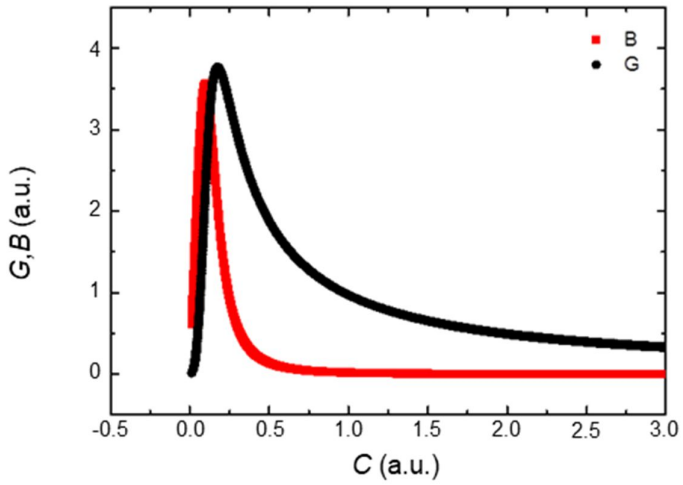

Figure 33. *G* and *B* calculated with Eqs.(2) and (3) under increasing *C* and *R*. Both are in good agreement with the experimental findings in Figure 32.

The possible physical mechanisms behind a change in C and R with temperature could be associated to changes in the intrinsic properties of the material:

$$C = \varepsilon \frac{A}{l} \qquad (4)$$

(where ε and ρ are the dielectric constant and resistivity of the material, respectively) or to changes in the dimensions:

$$R = \rho \frac{l}{A} \qquad (5)$$

(where A and l are the transversal area and longitudinal dimension, respectively). Intrinsic changes in ε or ρ could be originated by the reorganization or loss of the acetonitrile triggered by temperature, as previously demonstrated. Acetonitrile has one of the largest dielectric constants of common organic solvents which could explain the sharp rise in the capacitance. On the other hand, changes in the dimensions of the material are also experienced by the crystal when the acetonitrile is released. The DFT calculations predict a shortening of 0.8 %, 1.8 % and 5.5% of *a*, *b*, and *c* lattice parameters with a total decrease of volume of 8.1%. Changes in the crystal dimensions while increasing temperature were indeed observed, as seen in Annex A16.

To summarize, these peaks can be well described by a sharp increment of the capacitance and the resistance of the material, induced either by a change in the dimensions of the lattice, or by a change in the dielectric constant, both as a result of the release of interstitial acetonitrile. Nevertheless, the mechanism and origin of the conductivity will be further explored in the next chapter.

The second high-conductance peak seems also related to the second structural transition observed in the optical reflectivity and the DSC measurements. Interestingly, the peak shows up at exactly the acetonitrile boiling point temperature (355 K), indicating that the change in conductance is again linked to the reordering of acetonitrile.

2.3. CONCLUSIONS

To summarize a new non-porous crystalline one-dimensional coordination polymer acting as a porous material hosting acetonitrile has been synthetized. The release of interstitial acetonitrile from the crystal under increasing temperature is accompanied by sharp magneto-structural transitions that can be detected as a change of color. The change in the structure is in turn translated into an abrupt

high-current resonance in the electric transport through the crystal at well-defined temperatures close to ambient conditions. This represents the first example where an insulating non-porous coordination polymer acting as porous displays such an abrupt and temperature-specific change in the conductivity. Interestingly, the initial structure and therefore color and electrical transition are recovered once the crystal is exposed again to acetonitrile.

Therefore, this non-porous material can be a versatile platform to fabricate tailor-made detectors for acetonitrile with a versatile variety of read-out options from optical, magnetic to electric transport measurements. Furthermore, the fact that acetonitrile is bonded by weak interactions, offers the possibility of exchanging these molecules for other volatile organic or inorganic compounds. Ideally, this would result in different optical and transport properties, leading to a selective sensing device.

3. TUNABLE COLOR AND PROTON CONDUCTIVITY VIA LATTICE ACCOMMODATION OF SMALL MOLECULES

As previously stated, non-porous coordination polymers that can act as porous are remarkable materials, due to the weakly-coupled small molecules, that can be released or incorporated in the structure via internal lattice reorganization.[100,106,172] Even though this is a relatively recent research area, these complex molecular dynamics have been associated with a wide variety of applications from magnetic switching,[100,106,162] gas/vapor adsorption[5,192–194] and sensing,[9,162,195,196] energy storage[197] and catalysis.[198] These weak interactions enable non-porous CPs to show a greater affinity and sensitivity to guest molecules[100,106,172] in comparison to many MOFs where ligand functionalization is typically necessary.[7,199–201]

In general, electrical transport properties are of great interest in many applications, including sensing devices, as they provide a simple and automatic read-out. However, electron transport in coordination polymers has been generally difficult to attain, with a handful of examples described for specific MOFs.[139,174,182,190] Another alternative is provided by ionic transport, where the charge carrier can be either an anion or a cation. In the latter, the charge transport source would be protons or more complex cations. This type of conduction plays a crucial role in biological systems[202] and in electrolytes in batteries[203] and fuel cells.[204] Typical commercial proton conducting materials include inorganic compounds, like perovskite-type oxides, or amorphous organic polymers, such as the widely explored Nafion, that displays high proton conductivity and chemical stability in humid conditions. As of today, commercial Nafion-based polymeric membranes may achieve a conductivity of 10^{-1} S·cm^{-1} at 98% RH and 60–80 °C. Nevertheless, the applicability of Nafion is restricted because of its expensive price, poor thermal stability and limited working temperature. Furthermore, it is challenging to study the proton pathway in Nafion at the atomic level due to its amorphous nature.

Substantial work has been conducted recently to investigate promising alternative proton-conducting materials, with enhanced proton conductivity and long-term recyclability. To this end, numerous materials have been explored, including organic polymers, inorganic materials and covalent organic frameworks. In addition, metal–organic frameworks and coordination polymers (both porous and non-porous) are considered good candidates because an appropriate chemical design allows for tuning the transport properties.

Over recent years, considerable research has been conducted, mostly in MOFs, to understand proton transport and the role of ambient molecules, such as water.[205,206] Here, proton conductivity usually comes from adsorbed water molecules[207–211] or donor guest molecules in the pores[212–218] and can be tailored with the presence of acidic groups in the lattice structure[207,219–221] or by incorporating networks of van der Waals interactions or hydrogens bonds.[222,223] Most of the reported examples operate at high relative humidity levels (> 90% RH). At present, the conductivity value for several MOFs is of the order of magnitude of $10^{-1}/10^{-2}$ S·cm^{-1}, pointing to their potential application in

proton conduction. Some of these best reported values comprise PCMOF10 with $\sigma = 3.55 \times 10^{-2}$ $S \cdot cm^{-1}$ (at 343 K and 95% RH),[224] Al-HPB-NET with $\sigma = 5 \times 10^{-2}$ $S \cdot cm^{-1}$ (at 393 K, 50% RH),[225] and BUT-8(Cr)A with a value of 1.27×10^{-1} $S \cdot cm^{-1}$ (353 K, 100% RH),[226] all of which are comparable to commercially available Nafion materials.

On the other hand, the potential of non-porous CPs to display proton transport is still mostly unexplored, with just a limited number of examples, based on water-assisted transport, that reveal their potential to rival with or even surpass some of these MOFs.[227–231] As in MOFs, these studies reveal that the primary factor influencing the proton conductivities of non-porous CPs is their acidity, followed by the formation of continuous hydrogen bond networks.[227]

The highest proton conductivity reported values in non-porous coordination polymers include: $[Gd(H_4nmp)(H_2O)_2]Cl \cdot 2H_2O$;[230] $[Ni(4,4'\text{-bipyH})_2(H_2O)_4] \cdot 2(H_4bmt) \cdot 9H_2O$ and $[Co(4,4'\text{-bipy})(H_2O)_4][Co(4,4'\text{-bipyH})_2(H_2O)_4] \cdot 2(H_3bmt) \cdot 6H_2O$;[229] and $(\{[Co(orot)_2(bpy)]\text{-}[\mu\text{-}Cu(bpy)(H_2O)]\}_n[Co(orot)_2(bpy)]_n \cdot 5_nH_2O$.[228] The first case, reported by Almeida Paz *et al.*,[230] represents the non-porous CP with the highest proton conductivity, with a value of 0.51 $S \cdot cm^{-1}$, which occurs due to a structural transformation that takes place at 367 K and 98% RH, where $[Gd(H_4nmp)(H_2O)_2]Cl \cdot 2H_2O$ transforms into $[Gd_2(H_3nmp)_2] \cdot xH_2O$ (x= 1-4; H_6nmp = nitrilo-tris(methylenephosphonic)acid). Here, the key enabler for high proton conduction is the unique structural transformation with insertion of water and release of chloride ions. Other examples, reported by Hou and coworkers,[229] include $[Ni(4,4'\text{-bipyH})_2(H_2O)_4] \cdot 2(H_4bmt) \cdot 9H_2O$ and $[Co(4,4'\text{-bipy})(H_2O)_4][Co(4,4'\text{-bipyH})_2(H_2O)_4] \cdot {}_2(H_3bmt) \cdot 6H_2O$, ($H_6bmt$= benzene-1,3,5-tris(methyl-enephosphonic acid; 4,4′-bipy = 4,4'-bipyridine), which display conductivity values of 1.78×10^{-3} $S \cdot cm^{-1}$ and 9.87×10^{-3} $S \cdot cm^{-1}$ at 358 K, respectively (at 98% RH). Falvello *et al.*[228] reported an example in a copolymer formed by two alternating building blocks, with formula $(\{[Co(orot)_2(bpy)]\text{-}[\mu\text{-}Cu(bpy)(H_2O)]\}_n[Co(orot)_2(bpy)]_n \cdot 5_nH_2O$ (where bpy = 2,2′-bipyridyl; H_2orot = orotic acid), which presents a conductivity of 10^{-6} $S \cdot cm^{-1}$ at room temperature. In all these cases (summarized in Table 1), the conductivity values are highly dependent of the temperature and humidity conditions.

Table 1. Summary of the conductivity values of several MOFs and non-porous CPs.

Compound	Type	σ ($S \cdot cm^{-1}$)	Conditions	Ref.
PCMOF10	MOF	3.55×10^{-2}	343 K, 95% RH	224
Al-HPB-NET	MOF	5×10^{-2}	393 K, 50% RH	225
BUT-8(Cr)A	MOF	1.27×10^{-1}	353 K, 100% RH	226
$[Gd(H_4nmp)(H_2O)_2]Cl \cdot 2H_2O$	Non-porous CP	0.51	367 K, 98% RH	230
$[Ni(4,4'\text{-bipyH})_2(H_2O)_4] \cdot 2(H_4bmt) \cdot 9H_2O$	Non-porous CP	1.78×10^{-3}	358 K, 98% RH	229
$[Co(4,4'\text{-bipy})(H_2O)_4][Co(4,4'\text{-bipyH})_2(H_2O)_4] \cdot 2(H_3bmt) \cdot 6H_2O$	Non-porous CP	9.87×10^{-3}	358 K, 98% RH	229
$(\{[Co(orot)_2(bpy)]\text{-}[\mu\text{-}Cu(bpy)(H_2O)]\}_n[Co(orot)_2(bpy)]_n \cdot 5_nH_2O$	Non-porous CP	10^{-6}	298 K, 96% RH	228

In this chapter the mechanism of the current change caused by the phase transition of the non-porous **1**·2CH_3CN crystals will be discussed in more detail. To this end, and with the collaboration of Dr. Enrique Burzurí and his group, AC admittance spectroscopy was employed to unravel the charge transport mechanism, and whether it was of electronic or ionic origin.[232] As many MOFs and CPs display conductivity at high humidity levels, this effect was also explored. In addition, the effect that the incorporation of different molecules in the crystal lattice has on the structural and transport properties was studied. With this aim in mind, the uncoordinated acetonitrile molecules were exchanged *in-situ* by pyrrole, forming the new CP **1**·pyrrole.

3.1. SYNTHESIS OF COMPOUND 1·PYRROLE

3.1.1. Synthesis of $_\infty${[Fe(H_2O)$_2$(CH_3CN)$_2$(pyrazine)](BF_4)$_2$·pyrrole} (1·pyrrole)

Sample **1**·pyrrole was synthesized according to the following procedure. A screw vial for chromatography (diameter 12 mm, height 32 mm) displaying 10 mg of **1**·2CH_3CN was placed in a clear glass vial (diameter 27 mm, height 55 mm) containing 0.1 ml of pyrrole. The glass vial was sealed and kept at room temperature overnight to allow the gas-solid reaction between the VOC and **1**·2CH_3CN.

Anal calcd (%) for **1**·C_4H_5N·0.4CH_3CN·0.35H_2O (**1**·pyrrole): C 29.71, H 4.07, N 14.62; found C 29.49, H 4.01, N 14.47. FTIR **1**·pyrrole (cm^{-1}): ν = 3404 (m; ν(OH); $\nu(NH)_{pyrrole}$), 3128 (w; ν(CH)), 2950 (w), 2304 (w; ν(C≡N)), 2276 (w; ν(C≡N)), 1640 (w; ν(CC)), 1530 (w), 1422 (m; δ(CH)), 1371 (w), 1287 (w), 1045 (w, $\nu(ring)_{pyrrole}$), 1011 (b; $\nu(BF_4)$), 1010 (w, $\nu(ring)_{pyrrole}$), 883 (w), 814 (m; $\delta(ring)_{oop,pyrazine}$), 731 (s; $\delta(ring)_{oop,pyrrole}$), 553 (w), 520 (w), 492 (w), 456 (m).

The elemental analysis for **1**·pyrrole fits properly with the TGA analysis (see section **Error! Reference source not found.**), where the two weight losses are consistent with the loss of 0.4CH_3CN, 1 pyrrole and 0.35 H_2O molecules per unit formula.

3.2. RESULTS AND DISCUSSION

3.2.1. Physico-chemical study

The **1**·2CH_3CN crystals were exposed to vapors of pyrrole at room temperature, where a color change first from yellow to brownish green was observed within minutes. Then, the color turns to dark green (Figure 34). This color change was characterized by optical reflectivity measurements *vs.* the exposition time. The OR value starts decreasing almost immediately as the crystal becomes darker, reaching a small plate after 1.5 hours. The value continues decreasing progressively until it reaches a minimum after a total of 4 hours. This value remains constant if exposure continues (up to 14 hours).

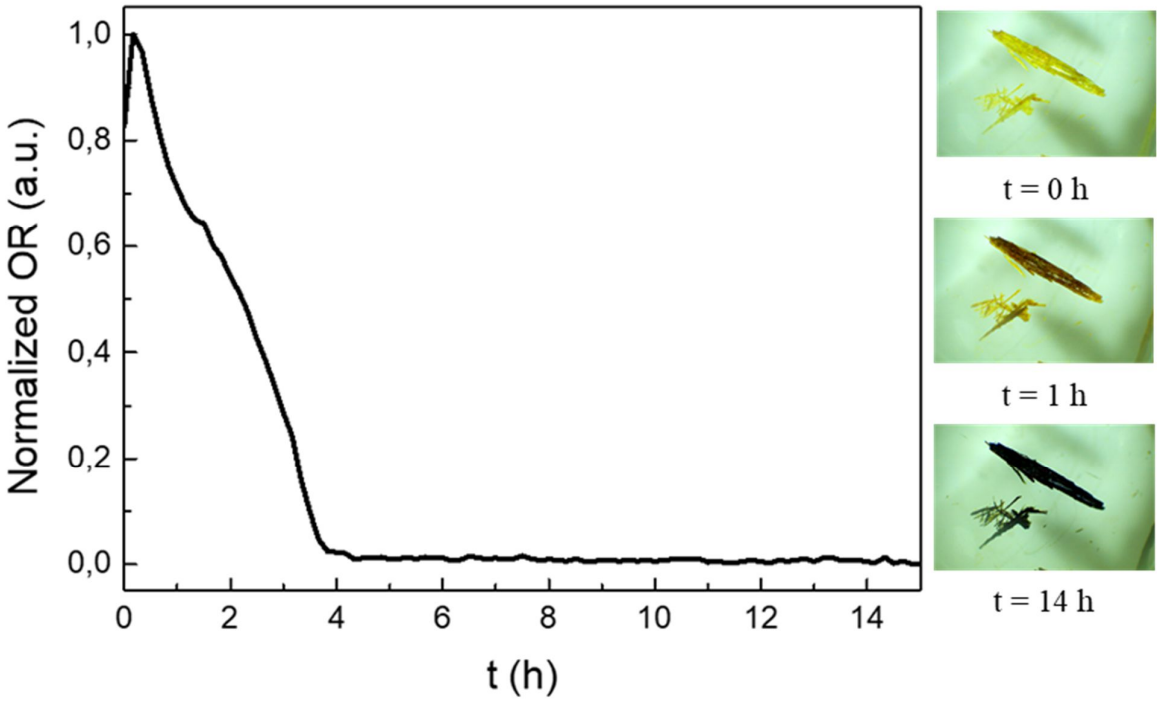

Figure 34. Optical reflectivity of **1**·2CH_3CN crystal turning into **1**·pyrrole under exposition to pyrrole. Right: images of the color variation of a **1**·2CH_3CN crystal turning into **1**·pyrrole under exposition to pyrrole. Images taken at time zero, 1 hour and 14 hours.

This new material was characterized by FTIR. Figure 35 shows the infrared spectra of **1**·2CH_3CN (yellow), pyrrole (brown) and **1**·pyrrole. For this last one, the characteristic bands of the backbone structure of **1** are represented in yellow, while the vibration bands that can be assigned to the inclusion of pyrrole are colored in brown. In the **1**·pyrroles spectrum, the doublet corresponding to the C≡N tension can be observed at 2304 cm^{-1} and 2276 cm^{-1}. However, the band at 766 cm^{-1}, assigned to the C≡N bend overtone is not visible, either because the uncoordinated acetonitrile is not present in this compound or because it is hidden in the bigger and broader pyrrole band at 731 cm^{-1}. Some other vibrational bands that can be clearly assigned to the **1** backbone are: the BF_4 broad band at 1011 cm^{-1} and the out of plane bending from pyrazine at 814 cm^{-1}. The bands that can be clearly associated with the inclusion of pyrrole in the structure include the appearance of small, defined peaks in the broad BF_4 band. These bands correspond to the pyrrole ring tension. And, as previously stated, the emergence of a band at 731 cm^{-1}, corresponding to the out of plane bending of the pyrrole ring. The rest of the bands arise from a combination of the bands from **1** and from pyrrole, and can not be unequivocally assigned to either.

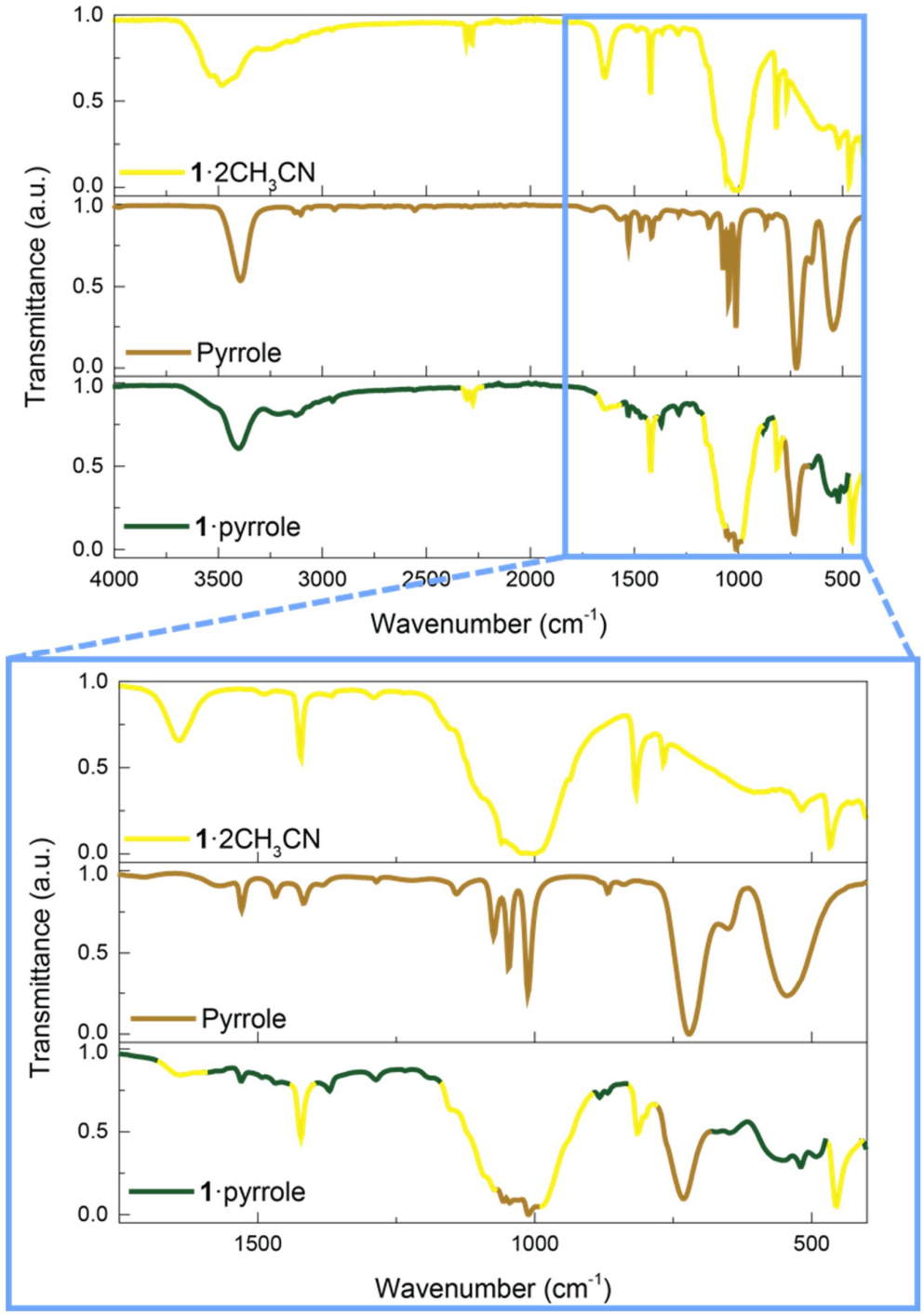

Figure 35. IR spectra of **1**·2CH_3CN, pyrrole and **1**·pyrrole between 4000 cm^{-1} and 400 cm^{-1}. A zoom for the 1750-400 cm^{-1} range can be observed at the bottom.

Even though the transformation of **1**·2CH_3CN crystals to **1**·pyrrole resulted in crystals that were good enough to measure the transport properties in single crystals, they did not retain crystallinity enough for the structure to be obtained by means of single crystal X-ray diffraction, even in the ALBA synchrotron. Powder X-ray diffraction measurements were performed on this compound as well as on the starting material, **1**·2CH_3CN. The key observation of this study is that both diffraction patterns are different, thereby providing further confirmation of the occurrence of structural modifications (Figure 36).

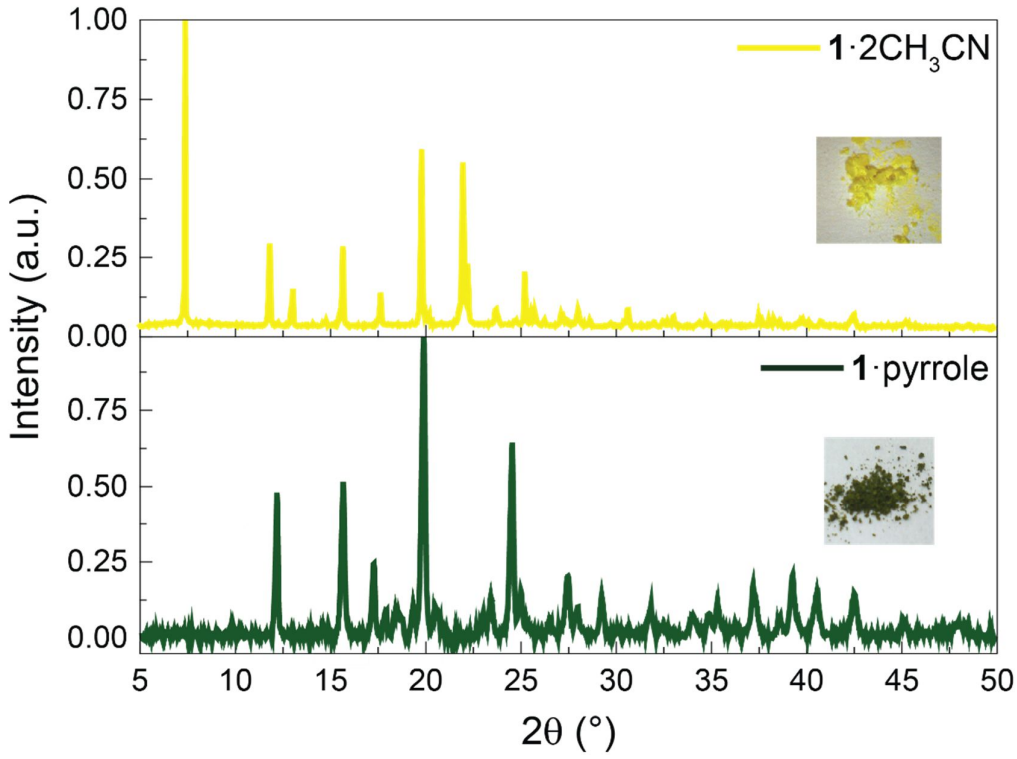

Figure 36. PXRD patterns of **1**·2CH_3CN and **1**·pyrrole. Insets show a picture of the powders.

This material was further characterized by thermogravimetric analyses. As expected, **1**·2CH_3CN and **1**·pyrrole display different thermal properties (Figure 37). As explained in section **Error! Reference source not found.**, in **1**·2CH_3CN, (Figure 28) a first weight loss (15.73 %) can be observed between 315 K and 345 K, that corresponds to the loss of two acetonitrile molecules (16.08 %). This polymer decomposes completely above 440 K.

However, in **1**·pyrrole, two weight losses can be seen in the low temperature region. The first one, (3.80 %), between 340 K and 356 K corresponds to the loss of 0.4 CH_3CN molecules (3.6 %) and fits well with the evaporation temperature of acetonitrile, and the second one (14.09 %) can be seen between 373 K and 440 K and fits well with the evaporation temperature of pyrrole and/or water. This weight loss can therefore be assigned to the loss of 1 pyrrole and 0.35 H_2O molecules (14.09 %), as is in agreement with the elemental analysis (section 3.1.1).

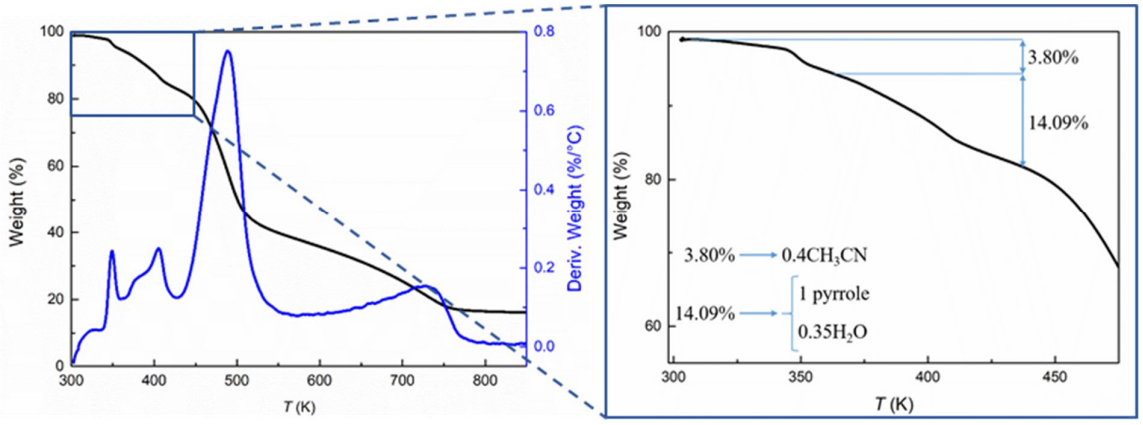

Figure 37. Left: thermogravimetric analysis of **1**·pyrrole between 303 K and 873 K. Right: zoom of the TGA region between 303 K and 475 K.

Density Functional Theory calculations are performed to try and gain insight into the crystalline structure of **1**·pyrrole and **1**·2CH_3CN under high humidity. In this last case, it is assumed that the two uncoordinated acetonitrile molecules are substituted by two water molecules, giving rise to **1**·2H_2O. For this, geometrical optimizations were performed for **1**, **1**·2CH_3CN and **1**·2H_2O compounds (*i.e.* empty, with interstitial acetonitrile and water, respectively).

A unit cell containing 204, 156, and 180 atoms is used respectively for **1**, **1**·2CH_3CN, and **1**·2H_2O. The Fe(II) ions are in high spin configuration and the use of the unit cell implies a ferromagnetic alignment of the Fe(II) ions along the chains (*a* axis). Upon acetonitrile and water uptake, the compound exhibits a volume expansion by 26% and 14%, respectively. The lattice parameters of **1**, **1**·2CH_3CN, and **1**·2H_2O are reported in Table 2.

Table 2. Lattice parameters of the optimized geometries computed using PBE+U+D2.

Compound	*a* (Å)	*b* (Å)	*c* (Å)	α (º)	β (º)	γ (º)
1	7.218	10.512	22.719	91.411	90.091	88.050
1·2CH_3CN	7.215	12.505	24.068	89.636	90.016	90.013
1·2H_2O	7.142	12.041	22.842	90.081	89.896	92.122

For the **1**·2CH_3CN complex, the geometry was optimized starting from the experimental coordinates. For **1**·2H_2O, the guest water molecules were placed forming a hydrogen bond with the water that is coordinated to Fe(II). Several orientations were tried but the result with the lowest energy configuration corresponds to adsorbate molecules forming a OH···O bond of 1.64 Å with the coordinated water molecule and pointing the OH groups towards the BF_4 ions as illustrated in Figure 38. For each molecule the two OH···F bond distances are ~1.94 Å and 1.88 Å.

The DFT calculations show that the binding energy of water (0.78 eV) and acetonitrile (0.85 eV) are similar and therefore, they can be expected to compete to be adsorbed within the material, especially at high humidity levels.

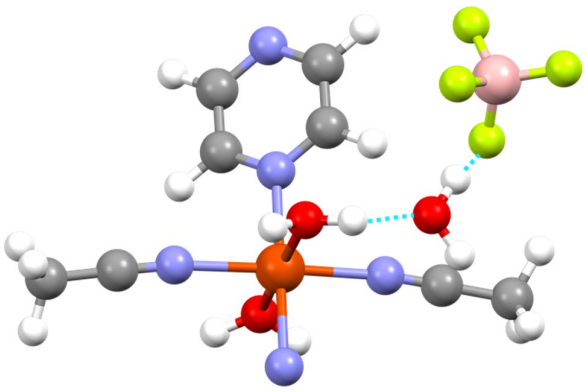

Figure 38. Illustration of the geometrically optimized **1**·2H_2O crystal. The guest water molecules forms an OH bond with the coordinated water and points towards the BF_4 ions possibly via electrostatic/hydrogen bond. Color code: Fe: orange; N: blue; O: red; B: pink; F: green; C: grey; H: white.

A full geometrical optimization of **1**·pyrrole was also attempted but the calculations were unable to converge to a fully relaxed geometry, possibly due to the large steric hindrance within the material when all weakly-bounded acetonitrile molecules were replaced by pyrrole. This is in agreement with the elemental analysis and TGA. Among the different studied configurations of the pyrrole inside

the material, the lowest energy calculation yields a structure with pyrrole bound in a π-π stacking with the pyrazine ligand.

3.2.2. Electric transport measurements

Figure 39a,b shows the temperature dependence of the real and imaginary components of the complex admittance (Y^*) measured on a **1**·2CH_3CN single crystal. These complex components correspond respectively to the conductance (G) and the susceptance (B) of the material such that $Y^* = G+iB$. In both G and B, a sharp peak centered at $T_c(CH_3CN)$ = 310 K appears by increasing the temperature, as previously observed in DC conductance measurements after the release of acetonitrile molecules. Here, the initial increment in G can be fitted to an Arrhenius law for thermally activated transport (Figure 39c). The activation energy barrier obtained from the fit is E_a = 1.28 eV. After that, the thermally activated conductance quenches above $T_c(CH_3CN)$ and G and B drop towards the initial background following a softer exponential decay with temperature. Note that no response is observed in either G nor B during cooling back to room temperature or in subsequent thermal cycles (see Annex B1). Optical and conductance reversibility are regained only once the crystal is exposed again to acetonitrile, as previously reported for DC measurements. The conductance is therefore intrinsically connected to the transient presence of free acetonitrile. This frequency and temperature perturbation in B, together with the progressive drop in G, cannot be understood in terms of a simple thermally activated transport mechanism through the crystal.

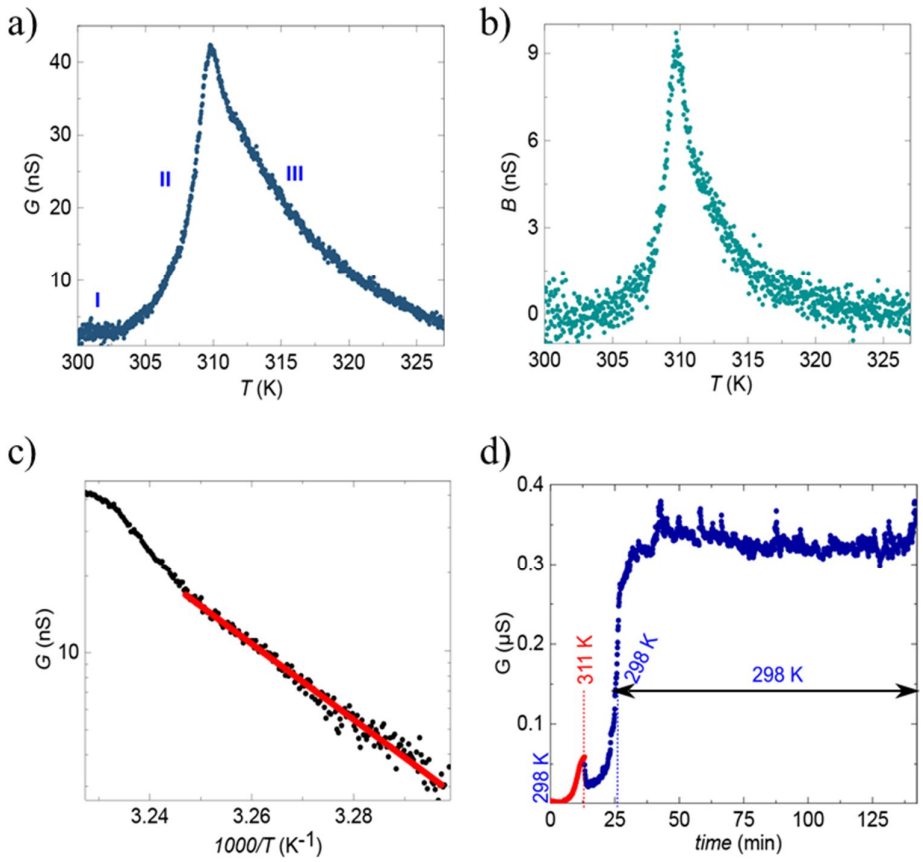

Figure 39. a) Conductance (G) and b) susceptance (B) measured as a function of the temperature in **1**·2CH_3CN. c) Arrhenius plot of G below $T_c(CH_3CN)$. d) G measured in **1**·2CH_3CN as a function of T until 312 K (red points), and back to room temperature (blue points). Thereafter the crystal is left to relax with time for two hours.

To disentangle the roles of temperature and time decay in the post-transition relaxation, an additional measurement is performed (Figure 39d) where the temperature is swept from room T to $T_c(CH_3CN)$ and ramped back to RT, where G is measured as a function of time at RT. Initially, G slightly decreases at T_c, most likely due to a thermal lag. Thereafter no significant decay of G is observed in timescales (2 hours) much larger than those employed in the temperature-dependent measurement (12 minutes) in Figure 39a. The dynamics are therefore predominantly governed by the increment in temperature and not the time decay.

The singular behavior of the admittance observed in these crystals can be explained in terms of proton transport, triggered by the acetonitrile molecules. The high E_a value is consistent with a vehicle transport mechanism where protons diffuse assisted by vehicle molecules in a liquid-like environment. This mechanism is typically described for solvent-assisted, typically water, proton transport in MOFs.[207] The release of acetonitrile molecules from the crystal lattice seems to enable a channel for vehicle transport of protons (scheme II in Figure 40).

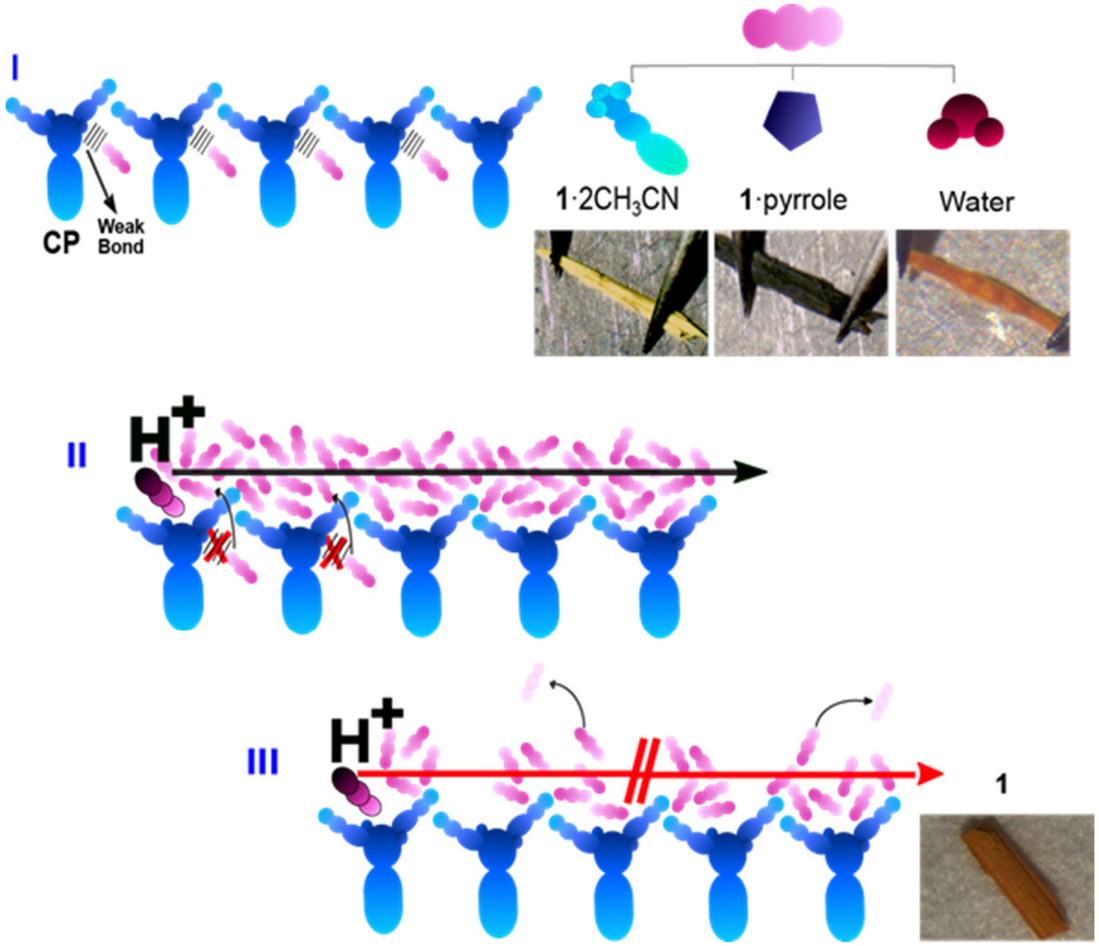

Figure 40. Schematics of the acetonitrile-mediated vehicle proton transport: (I) Acetonitrile is weakly bonded to the lattice. (II) Acetonitrile is released enabling a transient path for proton vehicle transport. (III) The evaporation of acetonitrile quenches the proton transport path.

A similar mechanism has been described for other non-porous coordination polymers where the sudden rotational motion of small molecules in the lattice induces a non-linear increase of the proton conductivity.[231] A possible proton source in **1**·2CH_3CN is moisture or from the coordinated water in the lattice. On the other hand, it has been recently shown that acetonitrile plays a fundamental role in the proton dynamics in zeolites. It was described that a protonated solvent cluster may form,

where acetonitrile dimers $[(CH_3CN)_2H]^+$ form under specific conditions of high acetonitrile pressure, temperature or in small pores.[233] The subsequent temperature-induced quenching of the conductance can be ascribed to the progressive evaporation of the acetonitrile molecules from the surface (Scheme III in Figure 40). A substantial evaporation of acetonitrile has been demonstrated on videos recorded on large amounts of crystals of the compound (Annex A21). This evaporation can be frozen to maintain a constant vehicle path and therefore conductance, as seen in Figure 39d. The conduction of BF_4 anions can safely be discarded since that would lead to the disintegration of the crystals and the process would be irreversible, whereas a clear reversibility in the crystals is observed.

Figure 41b shows the Nyquist plot of the admittance and its temperature dependence. This provides a direct measurement of the different contributions to the conduction in the crystal: (*i*) the intrinsic conductance of bulk, limited by charge traps, defects, etc. (C_c and R_c) defining the low frequency spectrum, and (*ii*) the internal interfaces created by grain boundaries, etc. (C_{gb} and R_{gb}), defining the high-frequency spectrum.[234]

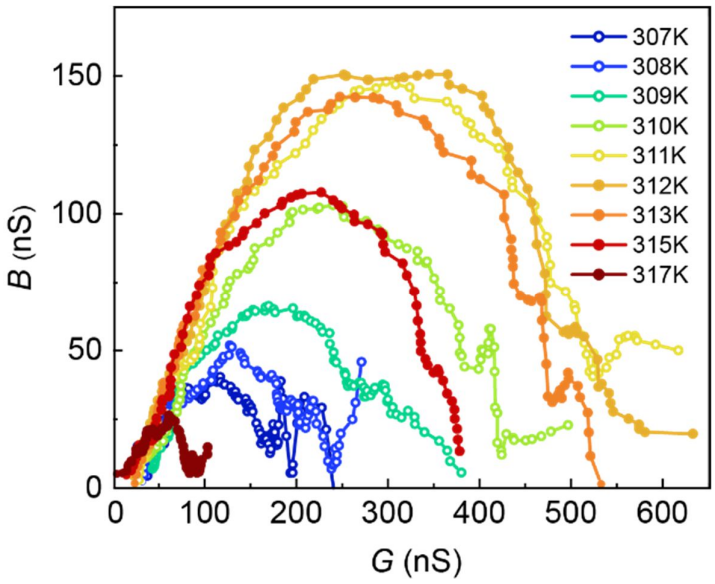

Figure 41. Nyquist representation of the admittance of a **1**·2CH_3CN crystal.

A single, almost complete semicircle is observed spanning over most of the frequency range. This indicates that C_c is predominant, giving rise to the semicircle, while C_{gb} is negligible in comparison, giving rise to the high-frequency tail. This has been reported for negligible grain boundaries in single crystals[228] and in the presence of an almost continuous path for proton transport, like a water or solvent film.[208] It therefore reinforces the vehicle transport of protons through an acetonitrile liquid-like environment scenario. The high-frequency tail becomes significant only at the lowest and the highest temperatures where the acetonitrile film may have discontinuities and therefore the grain boundaries may start to play a role.

To understand the role of humidity on proton transport the AC admittance spectroscopy at higher relative humidity (RH) levels was studied. The *G vs*. *T* at a fixed frequency behavior is observed in Figure 42a. Three main differences can be observed with respect to the sample measured at 32 % RH: (*i*) *G* is around one order of magnitude higher at room temperature. (*ii*) No peak is observed at $T_c(CH_3CN)$ = 310 K. (*iii*) The crystals change from yellow to orange at lower temperatures (291 K) and seem drastically modified after exposition to high humidity. In this case, the electro-optical properties are not reversible by adding acetonitrile again. This behavior was systematically observed in measurements where RH lies above 40 %.

To delve into the role of the weakly-coupled molecules in the crystal lattice, the uncoordinated acetonitrile was also replaced by pyrrole. Figure 42b shows G measured as a function of T and at a fixed frequency ($\omega/2\pi$ = 10 kHz) on a **1**·pyrrole crystal. G is non-zero at room temperature, in contrast with **1**·2CH_3CN. In addition, a sharp increment appears at T_c(pyrr) = 305 K and G remains roughly constant until 312 K where it rapidly decreases below the initial room temperature G. The decay temperature (~ 312 K) is similar to the one observed for the **1**·2CH_3CN crystals and the plateau can be roughly fitted by two contributions that tentatively can account for the initial loss of pyrrole (305 K) and a subsequent loss of remaining acetonitrile (310 K). The presence of both molecules in the lattice seems in accordance to the DFT calculations and the TGA and elemental analysis. This would explain the appearance of a plateau or double peak in the conductance. The larger conductance observed at room temperature when the **1**·2CH_3CN is in high humidity conditions could be due to additional water-assisted proton transport. The absence of a peak at T_c(CH_3CN) may indicate that acetonitrile has already been displaced by the water molecules. Thus, the acetonitrile-mediated proton transport mechanism is quenched. The lower T_c observed at high RH may be due to the slightly lower binding energy predicted by DFT calculations for water (0.78 eV) as compared to acetonitrile (0.85 eV). Also, it has been recently reported that water may displace not only acetonitrile but also other molecules in the bulk which would explain the irreversibility of the process.[230]

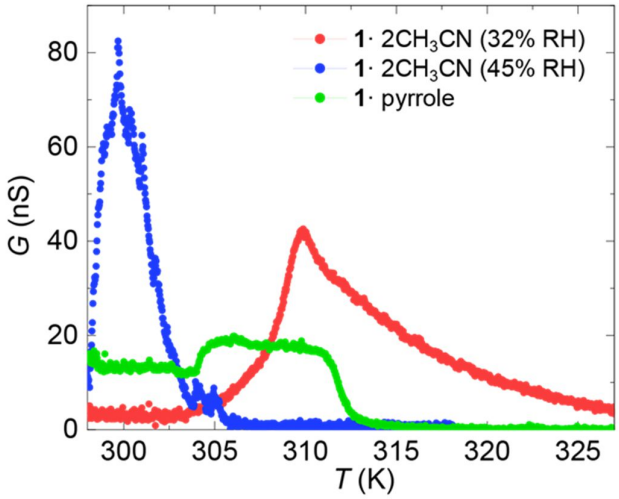

Figure 42. G measured as a function of T in a **1**·2CH_3CN crystal at 32 % RH, a **1**·2CH_3CN crystal at 45 % RH and a **1**·pyrrole crystal.

Therefore, the ability of the crystal to selectively accommodate different molecules in the lattice thus determines the optical properties as well as proton transport properties like conductance or transition temperature.

3.3. CONCLUSIONS

The charge transport properties of non-porous **1**·2CH_3CN have been studied by means of AC admittance spectroscopy, revealing that the conductance in the crystals is of protonic origin. Furthermore, the transport mechanism occurs through the formation of a conduction channel, due to the weakly coupled acetonitrile molecules. This acetonitrile based mechanism preserves proton transport even at low humidity levels (RH < 40%), in contrast to most CPs. This allows to activate and maintain a current level on the otherwise insulating material. Notably, this is the first example

of acetonitrile-mediated proton transport in a non-porous coordination polymer showing distinct optical response to different molecules.

In addition, the effect of higher humidity (RH > 40%) in the transport properties was also studied. This shows that the conductivity peak is shifted to lower temperatures, and results in higher conductivity values. The color of these crystals changes to orange at lower temperatures than **1**·2CH_3CN, and is not reversible upon acetonitrile absorption.

Moreover, a new material, **1**·pyrrole, was synthetized by exposing the **1**·2CH_3CN crystals to pyrrole vapor. This results in changes in the color and the proton conductivity. Hence, the optical response and the proton transport properties (critical temperature, conductance, etc) are determined by the nature of the weakly-bonded molecules, thanks to the particular sensitivity of non-porous CPs to perturbations to their lattices, which is not easily achieved by more rigid MOFs. Accordingly, these properties can be tuned, thanks to the ability of the crystals to reorganize when different molecules are incorporated into the lattice. This may serve as a starting point for the design of switchable protonic conductors and capacitive sensors with selectivity to different small molecules and at low humidity levels.

4. COVALENT POST-SYNTHETIC MODIFICATION BY VOLATILE ORGANIC COMPOUNDS

As it was previously explained in Chapter 1, SCO materials that exhibit low spin (LS) to high spin (HS) transition upon external stimuli (temperature, pressure, light irradiation and guest molecules) have been extensively investigated because of their controllable spin states. This has enabled their potential application into a number of molecular devices like in electronics,[14,235] photonics[235] and mechanics.[136] To develop such applications, certain SCO behavior (like abrupt changes) or transition temperatures are required.[70,72] Up to now, a large number of SCO compounds have been published, and in the last two decades, several MOFs exhibiting SCO have been reported as well.[236] Therefore, complete, abrupt, and hysteretic spin transitions are now all well documented. Nevertheless, the control of the transition remains an ongoing challenge,[237,238] where the generation of sharp and/or hysteretic spin transitions is of particular interest. So far, to tune the nature of a given observed spin transition the use of different ligands, the choice of the counter ion, and/or crystalizing solvent have all been employed.[238]

Recently, post-synthetic modification (PSM) has arisen as a powerful approach for modifying existing materials to create new products that are otherwise difficult or impossible to prepare directly, and as an alternative way to introduce chemical functionality while maintaining the original structure.[239,240] PSM was originally suggested by Hoskins and Robson[241] in 1990 and formally introduced by Wang and Cohen[242] in 2007, and has been widely applied to metal-organic frameworks.[243] It is defined as the chemical modification of a framework after it has been synthesized, performing heterogeneous reactions on the intact, crystalline material.[240,244] Among many recent developments in the study of MOFs, PSM has become both an active area of research and an important tool for exploiting and expanding their unique properties, including their photo-luminescence[245], magnetism[246] and gas adsorption properties.[247,248] Although coordination polymers are less robust than MOFs, many of them can undergo PSM.[10] Therefore, this approach could be a good strategy for developing novel SCO materials, and controlling the spin transition.

There are a variety of different ways in which a material can be modified in a post-synthetic manner, and each of these has the capacity to alter the physical and chemical properties of the framework.[249] For example, post-synthetic ion exchange[4] or modification of the guest molecules[97,106,250] have been used to modify the spin transition of SCO compounds. However, in a more strict sense, PSM can refer only to those modifications involving covalent modification of the organic ligand.[251,252] Covalent PSM (CPSM) is defined as the use of a reagent to modify a component of the material in a heterogeneous, post-synthetic manner to form a new covalent bond (Figure 43).[249]

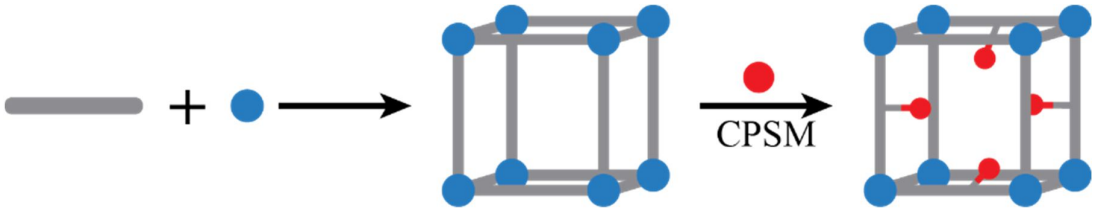

Figure 43. Schematic representation of covalent post-synthetic modification (CPSM).

In recent years, several cases of covalent PSM in SCO compounds have been reported by means of covalent reaction on the organic ligands. It was first achieved by Kepert and coworkers in 2014 (described in further detail in Chapter 1, section 1.1.3.4).[114] The same ligand modification was achieved by Hayami *et al.* following the same procedure in a dinuclear complex (Figure 44), which also results in the alteration of the spin transition.[253] Here, $[Fe(salten)_2(bipytz)](BPh_4)_2 \cdot EtOH$ (bipytz = 3,6-bis(4-pyridyl)-1,2,4,5-tetrazine) was transformed via post-synthetic modification into $[Fe(salten)_2(bipydz)](BPh_4)_2 \cdot EtOH$ ((bipydz = 3,6-bis(4- pyridyl)-1,2-diazine) by treating the dinuclear complex with 2,5-norbornadiene while heating. It should be noted that all efforts to obtain $[Fe(salten)_2(bipydz)](BPh_4)_2 \cdot EtOH$ from a direct reaction between the ligand and the iron salt in solution were unsuccessful. In both cases, a gradual one-step SCO behavior is exhibited, with a similar magnetic behavior at low temperatures but different in the high temperature region, with a more pronounced increase in the magnetic susceptibility value for $[Fe(salten)_2(bipytz)](BPh_4)_2 \cdot EtOH$.

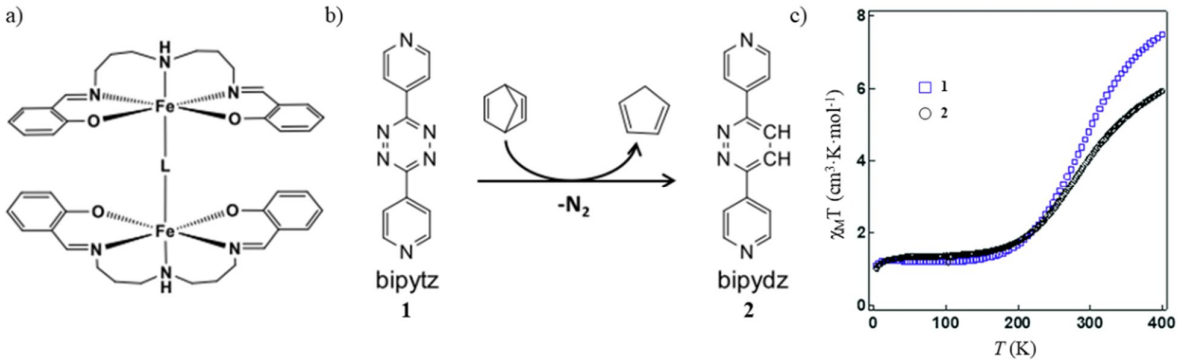

Figure 44. a) Structure, b) chemical modification and c) magnetic susceptibility data, before and after PSM. Reprinted with permission from ref 253. Copyright 2018 Journal of Inorganic and General Chemistry.[253]

The first example in the family of iron-triazole 1D chains was reported by Bousseksou and coworkers (Figure 45).[254] Here, they achieved a covalent modification in the amino group of 4-amino-1,2,4-triazole. This reaction was carried out at 35°C by dispersing the SCO complex in an ethanolic solution of *p*-anisaldehyde for 72h for completion, and thus in a conventional, wet manner.

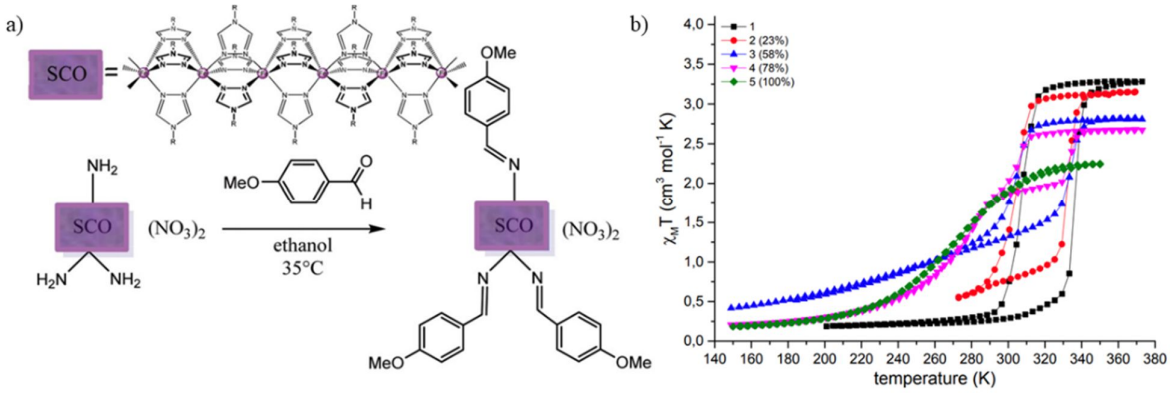

Figure 45. a) Post-synthetic reaction and b) magnetic measurements at different percentages of completion of the CPSM reaction. Reprinted with permission from ref 254. Copyright 2019 Dalton Trans.[254]

However, to the best of our knowledge, there is not any example of a covalent PSM achieved by means of a gas-solid reaction in a SCO compound. A logical next step is to try and achieve this solid-vapor reaction, which could in turn produce a spin transition. That way, these SCO polymers could be used as chemo sensors, since the main principle guiding the design of chemo-sensors is that they must be able to produce an easily measurable response, such as a change of color, upon the absorption of analytes.[255] As previously stated, in these switchable compounds, the inclusion of guest molecules (even in a non-covalent manner) can lead to reversible and dramatic changes.[256] Those can even be detectable by bare-eye at the macroscopic scale, in their physicochemical (*i.e.* optical, magnetic, electronic and elastic) properties associated with the spin state change.[257] Generally, MOFs have been used in advanced chemical sensing applications, as they contain the voids necessary to accommodate guest molecules and thus can act as molecular vessels.[258] In contrast, although 1D coordination polymers and 0D discrete compounds are non-porous by nature, in some exceptional cases they can behave as porous materials and can absorb guest molecules due to an unspecific diffusion process over the lattice.[170,259] Therefore, a reasonable approach is to include specific receptors for specific hazardous volatile molecules to induce a covalent PSM with a high level of selectivity. For example, the previously mentioned SCO coordination polymer with the 4-amino-1,2,4-triazole ligand contains an amino group, which could be a receptor for molecules containing a carbonyl group, such as formaldehyde.

Formaldehyde ($H_2C=O$), otherwise known as methanal, is one of the simplest volatile organic compounds (VOCs).[260,261] At room temperature, it is a colorless gas, with a pungent and irritating smell.[260–263] It is highly volatile, flammable, explosive and reactive and may exhibit various self-association reactions.[260,261,263] This molecule is released from both natural and anthropogenic sources. Environmental sources include its release during combustion of biomass, such as forest and brush fires.[260] Formaldehyde is one of the 25 most abundantly manufactured chemicals globally[263] and is employed worldwide on a grand scale, mainly for the production of resins, building materials, and as a constituent of numerous domestic products such as paint, insulating materials, chipboard and plywood, fabrics, furniture, paper, glues and adhesives, cosmetics, cigarette smoke, and is present in the atmosphere of cities from the incomplete combustion of organics.[260–263] Additionally, formaldehyde is extensively used in both industrial and medical fields, as a sterilizing, antiseptic, and preserving agent in mortuaries, medical laboratories disinfectants, medicines, cosmetics, soaps, shampoos, lotions, sunscreens, and cleaning products.[260–263] Formaldehyde can also be found as a preservative in food and is also present in many plant and animal species as a product of their normal metabolism.[264]

The main form of human exposure to formaldehyde is by inhalation, although it can also be ingested and absorbed through the skin.[262,263] Formaldehyde exposure has been associated with an increased risk of cancer, especially in the nasal cavity, paranasal sinuses, and leukemia.[260–263] Other symptoms include: neurotoxic and systemic toxic effects, watery eyes, stinging sensations in the eyes, nose, and throat, coughing, wheezing, nausea and skin irritation,[261,262] and has also been associated as a main contributor to Sick Building Syndrome (SBS).[265–268] It has also been suggested that formaldehyde inhalation at an early age is related to some neurological diseases in adults.[261]

The most common detection methods for formaldehyde include spectrophotometry, gas and liquid chromatography, fluorescence, HPLC (UV detection), ion cromatography, polarography and iodometric methods.[260,265] Because these methods involve expensive and bulky instrumentation with high energy demand and well-trained personnel,[269–273] they are unable to provide information on real-time on formaldehyde exposition levels.[265] Hence, field instruments with the following characteristics are needed: formaldehyde selectivity, real-time monitoring, low cost, low limit of detection and portable.[274]

With this aim in mind, a well-known[13,275,276] iron(II) 1D SCO coordination polymer $[Fe(NH_2trz)_3](X)_2$ (NH_2trz = 4-amino-1,2,4-triazole and X the monovalent counterion) has been used as a proof-of-concept. This polymer displays a backbone of linearly arranged Fe(II) ions connected by three amino-1,2,4-triazole ligands (Figure 46).

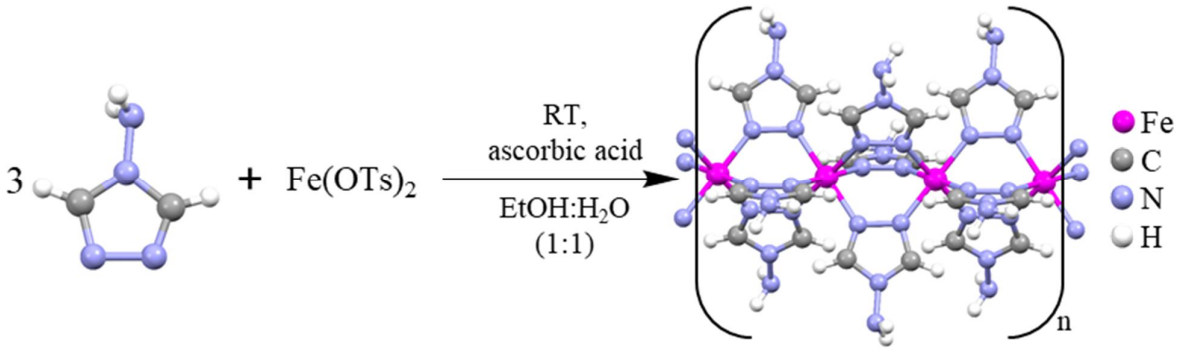

Figure 46. Schematic representation of the chemical reaction leading to the 1D $[Fe(NH_2trz)_3](X)_2$ polymer.

Importantly, the non-coordinated amino pendant group in NH_2trz ligands is free to undergo a covalent PSM.[277,278] According to this premise, the polymer $[Fe(NH_2trz)_3](OTs)_2$ (OTs = *p*-toluenesulfonate) (**1**) was exposed to vapors of different VOCs; precisely: formaldehyde (**2**; Figure 47), benzaldehyde (**3**; Figure 48), and acetone (**4**; Figure 49).[196] These new coordination polymers were characterized with several techniques, including: FTIR, ^{1}H-NMR, PXRD, TGA, elemental analyses, optical reflectivity and magnetic measurements. Furthermore, **1** was exposed to several other organic and inorganic molecules, to determine if a change of color due to a spin transition occurs in any of these cases.

In addition, **1** was embedded in two organic polymers (PMMA and PDMS) to facilitate the inclusion of this coordination polymer in devices. The reactions were also carried out from the composites **1@PMMA** and **1@PDMS**.

4.1. SYNTHESIS OF COMPOUNDS 1-4

4.1.1. Synthesis of compounds 1-4

Compound **1** was synthetized at room temperature. A solution of 0.20 mmol of $Fe(OTs)_2$ in 3 mL of distilled water was added on a drop by drop basis to a solution of 0.59 mmol of aminotriazole previously dissolved in 3 mL of ethanol. The $Fe(OTs)_2$ / aminotriazole H_2O:EtOH solution was stirred for 5 minutes, filtered and left in the freezer overnight. **1** was obtained as a pink powder in 87% yield.

Compounds **2**-**4** were synthetized by following the ensuing general procedure. A screw vial for chromatography (diameter 12 mm, height 32 mm) displaying 10 mg of **1** was placed in a clear glass vial (diameter 27 mm, height 55 mm) provided with 0.1 ml of the corresponding VOC (formaldehyde, benzaldehyde and acetone, to give **2**-**4**, respectively). The glass vial was sealed and kept at room temperature overnight to allow the gas -solid reaction between the corresponding volatile organic compound and **1**.

Anal. calcd (%) for **1**·0.35H_2O: C 36.93%, H 4.03%, N 25.84%; found C 36.34%, H 4.05%, N 25.79%. FTIR (cm^{-1}): 3441 (w), 3293 (m), 3210 (w), 3210 (m), 1631 (m), 1546 (w), 1496 (w), 1449 (w), 1396 (w), 1170 (s), 1122 (s), 1098 (m), 1033 (s), 1008 (s), 881 (w), 813 (m), 681 (s), 623 (s), 563 (s).

Anal. calcd (%) for **2**·0.1H_2O·1.95CH_2O: C 40.12%, H 4.06%, N 22.5%; found C 40.4%, H 4.34%, N 22.33%. FTIR (cm^{-1}): 3264 (b), 3099 (m), 2954 (w), 1655 (m), 1600 (w), 1530 (m), 1497 (w), 1379 (m), 1166 (s), 1122 (s), 1066 (m), 1031 (s), 1007 (s), 919 (m), 680 (s), 632 (m), 563 (s).

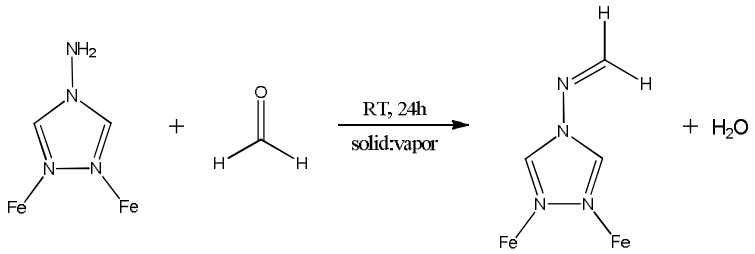

Figure 47. Illustration of the reaction between the organic ligand of **1** and formaldehyde, to give the ligand of compound **2**.

Anal. calcd (%) for **3**·2H_2O: C 51.79%, H 4.45%, N 17.68%; found C 51.51%, H 4.13% and N 18.01%. FTIR (cm^{-1}): 3083 (m), 1696 (m), 1603 (m), 1575 (w), 1532 (m), 1494 (m), 1397 (m), 1335 (w), 1313 (w), 1295 (w), 1167 (s), 1120 (s), 1070 (m), 1032 (s), 1009 (s), 992 (m), 881 (w), 813 (m), 750 (m), 711 (w), 680 (s), 625 (s), 590 (m), 563 (s), 512 (w), 495 (w).

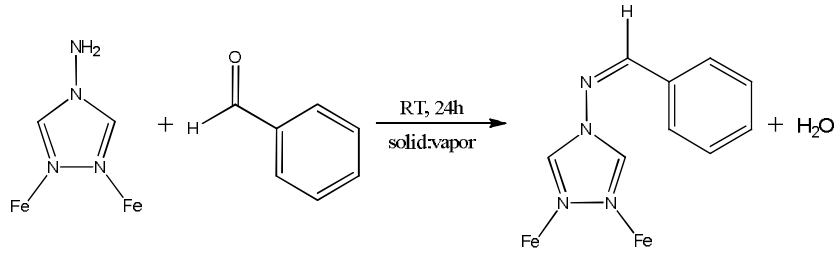

Figure 48. Illustration of the reaction between the organic ligand of **1** and benzaldehyde, to yield the ligand of compound **3**.

Anal. calcd (%) for **4**·0.55H_2O: C 44.62%, H 5.05%, N 21.53%; found C 44.42%, H 5.07%, N 21.78%. FTIR (cm^{-1}): 3085 (m), 2922 (w), 1706 (w), 1633 (w), 1527 (m), 1496 (w), 1434 (m), 1373 (m), 3147 (w), 1218 (m), 1164 (s), 1119 (s), 1084 (w), 1063 (m), 1032 (s), 1008 (s), 923 (w), 900 (w), 872 (w), 814 (s), 765 (w), 710 (w), 678 (s), 628 (s), 563 (s), 519 (w), 492 (w).

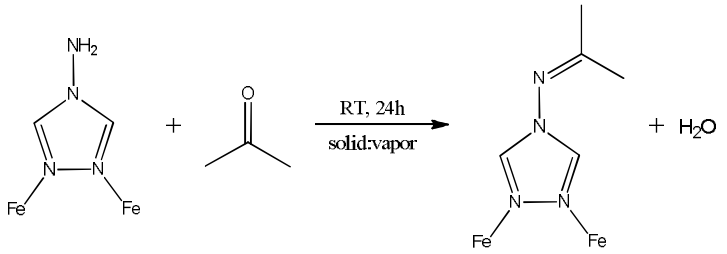

Figure 49. Illustration of the reaction between the organic ligand of **1** and acetone, that results in the ligand of compound **4**.

4.1.2. Synthesis of compounds 1@PMMA-4@PMMA

Compound **1@PMMA** (50% w/w) was prepared by mixing 0.15 g of the **1** powder with 0.15 g of PMMA (PMMA = poly(methyl methacrylate; average M_w ~120000 $g \cdot mol^{-1}$). This mixture was dissolved in $CHCl_3$, sonicated for 30 minutes and deposited in a mold (2.5 cm x 2.5 cm) which was placed in the fridge overnight to allow the $CHCl_3$ to evaporate slowly, so no bubbles appear. The **1@PMMA** film was then carefully removed from the mold.

FTIR **1@PMMA** (cm^{-1}): ν = 3290 (w), 3110 (w), 2995 (w), 2950 (m), 2851 (w), 1724 (s), 1614 (w), 1546 (w), 1480 (w), 1446 (w), 1435 (m), 1386 (w), 1269 (w), 1239 (w), 1189 (w), 1169 (w), 1146 (s), 1122 (s), 1098 (w), 1033 (m), 1009 (m), 988 (w), 966 (w), 912 (w), 880 (w), 841 (w), 812 (m), 749 (s), 683 (s), 625 (s), 563 (s), 481 (w).

To synthetize **2@PMMA-3@PMMA**, a piece of the **1@PMMA** film was put in a screw vial for chromatography (diameter 12 mm, height 32 mm). Afterwards, this tube was placed in a clear glass simple vial (diameter 27 mm, height 55 mm) containing a saturated atmosphere of the respective VOC for three days, resulting in the formation of **2@PMMA**, **3@PMMA** and **4@PMMA** (exposed to formaldehyde, benzaldehyde and acetone, respectively).

FTIR **2@PMMA** (cm^{-1}): ν = 3264 (b), 3100 (w), 2981 (w), 1724 (m), 1651 (w), 1599 (w), 1531 (m), 1449 (m), 1435 (m), 1383 (m), 1344 (w), 1161 (s), 1123 (s), 1067 (m), 1032 (s), 1000 (s), 990 (m), 924 (w), 841 (w), 815 (m), 749 (m), 709 (w), 682 (m), 633 (m), 565 (m), 491 (w).

FTIR **3@PMMA** (cm-1): ν = 3085 (w), 2992 (w), 2950 (w), 1722 (m), 1614 (m), 1603 (m), 1575 (w), 1532 (m), 1493 (w), 1450 (m), 1390 (w), 1337 (w), 1313 (w), 1222 (s), 1174 (s), 1122 (s), 1070 (m), 1034 (m), 1010 (s), 991 (m), 882 (w), 841 (m), 751 (m), 711 (w), 682 (s), 628 (m), 591(m), 565 (s), 490 (w), 452 (w).

FTIR **4@PMMA** (cm-1): ν = 3064 (w), 2981 (m), 1725 (m), 1635 (w), 1532 (w), 1474 (w), 1435 (m), 1266 (w), 1172 (s), 1147 (s), 1122 (s), 1063 (w), 1033 (m), 1009 (m), 994 (w), 966 (w), 913 (w), 841 (w), 815 (m), 750 (m), 711 (w), 681 (s), 627 (m), 566 (s), 530 (w), 484 (w).

4.1.3. Synthesis of compounds 1@PDMS-4@PDMS

The **1@PDMS** film was prepared by mixing 40 mg of **1** and 20 mg of Sylgard-184, which is a two-component kit commercially available (Dow Corning), until a uniform mixture is obtained.[279]

The mixture was degassed by vacuum for 10 minutes and then it was spin-coated on a Petri dish and curated in the oven at 70 °C for one hour.

FTIR (neat, cm^{-1}) of **1@PDMS**: 3282 (w), 3058 (w), 2962 (m), 1631 (w), 1545 (w), 1496 (w), 1410 (w), 1258 (m), 1170 (m), 1063 (s), 1030 (s), 1008 (s), 910 (w), 864 (m), 844 (m), 792 (s),757 (m), 681 (m), 624 (m), 563 (m).

The synthesis of **2@PDMS-4@PDMS** is performed identically to that of PMMA. **1@PDMS** was put in a screw vial for chromatography (diameter 12 mm, height 32 mm). Afterwards, this tube was placed in a clear glass simple vial (diameter 27 mm, height 55 mm) containing a saturated atmosphere of the respective VOC for six hours, resulting in the formation of **2@PDMS**, **3@PDMS** and **4@PDMS** (exposed to formaldehyde, benzaldehyde and acetone, respectively).

FTIR (neat, cm^{-1}) of **2@PDMS**: 3288 (b), 3101 (w), 2962 (m), 2904 (w), 1649 (w), 1599 (w), 1530 (w), 1411 (w), 1258 (m), 1167 (w), 1063 (s), 1008 (s), 913 (w), 843 (w), 789 (s), 755 (w), 685 (m), 600 (w), 565 (m).

FTIR (neat, cm^{-1}) of **3@PDMS**: 3061 (w), 2962 (m), 1697 (w), 1602 (w), 1576 (w), 1534 (w), 1495 (w), 1450 (w), 1409 (w), 1258 (m), 1169 (m), 1069 (s), 1031 (w), 1008 (s), 910 (w), 864 (w), 844 (w), 792 (s), 756 (w), 681 (m), 625 (m), 591 (w), 563 (m).

FTIR (neat, cm^{-1}) of **4@PDMS**: 3068 (w), 2962 (m), 2903 (w), 1710 (w), 1633 (w), 1530 (w), 1413 (w), 1363 (w), 1258 (m), 1176 (m), 1060 (s), 1009 (s), 911 (w), 864 (w), 843 (w), 791 (s), 757 (w), 680 (m), 627 (m), 600 (w), 564 (m), 530 (w).

4.2. RESULTS AND DISCUSSION

4.2.1. Physico-chemical study

Compound **1** was exposed at room temperature to a saturated atmosphere of the VOCs formaldehyde (**2**), benzaldehyde (**3**) and acetone (**4**) (Figure 50a).

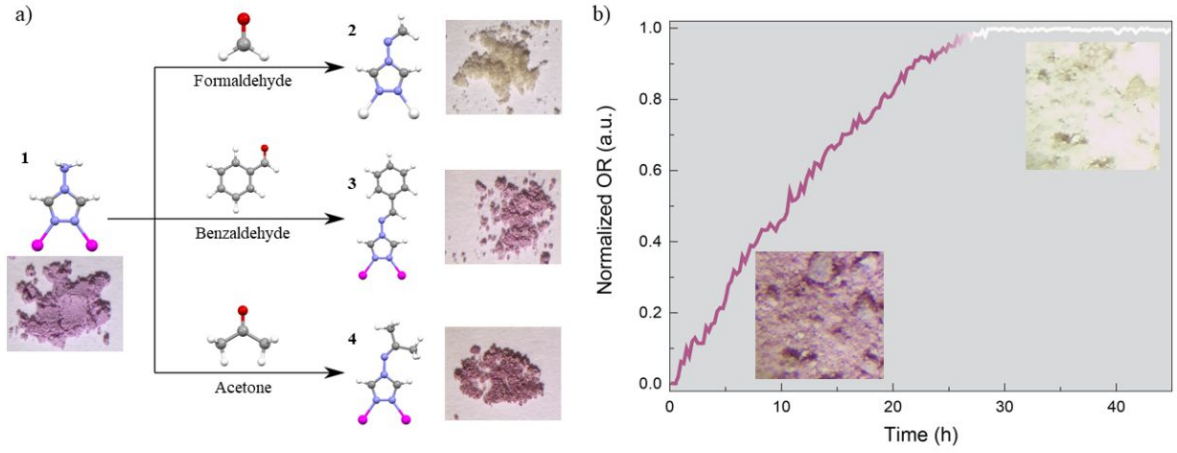

Figure 50. a) Illustration of the covalent post-synthetic modifications of $[Fe(NH_2triazole)_3](OTs)_2$ (**1**), including a picture of the powder of the starting and final (**2-4**) compounds. b) Optical reflectivity *vs*. time of the transformation of **1** to **2** upon exposure to formaldehyde vapors. Inset: pictures at time zero and 45 hours.

These expositions result in a covalent reaction between the amino group in NH_2triazole and the carbonyl group in the respective VOC, leading to the formation of the corresponding imine. When

3 and **4** are formed, the color of the compound remains pink. Interestingly, the color of the material changes to white upon exposition to formaldehyde. The optical reflectivity *vs*. exposure time is plotted in Figure 50b. Here, the OR increases as the color becomes lighter, up to 24 hours, where a plateau is reached when the material turns white. This plateau remains constant up to 45 hours.

Infrared (IR) spectroscopy was used to identify the functional groups reacting with the NH_2 pendant groups (**1**) for compounds **2**-**4**. FTIR spectra of the ligand NH_2trz and **1**-**4** are represented in Figure 51. A sharp band corresponding to the NH stretching mode (red) of the amino group, can be observed both in the ligand (3227 cm^{-1}) and in **1** (3293 cm^{-1}). The deformation of the NH band can also be seen in both, centered at 1529 cm^{-1} and 1546 cm^{-1}, respectively. As expected, none of these two bands appear in **2**-**4**, indicating that the covalent reaction with the amino group was completed. The stretching C=N mode can be seen in the free ligand, NH_2trz, and compounds **2**-**4** in blue (1522 cm^{-1}, 1529 cm^{-1}, 1532 cm^{-1} and 1527 cm^{-1}, respectively). In the first case, the band comes from the triazolyl moiety, while for **2**-**4**, it can be ascribed to the newly formed bond between the amino and aldehyde/ketone groups (imine group). The C=N stretching mode is not appreciated in **1** because the double bond character is lost upon coordination to the iron(II).

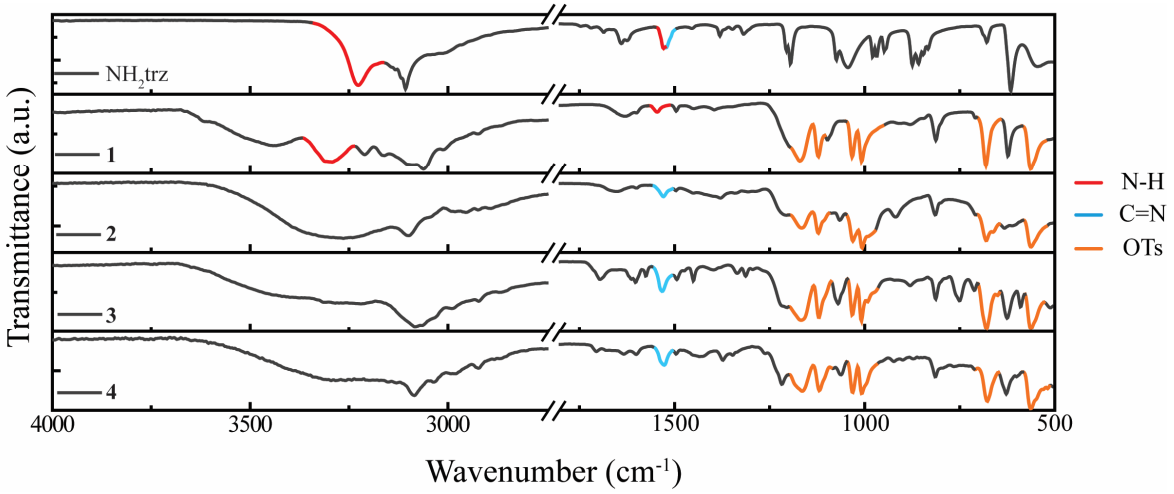

Figure 51. IR spectra of the organic ligand NH_2trz and CPs **1**-**4**.

In compounds **1**-**4**, the OTs^- counter ion is revealed (in orange) by two doublets (1179 cm^{-1} and 1122 cm^{-1}; 1036 cm^{-1} and 1009 cm^{-1}) associated to the skeletal C-C bending and stretching modes in the phenyl group and the SO_3 group symmetric stretching. Moreover, the singlet centered at 812 cm^{-1} can be attributed to the CC in-plane stretching of the phenyl ring and the symmetric stretching in SO_3. The bands *ca.* 676 cm^{-1} and 561 cm^{-1} can be associated with the C-S stretching mode. Importantly, the absence of the corresponding VOCs fingerprints bands (C=O stretching for formaldehyde: 1642 cm^{-1}; benzaldehyde: 1696 cm^{-1} and acetone: 1710 cm^{-1}) in the **2**-**4** spectra is consistent with the lack of remaining VOCs molecules in the solids.

Nuclear Magnetic Resonance (^{1}H-NMR) was also performed on all samples (see Figure 52 and Annex C1-Annex C4 for full spectra).

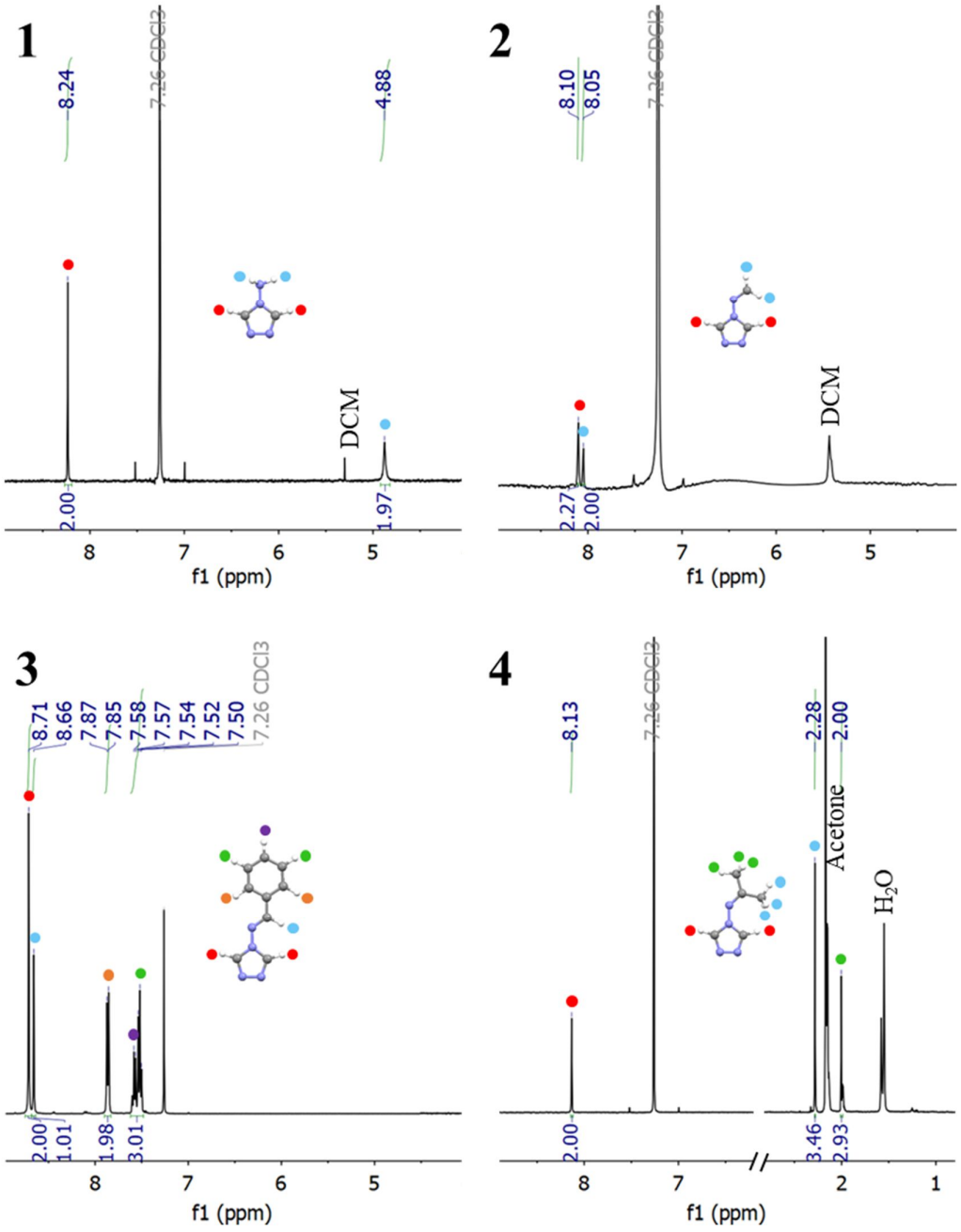

Figure 52. [1]H-NMR of **1-4** after digestion.

Samples **1-4** were evaluated after digestion in deuterated aqueous solution of K_3PO_4 followed by a $D_2O/CDCl_3$ extraction to determine the specific organic triazol moeity obtained as a result of the CPSM. The **1** spectrum shows two singlets from the methylene group in the triazole (2H, δ = 8.24 ppm) and the amino group (2H, δ = 4.88 ppm). The collected [1]H-NMR spectrum for **2** shows the characteristic signal corresponding to a primary imine (singlet at 8.05 ppm integrated by the two hydrogens in the $N=CH_2$ group) and the signal coming from the methylene groups in the triazole moiety (2H, δ = 8.10 ppm). For **3,** the signals associated to the aromatic ring appear in the form of a doublet (2H, δ = 7.86 ppm) and a multiplet (3H, δ = 7.57-7.52 ppm). Besides, the hydrogen resonance from the imine group can be seen as a singlet at 8.66 ppm. The methylene groups in the triazole moiety are noticeable at 8.71 ppm. Finally, in **4**, the methylene groups in $N=C-(CH_3)_2$ led to two singlets at 2.28 ppm and 2.00 ppm, whereas the methylene groups in the triazole moiety are

shown by the singlet at 8.13 ppm. Notably, the ^{1}H-NMR spectra confirm that the CPSM are complete in all cases (the signal at 4.88 ppm associated in the NH_2trz in **1** is absent in the ^{1}H-NMR spectra displayed by the new CPs).

Although all attempts to obtain single crystals of **1**-**4** have failed, PXRD analyses were performed to gain insight of the post-synthetized structure. The main conclusion in this study is that **2**-**4** PXRD patterns are different from the starting SCO polymer **1**, thus, confirming the occurrence of structural modifications which can be associated to the appearance of new different species (Figure 53).

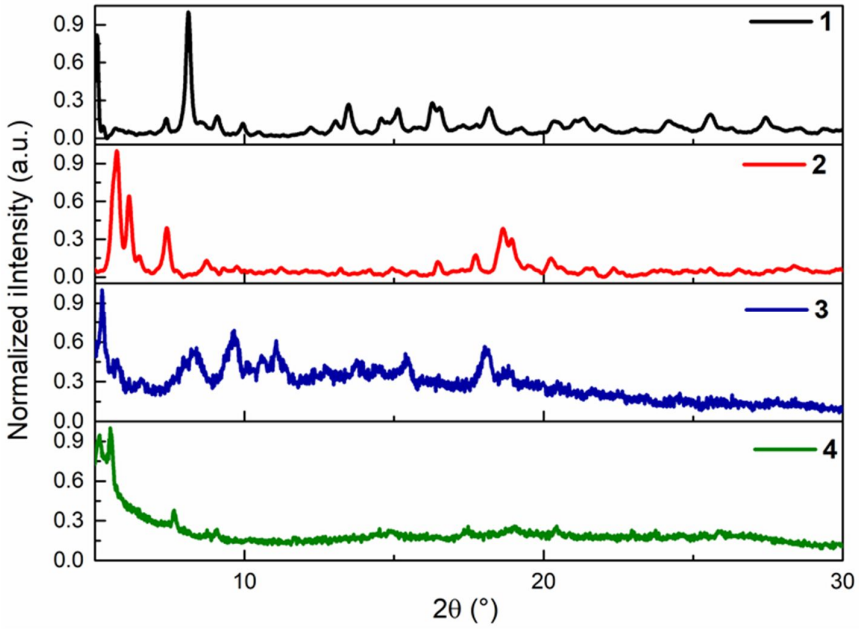

Figure 53. Powder X-ray diffractogram for compounds **1**-**4**.

4.2.2. Magnetic studies

As expected, **1**-**4** display different physico-chemical properties. Figure 54 depicts the magnetic properties of the compounds with varying temperature. Consistent variable-temperature OR measurements are included in Annex C6.

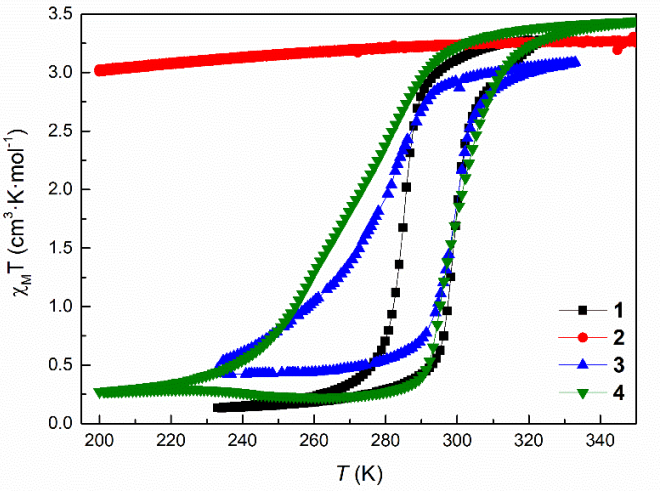

Figure 54. Magnetic susceptibility measurements for compounds **1**-**4**.

The $\chi_M T$ product (where χ_M is the molar magnetic susceptibility and *T* is the temperature) ranges from 3 to 3.3 $cm^3 \cdot K \cdot mol^{-1}$ for **1**-**4** above room temperature, in agreement with the presence of Fe(II) centers in the HS electronic state. Upon cooling, the $\chi_M T$ product decreases to 0 $cm^3 \cdot K \cdot mol^{-1}$ abruptly for **1** ($T_{1/2}\downarrow$ = 285.1 K), and in a more gradual way for **3** and **4** ($T_{1/2}\downarrow$ = 277.0 K and 270.1 K, respectively). In contrast, the $\chi_M T$ product for **2** remains almost constant in the temperature range of 220-340 K, showing an incipient decrease of the $\chi_M T$ value at low temperature (see Annex C5). Upon heating, the $\chi_M T$ product abruptly increases back to their initial values in compounds **1** ($T_{1/2}\uparrow$ = 299.5 K, with a hysteresis value of 14.4 K), **3** ($T_{1/2}\uparrow$ = 299.2 K, hysteresis = 22.2 K) and **4** ($T_{1/2}\uparrow$ = 300.2 K, with a hysteresis of 30.1 K), reflecting a complete LS→HS spin transition.

4.2.3. Sensing applications

As previously explained, formaldehyde is widely used in household materials and has been associated with many health risks.[266–268] However, conventional formaldehyde detection systems require the services of highly-trained operators.[269–273] In this Chapter, it has been established that when compound **1** is exposed to formaldehyde, a color change from pink to white takes place at room temperature, although exposure of **1** with other related molecules remains pink at the same temperature range. In other words, **1** would make a very promising easy-to-use formaldehyde sensing material, while also trapping this pollutant in the structure, through the formation of the covalent bond. To further explore the sensing abilities of this polymer and its selectivity towards formaldehyde, **1** was exposed to a saturated atmosphere of a variety of organic and inorganic volatile (see vapor pressures in Annex C7)[280,281] compounds (formic acid, HCl, ethyl isocyanate, H_2SO_4, NH_3, triethylamine (TEA), H_2O_2, acetaldehyde, acetophenone, salicylaldehyde propanal and butanal) at room temperature. These vapors can be classified under six different categories: ketones and aldehydes (involving a carbonyl group), carboxylic acids, molecules containing an isocyanate group, inorganic acids, amines and oxidation agents. In the IR spectra, the presence of the tosylate counterion is revealed in all cases by the signals *ca.* 1179 cm^{-1}, 1122 cm^{-1}, 1036 cm^{-1}, 1009 cm^{-1}, 812 cm^{-1}, 676 cm^{-1} and 561 cm^{-1} (Figure 55).

In the first group (Figure 55, blue background), compound **1** is exposed to guest molecules containing a carbonyl group, either from a ketone or an aldehyde: acetaldehyde, acetophenone, salicylaldehyde, propanal and butanal. In these cases, the expected reaction is a condensation between the amino and carbonyl groups, as is the case for compounds **2**-**4** (Annex C8). The IR spectra for acetophenone and salicylaldehyde exposure is identical to that of **1**, evidencing that the reaction did not take place and longer exposition times or higher temperatures are probably required. On the other hand, the presence of acetaldehyde, propanal and butanal results in the disappearance of the characteristic NH amine band at 3293 cm^{-1}, and the emergence of the C=N band at 1533 cm^{-1}, 1535 cm^{-1} and 1533 cm^{-1}, respectively. In all three cases, a small band can be seen around 1700 cm^{-1} (1710 cm^{-1}, 1703 cm^{-1} and 1709 cm^{-1}, respectively), characteristic of the carbonyl group, and evidence that a small amount of the VOC remains in the structures, regardless of every effort to dry them. Nevertheless, under exposure to any of these VOCs, the compound turns a brownish color (particularly with acetaldehyde). This change of color to brown is usually associated with an iron(II) to iron(III) oxidation.

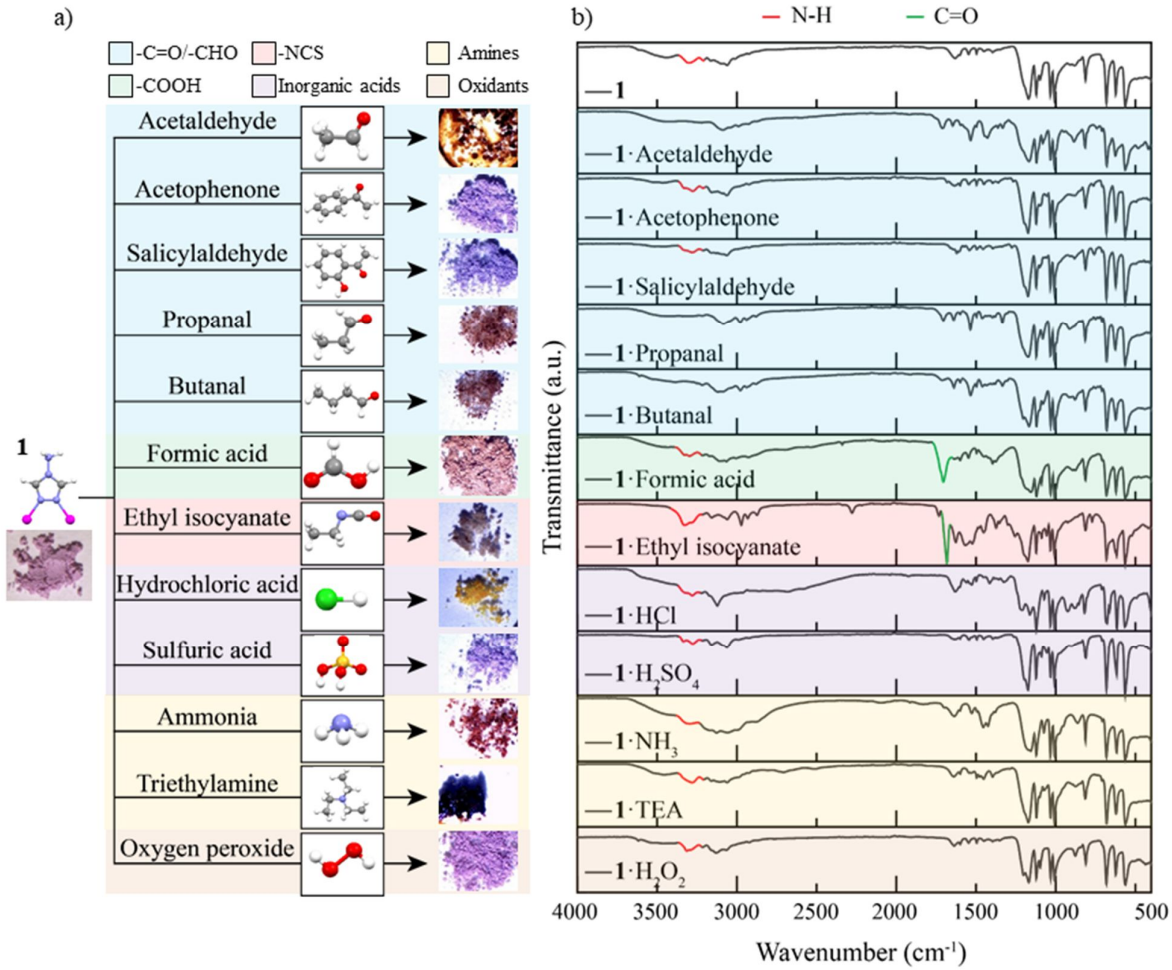

Figure 55. a) Scheme of reaction and b) IR spectra for exposition to other vapors. The colors represent the different groups in which the molecules used for exposition can be classified: containing a carbonyl group (blue), carboxylic acids (green), containing an isocyanate group (pink), inorganic acids (purple), amines (yellow) and oxidant agents (brown).

In addition, **1** was exposed to a compound containing a carboxylic acid (Figure 55, green background): formic acid. The expected reaction would be between the carbonyl and amino groups, resulting in the formation of an amide (Annex C9). In the IR spectra, a very sharp and intense singlet at 1705 cm^{-1} correlates well with the stretching mode of a C=O group. Furthermore, the presence of the NH signal at 3300 cm^{-1} also supports this hypothesis. Here, the color remains pink, but slightly paler than that of **1**.

In the case of ethyl isocyanate (Figure 55, pink background), the expected reaction would lead to the formation of a urea derivative (Annex C10).[282] In the IR spectra, the carbonyl group can be observed at 1683 cm^{-1} and the NH band is visible at 3327 cm^{-1}. Nevertheless, the color becomes slightly brownish, which could again mean the partial oxidation of iron(II) to iron(III).

Upon exposition to inorganic acids, like HCl and H_2SO_4 (Figure 55, purple background), two different behaviors are displayed. In the case of sulfuric acid, which is scarcely volatile, the IR spectrum and color of the compound remain unchanged compared to **1**, evidencing the exposition has not resulted in any chemical changes in the structure. However, upon exposure to HCl, the color of the compound changes to yellow and the IR spectra varies slightly, although no significant band

changes can be assigned. A similar experiment was carried out by Garcia and coworkers,[283] where they demonstrated that this color change is not caused by the oxidation of the Fe(II) nor by any changes in the coordination sphere of the metal center.

As with inorganic acids, the exposure to basic amines (NH_3, TEA; Figure 55, yellow background), was not expected to produce any changes due to a covalent reaction in the organic ligand. However, the exposition to these molecules was tested in the event that the absorption by diffusion through the crystal lattice could be achieved and resulted in visible color changes in the material. With ammonia, the color becomes a darker, redish pink, and with TEA the compound becomes oily. In both cases, the IR spectra differs slightly from the initial one, with the appearance of certain bands (NH_3: 1454 cm^{-1}, 1423 cm^{-1} and 1072 cm^{-1}; TEA: 1475 cm^{-1}, 1070 cm^{-1}).

Exposure to an oxidation agent like H_2O_2, (Figure 55, brown background) results in the same IR spectrum and color, indicating that the metal centers have not been oxidized from iron(II) to iron(III).

In conclusion, although exposure to other molecules has, in some cases, led to changes in the organic ligand, the oxidation state of the metal center or any other change in the material, none of these expositions result in a spin transition from LS to HS (and thus, a change of color from pink to white), like it occurs with formaldehyde. Therefore, while many more volatile molecules can be screened, **1** is a good candidate for selective formaldehyde sensing.

4.2.4. Implementation in organic matrixes

In order to employ **1** as a sensing device, the study of its implementation in different matrixes is of major importance. To this end, **1** was embedded in two organic polymers: PMMA and PDMS. Polymethyl methacrylate (PMMA) is a low-cost, biocompatible and easy to process in almost any shape polymer with excellent physico-mechanical properties, which could facilitate its implementation in devices.[284] The unique mechanical properties of this polymer render PMMA the strongest thermoplastic resistant to scratching and chemical attacks. In addition, it is optically transparent and resistant to UV radiation so it was first used as a substitute of glass, on account to its light weight, resistance to shattering and high impact strength. Other applications of this polymer range from optical, pneumatic actuators, drug delivery, electro diffusion, nanotechnology, as dental implants and as sensors.[285] Polydimethylsiloxane (PDMS) is the most frequently used silicon-based organic polymer,[286,287] as it is clear and transparent, non-toxic, non-flammable, highly flexible and has excellent biocompatibility. As a result, PDMS has emerged as a regular substrate in chemistry, physics, materials science, mechanical engineering and microelectronics. Therefore, it has been widely employed in a number of applications, including flow delivery in microfluidics, creation of lab-on-chip devices, in smart-window applications, defoamers, contact lenses, water-repellent coatings, cosmetics, lubricants and many others.[288] Furthermore, the porous nature of PDMS makes it highly permeable to small molecules, that can diffuse into the bulk polymer, which has enabled the use of PDMS in sensing devices.[289] Both organic polymers would be good candidates for the development of sensing devices, with each one presenting different properties, like porosity and flexibility.

The embedding process is different for the two organic matrixes. In the case of PMMA, a mixture of **1** and PMMA was dissolved in $CHCl_3$, sonicated and deposited in a mold for slow evaporation of the solvent. For PDMS, **1** and dimethylvinyl- terminated dimethylsiloxane (PMDS) were mixed until an homogeneous mixture was obtained, and then it was vacuumed and introduced in the oven at 70 °C for 1 hour for the curation process (details in section 4.1.3).[279] The exposition to the different VOCs of **1@PMMA** and **1@PDMS** is performed in the same manner as with the powder (see sections 4.1.2 and 4.1.3). For PMMA, although notably less porous than PDMS, the expected color

change from pink to white occurred when the composite was exposed to formaldehyde vapor for three days and **2@PMMA** was formed (Figure 56). Under the same conditions, **1@PMMA** was exposed to benzaldehyde (**3@PDMS**) and acetone (**4@PMMA**). **3@PDMS** turns brown, even though **3** remains pink in the bulk experiment. In the case of **4@PMMA**, the material retains the pink color, as expected. The IR spectra of **1@PMMA-4@PDMS**, show the characteristic bands from the respective coordination polymer and from PMMA (Figure 56).

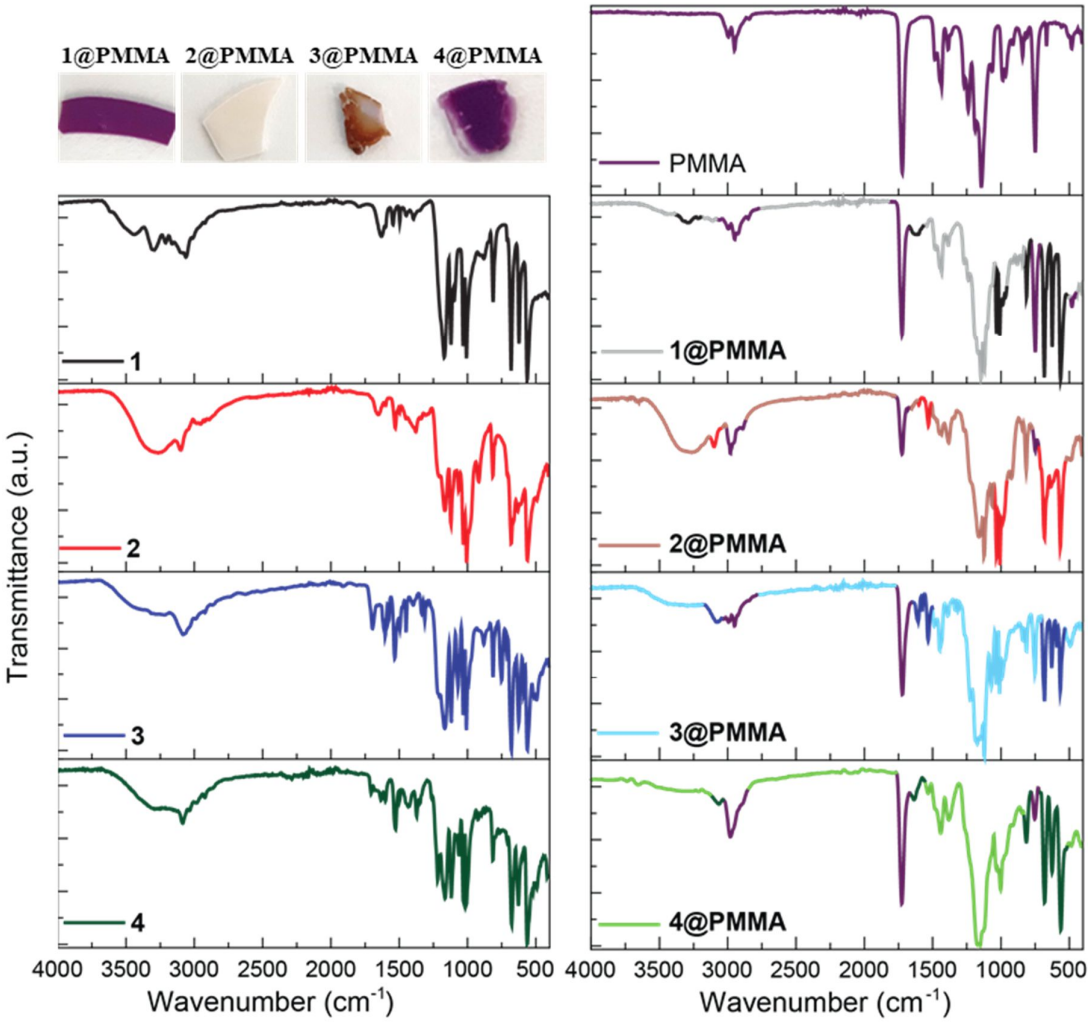

Figure 56. IR spectra of compounds **1**-**4** and composites **1@PMMA-4@PMMA**, and pictures of the latter. In the composites IR spectra, the bands that can be unambiguously assigned to PMMA are colored in purple, and those that can be attributed to the coordination polymer are shown in the respective color.

The optical reflectivity measurements *vs*. the temperature of **1@PMMA** and **2@PMMA** are plotted in Figure 57. The hysteresis cycle for **1@PMMA** shows that after **1** is embedded in the organic polymer, the transition becomes more gradual and the hysteresis, wider ($T_{1/2}\downarrow$ = 278.6; $T_{1/2}\uparrow$ = 296.9; hysteresis =18.3 K). When this polymer is exposed to formaldehyde vapors, it becomes white, and no spin transition is observed in this temperature range.

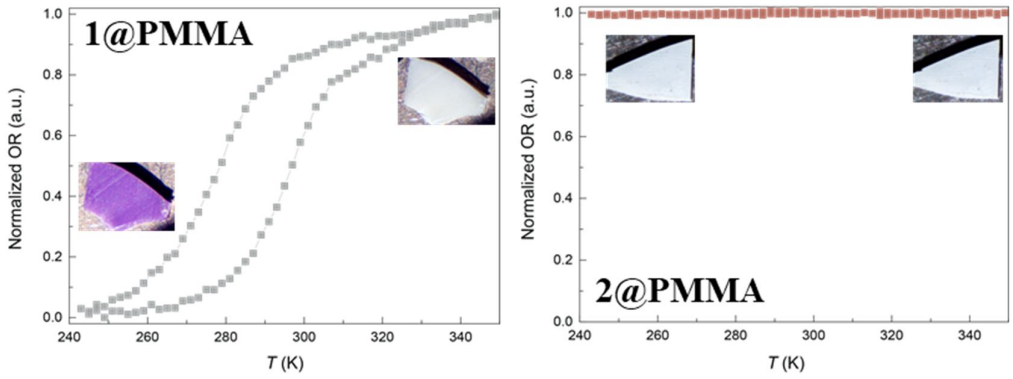

Figure 57. Optical reflectivity measurements of **1@PMMA** and **2@PMMA**. Normalized in respect to **1@PMMA**. Inset: pictures at the lowest and highest measured temperature.

In the case of the integration in PDMS, a porous polymer, the time for completion of the vapor-solid reactions is significantly faster, requiring only 4 hours for changes to be observed in the macroscopic scale and the IR spectra (Figure 58).

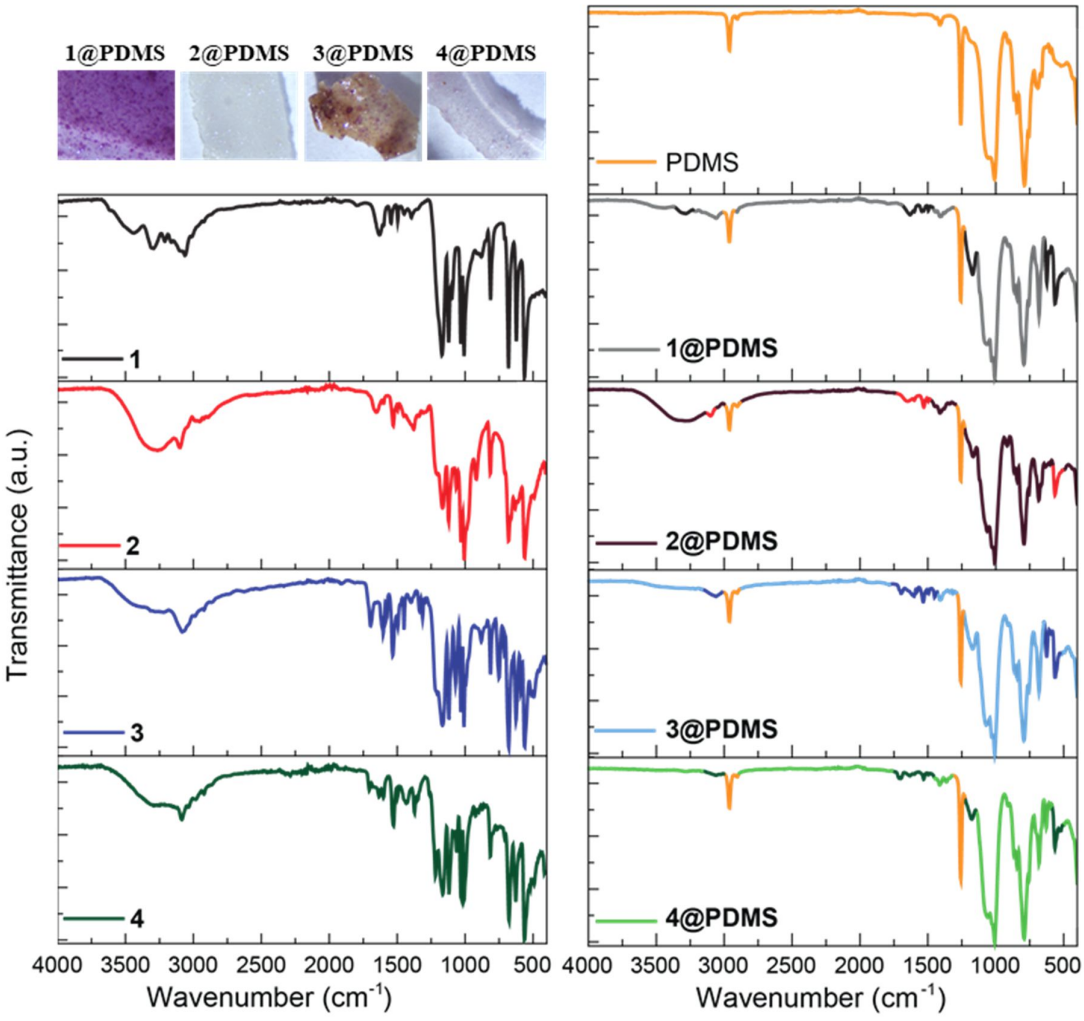

Figure 58. IR spectra of **1**-**4** and **1@PDMS**-**4@PDMS**, and images of the latter. In the IR spectra for the films, the characteristic bands of PDMS are shown in orange, and the ones that can be assigned to the respective compound are represented in the corresponding color.

Here, the characteristic bands of **1**-**4** can be observed, in combination from the ones arising from PDMS. In respect to the color, the changes observed for **2@PDMS** and **3@PDMS** are the same as with PMMA: change to white under exposure to formaldehyde, and to brown when exposed to benzaldehyde. Notably, when **1@PDMS** is exposed to acetone vapor, the color becomes a lighter shade of pink, nearly white. This means that in combination with PDMS, the hysteresis cycle of the spin transition is modified and **3@PDMS** is almost completely in its HS state at room temperature. While this result is somewhat contradictory to the premise that this material is selective to formaldehyde detection, it merely means that in order to implement **1** in devices, a substrate other than PDMS should be used to avoid acetone interferences.

In Figure 59, the optical reflectivity measurements of **1@PDMS** and **2@PDMS** are displayed. The spin transition in **1@PDMS** is more gradual than in **1** and **1@PMMA**, but exhibits the lowest hysteresis ($T_{1/2}\downarrow$ = 271.8; $T_{1/2}\uparrow$ = 285.5; hysteresis = 13.7 K). Again, upon formaldehyde exposure, the spin transition does not appear in this temperature window.

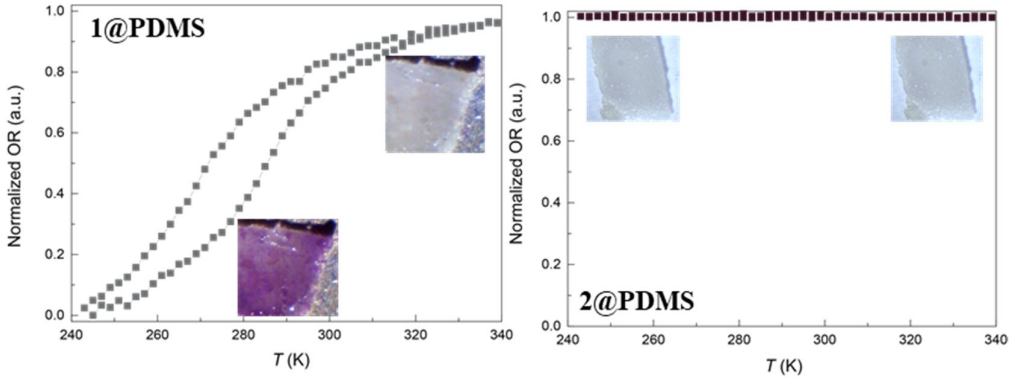

Figure 59. Optical reflectivity measurements of **1@PDMS** and **2@PDMS**. Normalized in respect to **1@PDMS**. Inset: pictures at the lowest and highest recorded temperature.

4.2.5. Reversibility

Another important aspect to study is the possibility of reversing the condensation reaction to recover compound **1** from compound **2**. Table 3 summarizes the different attempted synthetic routes. Most of these involve the use of water as a solvent, but since these coordination polymers are highly soluble in water, the reactions were also tested with the composites **2@PMMA** and **2@PDMS**. The synthetic routes include:

- The use of water as a solvent to hydrolyze the formed imine.
- The use of bases or acids to catalyze this reaction.
- The substitution of the newly formed ligand with NH_2trz in solution.
- Reversibility through a gas-solid reaction.

Each reaction has been tested with different conditions, including variations in the temperature, reagent concentration and time of the reaction. The red crosses symbolize the reactions that did not work. That is to say, the precipitated isolated after the reaction was characterized with FTIR, and identified as the starting CP. In addition, in some cases the color of the materials turned brown or black, showing that some degradation has occurred. Therefore, it is concluded that the reversibility of **2**→**1** could not be attained in this work.

Table 3. Reactions carried out to attempt reversibility from **2** to **1**.

		Reagents								
		H_2O	H_2O, TEA	H_2O, pyridine	H_2O, NaOH	H_2O, $CaCO_3$	H_2O, HCl	H_2O, NH_2trz	H_2O vapor	N_2H_4 vapor
Compound	**2**	X	X	X	X	X	X	X	X	X
	2@PMMA	X	X	X	X	X	X	X	X	X
	2@PDMS	X	X	X	X	X	X	X	X	X

4.3. CONCLUSIONS

In conclusion, new CPs displaying a wide range of properties have been easily prepared as a result of a simple covalent PSM between **1** and different VOCs. This method allows for the synthesis of new compounds, and could potentially be used to develop materials that could not be obtained through conventional routes. Compounds **3**-**4** feature the well-known SCO phenomena with abrupt and hysteretic spin transitions taking place near room temperature whereas compound **2** is paramagnetic until very low temperatures where it shows an incomplete spin transition. The fact that **1** generates different CPs with fully distinct properties when in contact with carbonyl-containing VOCs makes it ideal for sensing the presence of such organic compounds in the environment, while also trapping these contaminants in the structure. Moreover, in the presence of formaldehyde, a hazardous VOC, **1** undergoes a clear color change from pink to white, resulting in a less expensive and more manageable way of detecting this molecule (Figure 60). This color change has not been observed when **1** is exposed to several other volatile molecules.

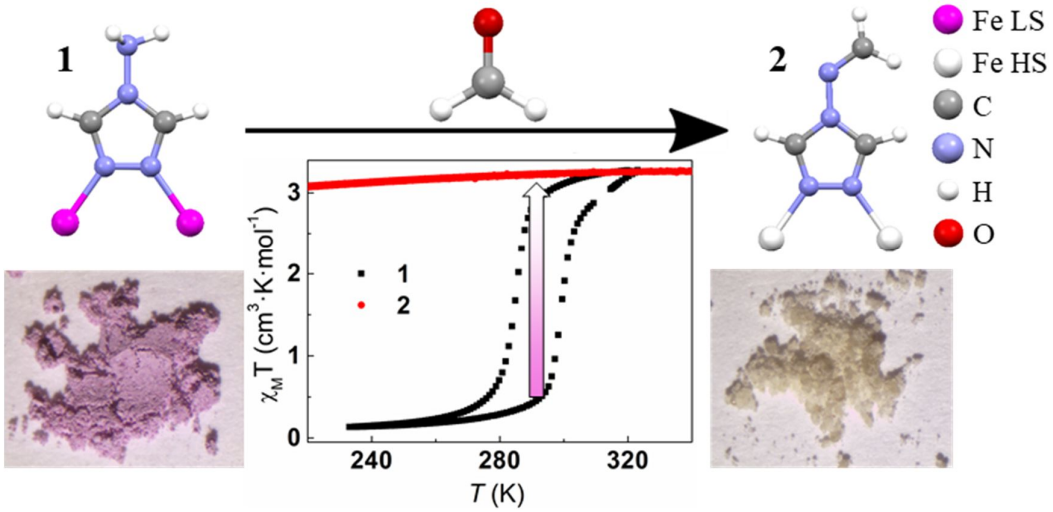

Figure 60. Scheme of reaction between **1** and formaldehyde to give **2**, color change and magnetic behavior.

In addition, **1** has been embedded in two organic polymers, PMMA and PDMS to facilitate its future implementation in devices. These two matrixes present different mechanical properties and porosity, but in both cases when exposed to formaldehyde vapor, the pink composite (**1@PMMA** or **1@PDMS**) turns to white (**2@PMMA** or **2@PDMS**). However, exposure of **1@PDMS** to acetone also results in a change of color. Therefore, PDMS is not the best substrate for future sensing applications, as to avoid acetone interferences. Thus, other substrates, preferably with high porosity, should be checked, for potential sensing applications.

Moreover, **1@PMMA** is an interesting material, as it exhibits the spin transition at temperatures close to RT, and it makes **1** easy-to-use in a number of applications, since it presents a certain rigidity, makes it portable and easy to manipulate and design in any shape.

5. SUNLIGHT-INDUCED SPIN TRANSITION AS A PASSIVE METHOD TO REDUCE TEMPERATURE FLUCTUATIONS IN BUILDINGS

Nowadays, building thermalization is a widespread human necessity, accounting for 30 % of the total final energy use and 28 % of energy-related carbon dioxide worldwide emissions between 2000 and 2017.[290] These CO_2 emissions are a major contributor to climate change, as they exhibit a strong greenhouse effect, which has become one of the biggest concerns of humankind.[291] A reduction in emissions could be achieved by eliminating coal, oil and natural gas as sources of building heating, and also by reducing the energy consumption derived from the use of air conditionings.[292] Thus, the growing energy saving demand and environmental protection has prompted the development and implementation of more energy-efficient and environmentally friendly thermalization technology that is cost-effective, ecological, reduces CO_2 emissions and that affords relief when electrical cooling is not available. One of the main focuses is the construction of high-performance buildings and the implementation of energy renovations. For this to take place, immediate action is required, especially in emerging economies.

In this regard, important efforts have been focused on the implementation of passive cooling systems, that can be incorporated directly in the roof or the walls of buildings and operate without the need for electricity.[293–295] Different approaches can be identified in materials for passive thermal regulation of buildings. The light absorption and reflection properties of building materials has been used for millennia, mainly in the form of coatings that reflect sunlight and allow keeping buildings cool. More sophisticated techniques are being reported now. The first one is based on the so-called radiative cooling technique, in which a surface is naturally cooled by reflecting sunlight and radiating heat to the cold outer space (Figure 61a).[296–300] Another effective way, inspired by the process of perspiration, is the use of hygroscopic and/or porous materials that can store and release water when heated, leading to evaporative cooling, where heat is dissipated through water evaporation (Figure 61b).[301–305] These materials are regenerated by nighttime humidity. The last one is the use of phase-change materials (PCMs), which present high-density thermal energy storage, therefore can minimize temperature fluctuations through the use of latent heat.[306–310] Employing the first two approaches, subambient cooling was achieved both during the day and the night. While this is interesting for places where the weather is hot throughout the whole day, certain regions of the world, with climates where high temperatures are reached during the day and low temperatures at night, require different materials to reduce temperature fluctuations in both directions. One example of this is the city of New Delhi, which is the fifth most populated city in the world.[311] Here, in autumn and spring, temperatures can oscillate as much as 30°C in one day (for example going in November 2020 from a minimum of 6.3°C and a maximum of 31.6 °C).[312]

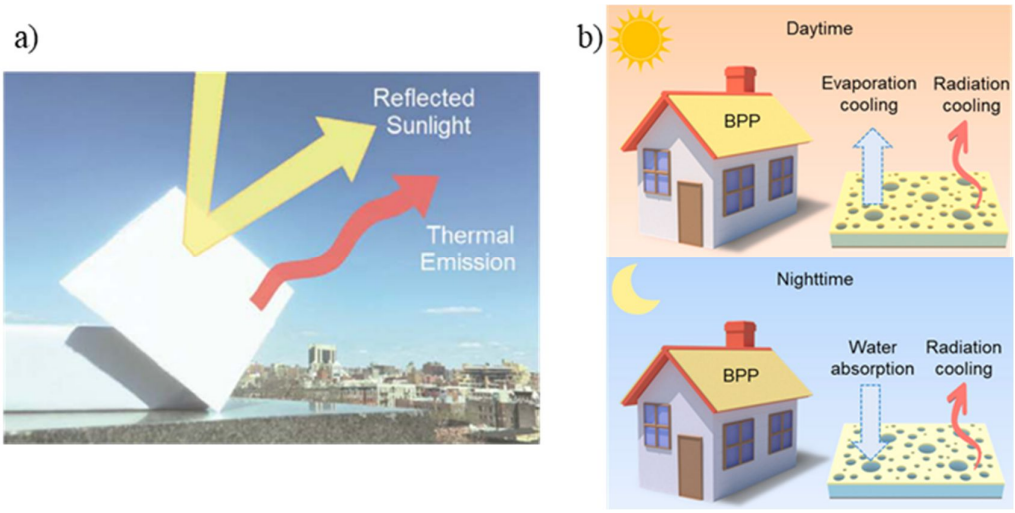

Figure 61. a) Photograph superimposed with schematics to show the mechanism of daytime radiative cooling. Reprinted with permission from ref 297. Copyright 2018 Science.[297] b) Working principle of the bilayer porous polymer for intelligent building cooling at daytime and nighttime. Reprinted with permission from ref 301. Copyright 2021 Nano Energy.[301]

In this respect, the most advanced materials so far for thermal regulation in both senses are PCM, although many of them do not exhibit control at lower temperatures.[313,314] The principle of using phase change materials (PCM) is simple: the material changes phase from solid to liquid as the temperature increases. As the reaction is endothermic, the PCM absorbs heat. Correspondingly, when the temperature decreases, the material changes phase from liquid to solid. As the reaction is exothermic, the PCM desorbs heat, contributing to reducing the in a room.[313]

Instead of using materials that simply reflect light, a more efficient way of exploiting the sunlight absorption and reflection would be the use thermochromic materials.[315] One can easily imagine the advantage for thermal efficiency of having a building with a coating that changes color from a clear, reflecting color in summer to a darker, absorbing color in winter, or in shorter day/night cycles. In fact, some results based on this approach have already been reported. For example, Yin *et al.*[315] reported the use of switchable amino-modified silica shell thermochromic nanoparticles, functionalized with epoxy (RTESN). At low temperatures, these nanocapsules exhibit a deep blue color. When the temperature is higher, the color of the RTESN particles becomes white, which results in more sunlight reflection. This decreases the absorption of thermal energy and reduces further temperature increase (Figure 62).

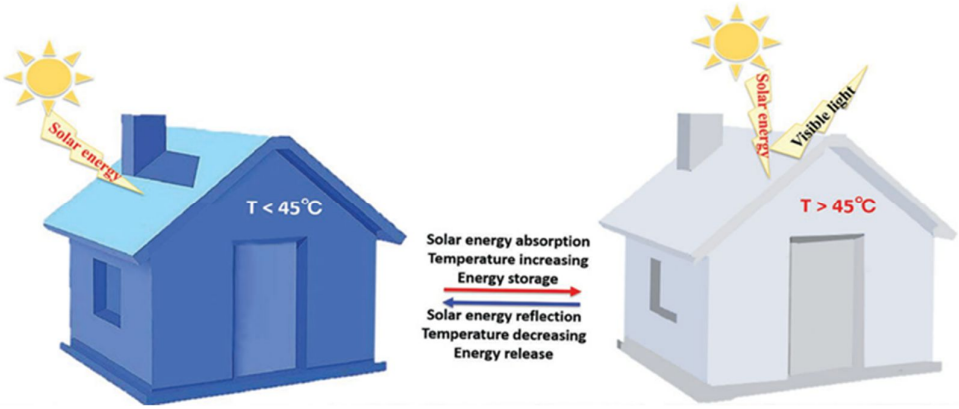

Figure 62. The schematic diagram of the temperature regulation of house models covered with TLD@SiO_2. Reprinted with permission from ref 315. Copyright 2019 Small.[315]

A radically new approach would be the use of SCO materials, which undergo a spin transition between low spin (LS) and high spin (HS) states upon external stimuli, one of which is the temperature.[8,14] This spin transition is associated with a color change,[12] which could result in a different capacity for reflecting sunlight.[315,316] To date, the application of SCO materials in this field has not been documented. The appropriate selection of a SCO material could result in effective passive temperature control in circumstances were large temperature fluctuations need to be avoided (unlike reflecting coatings, which are only beneficial to reduce warming during sunlight exposure). Moreover, the remarkable versatility of SCO compounds may allow adapting the desired phase change temperature and hysteresis to the climatic conditions and the desired comfort temperature.

Therefore, the objective of this Chapter is to give a proof-of-concept of this idea by demonstrating, in the first place, that the heat generated by the solar radiation is enough to produce a spin transition in a SCO material and secondly, that the use of this material allows to reduce temperature fluctuations (Figure 63). For this, three different coordination polymers $[Fe(NH_2trz)_3](OTs)_2$ (**1**), $[Fe(Htrz)_2(trz)[(BF_4)_2$ (**2**) and $[Zn(NH_2trz)_3](NO_3)_2$ (**3**) have been synthesized, where NH_2trz = 4-Amino-4H-1,2,4-triazole; OTs = *p*-toluenesulfonate; Htrz = 1,2,4-Triazole and trz = 1,2,4-triazolate. These materials present the widely studied structure of the family of the triazole-based SCO coordination polymers, also explained in previous sections (Annex D1).[15,275] That is to say, the metal center is in an octahedral environment, coordinated to six nitrogen atoms from six different triazole units. The triazoles act as bridging ligands between two metal centers, leading to the formation of 1D chains. When Fe(II) is used as the metal center, as is the case for **1** and **2**, these materials can exhibit spin crossover properties. Of particular interest for this work is that compound **1** displays the spin transition at room temperature. To investigate and compare the temperature control ability of **1**, two different compounds were synthetized: a compound that is only in its LS state in this temperature range (**2**), and thus remains pink, and another that is white (**3**). These materials were characterized by FTIR, PXRD, TGA, elemental analyses, absorption spectra, optical reflectivity and magnetic susceptibility measurements. Two different temperature dependence experiments were devised. In the first, only the increasing of the temperature is explored. Meanwhile, in the second one, both the cooling and heating of the samples was explored. In this chapter, temperature values will be given in °C, instead of K, to make it easier to associate them with meteorological temperatures.

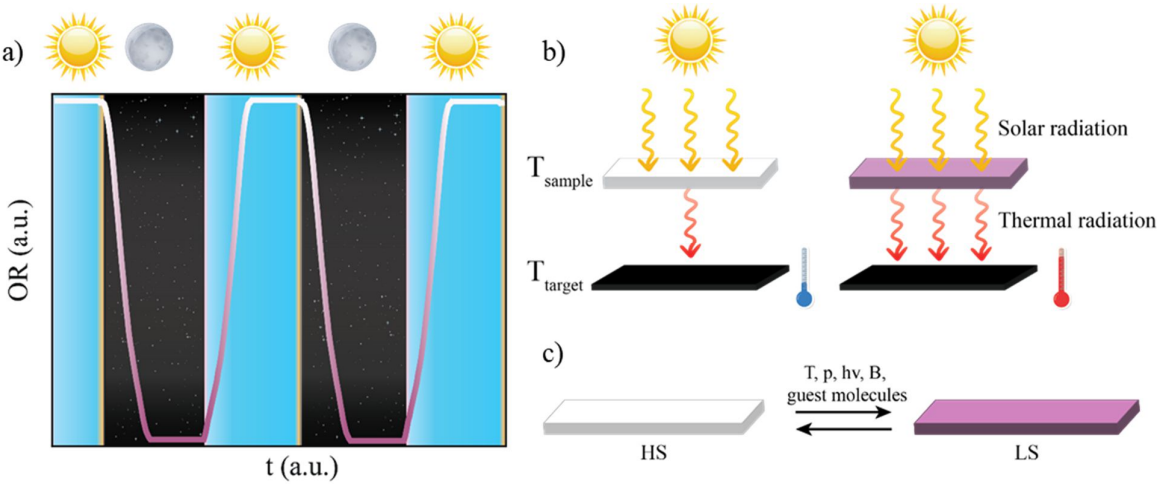

Figure 63. a) Scheme of the behavior of a SCO material during day-night cycles. b) Working scheme of a SCO material. When the weather is hot, and the material is in its HS state (white), the light is reflected and the increase in the temperature of room is controlled. On the contrary, under cold temperatures, the materials presents the LS state (pink), so more wavelengths are absorbed and the room is heated.

5.1. SYNTHESIS OF COMPOUNDS 1-4

5.1.1. Synthesis of compounds 1-3

Compound **1** was synthetized at room temperature, by adding drop by drop a solution of 0.59 mmol of NH_2trz (NH_2trz = 4-Amino-4H-1,2,4-triazole) in 3 mL of ethanol on top of a solution of 0.20 mmol of $Fe(OTs)_2$ (OTs = tosylate) in 3 mL of distilled water. The solution was stirred for 1 hour, filtered and washed with ethanol. **1** was obtained as a pink powder in 87% yield.

Anal. calcd (%) for **1**·0.4H_2O: C 36.53%, H 4.11%, N 25.56%; found C 36.34%, H 4.05%, N 25.79%. FTIR **1** (cm^{-1}): ν = 3441 (w; ν(OH)), 3293 (m; ν(NH)), 3210 (w), 3062 (m; $\nu(CH)_{ar}$), 3012 (w), 2924 (w), 1631 (m), 1600 (w), 1546 (m; δ(NH)), 1496 (w), 1449 (w; $\delta(CH)_{ar}$), 1396 (w), 1170 (s; $\nu(S{=}O)_{OTs}$), 1122 (s), 1098 (m), 1033 (s; $\nu(S{=}O)_{OTs}$), 1008 (s; $\nu(S{=}O)_{OTs}$), 908 (w), 881 (w), 813 (m; δ(ring)), 709 (w), 681 (s; $\nu(CS)_{OTs}$), 623 (s), 563 (s; $\nu(CS)_{OTs}$), 493 (w), 457 (w).

Compound **2** was synthetized at room temperature, dissolving 1 mmol of $Fe(BF_4)_2{\cdot}6H_2O$ in 3 ml of distilled water and adding it drop by drop to a solution of 3 mmol of Htrz (Htrz = 1,2,4-triazole) in 3 mL of ethanol. The resulting solution was stirred for 24 hours, filtered and washed with ethanol obtaining **2** as a pink powder (76% yield).

Anal. calcd (%) for **2**·1.35 H_2O: C 19.31, H 2.89, N 33.78; found C 19.07, H 2.66, N 33.79. FTIR **2** (cm^{-1}): ν = 3170 (w; ν(NH)), 3093 (w; $\nu(CH)_{ar}$), 3008 (w), 2915 (w), 2845 (w), 2698 (w), 2621 (w), 2535 (w), 2535 (w), 2457 (w), 1749 (w), 1719 (w) ,1639 (w), 1535 (m; δ(NH)), 1495 (m), 1453 (m; $\delta(CH)_{ar}$), 1309 (m), 1285(m), 1220 (w), 1190 (w), 1163 (m), 1144 (m), 1063 (s; $\nu(BF)_{BF4}$), 1034 (s; $\nu(BF)_{BF4}$), 977 (m), 912 (w), 866 (m), 827 (w), 765 (w), 679 (m), 631 (s), 523 (m), 468 (w), 437(w).

Compound **3** was synthetized by adding drop by drop a solution of 3 mmol of NH_2trz (NH_2trz = 4-Amino-4H-1,2,4-triazole) in 3 mL of ethanol on top of a solution of 1 mmol of $Zn(NO_3)_2$ in 3 mL of distilled water. The solution was stirred for 1 hour, and the white precipitate was filtered and washed with ethanol. **3** was obtained as a white powder (85% yield).

Anal. calcd (%) for **3**·1H_2O: C 15.68, H 3.07, N 42.66; found C 15.33, H 3.14, N 43.01. FTIR **3** (cm^{-1}): ν = 3520 (w), 3319 (m; ν(NH)), 3218 (w), 3070 (m; $\nu(CH)_{ar}$), 3004 (w), 1753 (w), 1632 (m; $\nu(NO)_{as,NO3}$), 1547 (m; δ(NH)), 1485 (w; $\delta(CH)_{ar}$), 1339 (s; $\nu(NO)_{sim,NO3}$), 1219 (m), 1088 (m), 1030 (m), 996 (m), 904 (w), 828 (m; $\nu(NO)_{trans/cis,NO3}$), 712 (w), 690 (w), 622 (s), 421 (w).

5.1.2. Synthesis of compounds 1@PMMA-3@PMMA

The **1@PMMA, 2@PMMA** and **3@PMMA** films (3% w/w) were prepared by mixing 0.2 g of the respective sample powder with 1.98 g of PMMA (PMMA = poly(methyl methacrylate; average M_w ~120,000 g·mol^{-1}). This mixture was dissolved in $CHCl_3$, sonicated for 30 minutes and deposited in a mold (5 cm x 5 cm), that was placed in the fridge overnight so the $CHCl_3$ evaporates slowly and no bubbles appear. The composite was then carefully extracted from the mold.

FTIR **1@PMMA** (cm^{-1}): ν = 3290 (w; ν(NH)), 3110 (w; $\nu(CH)_{ar}$), 2995 (w; PMMA), 2950 (m; PMMA), 2851 (w), 1724 (s; PMMA), 1614 (w), 1546 (w; δ(NH)), 1480 (w; PMMA), 1446 (w; PMMA), 1435 (m), 1386 (w; PMMA), 1269 (w; PMMA), 1239 (w; PMMA), 1189 (w; PMMA), 1169 (w; $\nu(S{=}O)_{OTs}$), 1146 (s; PMMA), 1122 (s), 1098 (w), 1033 (m; $\nu(S{=}O)_{OTs}$), 1009 (m; $\nu(S{=}O)_{OTs}$), 988 (w; PMMA), 966 (w; PMMA), 912 (w; PMMA), 880 (w), 841 (w; PMMA), 812 (m; δ(ring), 749 (s; PMMA), 683 (s; $\nu(CS)_{OTs}$), 625 (s), 563 (s; $\nu(CS)_{OTs}$), 481 (w; PMMA).

FTIR **2@PMMA** (cm^{-1}): ν = 3170 (m; ν(NH)), 3095 (w; $\nu(CH)_{ar}$), 3006 (m), 2915 (m), 2848 (m), 2748 (w), 2698 (w), 2622 (w), 2536 (w), 1728 (m; PMMA), 1644 (w), 1536 (m; δ(NH)), 1496 (m), 1453 (m), 1388 (w), 1309 (m), 1284 (w), 1221 (w; PMMA), 1190 (w; PMMA), 1162 (m), 1144 (m), 1109 (w), 1063 (s; $\nu(BF)_{BF4}$), 1034 (s; $\nu(BF)_{BF4}$), 977 (m), 912 (w), 866 (m), 826 (w; PMMA), 764 (s; PMMA), 679 (m), 631 (s), 524 (m), 482 (w; PMMA), 471 (w), 437 (w).

FTIR **3@PMMA** (cm^{-1}): ν = 3321 (w; ν(NH)), 3219 (w), 3070 (w; $\nu(CH)_{ar}$), 2998 (m; PMMA), 2950 (m; PMMA), 2844 (w), 1721 (s; PMMA), 1635 (w; $\nu(NO)_{as,NO3}$), 1547 (w; δ(NH)), 1481 (w; PMMA), 1434 (m; PMMA), 1363 (m; $\nu(NO)_{sim,NO3}$), 1269 (w; PMMA), 1238 (m; PMMA), 1190 (w; PMMA), 1143 (s; PMMA), 1088 (m), 1062 (w; PMMA), 1029 (w), 993 (m), 968 (w; PMMA), 913 (w), 842 (w; PMMA), 828 (w; $\nu(NO)_{trans/cis,NO3}$), 748 (s; PMMA), 667 (m; PMMA), 623 (m), 554 (w; PMMA), 479 (w; PMMA), 458 (w).

5.2. RESULTS AND DISCUSSION

5.2.1. Physico-chemical study

To facilitate the use of these powder-like materials, compounds **1-3** were embedded[279] in the organic polymer polymethyl methacrylate (PMMA), from here on **1@PMMA**, **2@PMMA**, and **3@PMMA**, respectively. The resulting composites are partially transparent, as can be observed in Annex D2. These materials were characterized by FTIR spectroscopy (Figure 64), where the distinctive signals from the coordination polymers can be observed in **1-3** and **1@PMMA-3@PMMA**. In addition, the composites display the bands arising from the presence of PMMA. In all compounds the presence of the N-H vibration is revealed in the form of a small band displayed in an interval between 3293 cm^{-1} and 3170 cm^{-1} and the C-$H_{aromatic}$ tension through a series of bands around 2950 cm^{-1}. The first band originates either from the presence of NH_2trz (**1**, **1@PMMA**, **3** and **3@PMMA**) or the Htrz ligand (**2** and **2@PMMA**). PMMA and the composites **1@PMMA-3@PMMA** display a band at ~1720 cm^{-1} arising from the C=O vibration and another band ascribed to the C-O tension at 1142 cm^{-1}.

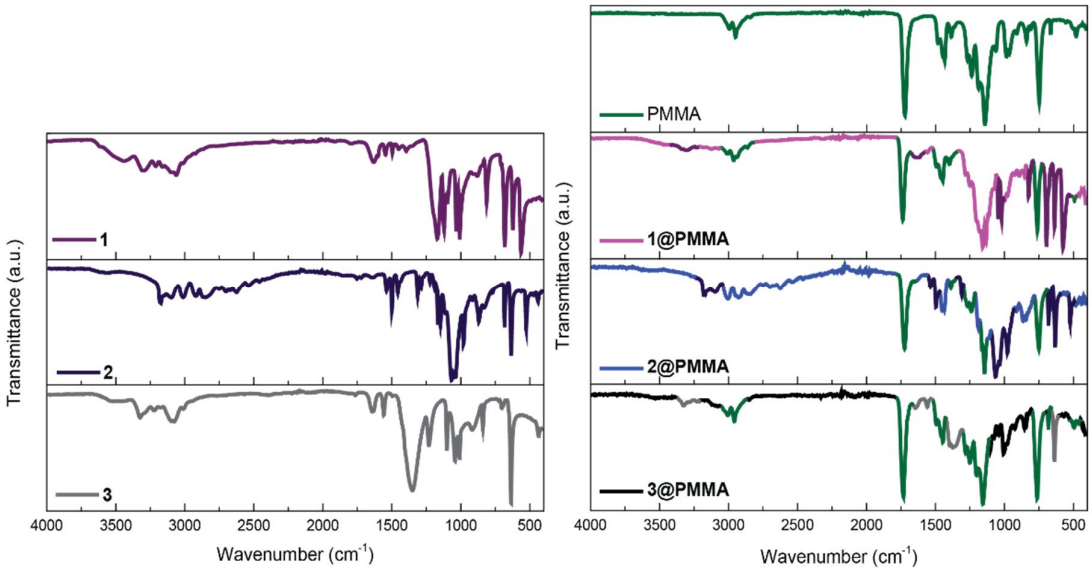

Figure 64. IR spectra of compounds **1-3** on the left, and PMMA and compounds **1@PMMA-3@PMMA** on the right. In the composites, the signals arising from the CP or PMMA are colored in their respective color.

In addition, the CPs exhibit the bands derived from the presence of the respective counterion. Thus, the IR spectra of **1** and **1@PMMA** show the characteristic signals of the counterion tosylate *ca*. 1033 cm^{-1}, 1008 cm^{-1}, 813 cm^{-1}, 681 cm^{-1} and 563 cm^{-1}. In the IR spectra of **2** and **2@PMMA**, a band arising from the B-F tension of BF_4 is displayed at 1063 cm^{-1}. The IR spectra of **3** and **3@PMMA** reveal the typical signals of the counterion NO_3 at 1632 cm^{-1}, 1339 cm^{-1}, 828 cm^{-1}.

Even though single crystals of **1-3** could not be obtained, the polycrystalline samples were measured by powder X-ray diffraction (Figure 65). The main conclusion that can be drawn from this study is that the diffraction patterns are different for the three compounds, thus concurring with the synthesis of the three reported materials.[317]

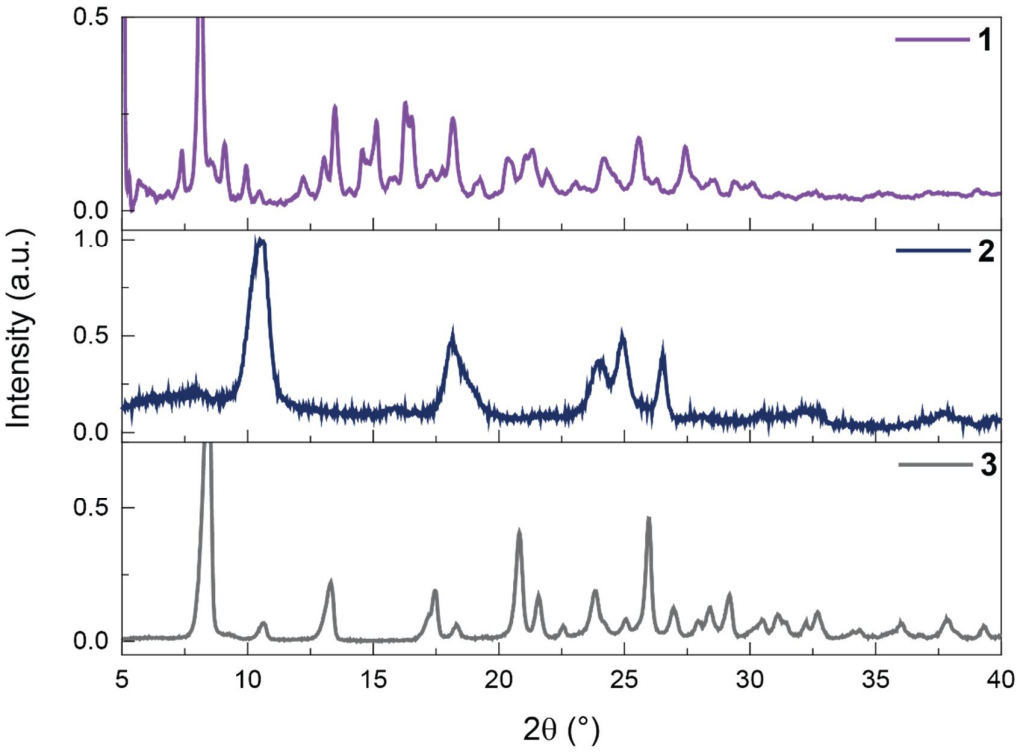

Figure 65. PXRD pattern of **1**, **2** and **3**.

The thermogravimetric analyses for all compounds were measured (Figure 66 and Annex D3-Annex D9), where the observed profiles are different for the three samples. When embedded in PMMA, in the temperature range between 30 °C and 240 °C the profile of **1@PMMA-3@PMMA** is consistent with that of PMMA, with a weight loss between 125 °C and 200 °C. At temperatures higher than 240 °C the weight loss curve follows a similar pattern to that of the corresponding coordination polymer. Hence, **1@PMMA** presents the most gradual weight loss above 240 °C, and a slight plateau can be seen at 300 °C, similarly to **1**. On the other hand, **2** and **2@PMMA** exhibit a one-step abrupt weight loss. Compounds **3** and **3@PMMA** display the most abrupt weight loss, and a plateau can be observed at 300 °C for **3**. While this plateau is not evident in **3@PMMA**, a change in the slope can be found at this temperature.

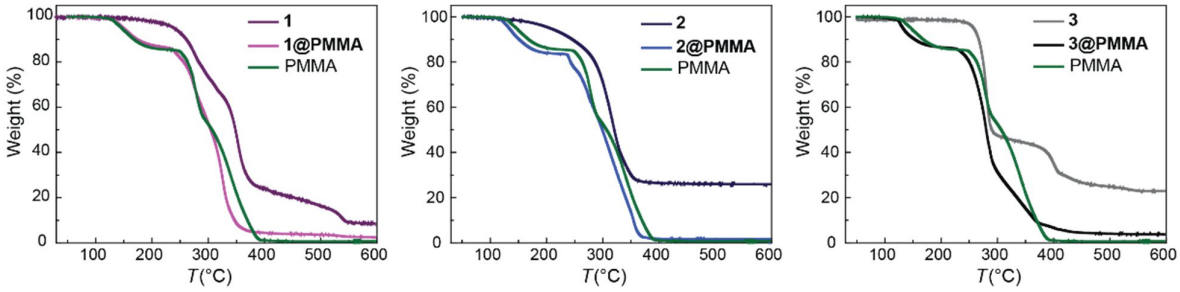

Figure 66. Thermogravimetric analyses of **1-3**, PMMA and **1@PMMA-3@PMMA** between 30 °C and 600°C.

The SCO properties were explored by optical reflectivity (OR) and magnetic measurements, both in the coordination polymers and when combined with PMMA (Figure 67 and Annex D10). It should be noted that at temperatures above 125 °C the PMMA starts decomposing and consequently, **2@PMMA**, which undergoes the spin transition at higher temperatures, could not be characterized by magnetic susceptibility measurements and only partially by optical reflectivity, since the appearance of bubbles renders the optical reflectivity measurements impossible.

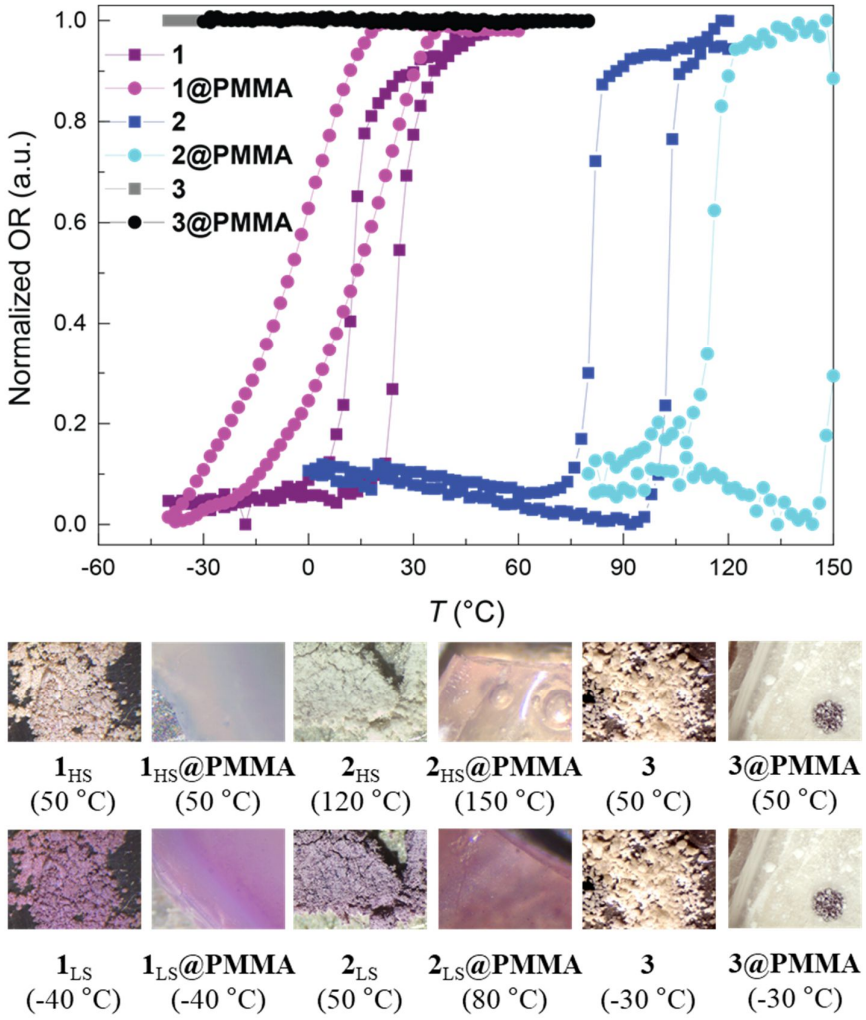

Figure 67. Optical reflectivity measurements for **1-3** and **1@PMMA-3@PMMA**. The optical reflectivity has been normalized in respect to **1**. The images correspond to the respective compound or composite at the highest and lowest temperature, associated with their spin state.

As expected, the spin transition is modified when **1** and **2** are combined with the organic polymer. Compound **1** presents the HS state above room temperature, and changes abruptly to LS state upon cooling down. When the sample is heated, the HS state is recovered with a hysteresis of 14°C ($T_{1/2}\downarrow$= 12 °C; $T_{1/2}\uparrow$= 26 °C). The same type of behavior is observed for **1@PMMA** although with a much more gradual transition (hysteresis 19 °C; $T_{1/2}\downarrow$= -5 °C; $T_{1/2}\uparrow$= 14 °C). Importantly, this thermochromic process is reversible, and can be maintained for several thermal cycles (see Figure 68 for 40 cooling-heating cycles).[318] Compound **2** also exhibits a hysteretic SCO behavior between 80 °C and 103 °C. This transition is shifted to even higher temperatures when combined with PMMA ($T_{1/2}\downarrow$= 115 °C). Hence, **2@PMMA** exhibits a pink color up to 80 °C. Naturally, neither compound **3** nor **3@PMMA** display a spin transition, since Zn(II) is a d^{10} transition metal, and the possibility of SCO is nonexistent. Thus, this compound remains white throughout the whole temperature range, to simulate white paint which is widely used to reduce temperature during the summer. The magnetic susceptibility measurements are in agreement with these observations (Annex D10).

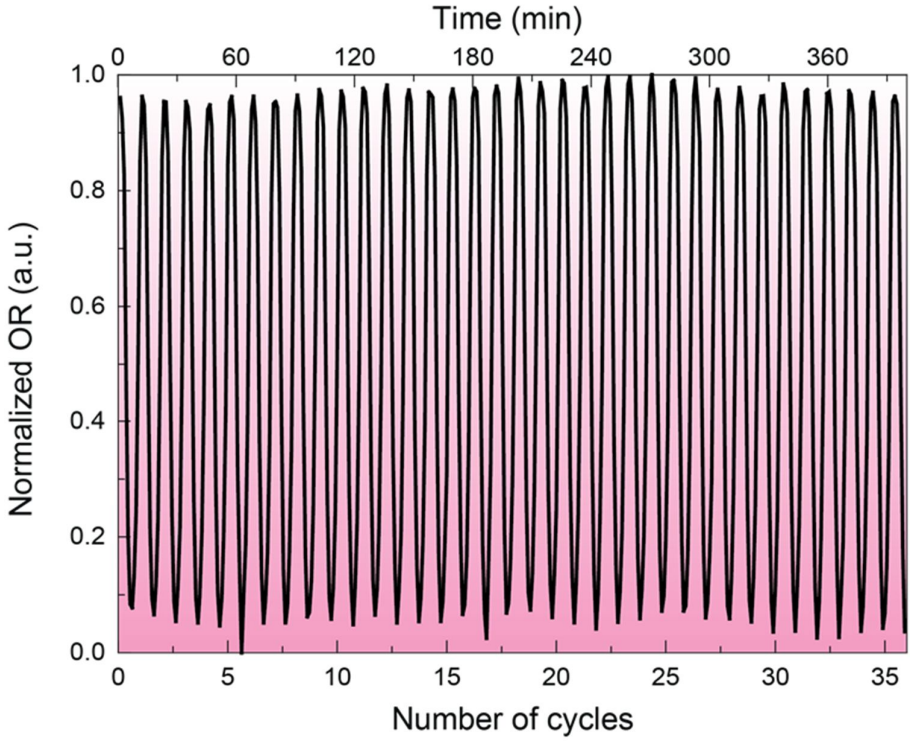

Figure 68. Thermochromic reversibility of **1@PMMA** between -50 °C and 60 °C. The color of the background is associated with the color of the composite: white at high temperatures (HS) and pink at low temperatures (LS).

The absorption spectra for **1@PMMA-3@PMMA** and PMMA (Figure 69) were measured in the temperature range where the experiment takes place. The spectra remain constant with the temperature for **2@PMMA**, **3@PMMA** and PMMA, while clear differences can be observed for **1@PMMA**. In this case, as the temperature increases and the composite becomes light pink and the light absorption decreases. This is in accordance with the optical reflectivity measurements.

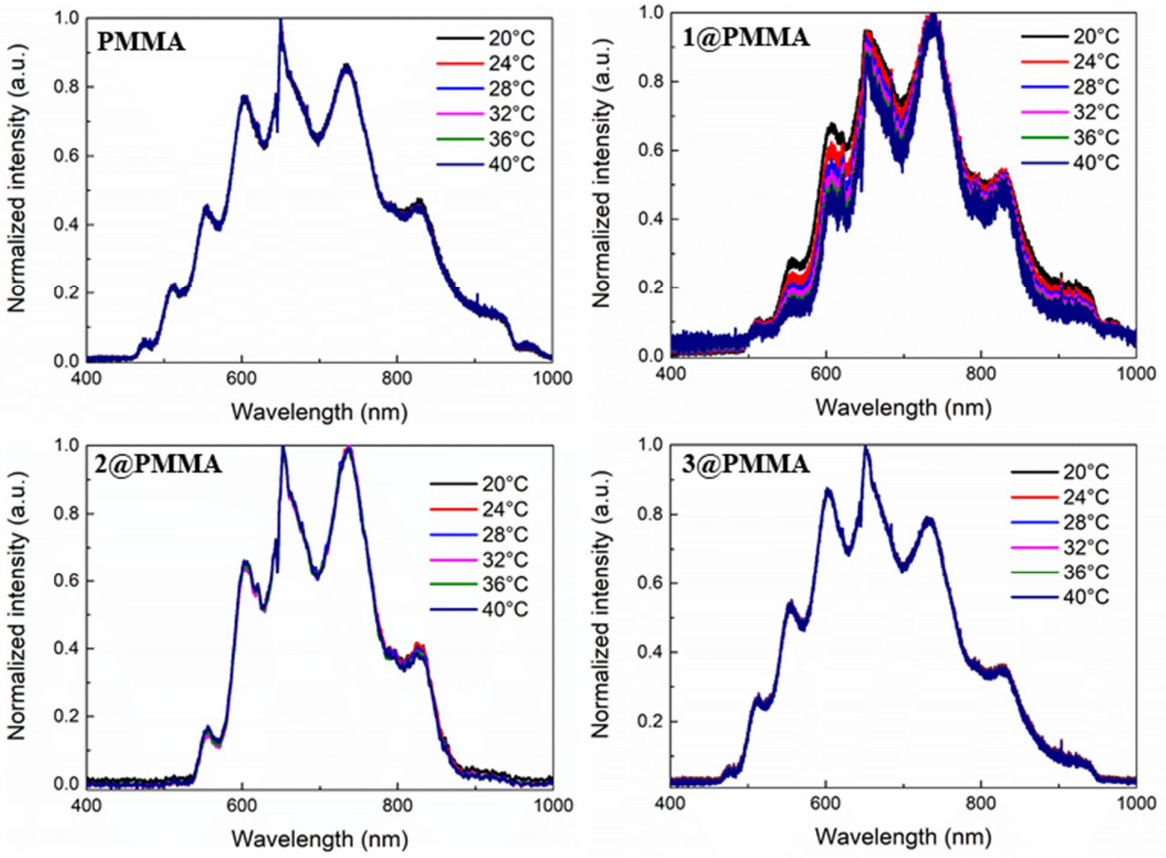

Figure 69. Absorption spectra for PMMA, **1@PMMA-3@PMMA** at different temperatures.

5.2.2. Temperature fluctuation studies

In order to simulate temperature fluctuations in a room, two different experiments were devised. The first one (Figure 70a and Annex D11) consists on placing the polymers (**1@PMMA-3@PMMA** and PMMA) on top of an empty glass vial under the irradiation of a solar lamp. This process was recorded with a thermal imaging camera, so that the temperature on the polymer and on the floor (both outside and inside the vial) could be characterized at all times. This configuration mimics the temperature in a closed room.

The results of the first experimental setup are shown in Figure 70. The recorded infrared thermal images can be seen in Figure 70a, at times 0 and 600 s from the start of irradiation. Three different spots have been measured in relation to the irradiation time (Figure 70e): the sample temperature (T_1) and two temperatures underneath the vial: one inside the vial (T_2) and another outside (T_3). The sample temperature (T_1, top graph) shows that **2@PMMA** increases from 24 °C to 41.6 °C (ΔT = 17.6 °C). Therefore, starting from roughly the same temperature, the **2@PMMA** temperature increases 8 °C more than that of **1@PMMA** (ΔT = 10 °C), and 16 °C more than in **3@PMMA** and PMMA (ΔT = 1.3 °C). The rate at which the temperature increases in the first two minutes is as follows: **1@PMMA** 4 °C·min^{-1}, **2@PMMA** 8 °C·min^{-1}, **3@PMMA** 0.5 °C·min^{-1} and PMMA 0.4 °C·min^{-1}.

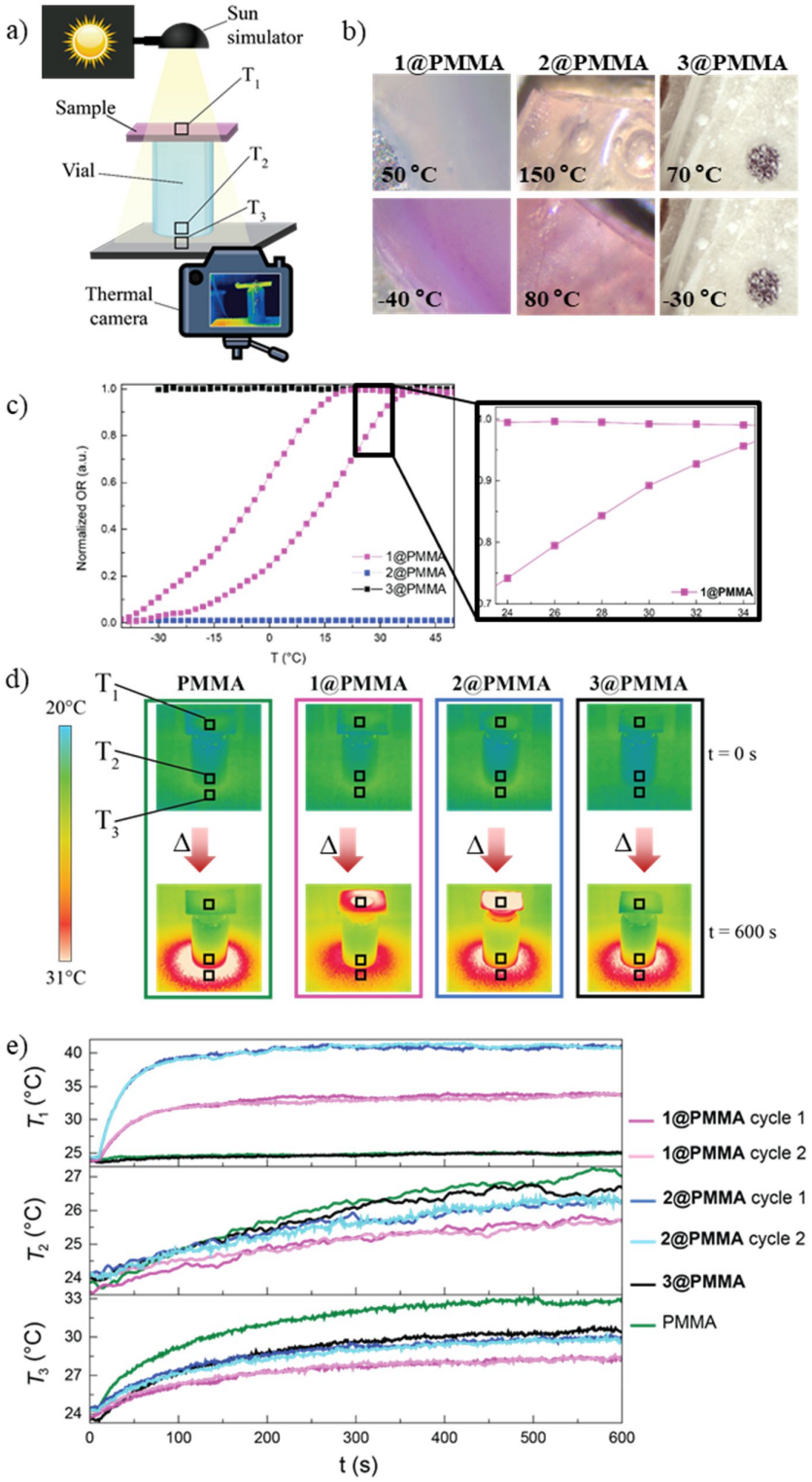

Figure 70. a) Scheme of the experimental setup. b) Images of the composites at the highest and lowest measured temperature. c) Optical reflectivity measurements for **1@PMMA-3@PMMA** with a zoom for **1@PMMA** in the temperature region encompassed by these sunlight exposure measurements. The optical reflectivity has been normalized in respect to **1@PMMA**. d) Thermal infrared images for **1@PMMA-3@PMMA** and PMMA at time 0 and 600 s. The measured area in each sample is marked with a square in the images. e) Temperature *vs.* exposure time (the sun simulator is turned on at time 10 seconds) at the three different measured spots.

On the other hand, in the middle graph (T_2), in the temperature at the bottom of the vial the greatest temperature increment is observed for **3@PMMA** and PMMA. This indicates that the sunlight is able to pass through the white materials, and raise the temperature inside the room. **2@PMMA** follows as the next sample that reaches the highest temperature on the floor. We believe that the tendency: PMMA > **3@PMMA** > **2@PMMA** > **1@PMMA** can be explained by a synergy occurring between two different effects. The first is that the completely white samples do not heat up, but allow solar radiation to pass through and, as a consequence, the temperature increases. The opposite effect is observed in the case of **2@PMMA**, where the material itself is the one that heats up the most, but also results in a temperature increase. This is because dark materials absorb more wavelengths of light and convert them into heat. It is important to note that **1@PMMA** is in a bistable region, so it is neither completely white nor as pink as it would be when it is completely in LS. It therefore shows a synergy of these two effects: it is almost white, (allowing it to absorb fewer wavelengths) but with a slight pink color, which impedes solar radiation from passing through the material. This same behavior can be observed for T_3. To confirm that this behavior can be replicated, the **1@PMMA** and **2@PMMA** materials were measured twice. In between the measurements, the samples were cooled, so that the materials recover their initial state. For both materials and in the three measured spots, it is evident that the temperature dependence with time is replicable.

The different behaviors between **1@PMMA** and **2@PMMA** can be explained by plotting the temperature in the **1@PMMA** polymer (Figure 70b, top graph: T_1). At the beginning of the measurement, the **1@PMMA** film is at 23.8 °C, which according to the optical reflectivity measurements (Figure 70c), corresponds to a 74% of HS, while by the end of the measurement, the temperature of the composite reaches a maximum of 33.9 °C, where 95 % of the iron centers in the composite are in HS. This indicates that the heat generated by the sun simulator (or the sun itself) is enough to provoke a partial spin transition in the material. As previously discussed, the spin transition from LS to HS results in a color change from pink (LS) to white (HS). Although the spin transition is only partial, a fraction of 21 % of the iron(II) ions changed from LS to HS in this temperature range, which is sufficient for a color change to be seen by the naked-eye (Annex D15). Thus, the material is able to dissipate heat more efficiently than the analogous pink sample **2@PMMA** in which the SCO does not occur in this temperature range.

The second setup (Figure 71a and Annex D12) was designed to characterize hot-cold cycles and avoid contributions from conduction and convection (due to sample contact with the vial). This experimental setup consists on two Peltiers, which are in contact with a copper sheet of 0.5 mm, that acts as a sample holder. A round hole (d = 10 mm) is drilled into this copper foil. On top of this there is another copper sheet with a square window (40 mm x 40 mm) where the sample is placed. Another sheet, equal to the first one, goes on top of the sample, so that it is sandwiched by copper sheets from all directions, except the hole, that allows the light irradiation to pass through the sample. To avoid heating of the copper foils with the solar simulator, a piece of insulating foam is placed on top, covering the copper sheets, except the transmission aperture. Directly below this orifice, there is an anodized aluminum sensor (area 10 mm x 10 mm; distance from sample: 25 mm), surrounded from all sides, except from above, by insulating foam. To eliminate temperature fluctuations coming from the Peltiers, two metal sheets (225 mm x 95 mm x 1 mm) are placed in between them and the sensor, so the temperature flow is perpendicular to the Peltier-sensor-Peltier direction. The temperature is monitored in the sensor by a thermocouple (T_{target}). Right next to the sample there is another thermocouple attached, but to accurately control the sample temperature the thermal camera is used (T_{sample}). The solar simulator is placed on top of this setup (distance to the sample 120 mm).

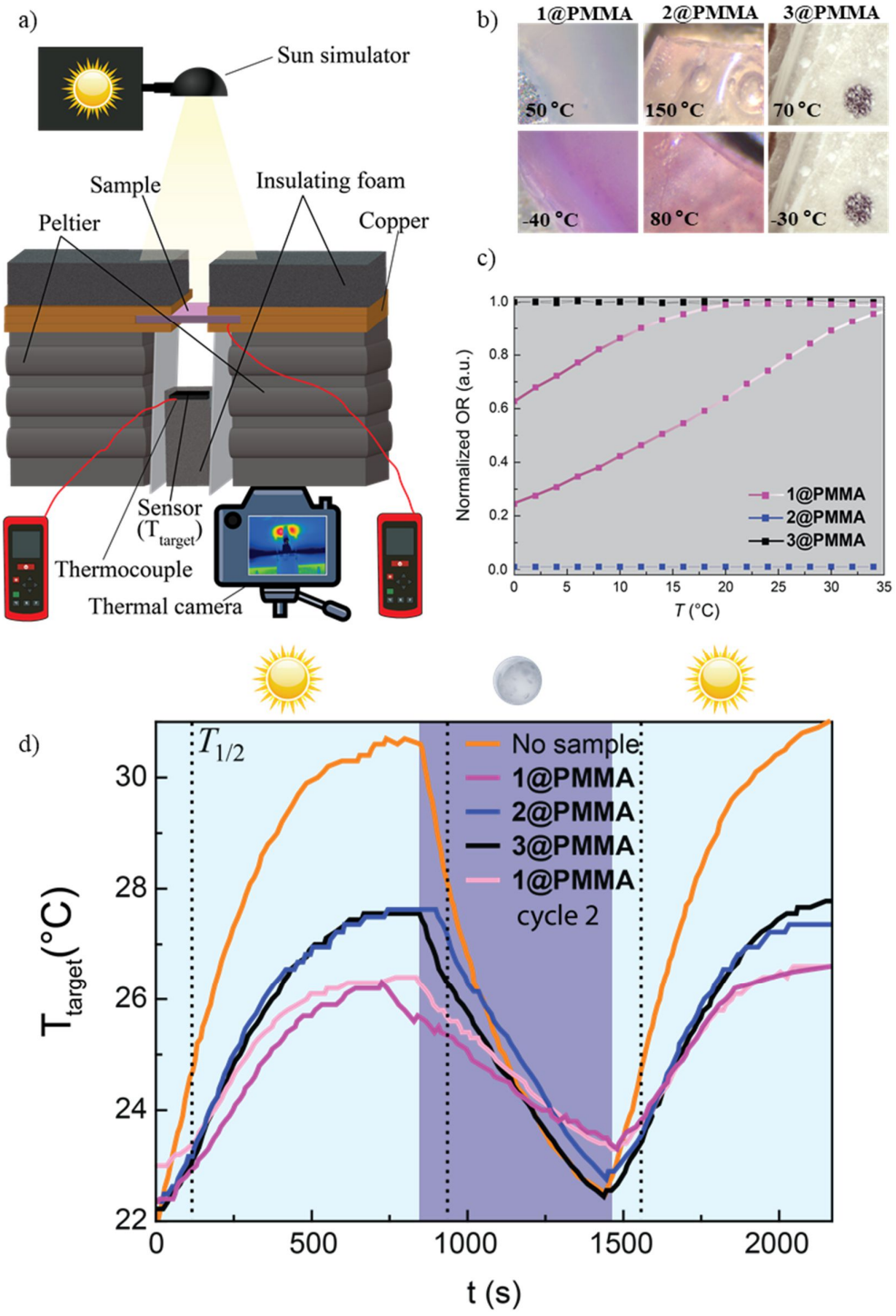

Figure 71. a) Scheme of the experimental setup. b) Images of the composites at the highest and lowest measured temperature. c) Optical reflectivity measurements for **1@PMMA-3@PMMA** in the temperature region encompassed by these sunlight exposure measurements. The optical reflectivity has been normalized in respect to **1@PMMA**. d) Temperature *vs.* exposure time in the sensor (T_{target}) with on-off solar simulator cycles.

Using this experimental setup, the samples were subjected to hot-cold cycles, simulating day and night conditions (Figure 71a). The experiment starts with the Peltier on and the solar lamp off. Then, the solar simulator is turned on and the Peltier turned off, which corresponds to the heating process

(colored in light blue). Here, T_{sample} increases following this sequence: **2@PMMA** > **1@PMMA** > **3@PMMA** (Annex D13). However, when T_{target} is plotted, this is translated into a rise in temperature that follows this order: **3@PMMA** > **2@PMMA** > **1@PMMA**. When the experiment is carried out without the presence of a sample, T_{target} increases rapidly, reaching the highest temperature. The cooling cycle starts at time 800 s, when the solar lamp is switched off and the Peltier on (dark blue background). Immediately, both T_{sample} and T_{target} begin to drop. T_{target} reaches a minimum temperature at 1480 s. Interestingly, this minimum is higher for **1@PMMA** in respect to the references **2@PMMA** and **3@PMMA**, and also higher than when no sample is employed. Again, the system is set in heating mode (at 1480 s) and the same behavior as in the first cycle is observed. Therefore, the SCO sample is able to control temperature fluctuations in both directions, in respect with the pink and white references, and also with PMMA and when no sample is employed. A second set of experiments was carried out (Annex D14), where the same behavior is observed.

From the sample temperature, it can be stated that **1@PMMA** is shifting from a 22 % of HS iron(II) ions (at -2 °C), to 88 % of HS at the highest temperature (29.6 °C). This translates into less temperature fluctuations during both cooling and heating, which can be associated with the synergy derived from its bistable behavior.

In addition, to simulate what would occur upon a temperature decrease under solar irradiation, this same setup was used but in this case the solar lamp remains lit during the entire experiment, accompanied by Peltier on-off cycles (Figure 72).

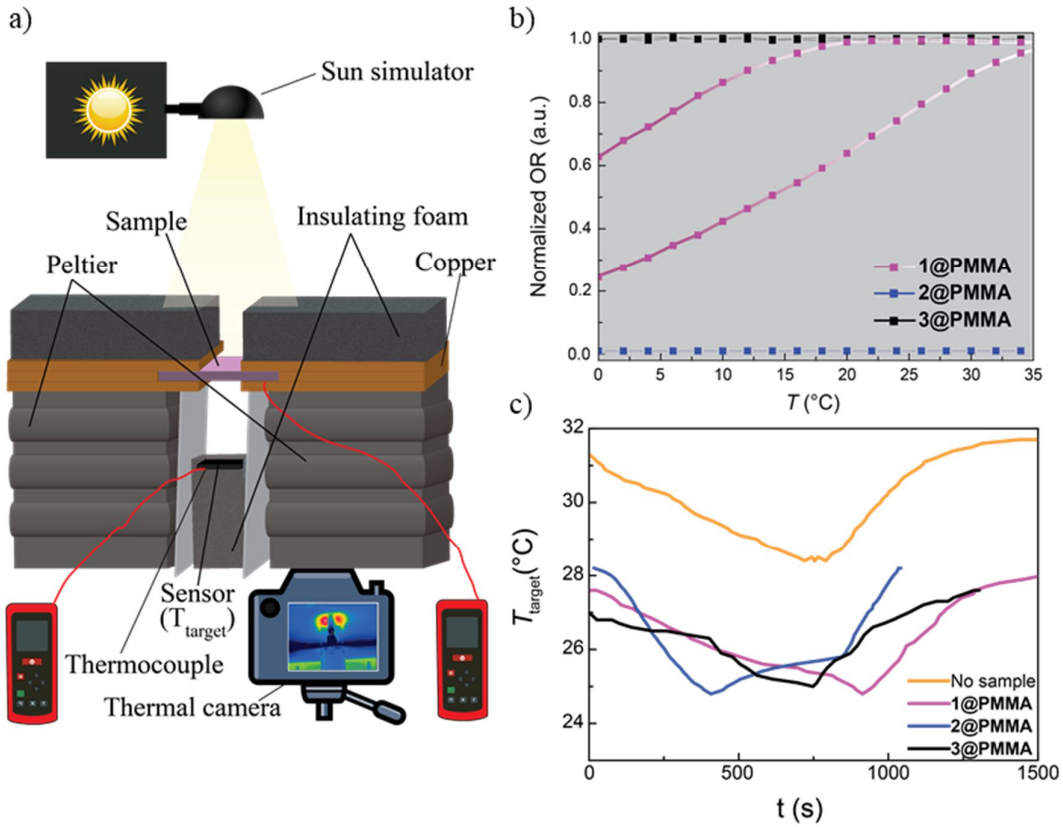

Figure 72. a) Scheme of the experimental setup. b) Optical reflectivity measurements for **1@PMMA-3@PMMA** in the temperature region encompassed by these sunlight exposure measurements. The optical reflectivity has been normalized in respect to **1@PMMA**. c) T_{target} *vs.* exposure time with the solar simulator turned on and on-off Peltier cycles.

At the beginning of the experiment, the Peltier is switched on, resulting in a cooling of the sample, and to some extent, also of the sensor. The main observation here is that the minimum recorded T_{target} (25 °C) is reached more slowly for **1@PMMA** when in comparison with the references (at times 400 s, 750 s and 910 s, for **2@PMMA**, **3@PMMA** and **1@PMMA**, respectively). When no sample is used, the minimum T_{target} recorded is 29 °C. This result reinforces the conclusion that the material exhibiting SCO is capable of reducing temperature fluctuations, and providing certain control over the temperature.

5.3. CONCLUSIONS

Three different coordination polymers have been synthetized: $[Fe(NH_2trz)_3](OTs)_2$ (**1**), $[Fe(Htrz)_2(trz)[(BF_4)_2$ (**2**) and $[Zn(NH_2trz)_3](NO_3)_2$ (**3**). Compound **1** displays spin transition, which results in a color change between pink and white, in the room temperature range, where the experiments take place. Meanwhile, **2** remains pink and **3** stays white, and both are used to serve as a comparison. To facilitate their usage and potential implementation, these three compounds were embedded in PMMA (**1@PMMA-3@PMMA**). For compounds **1@PMMA** and **2@PMMA**, the SCO behavior is altered from the initial CPs. Nevertheless, **1@PMMA** still displays a spin transition at room temperature, although much more gradual, and **2@PMMA** remains pink in the whole temperature interval.

These composites were used in three different experiments to simulate temperature fluctuations in a room. In all of them, a different behavior can be observed for the composite presenting SCO with respect to the pink one, when **1@PMMA** changes from LS to HS. This demonstrates that the spin transition can be triggered by the heat provided by the Sun. Furthermore, these proof-of-concept experiments show that a certain temperature control, in both heating and cooling, can be achieved with the SCO sample, due to a synergy because of its bistable nature. Importantly, this introduces the possibility of using SCO materials in the passive thermal control of buildings, in areas where the temperatures are hot during the day and cold during the night.

CONCLUSIONS

The following conclusions have been drawn from the results presented in the different chapters:

In Chapter 2, a novel 1D non-porous crystalline coordination polymer $_{\infty}\{[Fe(H_2O)_2(CH_3CN)_2(pyrazine)](BF_4)_2 \cdot 2CH_3CN\}$ has been synthetized from a simple reaction between pyrazine and $Fe(BF_4)_2 \cdot 6H_2O$ in acetonitrile. This compound exhibits a non-coordinated acetonitrile molecule in its crystalline structure. This non-porous CP can act as porous, since the uncoordinated acetonitrile molecules can be released from the structure under increasing temperature, while also retaining the structural integrity. The acetonitrile evacuation is accompanied by sharp magneto-structural transitions that can be detected as a change of color from yellow to orange, and has been characterized by various techniques. In addition, the transport measurements through the crystal have been carried out as the temperature is increased. Interestingly, the polymer behaves as an insulator, as is generally to be expected from coordination polymers, but the change in the structure leads to an abrupt high-current peak in the electric transport at well-defined temperatures near RT. This marks the first reported example in which an insulating non-porous acting as porous coordination polymer exhibits such a sharp and temperature-specific change in the electrical properties. This peak is highly reproducible when measuring different samples, and is not present if the sample has been previously heated and the color of the crystal has changed to orange. Remarkably, upon exposure of the orange, empty crystals to acetonitrile, the initial yellow color and electrical properties are recovered. PXRD measurements confirm the recovery of the initial structure. This interesting behavior would allow for the use of this coordination polymer, which is easy to synthetize, manipulate and carry, as an acetonitrile sensor (after the polymer has been previously heated). The response of this sensor would not only be optical, but also electrical, at a temperature very near room temperature. Therefore, this CP would make a versatile platform to develop an acetonitrile sensor, with a wide range of read-out options from optical, magnetic to electric transport measurements.

In Chapter 3, the mechanism of conduction in the coordination polymer $_{\infty}\{[Fe(H_2O)_2(CH_3CN)_2(pyrazine)](BF_4)_2 \cdot 2CH_3CN\}$ has been studied in more detail through AC admittance spectroscopy. Here, the mechanism behind the conductivity is revealed to be of protonic origin. The non-coordinated acetonitrile molecules form a conduction channel. Unlike many conductive MOFs and CPs, the proton transport is displayed at low relative humidity levels (RH < 40%). Remarkably, this represents the first example of proton transport mediated by acetonitrile in a non-porous coordination polymer. When the humidity is higher (RH > 40%) a different behavior in the transport properties is exhibited: the peak in conductivity is more pronounced and is shifted to lower temperatures. In this case, the crystals change color to orange at lower temperatures, and is irreversible when the CP is exposed to acetonitrile again.

In addition, this material was exposed to pyrrole, a volatile organic molecule, which leads to a change of color from yellow to green. This new polymer has been characterized by PXRD, FTIR, elemental analysis, OR and TGA, and proton conductivity measurements. The latter are also

modified upon pyrrole exposition, indicating that the transport properties are determined by the nature of the non-coordinated solvent molecules, due to the sensitivity of non-porous CPs to perturbations of their lattices, something that is not as easily achieved in MOFs. As a result, these properties can be tailored, because of the capacity of these CPs to reorganize upon the insertion of different molecules into the lattice. Therefore, this material can provide the basis for the development of switchable proton conductors and capacitive sensors, that exhibit a distinct optical response to different small molecules and are capable of working at low humidity levels.

In Chapter 4, three new CPs have been obtained by means of a gas-solid covalent post-synthetic modification between the SCO coordination polymer $[Fe(NH_2trz)_3](OTs)_2$ and three volatile organic compounds: formaldehyde, benzaldehyde and acetone (giving rise to **2**, **3** and **4**, respectively). This approach enables the synthesis of new compounds and may be applied to develop materials impossible to produce by conventional synthetic routes. These CPs, characterized with FTIR, ^{1}H-NMR, PXRD, TGA, elemental analyses, optical reflectivity and magnetic measurements, display different properties. Compounds **3** and **4** display SCO behavior, similarly to **1**, but with wider hysteresis cycles. On the other hand, **2** is paramagnetic until very low temperatures where an incomplete spin transition is exhibited. Since by placing in contact **1** and different VOCs displaying a carbonyl group a covalent reaction is achieved, this could be an elegant way of developing sensors of this type of contaminants. Interestingly, out of the several tested volatile molecules, only in presence of formaldehyde does **1** change from pink to white at room temperature, resulting in an inexpensive and easy way of detecting this contaminant. This reaction is irreversible, so the pollutant becomes trapped in the structure.

To facilitate its potential implementation in devices, **1** was also embedded in two organic matrixes, PMMA and PDMS (**1@PMMA** or **1@PDMS**). While the two polymers differ in nature and physical properties like porosity, exposition of both of these pink composites to formaldehyde, result in a change of color to white. However, this color change also occurs when **1@PDMS** is exposed to acetone. Hence, to prevent acetone interferences, PDMS is not the optimal substrate for future sensing applications.

In Chapter 5, three different coordination polymers have been synthetized: $[Fe(NH_2trz)_3](OTs)_2$ (**1**), $[Fe(Htrz)_2(trz)[(BF_4)_2$ (**2**) and $[Zn(NH_2trz)_3](NO_3)_2$ (**3**) and characterized by FTIR, PXRD, TGA, absorption spectra, optical reflectivity and magnetic susceptibility measurements. Compound **1** exhibits a spin transition in the room temperature region, which leads to a color change from pink to white. On the other hand, in this temperature range, **2** stays pink and **3** remains white. To simplify their use and potential implementation, the three compounds were combined with PMMA (**1@PMMA-3@PMMA**). The initial SCO behavior is modified in the case of composites **1@PMMA** and **2@PMMA**. In any case, **1@PMMA** still displays SCO at room temperature, albeit significantly more gradual, and **2@PMMA** stays pink up to 80 °C.

These compounds were employed in three separate experiments to emulate temperature fluctuations in a room. A different behavior is observed in all of them when comparing the composite displaying a spin transition with the pink one, as **1@PMMA** transitions from LS to HS. This illustrates that the heat generated by the Sun is sufficient to trigger a spin transition. Moreover, these proof-of-concept experiments demonstrate that it is possible to reduce temperature fluctuations, both when heating and cooling, by using a SCO material, with a transition around room temperature, because of a synergy due to its bistable nature. Notably, this result introduces the possibility of employing materials from the SCO family in the passive thermal control of buildings, specifically in regions where temperatures are warm during daytime and cold at night.

In conclusion, in this thesis non-porous coordination polymers of diverse nature have been synthetized, which present several interesting physico-chemical properties that could lead to potential multifunctional applications.

REFERENCES

1 S. R. Batten, N. R. Champness, X. Chen, J. Garcia-martinez, S. Kitagawa, L. Öhrström, M. O. Keeffe, M. P. Suh, J. Reedijk, *Pure Appl. Chem.* **2013**, *85*, 1715–1724.

2 S. Henke, Metal-Organic Frameworks with Additional Flexible Substituents – Modulating Responsiveness, Gas Sorption Selectivity & Network Topologies, Ruhr-University Bochum, **2011**.

3 B. F. Hoskins, R. Robson, *J. Am. Chem. Soc.* **1989**, *111*, 5962–5964.

4 J. H. Askew, H. J. Shepherd, *Dalt. Trans.* **2020**, *49*, 2966–2971.

5 B. Xiao, P. J. Byrne, P. S. Wheatley, D. S. Wragg, X. Zhao, A. J. Fletcher, K. M. Thomas, L. Peters, J. S. O. Evans, J. E. Warren, W. Zhou, R. E. Morris, *Nat. Chem.* **2009**, *1*, 289–294.

6 I. Imaz, M. Rubio-Martínez, L. García-Fernández, F. García, D. Ruiz-Molina, J. Hernando, V. Puntes, D. Maspoch, *Chem. Commun.* **2010**, *46*, 4737–4739.

7 A. Gamonal, C. Sun, A. Lorenzo Mariano, E. Fernandez-Bartolome, E. SanVicente, B. Vlaisavljevich, J. Castells, C. Marti-Gastaldo, R. Poloni, R. Wannemacher, J. Cabanillas-Gonzalez, J. Sanchez Costa, *J. Phys. Chem. Lett.* **2020**, *11*, 3362–3368.

8 O. Roubeau, *Chem. - A Eur. J.* **2012**, *18*, 15230–15244.

9 S. Rodríguez-Jimenez, H. L. C. Feltham, S. Brooker, *Angew. Chemie - Int. Ed.* **2016**, *55*, 15067–15071.

10 J. P. Zhang, P. Q. Liao, H. L. Zhou, R. B. Lin, X. M. Chen, *Chem. Soc. Rev.* **2014**, *43*, 5789–5814.

11 O. M. Yaghi, G. Li, H. Li, *Nature* **1995**, *378*, 703–706.

12 M. A. Halcrow, *Chem. Soc. Rev.* **2011**, *40*, 4119–4142.

13 P. Gütlich, A. B. Gaspar, Y. Garcia, *Beilstein J. Org. Chem.* **2013**, *9*, 342–391.

14 K. Senthil Kumar, M. Ruben, *Coord. Chem. Rev.* **2017**, *346*, 176–205.

15 J. A. Real, A. B. Gaspar, M. C. Muñoz, *Dalt. Trans.* **2005**, 2062–2079.

16 O. Kahn, C. J. Martinez, *Science* **1998**, *279*, 44–48.

17 J.-F. Létard, P. Guionneau, L. Goux-Capes, *Towards Spin Crossover Applications (Spin Crossover in Transition Metal Compounds III)*, Springer-Verlag, Berlin, Heidelberg, **2004**.

18 S. Sanvito, *Chem. Soc. Rev.* **2011**, *40*, 3336–3355.

19 M. D. Manrique-Juárez, S. Rat, L. Salmon, G. Molnár, C. M. Quintero, L. Nicu, H. J. Shepherd, A. Bousseksou, *Coord. Chem. Rev.* **2016**, *308*, 395–408.

20 R. N. Muller, L. Vander Elst, S. Laurent, *J. Am. Chem. Soc.* **2003**, *125*, 8405–8407.

21 C. M. Quintero, G. Félix, I. Suleimanov, J. Sanchez Costa, G. Molnár, L. Salmon, W. Nicolazzi, A. Bousseksou, *Beilstein J. Nanotechnol.* **2014**, *5*, 2230–2239.

22 R. Travieso-Puente, J. O. P. Broekman, M. C. Chang, S. Demeshko, F. Meyer, E. Otten, *J.*

Am. Chem. Soc. **2016**, *138*, 5503–5506.

23 S. E. Creutz, J. C. Peters, *Inorg. Chem.* **2016**, *55*, 3894–3906.

24 O. Sato, *Nat. Chem.* **2016**, *8*, 644–656.

25 M. C. Muñoz, J. A. Real, *Coord. Chem. Rev.* **2011**, *255*, 2068–2093.

26 D. M. Halepoto, D. G. L. Holt, L. F. Larkworthy, G. J. Leigh, D. C. Povey, G. W. Smith, *J. Chem. Soc. Chem. Commun.* **1989**, 1322–1323.

27 A. K. Hughes, V. J. Murphy, D. O'Hare, *J. Chem. Soc. Chem. Commun.* **1994**, *409*, 163–164.

28 M. E. Switzer, R. Wang, M. F. Rettig, A. H. Maki, *J. Am. Chem. Soc.* **1974**, *96*, 7669–7674.

29 N. Hebendanz, F. H. Köhler, G. Müller, J. Riede, *J. Am. Chem. Soc.* **1986**, *108*, 3281–3289.

30 P. G. Sim, E. Sinn, *J. Am. Chem. Soc.* **1981**, *103*, 241–243.

31 L. Kaustov, M. E. Tal, A. I. Shames, Z. Gross, *Inorg. Chem.* **1997**, *36*, 3503–3511.

32 M. Nihei, T. Shiga, Y. Maeda, H. Oshio, *Coord. Chem. Rev.* **2007**, *251*, 2606–2621.

33 S. Hayami, Z. Z. Gu, M. Shiro, Y. Einaga, A. Fujishima, O. Sato, *J. Am. Chem. Soc.* **2000**, *122*, 7126–7127.

34 L. Sacconi, *Pure Appl. Chem.* **1971**, *27*, 161–192.

35 R. C. Stoufer, D. W. Smith, E. A. Clevenger, T. E. Norris, *Inorg. Chem.* **1966**, *5*, 1167–1161.

36 D. Gatteschi, C. A. Ghilardi, A. Orlandini, L. Sacconi, *Inorg. Chem.* **1978**, *17*, 3023–3026.

37 J. Faus, M. Julve, F. Lloret, J. A. Real, J. Sletten, *Inorg. Chem.* **1994**, *33*, 5535–5540.

38 P. Gütlich, B. R. Mcgarvey, W. Kläui, *Inorg. Chem.* **1980**, *19*, 3704–3706.

39 F. Bigdeli, C. T. Lollar, A. Morsali, H. C. Zhou, *Angew. Chemie - Int. Ed.* **2020**, *59*, 4652–4669.

40 A. Bousseksou, G. Molnár, P. Demont, J. Menegotto, *J. Mater. Chem.* **2003**, *13*, 2069–2071.

41 M. Matsuda, H. Tajima, *Chem. Lett.* **2007**, *36*, 700–701.

42 C. Bartual-Murgui, A. Akou, C. Thibault, G. Molnár, C. Vieu, L. Salmon, A. Bousseksou, *J. Mater. Chem. C* **2015**, *3*, 1277–1285.

43 I. Suleimanov, O. Kraieva, G. Molnár, L. Salmon, A. Bousseksou, *Chem. Commun.* **2015**, *51*, 15098–15101.

44 P. G. Lacroix, I. Malfant, J. A. Real, V. Rodriguez, *Eur. J. Inorg. Chem.* **2013**, *5–6*, 615–627.

45 P. Gütlich, Y. Garcia, H. Spiering, *Spin Transition Phenomena (Magnetism: Molecules to Materials IV)*, WILEY-VCH, Weinheim, **2001**.

46 B. Weber, W. Bauer, J. Obel, *Angew. Chemie - Int. Ed.* **2008**, *47*, 10098–10101.

47 L. Cambi, L. Szegö, *Chem. Ber. Dtsch. Ges.* **1931**, *64*, 2591–2598.

48 C. D. Coryell, F. Stitt, L. Pauling, *J. Am. Chem. Soc.* **1937**, *59*, 633–642.

49 J. S. Griffith, L. E. Orgel, *Q. Rev. Chem. Soc.* **1957**, *11*, 381–393.

50 A. H. Ewald, R. L. Martin, I. G. Ross, A. H. White, *Proc. R. Soc. London, Ser. A* **1964**, *280*, 235–257.

51 W. A. Baker, H. M. Bobonich, *Inorg. Chem.* **1964**, *3*, 1184–1188.

52 E. König, K. Madeja, *Inorg. Chem.* **1967**, *6*, 48–55.

53 P. Gütlich, A. Hauser, H. Spiering, *Angew. Chemie Int. Ed.* **1994**, *33*, 2024–2054.

54 E. König, G. Ritter, S. K. Kulshreshtha, *Chem. Rev.* **1985**, *85*, 219–234.

55 K. S. Murray, *Eur. J. Inorg. Chem.* **2008**, *20*, 3101–3121.

56 M. Nakamura, *Coord. Chem. Rev.* **2006**, *250*, 2271–2294.

57 I. Krivokapic, M. Zerara, M. L. Daku, A. Vargas, C. Enachescu, C. Ambrus, P. Tregenna-Piggott, N. Amstutz, E. Krausz, A. Hauser, *Coord. Chem. Rev.* **2007**, *251*, 364–378.

58 H. Sitzmann, *Coord. Chem. Rev.* **2001**, *214*, 287–327.

59 A. E. Ashley, R. T. Cooper, G. G. Wildgoose, J. C. Green, D. O'Hare, *J. Am. Chem. Soc.* **2008**, *130*, 15662–15677.

60 P. Angaridis, F. A. Cotton, C. A. Murillo, D. Villagrán, X. Wang, *J. Am. Chem. Soc.* **2005**, *127*, 5008–5009.

61 V. D. Reinen, C. Friebel, V. Propach, *Z. anorg. allg. Chem.* **1974**, *408*, 187–204.

62 B. Weber, E. Kaps, J. Weigand, C. Carbonera, J. F. Létard, K. Achterhold, F. G. Parak, *Inorg. Chem.* **2008**, *47*, 487–496.

63 J. Klingele, D. Kaase, J. Hilgert, G. Steinfeld, M. H. Klingele, J. Lach, *Dalt. Trans.* **2010**, *39*, 4495–4507.

64 A. Arroyave, A. Lennartson, A. Dragulescu-Andrasi, K. S. Pedersen, S. Piligkos, S. A. Stoian, S. M. Greer, C. Pak, O. Hietsoi, H. Phan, S. Hill, C. J. McKenzie, M. Shatruk, *Inorg. Chem.* **2016**, *55*, 5904–5913.

65 T. Sugaya, T. Fujihara, T. Naka, T. Furubayashi, A. Matsushita, H. Isago, A. Nagasawa, *Chem. - A Eur. J.* **2018**, *24*, 17955–17963.

66 E. König, G. Ritter, S. K. Kulshreshtha, J. Waigel, L. Sacconi, *Inorg. Chem.* **1984**, *23*, 1241–1246.

67 E. König, in *Prog. Inorg. Chem.*, Wiley, **2007**, pp. 527–622.

68 G. Aromí, L. A. Barrios, O. Roubeau, P. Gamez, *Coord. Chem. Rev.* **2011**, *255*, 485–546.

69 O. Kahn, J. Kröber, C. Jay, *Adv. Mater.* **1992**, *4*, 718–728.

70 L. Salmon, L. Catala, *Comptes Rendus Chim.* **2018**, *21*, 1230–1269.

71 P. Grondin, O. Roubeau, M. Castro, H. Saadaoui, A. Colin, R. Clérac, *Langmuir* **2010**, *26*, 5184–5195.

72 T. Mallah, M. Cavallini, *Comptes Rendus Chim.* **2018**, *21*, 1270–1286.

73 Y. Wei, P. Sonar, M. Grunert, J. Kusz, A. D. Schlüter, P. Gütlich, *Eur. J. Inorg. Chem.* **2010**, 3930–3941.

74 P. Grondin, D. Siretanu, O. Roubeau, M. F. Achard, R. Clérac, *Inorg. Chem.* **2012**, *51*, 5417–5426.

75 F. Prins, M. Monrabal-Capilla, E. A. Osorio, E. Coronado, H. S. J. Van Der Zant, *Adv. Mater.* **2011**, *23*, 1545–1549.

76 A. Michalowicz, J. Moscovici, B. Ducourant, D. Cracco, O. Kahn, *Chem. Mater.* **1995**, *7*, 1833–1842.

77 N. Pittala, F. Thétiot, C. Charles, S. Triki, K. Boukheddaden, G. Chastanet, M. Marchivie, *Chem. Commun.* **2017**, *53*, 8356–8359.

78 A. Grosjean, N. Daro, B. Kauffmann, A. Kaiba, J.-F. Létard, P. Guionneau, *Chem. Commun.* **2011**, *47*, 12382.

79 J. Kröber, J.-P. Audière, R. Claude, E. Codjovi, O. Kahn, J. G. Haasnoot, F. Grolière, C. Jay, B. Azzedine, J. Linarès, F. Varret, G. V. Anne, *Chem. Mater.* **1994**, *6*, 1404–1412.

80 A. Lapresta-Fernández, S. Titos-Padilla, J. M. Herrera, A. Salinas-Castillo, E. Colacio, L. F. Capitán Vallvey, *Chem. Commun.* **2013**, *49*, 288–290.

81 O. Roubeau, M. Castro, R. Burriel, J. G. Haasnoot, J. Reedijk, *J. Phys. Chem. B* **2011**, *115*, 3003–3012.

82 M. Seredyuk, A. B. Gaspar, M. C. Muñoz, M. Verdaguer, F. Villain, P. Gütlich, *Eur. J. Inorg. Chem.* **2007**, *28*, 4481–4491.

83 O. Roubeau, J. G. Haasnoot, E. Codjovi, F. Varret, J. Reedijk, *Chem. Mater.* **2002**, *14*, 2559–2566.

84 Z. Yan, M. Li, H. L. Gao, X. C. Huang, D. Li, *Chem. Commun.* **2012**, *48*, 3960–3962.

85 A. Vef, U. Manthe, P. Gütlich, A. Hauser, *J. Chem. Phys.* **1994**, *101*, 9326–9332.

86 M. M. Khusniyarov, *Chem. - A Eur. J.* **2016**, *22*, 15178–15191.

87 N. Li, J. P. Xue, J. L. Liu, Y. Y. Wang, Z. S. Yao, J. Tao, *Dalt. Trans.* **2020**, *49*, 998–1001.

88 M. Nihei, Y. Yanai, I. Hsu, Y. Sekine, H. Oshio, *Angew. Chemie Int. Ed.* **2017**, *56*, 591–594.

89 B. Li, R. J. Wei, J. Tao, R. Bin Huang, L. S. Zheng, Z. Zheng, *J. Am. Chem. Soc.* **2010**, *132*, 1558–1566.

90 L. Piñeiro-López, M. Seredyuk, M. C. Muñoz, J. A. Real, *Eur. J. Inorg. Chem.* **2020**, *9*, 764–769.

91 Y. Meng, Y. J. Dong, Z. Yan, Y. C. Chen, X. W. Song, Q. W. Li, C. L. Zhang, Z. P. Ni, M. L. Tong, *Cryst. Growth Des.* **2018**, *18*, 5214–5219.

92 G. J. Halder, C. J. Kepert, B. Moubaraki, K. S. Murray, J. D. Cashion, *Science* **2002**, *298*, 1762–1765.

93 W. Phonsri, P. Harding, L. Liu, S. G. Telfer, K. S. Murray, B. Moubaraki, T. M. Ross, G. N. L. Jameson, D. J. Harding, *Chem. Sci.* **2017**, *8*, 3949–3959.

94 F. J. Valverde-Muñoz, C. Bartual-Murgui, L. Piñeiro-López, M. C. Muñoz, J. A. Real, *Inorg. Chem.* **2019**, *58*, 10038–10046.

95 C. Bartual-Murgui, L. Salmon, A. Akou, N. A. Ortega-Villar, H. J. Shepherd, M. C. Muñoz, G. Molnár, J. A. Real, A. Bousseksou, *Chem. - A Eur. J.* **2012**, *18*, 507–516.

96 D. Aravena, Z. A. Castillo, M. C. Muñoz, A. B. Gaspar, K. Yoneda, R. Ohtani, A. Mishima, S. Kitagawa, M. Ohba, J. A. Real, E. Ruiz, *Chem. - A Eur. J.* **2014**, *20*, 12864–12873.

97 A. Lennartson, P. Southon, N. F. Sciortino, C. J. Kepert, C. Frandsen, S. Mørup, S. Piligkos, C. J. McKenzie, *Chem. - A Eur. J.* **2015**, *21*, 16066–16072.

98 M. J. Murphy, K. A. Zenere, F. Ragon, P. D. Southon, C. J. Kepert, S. M. Neville, *J. Am. Chem. Soc.* **2017**, *139*, 1330–1335.

99 A. Galet, M. C. Muñoz, J. A. Real, *Chem. Commun.* **2006**, *41*, 4321–4323.

100 E. Coronado, M. Giménez-Marqués, G. M. Espallargas, L. Brammer, *Nat. Commun.* **2012**, *3*, 1–8.

101 A. M. Greenaway, E. Sinn, *J. Am. Chem. Soc.* **1978**, *100*, 8080–8084.

102 K. H. Sugiyarto, D. C. Craig, A. D. Rae, H. A. Goodwin, *Aust. J. Chem.* **1994**, *47*, 869.

103 M. Wriedt, A. A. Yakovenko, G. J. Halder, A. V. Prosvirin, K. R. Dunbar, H. C. Zhou, *J. Am. Chem. Soc.* **2013**, *135*, 4040–4050.

104 P. D. Southon, L. Liu, E. A. Fellows, D. J. Price, G. J. Halder, K. W. Chapman, B. Moubaraki, K. S. Murray, J. F. Létard, C. J. Kepert, *J. Am. Chem. Soc.* **2009**, *131*, 10998–11009.

105 E. Coronado, M. Giménez-Marqués, G. Mínguez Espallargas, F. Rey, I. J. Vitórica-Yrezábal, *J. Am. Chem. Soc.* **2013**, *135*, 15986–15989.

106 J. Sanchez Costa, S. Rodríguez-Jiménez, G. A. Craig, B. Barth, C. M. Beavers, S. J. Teat, G. Aromí, *J. Am. Chem. Soc.* **2014**, *136*, 3869–3874.

107 M. M. Khusniyarov, E. Bill, T. Weyhermüller, E. Bothe, K. Wieghardt, *Angew. Chemie - Int. Ed.* **2011**, *50*, 1652–1655.

108 M. Schmitz, M. Seibel, H. Kelm, S. Demeshko, F. Meyer, H. J. Krüger, *Angew. Chemie - Int. Ed.* **2014**, *53*, 5988–5992.

109 M. M. Khusniyarov, T. Weyhermüller, E. Bill, K. Wieghardt, *Angew. Chemie - Int. Ed.* **2008**, *47*, 1228–1231.

110 H. Y. Wang, J. Y. Ge, C. Hua, C. Q. Jiao, Y. Wu, C. F. Leong, D. M. D'Alessandro, T. Liu, J. L. Zuo, *Angew. Chemie - Int. Ed.* **2017**, *56*, 5465–5470.

111 Y. Q. Hu, M. Q. Li, Y. Wang, T. Zhang, P. Q. Liao, Z. Zheng, X. M. Chen, Y. Z. Zheng, *Chem. - A Eur. J.* **2017**, *23*, 8409–8413.

112 A. D. Naik, K. Robeyns, C. F. Meunier, A. F. Léonard, A. Rotaru, B. Tinant, Y. Filinchuk, B. L. Su, Y. Garcia, *Inorg. Chem.* **2014**, *53*, 1263–1265.

113 C. F. Wang, R. F. Li, X. Y. Chen, R. J. Wei, L. S. Zheng, J. Tao, *Angew. Chemie - Int. Ed.* **2015**, *54*, 1574–1577.

114 J. E. Clements, J. R. Price, S. M. Neville, C. J. Kepert, *Angew. Chemie - Int. Ed.* **2014**, *53*, 10164–10168.

115 S. Zaiter, C. Kirk, M. Taylor, Y. M. Klein, C. E. Housecroft, N. F. Sciortino, J. E. Clements, R. I. Cooper, C. J. Kepert, S. M. Neville, *Dalt. Trans.* **2019**, *48*, 7337–7343.

116 Y. H. Luo, M. Nihei, G. J. Wen, B. W. Sun, H. Oshio, *Inorg. Chem.* **2016**, *55*, 8147–8152.

117 A. B. Gaspar, G. Molnár, A. Rotaru, H. J. Shepherd, *Comptes Rendus Chim.* **2018**, *21*, 1095–1120.

118 P. Gütlich, A. B. Gaspar, Y. Garcia, V. Ksenofontov, *Comptes Rendus Chim.* **2007**, *10*, 21–36.

119 A. Galet, A. B. Gaspar, G. Agusti, M. C. Muñoz, G. Levchenko, J. A. Real, *Eur. J. Inorg. Chem.* **2006**, *18*, 3571–3573.

120 A. H. Ewald, R. L. Martin, E. Sinn, A. H. White, *Inorg. Chem.* **1969**, *8*, 1837–1846.

121 V. Niel, A. Galet, A. B. Gaspar, M. C. Muñoz, J. A. Real, *Chem. Commun.* **2003**, *3*, 1248–1249.

122 J. Li, S. Chen, L. Jiang, Y. Li, B. Li, *Cryst. Growth Des.* **2018**, *18*, 1931–1934.

123 B. Brachňaková, I. Šalitroš, *Chem. Pap.* **2018**, *72*, 773–798.

124 J. J. McGarvey, I. Lawthers, *J. Chem. Soc. Chem. Commun.* **1982**, *16*, 906–907.

125 S. Decurtins, P. Gütlich, C. P. Köhler, H. Spiering, A. Hauser, *Chem. Phys. Lett.* **1984**, *105*, 1–4.

126 W. Lan, F. J. Valverde-Muñoz, Y. Dou, X. Hao, M. C. Muñoz, Z. Zhou, H. Liu, Q. Liu, J. A. Real, D. Zhang, *Dalt. Trans.* **2019**, *48*, 17014–17021.

127 C. Roux, J. Zarembowitch, B. Gailois, T. Granier, R. Claude, *Inorg. Chem.* **1994**, *33*, 2273–2279.

128 J. Zarembowitch, C. Roux, M.-L. Boillot, R. Claude, J. Itie, A. Polian, M. Bolte, *Mol. Cryst. Liq. Cryst.* **1993**, *234*, 247–254.

129 M. L. Boillot, C. Roux, J. P. Audière, A. Dausse, J. Zarembowitch, *Inorg. Chem.* **1996**, *35*, 3975–3980.

130 K. Takahashi, Y. Hasegawa, R. Sakamoto, M. Nishikawa, S. Kume, E. Nishibori, H. Nishihara, *Inorg. Chem.* **2012**, *51*, 5188–5198.

131 A. Enriquez-Cabrera, A. Rapakousiou, M. Piedrahita Bello, G. Molnár, L. Salmon, A. Bousseksou, *Coord. Chem. Rev.* **2020**, *419*, 213396.

132 K. Friedrich, A. A. Almajid, *Appl Compos Mater* **2013**, *20*, 107–128.

133 S. Rat, M. Piedrahita-Bello, L. Salmon, G. Molnár, P. Demont, A. Bousseksou, *Adv. Mater.* **2018**, *30*, 1705275.

134 S. Park, H. Kim, M. Vosgueritchian, S. Cheon, H. Kim, J. H. Koo, T. R. Kim, S. Lee, G. Schwartz, H. Chang, Z. Bao, *Adv. Mater.* **2014**, *26*, 7324–7332.

135 H. J. Shepherd, I. A. Gural'Skiy, C. M. Quintero, S. Tricard, L. Salmon, G. Molnár, A. Bousseksou, *Nat. Commun.* **2013**, *4*, 2607.

136 M. D. Manrique-Juarez, F. Mathieu, V. Shalabaeva, J. Cacheux, S. Rat, L. Nicu, T. Leïchlé, L. Salmon, G. Molnár, A. Bousseksou, *Angew. Chemie - Int. Ed.* **2017**, *56*, 8074–8078.

137 S. Rat, V. Nagy, I. Suleimanov, G. Molnár, L. Salmon, P. Demont, L. Csóka, A. Bousseksou, *Chem. Commun.* **2016**, *52*, 11267–11269.

138 A. W. Martinez, S. T. Phillips, E. Carrilho, S. W. Thomas III, H. Sindi, G. M. Whitesides, *Anal. Chem.* **2008**, *80*, 3699–3707.

139 V. Rubio-Giménez, S. Tatay, C. Martí-Gastaldo, *Chem. Soc. Rev.* **2020**, *49*, 5601–5638.

140 H. N. Wang, X. Meng, L. Z. Dong, Y. Chen, S. L. Li, Y. Q. Lan, *J. Mater. Chem. A* **2019**, *7*, 24059–24091.

141 G. Givaja, P. Amo-Ochoa, C. J. Gómez-García, F. Zamora, *Chem. Soc. Rev.* **2012**, *41*, 115–147.

142 I. Stassen, N. Burtch, A. Talin, P. Falcaro, M. Allendorf, R. Ameloot, *Chem. Soc. Rev.* **2017**, *46*, 3185–3241.

143 X. Huang, P. Sheng, Z. Tu, F. Zhang, J. Wang, H. Geng, Y. Zou, C. A. Di, Y. Yi, Y. Sun, W. Xu, D. Zhu, *Nat. Commun.* **2015**, *6*, 1–8.

144 A. Kobayashi, S. I. Imada, Y. Shigeta, Y. Nagao, M. Yoshida, M. Kato, *J. Mater. Chem. C* **2019**, *7*, 14923–14931.

145 European Environment Agency, "Emissions of the main air pollutants in Europe," accessed 5 April **2020**.

146 F. Wang, Y. T. Wang, H. Yu, J. X. Chen, B. Bin Gao, J. P. Lang, *Inorg. Chem.* **2016**, *55*, 9417–9423.

147 P. Kumar, A. Deep, K. H. Kim, R. J. C. Brown, *Prog. Polym. Sci.* **2015**, *45*, 102–118.

148 World Health Organization, *Guidelines for Air Quality*, **2000**.

149 J. C. Gasparetto, R. Pontarolo, T. M. G. de Francisco, *Acetonitrile: Properties, Exposure, Metabolism and Toxicity*, **2012**.

150 Institute for Health and Consumer Protection, European Chemicals Bureau, *European Union Risk Assessment Report*, **2002**.

151 Y. Wang, X. Mei, T. Ma, C. Xue, M. Wu, M. Ji, Y. Li, *J. Clean. Prod.* **2018**, *197*, 742–749.

152 J. Q. Ni, W. P. Robarge, C. Xiao, A. J. Heber, *Chemosphere* **2012**, *89*, 769–788.

153 J. Dewulf, H. Van Langenhove, *Trends Anal. Chem.* **2002**, *21*, 637–646.

154 B. Buszewski, D. Grzywinski, T. Ligor, T. Stacewicz, Z. Bielecki, J. Wojtas, *Bioanalysis* **2013**, *5*, 2287–2306.

155 World Health Organization, *Int. Program. Chem. Saf.* **1993**, *154*, 1–110.

156 P. Wang, J. Xu, Q. D. Zhuo, Y. S. Ma, H. J. Cheng, X. Y. Tang, R. X. Yuan, *Inorg. Chem. Commun.* **2016**, *67*, 14–16.

157 H. Furukawa, K. E. Cordova, M. O'Keeffe, O. M. Yaghi, *Science* **2013**, *341*, 974–986.

158 A. P. Côté, A. I. Benin, N. W. Ockwig, M. Keeffe, A. J. Matzger, O. M. Yaghi, **2010**, *1166*, 1166–1171.

159 R. Chan-Navarro, D. Corpus-Coronado, B. M. Muñoz-Flores, M. Loredo-Cancino, N. Waksman, R. Ramírez, V. M. Jiménez-Pérez, *J. Inorg. Organomet. Polym. Mater.* **2017**, *27*, 467–473.

160 Y. Deng, Z. Y. Yao, P. Wang, Y. Zhao, Y. S. Kang, M. Azam, S. I. Al-Resayes, W. Y. Sun, *RSC Adv.* **2017**, *7*, 44639–44646.

161 J. Chen, F.-Y. Yi, H. Yu, S. Jiao, G. Pang, Z.-M. Sun, *Chem. Commun.* **2014**, *50*, 10506–10509.

162 J. Miguel-Donet, J. López-Cabrelles, C. Galve, E. Coronado, *Chem. Eur. J.* **2018**, *24*, 12426–

12432.

163 E. Fernandez-Bartolome, J. Santos, A. Gamonal, S. Khodabakhshi, L. J. McCormick, S. J. Teat, E. C. Sañudo, J. Sanchez Costa, N. Martín, *Angew. Chemie - Int. Ed.* **2019**, *58*, 2310–2315.

164 G. K. Kole, J. J. Vittal, *Chem. Soc. Rev.* **2013**, *42*, 1755–1775.

165 E. Li, K. Jie, M. Liu, X. Sheng, W. Zhu, F. Huang, *Chem. Soc. Rev.* **2020**, *49*, 1517–1544.

166 L. Shahhoseini, R. Mohammadi, B. Ghanbari, S. Shahrokhian, *Appl. Surf. Sci.* **2019**, *478*, 361–372.

167 X. Fang, B. Zong, S. Mao, *Nano-Micro Lett.* **2018**, *10*, 1–19.

168 A. M. Al'Abri, S. N. Abdul Halim, N. K. Abu Bakar, S. M. Saharin, B. Sherino, H. Rashidi Nodeh, S. Mohamad, *J. Environ. Sci. Heal. - Part B* **2019**, *54*, 930–941.

169 S. Wang, J. Liu, H. Zhao, Z. Guo, H. Xing, Y. Gao, *Inorg. Chem.* **2018**, *57*, 541–544.

170 E. Resines-Urien, E. Burzurí, E. Fernandez-Bartolome, M. Á. García García-Tuñón, P. De La Presa, R. Poloni, S. J. Teat, J. Sanchez Costa, *Chem. Sci.* **2019**, *10*, 6612–6616.

171 A. Białońska, R. Bronisz, K. Darowska, K. Drabent, J. Kusz, M. Siczek, M. Weselski, M. Zubko, A. Ozarowski, *Inorg. Chem.* **2010**, *49*, 11267–11269.

172 J. Sanchez Costa, S. Rodríguez-Jiménez, G. A. Craig, B. Barth, C. M. Beavers, S. J. Teat, K. J. Gagnon, L. A. Barrios, O. Roubeau, G. Aromí, *Inorg. Chem. Front.* **2020**, *7*, 3165–3175.

173 L. Sun, S. S. Park, D. Sheberla, M. Dincă, *J. Am. Chem. Soc.* **2016**, *138*, 14772–14782.

174 L. Sun, M. G. Campbell, M. Dincă, *Angew. Chemie - Int. Ed.* **2016**, *55*, 3566–3579.

175 A. L. Spek, *Acta Crystallogr. Sect. E Crystallogr. Commun.* **2020**, *E76*, 1–11.

176 J. S. Loring, W. Ronald Fawcett, *J. Phys. Chem. A* **1999**, *103*, 3608–3617.

177 E. L. Pace, L. J. Noe, *J. Chem. Phys.* **1968**, *49*, 5317–5325.

178 T. Degen, M. Sadki, E. Bron, U. König, G. Nénert, in *Powder Diffr.*, **2014**, pp. S13–S18.

179 L. E. Kreno, K. Leong, O. K. Farha, M. Allendorf, R. P. Van Duyne, J. T. Hupp, *Chem. Rev.* **2012**, *112*, 1105–1125.

180 R. Shevate, M. A. Haque, F. H. Akhtar, L. F. Villalobos, T. Wu, K. V. Peinemann, *Angew. Chemie - Int. Ed.* **2018**, *57*, 11218–11222.

181 H. J. Bae, S. Bae, C. Park, S. Han, J. Kim, L. N. Kim, K. Kim, S. H. Song, W. Park, S. Kwon, *Adv. Mater.* **2015**, *27*, 2083–2089.

182 L. Sun, S. S. Park, D. Sheberla, M. Dincă, *J. Am. Chem. Soc.* **2016**, *138*, 14772–14782.

183 L. Sun, C. H. Hendon, S. S. Park, Y. Tulchinsky, R. Wan, F. Wang, A. Walsh, M. Dincă, *Chem. Sci.* **2017**, *8*, 4450–4457.

184 M. del C. Gimenez Lopez, M. Clemente Leon, C. Gimenez-Saiz, *Dalt. Trans.* **2018**, *47*, 10453–10462.

185 F. A. Harraz, A. A. Ismail, H. Bouzid, S. A. Al-Sayari, A. Al-Hajry, M. S. Al-Assiri, *Phys. Status Solidi Appl. Mater. Sci.* **2015**, *212*, 1851–1857.

186 F. A. Harraz, A. A. Ismail, S. A. Al-Sayari, A. Al-Hajry, M. S. Al-Assiri, *Superlattices Microstruct.* **2016**, *100*, 1064–1072.

187 T. Wagner, S. Haffer, C. Weinberger, D. Klaus, M. Tiemann, *Chem. Soc. Rev.* **2013**, *42*, 4036–4053.

188 A. Chidambaram, K. C. Stylianou, *Inorg. Chem. Front.* **2018**, *5*, 979–998.

189 J. Liu, F. Sun, F. Zhang, Z. Wang, R. Zhang, C. Wang, S. Qiu, *J. Mater. Chem.* **2011**, *21*, 3775–3778.

190 D. Sheberla, J. C. Bachman, J. S. Elias, C. J. Sun, Y. Shao-Horn, M. Dincă, *Nat. Mater.* **2017**,

16, 220–224.

191 J. C.Whitaker, *The Electronics Handbook*, CRC Press, **1996**.

192 A. Thirumurugan, W. Li, A. K. Cheetham, *Dalt. Trans.* **2012**, *41*, 4126–4134.

193 C. Yu, M. G. Cowan, R. D. Noble, W. Zhang, *Chem. Commun.* **2014**, *50*, 5745–5747.

194 A. Tarassoli, V. Nobakht, E. Baladi, L. Carlucci, D. M. Proserpio, *CrystEngComm* **2017**, *19*, 6116–6126.

195 E. Fernandez-Bartolome, E. Resines-Urien, M. Murillo-Vidal, L. Piñeiro-Lopez, J. Sanchez Costa, *Inorg. Chem. Front.* **2021**, *8*, 2426–2432.

196 E. Resines-Urien, L. Piñeiro-López, E. Fernandez-Bartolome, A. Gamonal, M. Garcia-Hernandez, J. Sanchez Costa, *Dalt. Trans.* **2020**, *49*, 7315–7318.

197 S. Jeoung, S. H. Sahgong, J. H. Kim, S. M. Hwang, Y. Kim, H. R. Moon, *J. Mater. Chem. A* **2016**, *4*, 13468–13475.

198 U. S. F. Arrozi, V. Bon, C. Kutzscher, I. Senkovska, S. Kaskel, *Dalt. Trans.* **2019**, *48*, 3415–3421.

199 X. Su, L. Bromberg, V. Martis, F. Simeon, A. Huq, T. Alan Hatton, *ACS Appl. Mater. Interfaces* **2017**, *9*, 11299–11306.

200 C. T. Yang, A. R. Kshirsagar, A. C. Eddin, L. C. Lin, R. Poloni, *Chem. - A Eur. J.* **2018**, *24*, 15167–15172.

201 J. Li, X. Wang, G. Zhao, C. Chen, Z. Chai, A. Alsaedi, T. Hayat, X. Wang, *Chem. Soc. Rev.* **2018**, *47*, 2322–2356.

202 J. . F. Nagle, H. J. Morowitz, *Proc. Natl. Acad. Sci. USA* **1978**, *75*, 298–302.

203 K. Miyatake, T. Tombe, Y. Chikashige, H. Uchida, M. Watanabe, *Angew. Chemie - Int. Ed.* **2007**, *46*, 6646–6649.

204 H. Ding, W. Wu, C. Jiang, Y. Ding, W. Bian, B. Hu, P. Singh, C. J. Orme, L. Wang, Y. Zhang, D. Ding, *Nat. Commun.* **2020**, *11*, 1–11.

205 M. Yoon, K. Suh, S. Natarajan, K. Kim, *Angew. Chemie - Int. Ed.* **2013**, *52*, 2688–2700.

206 D. W. Lim, H. Kitagawa, *Chem. Rev.* **2020**, *120*, 8416–8467.

207 P. Rought, C. Marsh, S. Pili, I. P. Silverwood, V. G. Sakai, M. Li, M. S. Brown, S. P. Argent, I. Vitorica-Yrezabal, G. Whitehead, M. R. Warren, S. Yang, M. Schröder, *Chem. Sci.* **2019**, *10*, 1492–1499.

208 P. Barbosa, N. C. Rosero-Navarro, F. N. Shi, F. M. L. Figueiredo, *Electrochim. Acta* **2015**, *153*, 19–27.

209 H. Zhang, Z. A. Yan, Z. M. Wu, Z. Q. Lin, W. M. Liao, J. He, *J. Solid State Chem.* **2020**, *287*, 1–5.

210 S. Wang, M. Wahiduzzaman, L. Davis, A. Tissot, W. Shepard, J. Marrot, C. Martineau-Corcos, D. Hamdane, G. Maurin, S. Devautour-Vinot, C. Serre, *Nat. Commun.* **2018**, *9*, 1–9.

211 K. Zhang, X. Xie, H. Li, J. Gao, L. Nie, Y. Pan, J. Xie, D. Tian, W. Liu, Q. Fan, H. Su, L. Huang, W. Huang, *Adv. Mater.* **2017**, *29*, 1701804.

212 E. Pardo, C. Train, G. Gontard, K. Boubekeur, O. Fabelo, H. Liu, B. Dkhil, F. Lloret, K. Nakagawa, H. Tokoro, S. I. Ohkoshi, M. Verdaguer, *J. Am. Chem. Soc.* **2011**, *133*, 15328–15331.

213 H. Xu, S. Tao, D. Jiang, *Nat. Mater.* **2016**, *15*, 722–726.

214 Y. Ye, W. Guo, L. Wang, Z. Li, Z. Song, J. Chen, Z. Zhang, S. Xiang, B. Chen, *J. Am. Chem. Soc.* **2017**, *139*, 15604–15607.

215 Y. S. Wei, X. P. Hu, Z. Han, X. Y. Dong, S. Q. Zang, T. C. W. Mak, *J. Am. Chem. Soc.* **2017**, *139*, 3505–3512.

216 K. Müller, J. Helfferich, F. Zhao, R. Verma, A. B. Kanj, V. Meded, D. Bléger, W. Wenzel, L. Heinke, *Adv. Mater.* **2018**, *30*, 1706551.

217 S. S. Liu, Z. Han, J. Sen Yang, S. Z. Huang, X. Y. Dong, S. Q. Zang, *Inorg. Chem.* **2020**, *59*, 396–402.

218 W. L. Xue, W. H. Deng, H. Chen, R. H. Liu, J. M. Taylor, Y. kun Li, L. Wang, Y. H. Deng, W. H. Li, Y. Y. Wen, G. E. Wang, C. Q. Wan, G. Xu, *Angew. Chemie - Int. Ed.* **2021**, *60*, 1290–1297.

219 A. Shigematsu, T. Yamada, H. Kitagawa, *J. Am. Chem. Soc.* **2011**, *133*, 2034–2036.

220 P. Ramaswamy, R. Matsuda, W. Kosaka, G. Akiyama, H. Joon Jeon, S. Kitagawa, *Chem. Commun.* **2014**, *50*, 1144–1146.

221 D. Umeyama, S. Horike, M. Inukai, T. Itakura, S. Kitagawa, *J. Am. Chem. Soc.* **2012**, *134*, 12780–12785.

222 F. Yang, G. Xu, Y. Dou, B. Wang, H. Zhang, H. Wu, W. Zhou, J. R. Li, B. Chen, *Nat. Energy* **2017**, *2*, 877–883.

223 S. Pili, S. P. Argent, C. G. Morris, P. Rought, V. García-Sakai, I. P. Silverwood, T. L. Easun, M. Li, M. R. Warren, C. A. Murray, C. C. Tang, S. Yang, M. Schröder, *J. Am. Chem. Soc.* **2016**, *138*, 6352–6355.

224 P. Ramaswamy, N. E. Wong, B. S. Gelfand, G. K. H. Shimizu, *J. Am. Chem. Soc.* **2015**, *137*, 7640–7643.

225 J. Wegener, A. Kaltbeitzel, R. Graf, M. Klapper, K. Müllen, *ChemSusChem* **2014**, *7*, 1148–1154.

226 F. Yang, G. Xu, Y. Dou, B. Wang, H. Zhang, H. Wu, W. Zhou, J. R. Li, B. Chen, *Nat. Energy* **2017**, *2*, 877–883.

227 H. Liu, R. Li, J. Lu, Z. Liu, S. Wang, H. Tian, *CrystEngComm* **2020**, *22*, 6935–6946.

228 J. Stankiewicz, M. Tomás, I. T. Dobrinovitch, E. Forcén-Vázquez, L. R. Falvello, *Chem. Mater.* **2014**, *26*, 5282–5287.

229 L. Feng, Z. Q. Pan, H. Zhou, M. Zhou, H. B. Hou, *Dalt. Trans.* **2019**, *48*, 16493–16496.

230 R. F. Mendes, P. Barbosa, E. M. Domingues, P. Silva, F. Figueiredo, F. A. Almeida Paz, *Chem. Sci.* **2020**, *11*, 6305–6311.

231 S. Horike, D. Umeyama, S. Kitagawa, *Acc. Chem. Res.* **2013**, *46*, 2376–2384.

232 A. Develioglu, E. Resines-Urien, R. Poloni, L. Martín-Pérez, J. Sanchez Costa, E. Burzurí, *Adv. Sci.* **2021**, *8*, 2102619.

233 S. Tao, L. Zhai, A. D. Dinga Wonanke, M. A. Addicoat, Q. Jiang, D. Jiang, *Nat. Commun.* **2020**, *11*, 1–8.

234 P. R. Bueno, J. A. Varela, E. Longo, *J. Eur. Ceram. Soc.* **2007**, *27*, 4313–4320.

235 A. B. Gaspar, V. Ksenofontov, M. Seredyuk, P. Gütlich, *Coord. Chem. Rev.* **2005**, *249*, 2661–2676.

236 M.-J. Sun, C.-F. Wang, J. Tao, L.-S. Zheng, Q.-J. Guo, Z.-X. Cao, *Chem. Commun.* **2016**, *52*, 14322–14325.

237 I. R. Jeon, O. Jeannin, R. Clérac, M. Rouzières, M. Fourmigué, *Chem. Commun.* **2017**, *53*, 4989–4992.

238 S. M. Fatur, S. G. Shepard, R. F. Higgins, M. P. Shores, N. H. Damrauer, *J. Am. Chem. Soc.* **2017**, *139*, 4493–4505.

239 D. A. Roberts, B. S. Pilgrim, J. D. Cooper, T. K. Ronson, S. Zarra, J. R. Nitschke, *J. Am. Chem. Soc.* **2015**, *137*, 10068–10071.

240 S. M. Cohen, *Chem. Sci.* **2010**, *1*, 32–36.

241 B. F. Hoskins, R. Robson, *J. Am. Chem. Soc.* **1990**, *112*, 1546–1554.

242 Z. Wang, S. M. Cohen, *J. Am. Chem. Soc.* **2007**, *129*, 12368–12369.

243 Z. Yin, S. Wan, J. Yang, M. Kurmoo, M. H. Zeng, *Coord. Chem. Rev.* **2019**, *378*, 500–512.

244 K. K. Tanabe, S. M. Cohen, *Chem. Soc. Rev.* **2011**, *40*, 498–519.

245 X. Wang, M. Feng, L. Xiao, A. Tong, Y. Xiang, *ACS Chem. Biol.* **2016**, *11*, 444–451.

246 K. S. Asha, N. Ahmed, R. Nath, D. Kuznetsov, S. Mandal, *Inorg. Chem.* **2017**, *56*, 7316–7319.

247 T. Grancha, J. Ferrando-Soria, H.-C. Zhou, J. Gascon, B. Seoane, J. Pasán, O. Fabelo, M. Julve, E. Pardo, *Angew. Chemie Int. Ed.* **2015**, *54*, 6521–6525.

248 S. A. Amolegbe, H. Ohmagari, K. Wakata, H. Takehira, R. Ohtani, M. Nakamura, C. Yu, S. Hayami, *J. Mater. Chem. B* **2016**, *4*, 1040–1043.

249 S. M. Cohen, *Chem. Rev.* **2012**, *112*, 970–1000.

250 M. Ohba, K. Yoneda, G. Agusti, M. C. Muñoz, A. B. Gaspar, J. A. Real, M. Yamasaki, H. Ando, Y. Nakao, S. Sakaki, S. Kitagawa, *Angew. Chemie - Int. Ed.* **2009**, *48*, 4767–4771.

251 Z. Wang, S. M. Cohen, *Chem. Soc. Rev.* **2009**, *38*, 1315–1329.

252 S. M. Cohen, *J. Am. Chem. Soc.* **2017**, *139*, 2855–2863.

253 Y. Komatsumaru, M. Nakaya, F. Kobayashi, R. Ohtani, M. Nakamura, L. F. Lindoy, S. Hayami, *Zeitschrift für Anorg. und Allg. Chemie* **2018**, *644*, 729–734.

254 A. Enríquez-Cabrera, L. Routaboul, L. Salmon, A. Bousseksou, *Dalt. Trans.* **2019**, *48*, 16853–16856.

255 C. W. Rogers, M. O. Wolf, *Coord. Chem. Rev.* **2002**, *233–234*, 341–350.

256 J. Sanchez Costa, *Comptes Rendus Chim.* **2018**, *21*, 1121–1132.

257 D. Gentili, N. Demitri, B. Schäfer, F. Liscio, I. Bergenti, G. Ruani, M. Ruben, M. Cavallini, *J. Mater. Chem. C* **2015**, *3*, 7836–7844.

258 S. Horike, S. Shimomura, S. Kitagawa, *Nat. Chem.* **2009**, *1*, 695–704.

259 G. Aromí, C. M. Beavers, J. Sanchez Costa, G. A. Craig, G. Mínguez Espallargas, A. Orera, O. Roubeau, *Chem. Sci.* **2016**, *7*, 2907–2915.

260 World Health Organization, “Formaldehyde,” accessed 12 April **2020**.

261 A. Songur, O. A. Ozen, M. Sarsilmaz, *Rev. Environ. Contam. Toxicol.* **2010**, *203*, 105–118.

262 American Cancer Society, “Formaldehyde,” accessed 17 April **2020**.

263 Centers for Disease Control, *Medical Management Guidelines for Formaldehyde (HCHO)*, **2014**.

264 F. Nowshad, M. N. Islam, M. S. Khan, *Agric. Food Secur.* **2018**, *7*, 1–8.

265 P. R. Chung, C. T. Tzeng, M. T. Ke, C. Y. Lee, *Sensors* **2013**, *13*, 4468–4484.

266 Y. I. Korpan, M. V Gonchar, A. A. Sibirny, C. Martelet, A. V El’skaya, T. D. Gibson, A. P. Soldatkin, *Biosens. Bioelectron.* **2000**, *15*, 77–83.

267 R. Kataky, M. R. Bryce, L. Goldenberg, S. Hayes, A. Nowak, *Talanta* **2002**, *56*, 451–458.

268 W. J. Kim, N. Terada, T. Nomura, R. Takahashi, S. D. Lee, J. H. Park, A. Konno, *Clin. Exp. Allergy* **2002**, *32*, 287–295.

269 G. R. Möhlmann, *Appl. Spectrosc. Vol. 39, Issue 1, pp. 98-101* **1985**, *39*, 98–101.

270 T. Dumas, *J. Chromatogr. A* **1982**, *247*, 289–295.

271 B. Mann, M. L. Grayeski, *J. Chromatogr. A* **1987**, *386*, 149–158.

272 J. M. Lorrain, C. R. Fortune, B. Dellinger, *Anal. Chem.* **1981**, *53*, 1302–1305.

273 J. C. Septon, J. C. Ku, *Am. Ind. Hyg. Assoc. J.* **1982**, *43*, 845–852.

274 M. N. Descamps, T. Bordy, J. Hue, S. Mariano, G. Nonglaton, E. Schultz, T. H. Tran-Thi, S. Vignoud-Despond, *Sensors Actuators, B Chem.* **2012**, *170*, 104–108.

275 A. Tokarev, L. Salmon, Y. Guari, W. Nicolazzi, G. Molnár, A. Bousseksou, *Chem. Commun.* **2010**, *46*, 8011–8013.

276 Y. Garcia, V. Niel, M. C. Muñoz, J. A. Real, M. Carmen Muñoz, J. A. Real, *Top. Curr. Chem.* **2004**, *233*, 229–257.

277 O. Roubeau, J. M. Alcazar Gomez, E. Balskus, J. J. A. a. Kolnaar, J. G. Haasnoot, J. Reedijk, *New J. Chem.* **2001**, *25*, 144–150.

278 L. G. Lavrenova, E. V. Kirillova, V. N. Ikorskii, Y. G. Shvedenkov, V. A. Varnek, L. A. Sheludyakova, S. V. Larionov, *Russ. J. Coord. Chem. Khimiya* **2001**, *27*, 46–50.

279 A. Sousaraei, C. Queirós, F. G. Moscoso, T. Lopes-Costa, J. M. Pedrosa, A. M. G. Silva, L. Cunha-Silva, J. Cabanillas-Gonzalez, *Anal. Chem.* **2019**, *91*, 15853–15859.

280 C. L. Yaws, *The Yaws Handbook of Vapor Pressure*, Elsevier Inc., Oxford, **2015**.

281 T. E. Daubert, R. P. Danner, *Physical and Thermodynamic Properties of Pure Chemicals: Data Compilation*, Hemisphere Pub. Corp, New York, **1989**.

282 M. Klikar, V. Jelínková, Z. Růžičková, T. Mikysek, O. Pytela, M. Ludwig, F. Bureš, *European J. Org. Chem.* **2017**, *19*, 2764–2779.

283 Y. Guo, S. Xue, M. M. Dîrtu, Y. Garcia, *J. Mater. Chem. C* **2018**, *6*, 3895–3900.

284 A. Barui, *Polymeric Gels: Characterization, Properties and Biomedical Applications*, Elsevier, Rourkela, **2018**.

285 S. K. Mishra, S. N. Tripathi, V. Choudhary, B. D. Gupta, *Sensors Actuators B* **2014**, *199*, 190–200.

286 M. W. Toepke, D. J. Beebe, *Lab Chip* **2006**, *6*, 1484–1486.

287 J. Yu, X. Hou, M. Cui, S. Shi, J. He, Y. Sun, C. Wang, X. Chou, *Sci. China Mater.* **2019**, *62*, 1423–1432.

288 S. Vlassov, S. Oras, M. Antsov, I. Sosnin, B. Polyakov, A. Shutka, M. Y. Krauchanka, L. M. Dorogin, *Rev. Adv. Mater. Sci.* **2018**, *56*, 62–78.

289 P. Kumar, R. Khosla, M. Soni, D. Deva, S. K. Sharma, *Sensors Actuators, B Chem.* **2017**, *246*, 477–486.

290 International Energy Agency, "The Critical Role of Buildings, Perspectives for the Clean Energy Transition – Analysis," accessed 15 November **2021**.

291 T. J. Crowley, R. A. Berner, *Science* **2001**, *292*, 870–872.

292 M. O. McLinden, C. J. Seeton, A. Pearson, *Science* **2020**, *370*, 791–796.

293 C. G. Granqvist, *Adv. Mater.* **2003**, *15*, 1789–1803.

294 H. Ben Cheikh, A. Bouchair, *Renew. Energy* **2004**, *29*, 1877–1886.

295 Y. ling Song, K. S. Darani, A. I. Khdair, G. Abu-Rumman, R. Kalbasi, *Energy Reports* **2021**, *7*, 2784–2820.

296 A. P. Raman, M. A. Anoma, L. Zhu, E. Rephaeli, S. Fan, *Nature* **2014**, *515*, 540–544.

297 J. Mandal, Y. Fu, A. C. Overvig, M. Jia, K. Sun, N. N. Shi, H. Zhou, X. Xiao, N. Yu, Y. Yang, *Science* **2018**, *362*, 315–319.

298 A. Leroy, B. Bhatia, C. C. Kelsall, A. Castillejo-Cuberos, M. H. Di Capua, L. Zhao, L. Zhang, A. M. Guzman, E. N. Wang, *Sci. Adv.* **2019**, *5*, 1–9.

299 T. Wang, Y. Wu, L. Shi, X. Hu, M. Chen, L. Wu, *Nat. Commun.* **2021**, *12*, 1–12.

300 Z. Huang, X. Ruan, *Int. J. Heat Mass Transf.* **2017**, *104*, 890–896.

301 C. Feng, P. Yang, H. Liu, M. Mao, Y. Liu, T. Xue, J. Fu, T. Cheng, X. Hu, H. J. Fan, K. Liu, *Nano Energy* **2021**, *85*, 105971.

302 A. C. C. Rotzetter, C. M. Schumacher, S. B. Bubenhofer, R. N. Grass, L. C. Gerber, M. Zeltner, W. J. Stark, *Adv. Mater.* **2012**, *24*, 5352–5356.

303 S. Pu, J. Fu, Y. Liao, L. Ge, Y. Zhou, S. Zhang, S. Zhao, X. Liu, X. Hu, K. Liu, J. Chen, *Adv. Mater.* **2020**, *32*, 1907307.

304 Z. Lu, E. Strobach, N. Chen, N. Ferralis, J. C. Grossman, *Joule* **2020**, *4*, 2693–2701.

305 D. Zhao, A. Aili, Y. Zhai, J. Lu, D. Kidd, G. Tan, X. Yin, R. Yang, *Joule* **2019**, *3*, 111–123.

306 H. Akeiber, P. Nejat, M. Z. A. Majid, M. A. Wahid, F. Jomehzadeh, I. Zeynali Famileh, J. K. Calautit, B. R. Hughes, S. A. Zaki, *Renew. Sustain. Energy Rev.* **2016**, *60*, 1470–1497.

307 M. Kenisarin, K. Mahkamov, *Renew. Sustain. Energy Rev.* **2016**, *55*, 371–398.

308 S. Ramakrishnan, X. Wang, J. Sanjayan, J. Wilson, *Appl. Energy* **2017**, *194*, 410–421.

309 G. Gholamibozanjani, M. Farid, *Energy* **2020**, *210*, 118572.

310 A. de Gracia, *Appl. Energy* **2019**, *235*, 1245–1253.

311 "Delhi Population 2021," accessed 16 November **2021**.

312 "IMD New Delhi, SFD current month extremes," accessed 15 November **2021**.

313 F. Kuznik, J. Virgone, *Appl. Energy* **2009**, *86*, 2038–2046.

314 S. Gobinath, G. Senthilkumar, N. Beemkumar, *Energy Sources, Part A Recover. Util. Environ. Eff.* **2018**, *40*, 1765–1771.

315 W. Zhang, C. Wang, K. Chen, Y. Yin, *Small* **2019**, *15*, 1903750.

316 L. Zhu, A. Raman, S. Fan, *Appl. Phys. Lett.* **2013**, *103*, 223902.

317 A. Grosjean, P. Négrier, P. Bordet, C. Etrillard, D. Mondieig, S. Pechev, E. Lebraud, J. F. Létard, P. Guionneau, *Eur. J. Inorg. Chem.* **2013**, *2*, 796–802.

318 K. Ridier, A. C. Bas, Y. Zhang, L. Routaboul, L. Salmon, G. Molnár, C. Bergaud, A. Bousseksou, *Nat. Commun.* **2020**, *11*, 3611.

ANNEX A

Annex A1. Crystallographic data of **1**·2CH_3CN.

Compound	1·2CH_3CN
CCDC	1895056
Chemical formula	C_{12} H_{20} B_2 F_8 Fe N_6 O_2
Formula mass	510.11 g/mol
Temperature (K)	250.0
Crystal system	Orthorhombic
Space group	*Cmca*
***a*/Å**	7.2430(17)
***b*/Å**	12.882(2)
***c*/Å**	23.908(6)
α/°	90
β/°	90
γ/°	90
***V*(Å^3)**	2230.8(9)
Z	4
Radiation type	Synchrotron
Density (calculated mg m^{-3})	1.518
Absorption coefficient (mm^{-1})	0.76
***F*(000)**	1032.0
Crystal size (mm^3)	0.000576
Goodness of fit on F^2	1.112
***R*1, *wR*2 [*I*>2σ(*I*)]**	0.0719, 0.2069
***R*1, *wR*2 (all data)**	0.0930, 0.2330

Annex A2. Selected bond and interaction lengths for compound **1·2CH$_3$CN**.

Atoms	Distance (Å)
Fe1-N1	2.225(6)
Fe1-N2	2.163(6)
Fe1-O1	2.058(5)
F1-O1	2.655
F1-H2W	1.795
F3-C1	3.276
F3-H1A	2.657
N3-O1	2.744
N3-H1W	1.862
F2-C3	3.066
F2-H3C	2.270
F1-C5	3.193
F1-H5A	2.667
N3-centroid(N1C1)	3.226

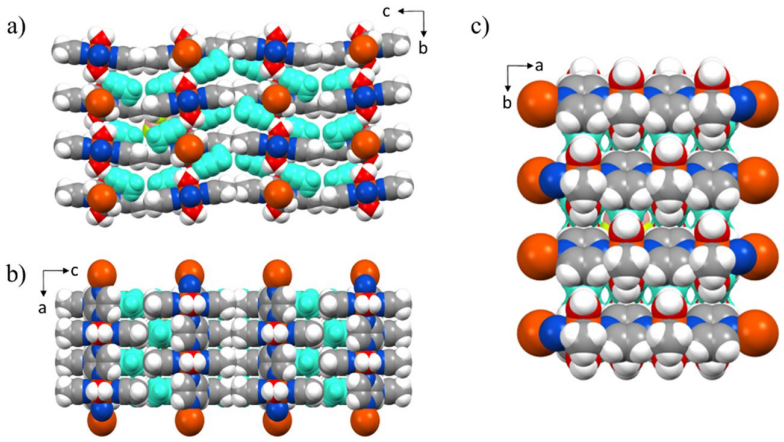

Annex A3. View of **1**·2CH$_3$CN in the spacefill mode (covalent ratii) along the a) *a* axis, b) *b* axis and c) *c* axis.

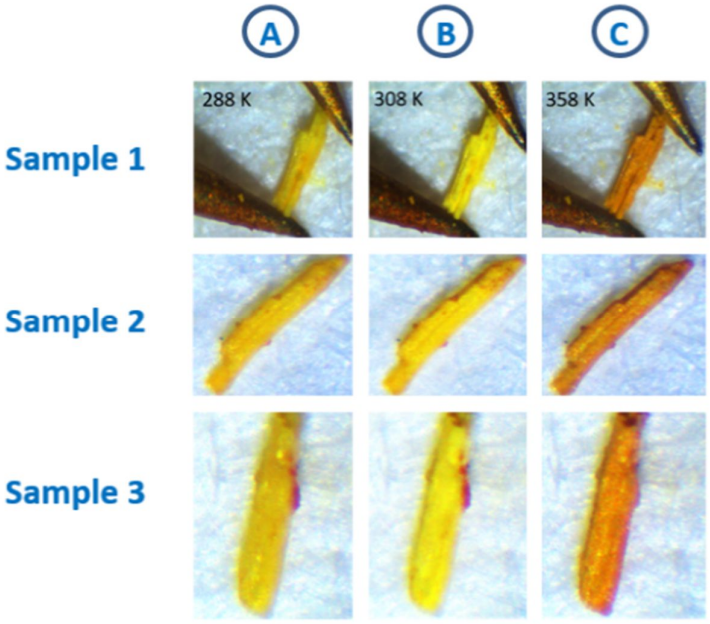

Annex A4. Color change in three different **1**·2CH_3CN crystals at the three relevant temperatures for the OR and transport measurements: before the first OR transition, b) at the first OR and conductance transition and c) at the second OR and conductance transition.

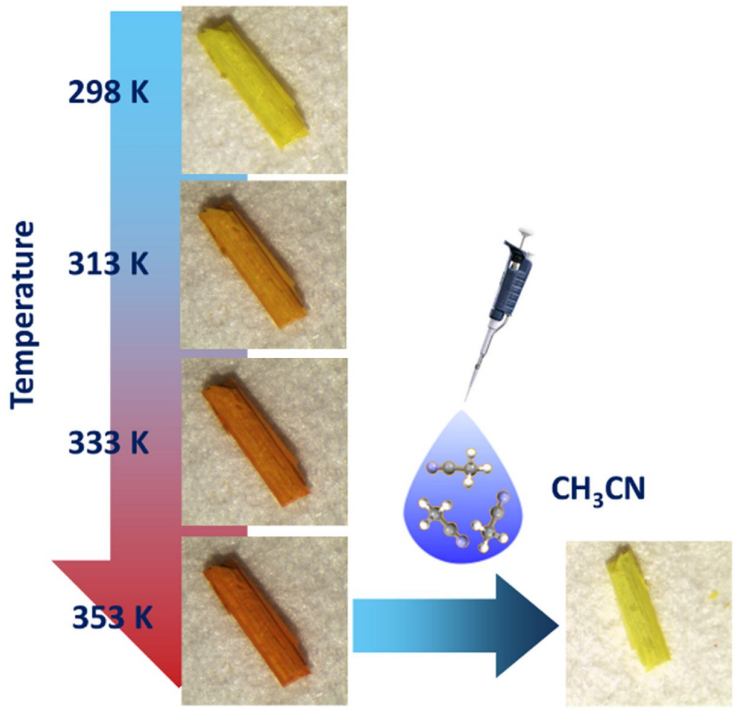

Annex A5. Color variation of a **1**·2CH_3CN crystal under increasing temperature. The color is recovered after a drop of acetonitrile is added at room temperature.

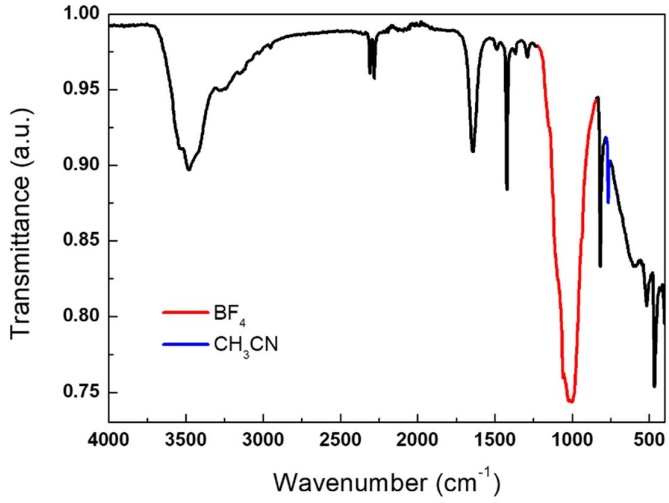

Annex A6. IR spectrum of **1**·2CH_3CN between 4000 cm^{-1} and 400 cm^{-1}. The band corresponding to ν(BF_4) at 1022 cm^{-1} is represented in red, while the C-C≡N bend overtone of acetonitrile, at 766 cm^{-1}, is colored in blue.

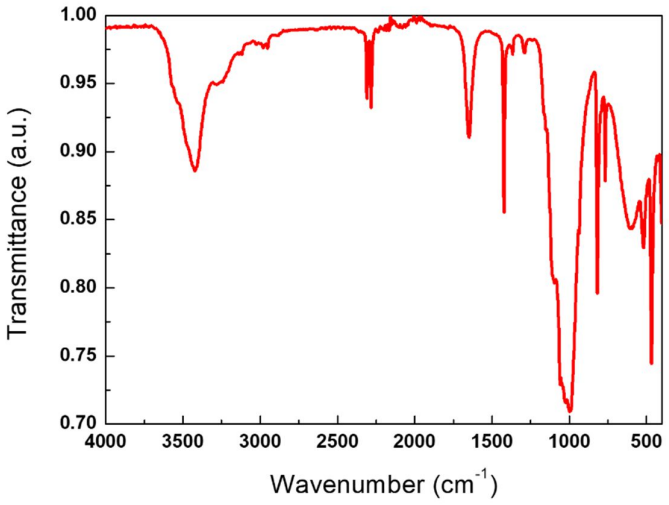

Annex A7. IR spectrum of **1**·2CH_3CN between 4000 cm^{-1} and 400 cm^{-1} at 317 K.

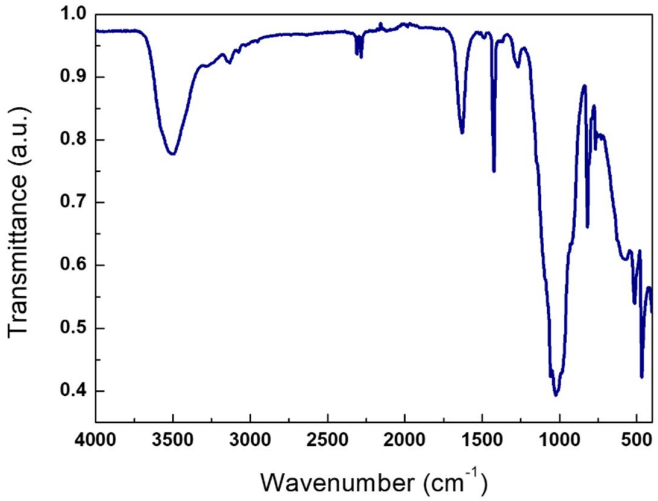

Annex A8. IR spectrum of **1**·2CH_3CN between 4000 cm^{-1} and 400 cm^{-1} at 333 K.

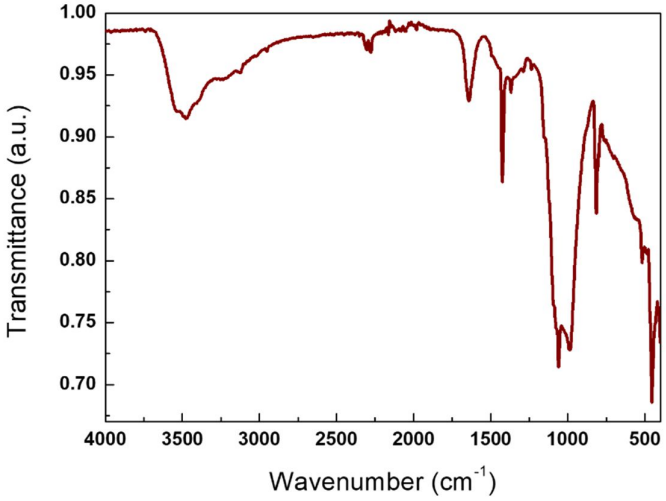

Annex A9. IR spectrum of **1**·2CH_3CN between 4000 cm^{-1} and 400 cm^{-1} at 353 K.

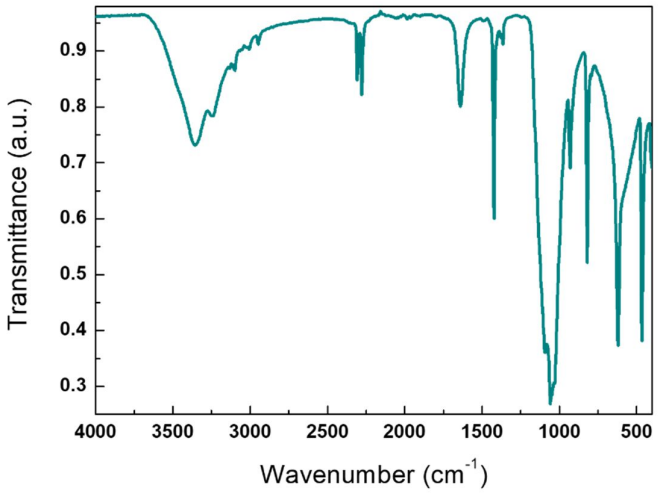

Annex A10. IR spectrum of pyrazine-ClO_4 between 4000 cm^{-1} and 400 cm^{-1}.

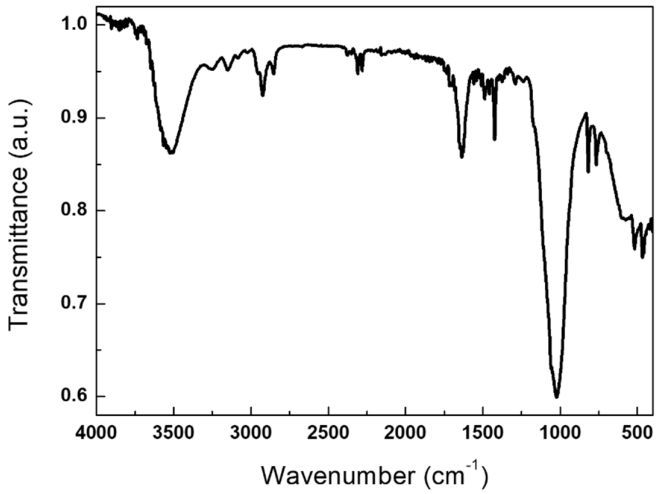

Annex A11. IR spectrum of **1**·2CH_3CN between 4000 cm^{-1} and 400 cm^{-1} at room temperature after a drop of acetonitrile was added to the "dry" crystal. The 766 cm^{-1} band is recovered.

Annex A12. Cell parameters obtained after fitting the diffraction peaks obtained from the three phases by using the HighScore Plus Software.

	a (Å)	*b* (Å)	*c* (Å)	α (°)	β (°)	γ (°)	V (Å^3)	FOM
1·2CH_3CN (single crystal)	7.2430	12.862	23.908	90	90	90	2230.7	-
1·2CH_3CN	7.516	12.82	24.01	90	90	90	2313.36	10
1	7.92	12.40	18.1	90	97.98	90	1760.56	3.51
1 after exposure to acetonitrile	6.893	11.389	23.92	90	90	90	1877.82	7

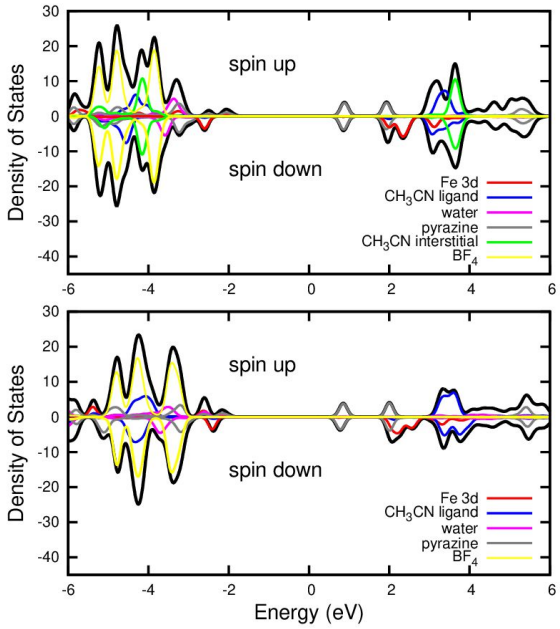

Annex A13. Projected density of states of **1**·2CH_3CN (upper panel) and **1** (lower panel) computed for a ferromagnetic ordering along the chains. The valence band maxima are set to -2 eV. The states of uncoordinated acetonitrile are far from valence and conduction bands. A unit cell containing 156 and 204 atoms is used for **1** and **1**·2CH_3CN, respectively.

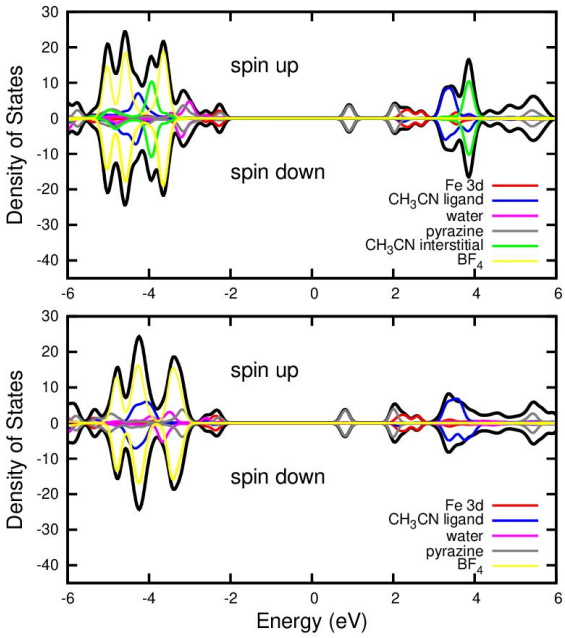

Annex A14. Projected density of states of **1**·2CH_3CN (upper panel) and **1** (lower panel) computed for an antiferromagnetic ordering along the chains. The valence band maxima are set to -2 eV.

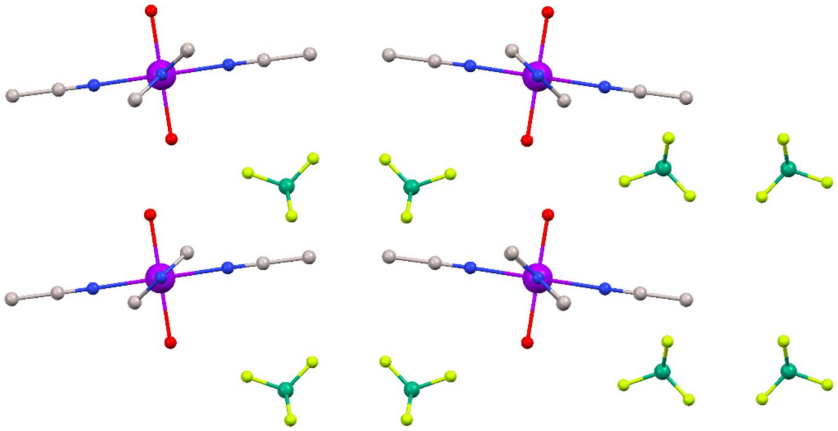

Annex A15. Simulated structure of **1**.

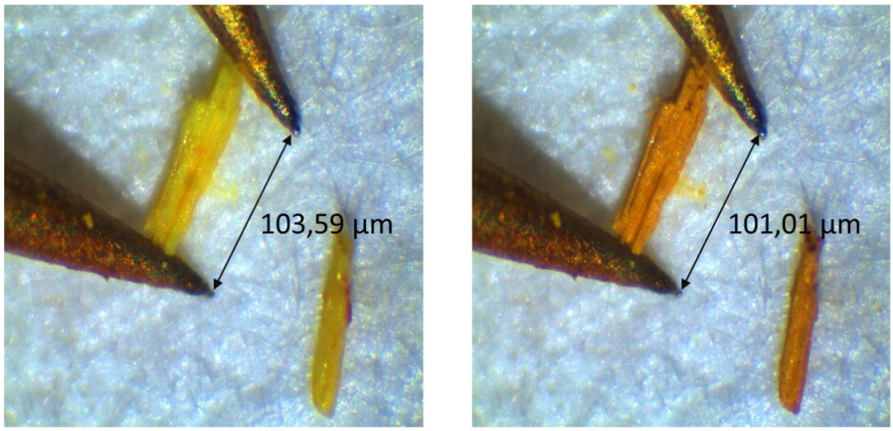

Annex A16. Change on the size and length (2.5%) from **1**·2CH_3CN to **1** solid-state transformation.

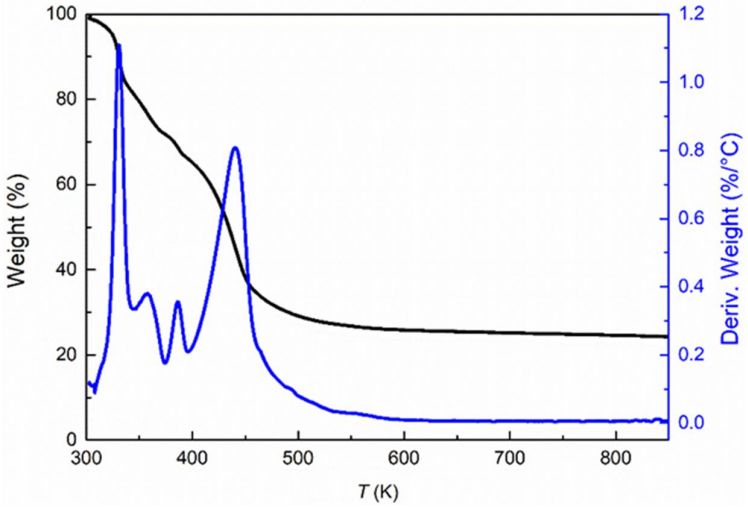

Annex A17. Thermogravimetric analysis of **1**·2CH_3CN between 303 K and 873 K.

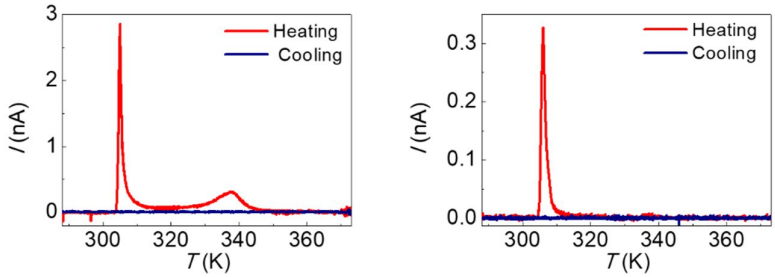

Annex A18. Electrical current measured at V = 1 V between 288 K and 330 K. Two resonances in current show up at roughly the same temperature than in the crystal in the main text.

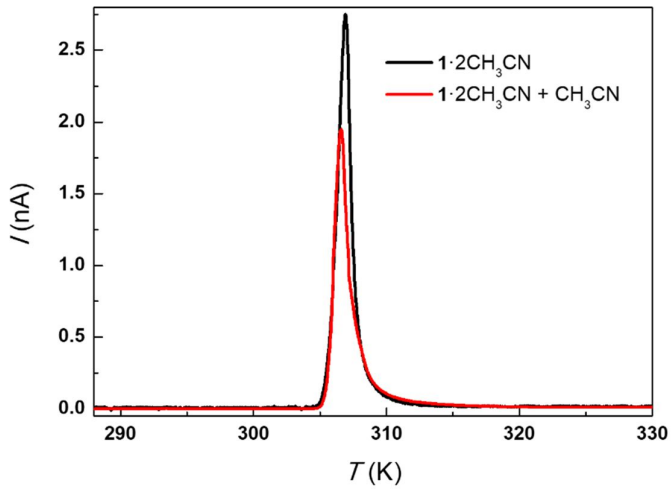

Annex A19. Electrical conductivity measurements between 288 K and 330 K. The black line corresponds to the original **1**·2CH_3CN (first thermal cycle) and the red one to the same crystal after a drop of acetonitrile was added in a subsequent thermal cycle.

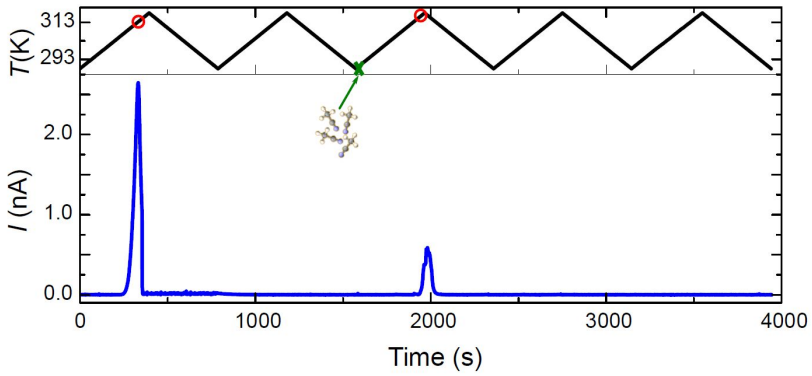

Annex A20. Current measured across a **1**·2CH_3CN crystal while cycling the temperature between 288 K and 318 K. A resonance in the current (red circle) appears in the cycle where the **1**·2CH_3CN is exposed to acetonitrile vapor (green crosses).

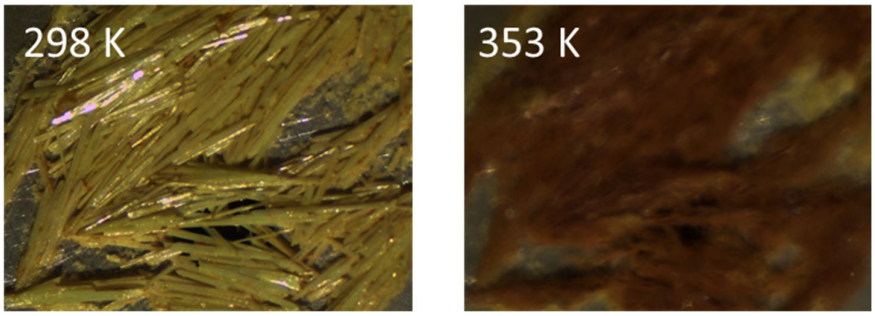

Annex A21. Image of **1**·2CH_3CN crystals at two different temperatures. Release of acetonitrile can be seen as blurriness in the second image.

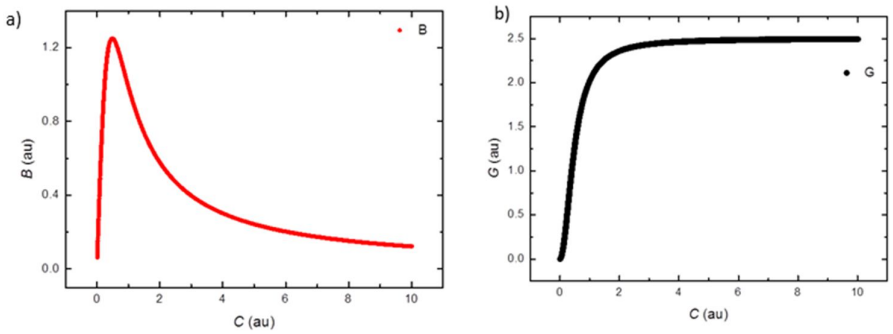

Annex A22. Calculated (a) *B* and b) *G* as a function of the temperature with an AC excitation V_{AC} = 100 mV and f = 510 kHz.

ANNEX B

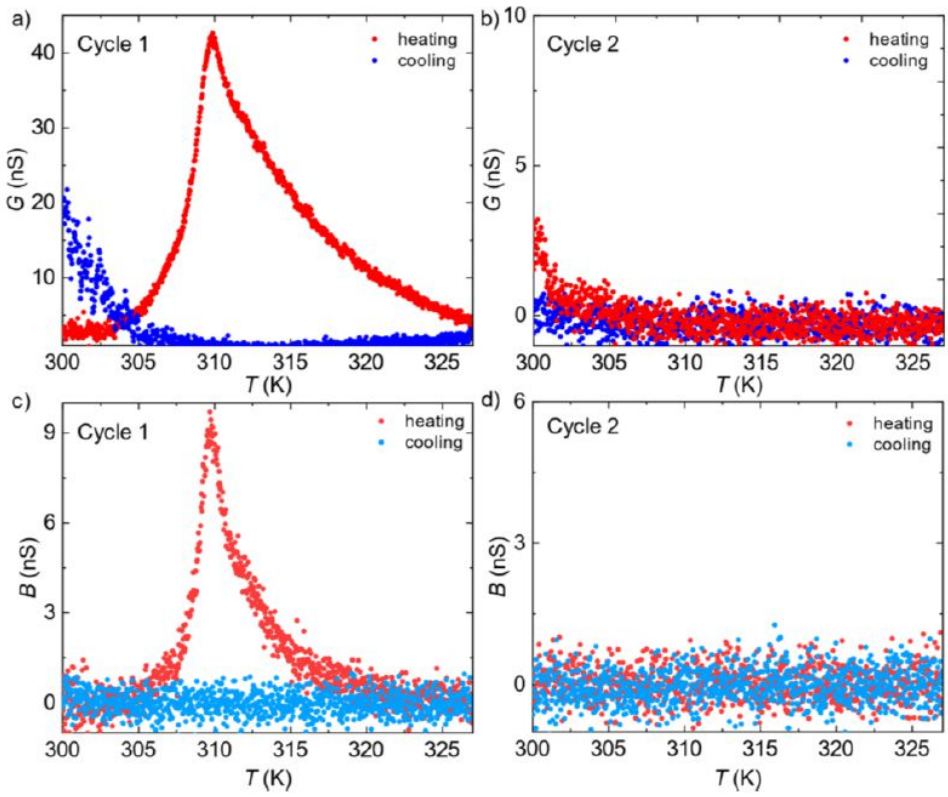

Annex B1. *G* and *B* measured during (a,c) a first and (b,d) a second thermal (heating-cooling) cycle. The peak in G and B is only observed during the first heating cycle.

ANNEX C

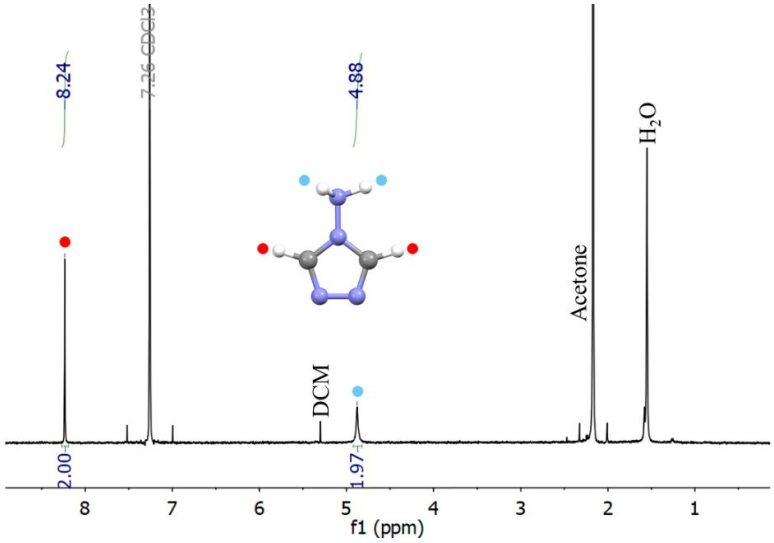

Annex C1. [1]H-NMR of **1** after digestion.

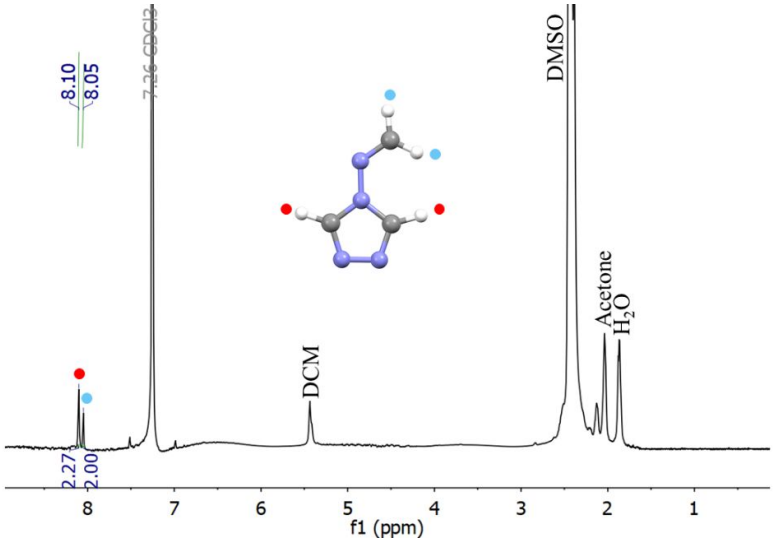

Annex C2. [1]H-NMR of **2** after digestion ($CDCl_3$+1 drop of DMSO-d_6).

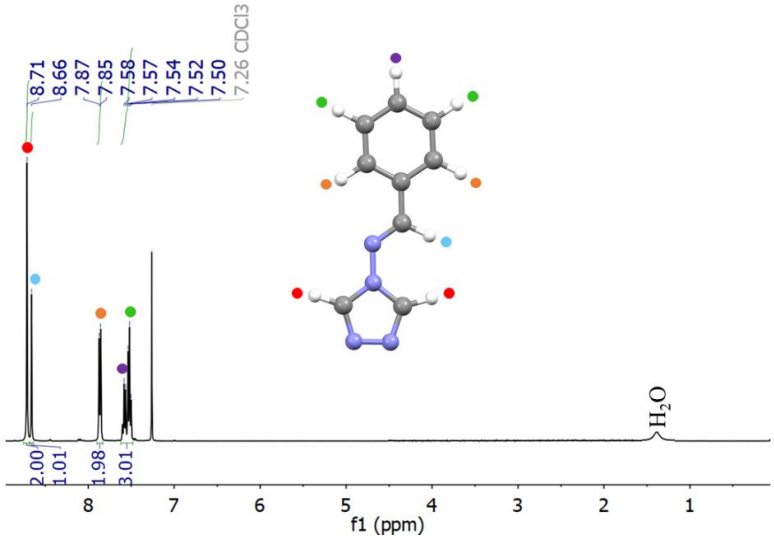

Annex C3. [1]H-NMR of **3** after digestion.

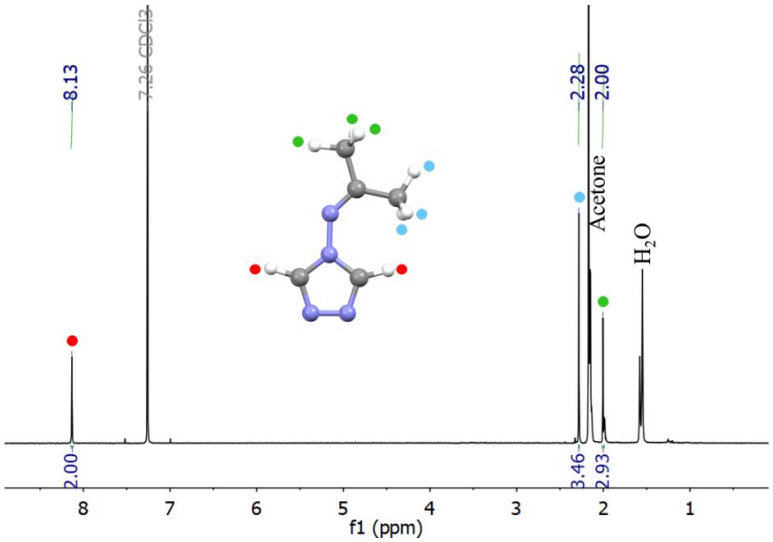

Annex C4. [1]H-NMR of **4** after digestion.

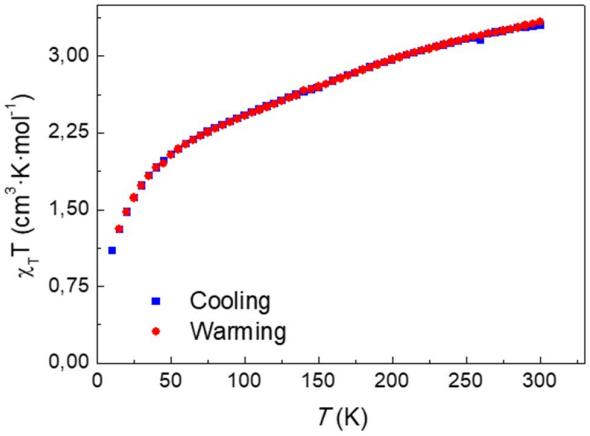

Annex C5. Magnetic behavior of **2** between 2 K and 300 K.

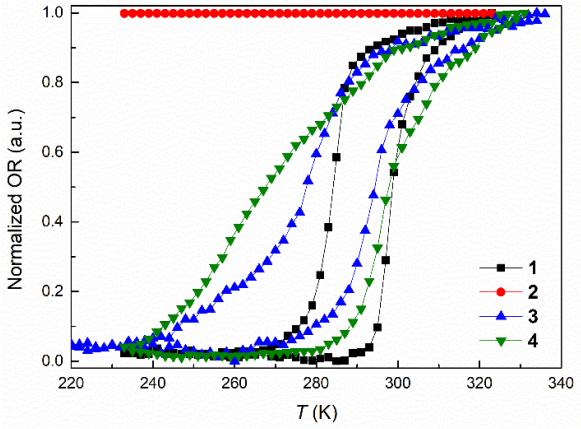

Annex C6. Normalized optical reflectivity (in respect to **1**) *vs.* *T* for **1**-**4**.

Annex C7. Vapor pressure of the tested molecules.

Vapor	Vapor pressure at 25°C (mm Hg)[280,281]
Formaldehyde	$5{,}69 \cdot 10^{-5}$
Benzaldehyde	$7{,}81 \cdot 10^{-8}$
Acetone	$1{,}18 \cdot 10^{-5}$
Acetaldehyde	$4{,}56 \cdot 10^{-5}$
Acetophenone	$1{,}69 \cdot 10^{-8}$
Salicylaldehyde	$2{,}60 \cdot 10^{-9}$
Propanal	$1{,}79 \cdot 10^{-5}$
Butanal	$6{,}98 \cdot 10^{-6}$
Formic acid	$2{,}95 \cdot 10^{-6}$
Ethyl isocyanate	$5{,}18 \cdot 10^{-6}$
Hydrochloric acid	35,424
Sulfuric acid	$5{,}93 \cdot 10^{-5}$
Ammonia	$2{,}11 \cdot 10^{-4}$
Triethylamine	$1{,}54 \cdot 10^{-5}$
Oxygen peroxide	1,97

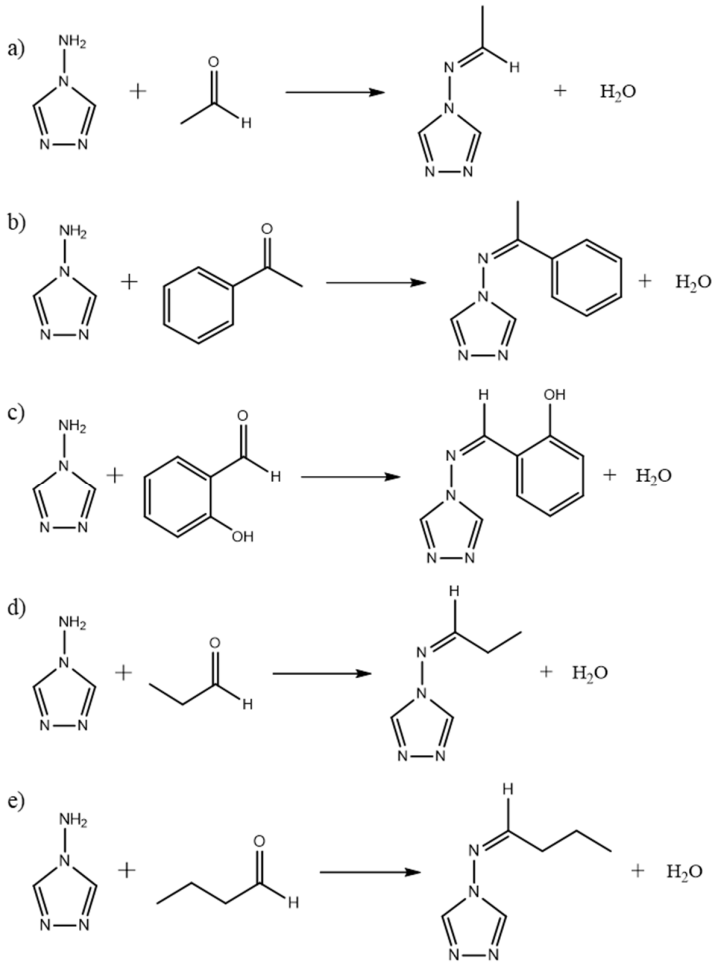

Annex C8. Expected reactions between the ligand in **1** and a) acetaldehyde, b) acetophenone, c) salicylaldehyde, d) propanal and e) butanal.

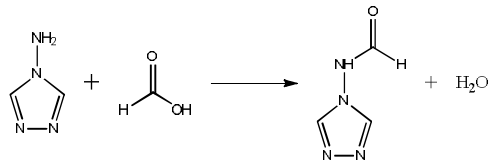

Annex C9. Expected reaction between the ligand in **1** and formic acid.

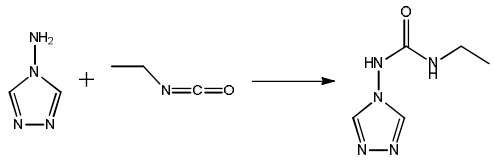

Annex C10. Expected reaction between the ligand in **1** and ethyl isocyanate.

ANNEX D

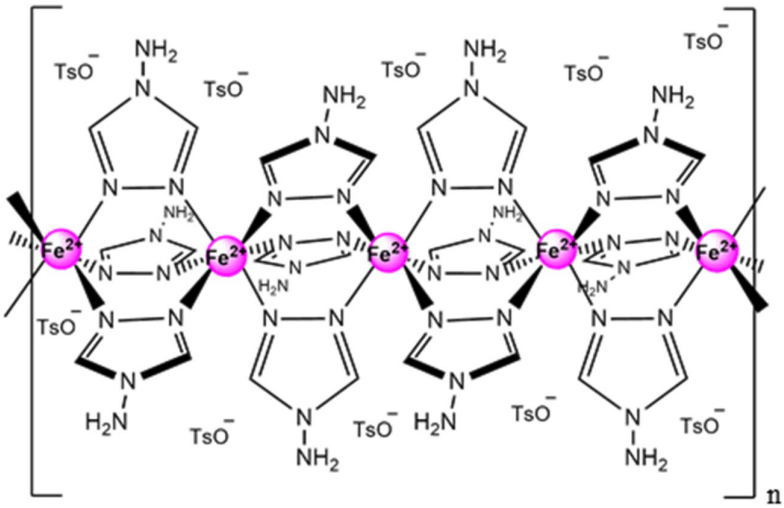

Annex D1. Illustration of the 1D structure of **1**. Compounds **2** and **3** present this same general backbone.

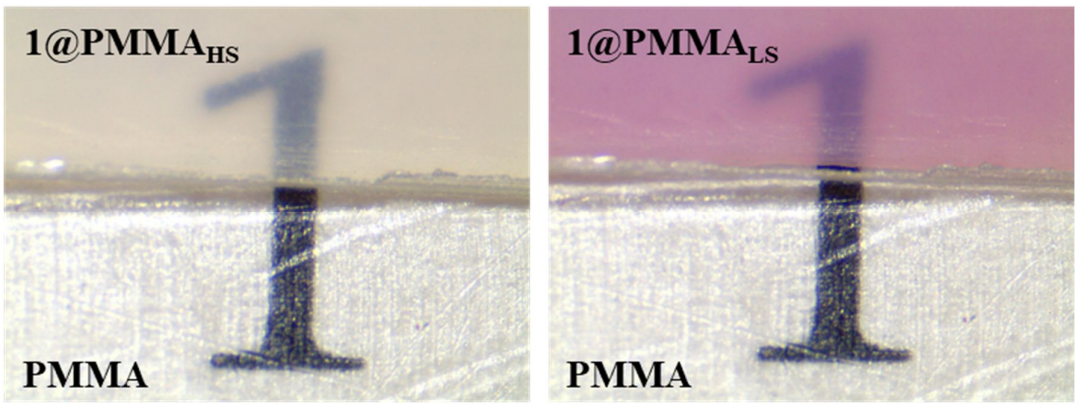

Annex D2. Images of **1@PMMA** (in HS and LS) and PMMA to show the transparency of the composites.

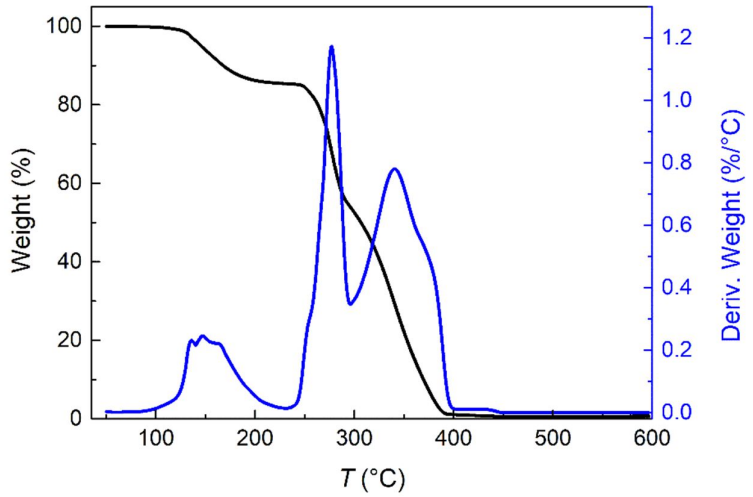

Annex D3. Thermogravimetric analysis of PMMA.

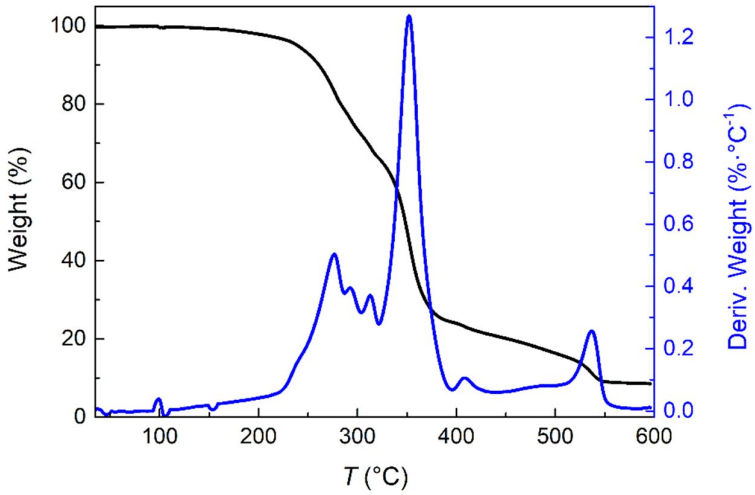

Annex D4. Thermogravimetric analysis of **1**.

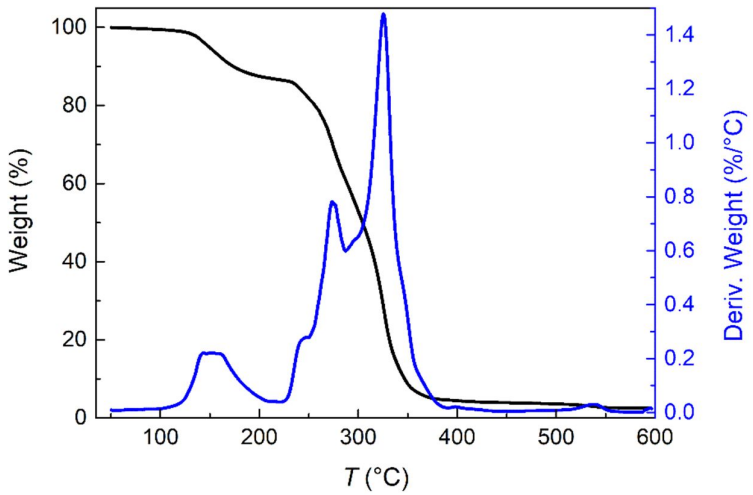

Annex D5. Thermogravimetric analysis of **1@PMMA**.

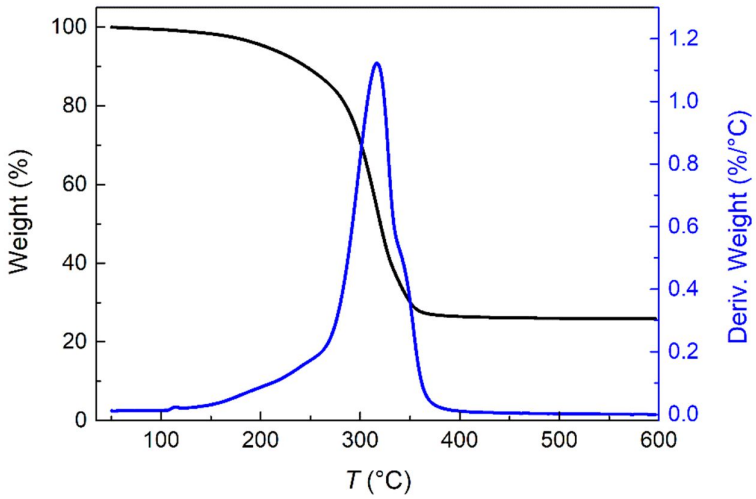

Annex D6. Thermogravimetric analysis of **2**.

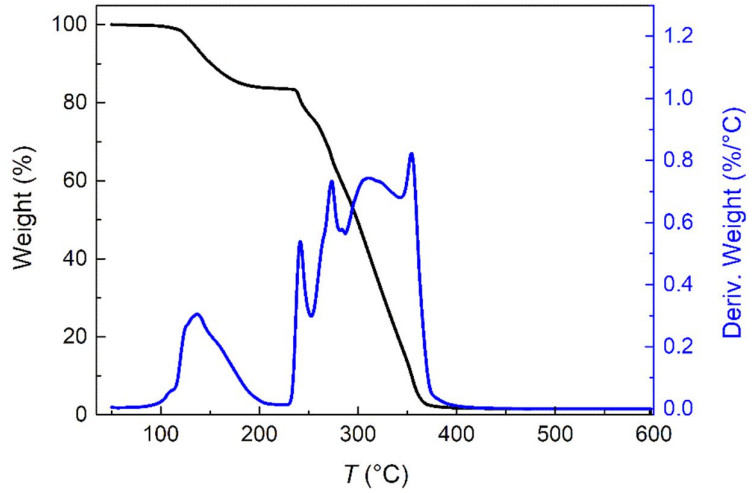

Annex D7. Thermogravimetric analysis of **2@PMMA**.

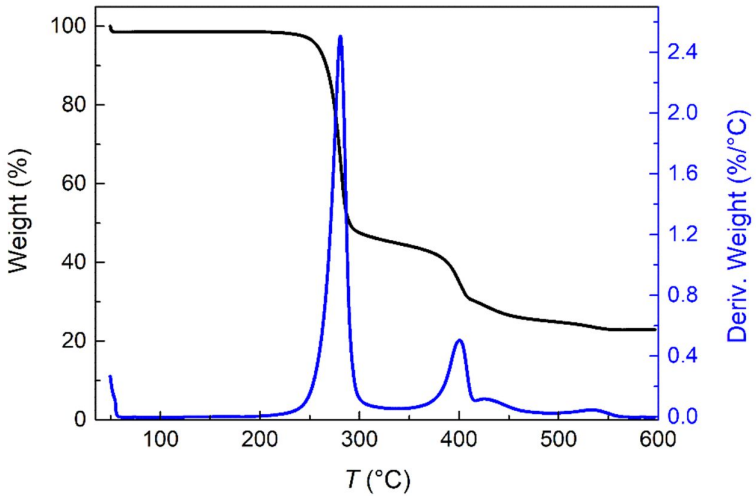

Annex D8. Thermogravimetric analysis of **3**.

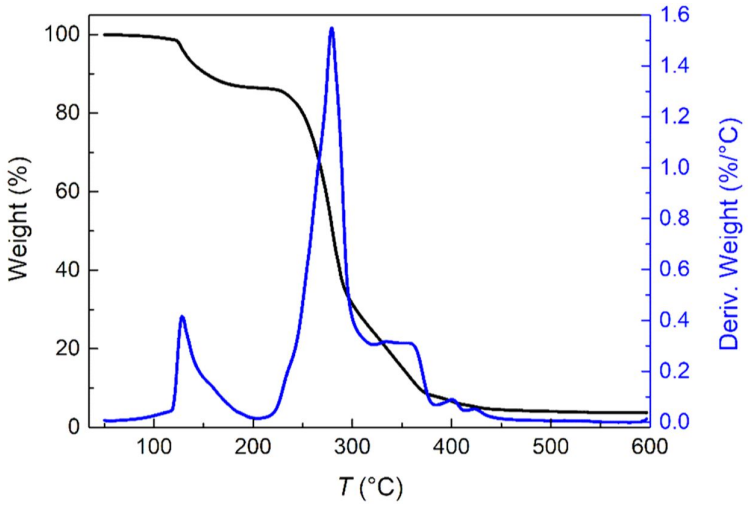

Annex D9. Thermogravimetric analysis of **3@PMMA**.

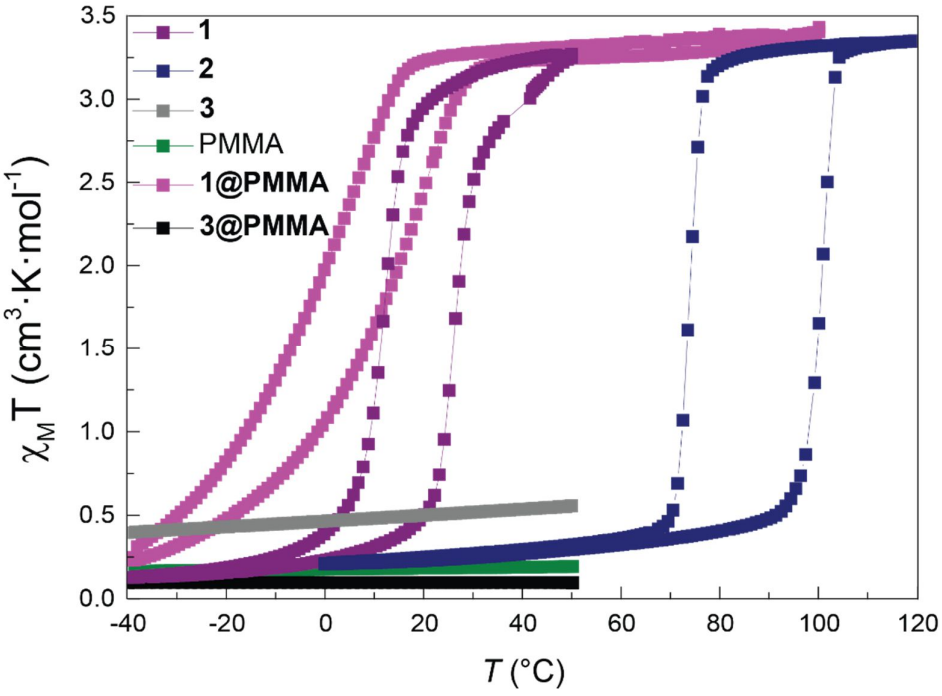

Annex D10. $\chi_M T$ measured as a function of the temperature for **1-3**, PMMA, **1@PMMA** and **3@PMMA**.

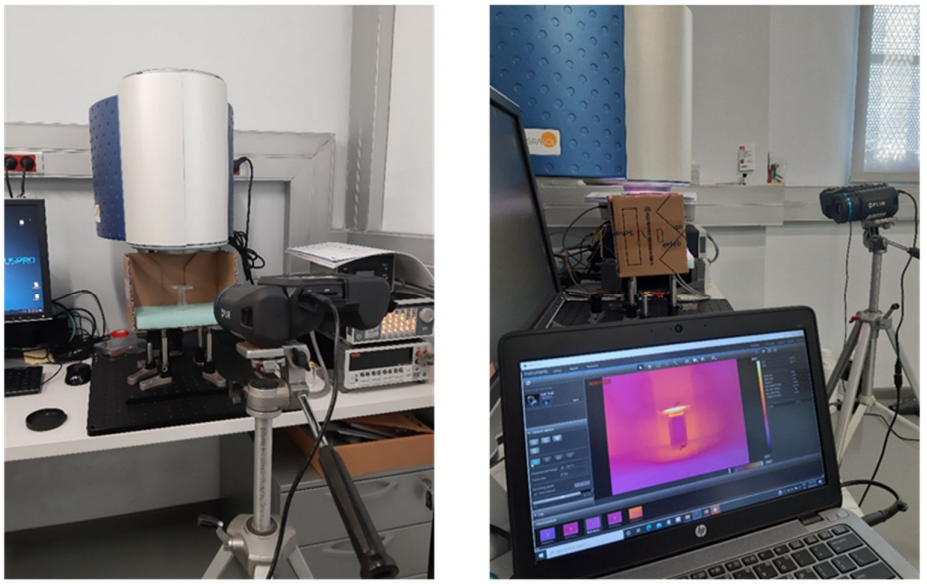

Annex D11. First experimental setup.

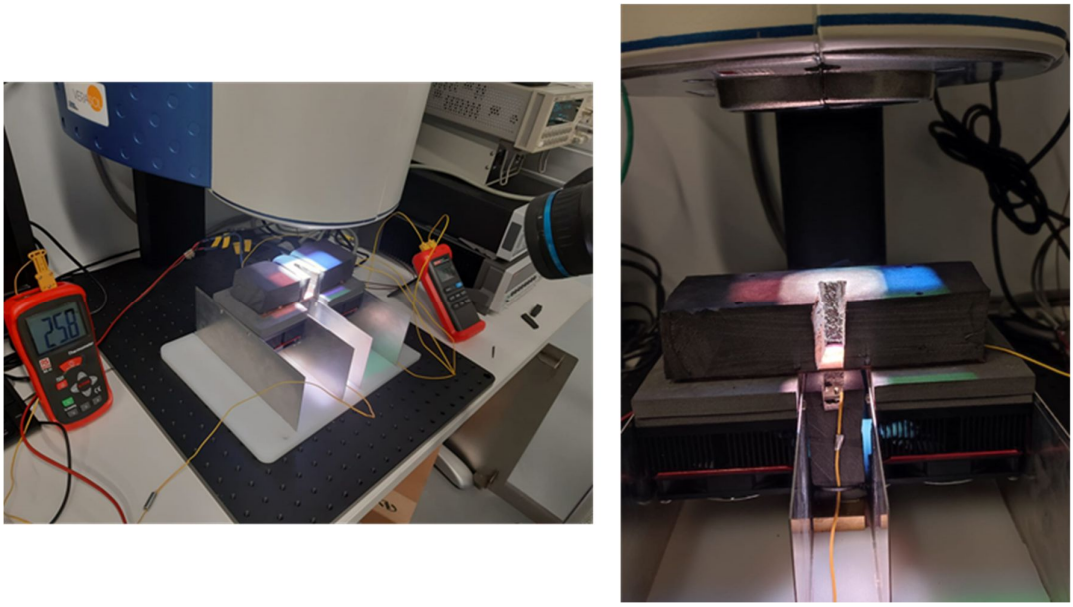

Annex D12. Second experimental setup.

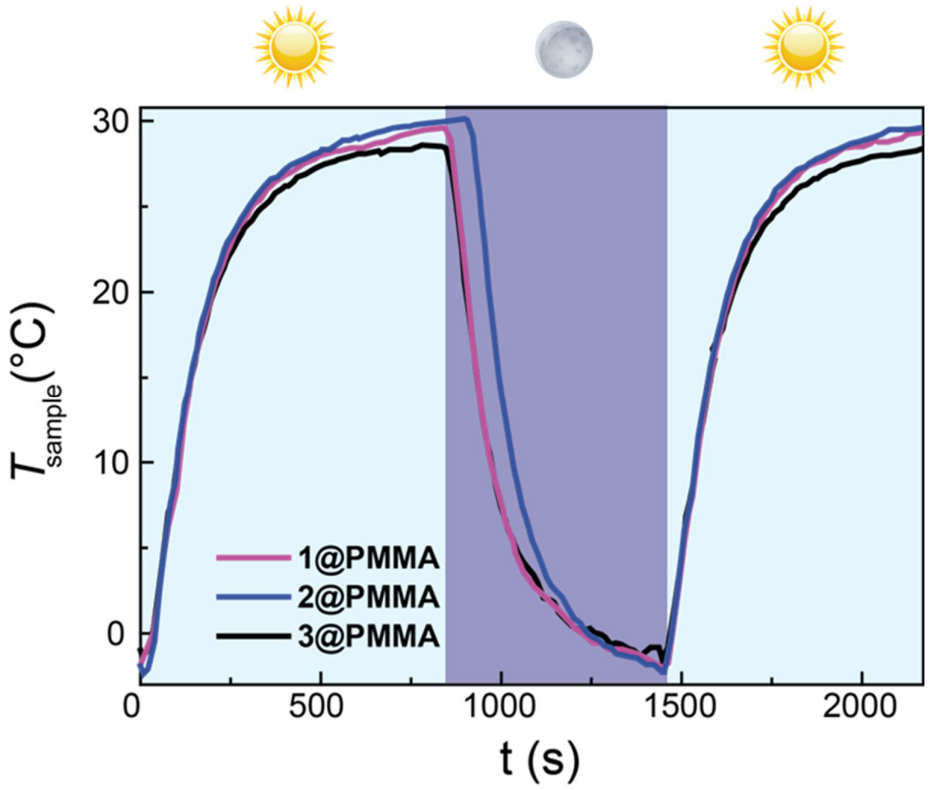

Annex D13. Temperature in the sample *vs.* exposure time with on-off solar simulator cycles, corresponding with the experiment in Figure 71.

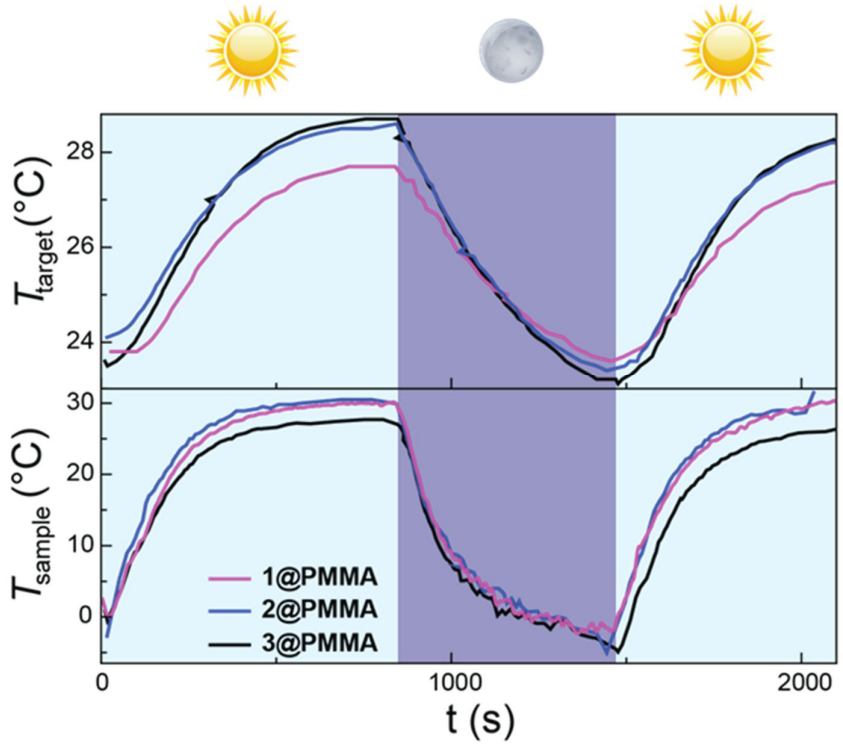

Annex D14. Repetition of the on-off solar simulator cycles experiments.

Annex D15. Composite **1@PMMA** after exposition to the solar lamp, where the HS and LS phases can be seen by bare-eye.

ANNEX E. PHYSICAL TECHNIQUES

- FT-IR spectra were recorded as neat samples in the 400-4000 cm^{-1} range on a Bruker Tensor 27 (ATR device) Spectrometer. The temperature dependence experiments were performed in the same instrument, using a thermometer and a heat gun.
- TGA was performed using a TA Instrument TGAQ500 under air from 303 to 873 K.
- Elemental analyses (C, H and N) were performed on a LECO CHNS-932 Analyzer at the "Servicio Interdepartamental de Investigación (SIdI)" at Autónoma University of Madrid.
- Optical reflectivity measurements were performed using a MOTIC SMZ-171 optical stereoscope coupled with a MOTICAM 3. Images were collected in BMP format without any filter using the Motic Images Plus 3.0 software, with the mean value from each region of interest (ROI) analyzed under the ImageJ program. The temperature was controlled using a Linkam T95 system controller and a LNP 95 Liquid Nitrogen Cooling System.
- Powder X-ray diffraction data was collected in a Rigaku Smartlab SE diffractometer with a Bragg-Brentano configuration, using Cu-Kα radiation (λ = 0.1541 nm). Samples were measured with a speed of $1.8°\cdot min^{-1}$ under an X-ray fluorescence reduction mode, at room temperature. Treatment of data and estimation of the unit cell were performed using the software HighScore Plus.
- NMR spectra were recorded on a Bruker Advance 300 (1H: 400 MHz) spectrometer at 298 K using partially deuterated solvents as internal standards. Coupling constants (J) are denoted in Hz and chemical shifts (δ) in ppm. Multiplicities are denoted as follows: s = singlet, d = doublet, t = triplet, m = multiplet.
- Differential Scanning Calorimetry (DSC) measurements were performed in a TA Instruments Discovery MDSC 25 between 273 K and 393 K under a N_2 atmosphere with a ramp of $1\ °C\cdot min^{-1}$. The sample was secured in a hermetically sealed aluminum sample pan.
- Magnetic susceptibility measurements were carried out in a Quantum Design MPMS-5S SQUID magnetometer under a 2000 Oe field. Each sample was secured inside a plastic capsule with cotton. Pascal constants were used to correct for the diamagnetic contribution.
- Electrical conductivity measurements (DC) were carried out on single crystals by a two-probe method using a Keithley 2450 SourceMeter under light and in a nitrogen atmosphere. Electrical contact to individual crystals is made directly via the conducting tips of the electrical probe station. Charge transport is probed along the long axis of the crystals that coincides with the orientation of the molecular chains. The length of the crystals and the separation between the tips is typically a few hundred micrometers (200-500μm). The temperature was controlled using a Linkam T95 system with a LNP 95 Liquid Nitrogen Cooling System.
- AC admittance spectroscopy measurements were performed in a Lakeshore Cryogenics (Model PS-100 Tabletop) probe station, equipped with a Zurich Instruments MLI500 kHz Lock-in-Amplifier. Measurements were carried out with a heating rate of $+1\ K\cdot min^{-1}$ and AC excitation frequency: $\omega/2\pi$= 10 kHz; AC voltage V_{ac} = 100 mV; offset DC bias voltage: V = 1 V).

- Crystal Structure Determination has been carried out in the ALBA Synchrotron. The data were collected with a MD2M–Maatel diffractometer at the XALOC beamline (BL13) with the collaboration of ALBA staff, from a Silicon (111) monochromator (T = 100 K, λ = 0.82656 Å).[1] The crystal was taken directly from its solution, mounted with a drop of Paratone-N oil and immediately put into the cold stream of dry N_2 on the goniometer. The structures were solved by direct methods and the refinement on F^2 and all further calculations were carried out with the SHELX-TL suite[2] and OLEX2 program.[3]
- DFT calculations were performed using PWscf utility of QUANTUM ESPRESSO.[4] Exchange and correlation is treated using the PBE (Perdew-Burke-Ernzerhof) functional and a *Hubbard U* correction of 5 eV applied to d electrons was employed. Ultrasoft Rappe Rabe Kaxiras Joannopoulos pseudopotentials were used, and a wave-function with charge density cutoffs of 60 Ry and 600 Ry, respectively, was set. Geometrical optimizations were performed until the forces on atoms were less than 0.003 $eV \cdot Å^{-1}$ and the stress was less than 0.015 kbar.
- The thermal images were acquired with a real-time infrared camera FLIR T540 (FLIR Ltd, USA).

1. J. Juanhuix, F. Gil-Ortiz, G. Cuní, C. Colldelram, J. Nicolás, J. Lidón, E. Boter, C. Ruget, S. Ferrer, J. Benach, *J. Synchrotron Radiat.* **2014**, *21*, 679–689.

2. G. M. Sheldrick, *Acta Cryst.* **2008**, *64*, 112–122.

3. O. V. Dolomanov, L. J. Bourhis, R. J. Gildea, J. A. K. Howard, H. Puschmann, *J. Appl. Crystallogr.* **2009**, *42*, 339–341.

4. P. Giannozzi, S. Baroni, N. Bonini, M. Calandra, R. Car, C. Cavazzoni, D. Ceresoli, G. L. Chiarotti, M. Cococcioni, I. Dabo, A. Dal Corso, S. de Gironcoli, S. Fabris, G. Fratesi, R. Gebauer, U. Gerstmann, C. Gougoussis, A. Kokalj, M. Lazzeri, L. Martin-Samos, N. Marzari, F. Mauri, R. Mazzarello, S. Paolini, A. Pasquarello, L. Paulatto, C. Sbraccia, S. Scandolo, G. Sclauzero, A. P. Seitsonen, A. Smogunov, P. Umari, R. M. Wentzcovitch, *J. Phys. Condens. Matter* **2009**, *21*, 395502–395521.

ANNEX F. PUBLISHED ARTICLES AND PATENTS

1. A switchable iron-based coordination polymer toward reversible acetonitrile electro-optical readout, Esther Resines-Urien, Enrique Burzurí*, Estefania Fernandez-Bartolome, Miguel Ángel García García-Tuñón, Patricia de la Presa, Roberta Poloni, Simon J. Teat and Jose Sanchez Costa*, *Chem. Sci.*, **2019**, *10*, 6612-6616. Back cover.

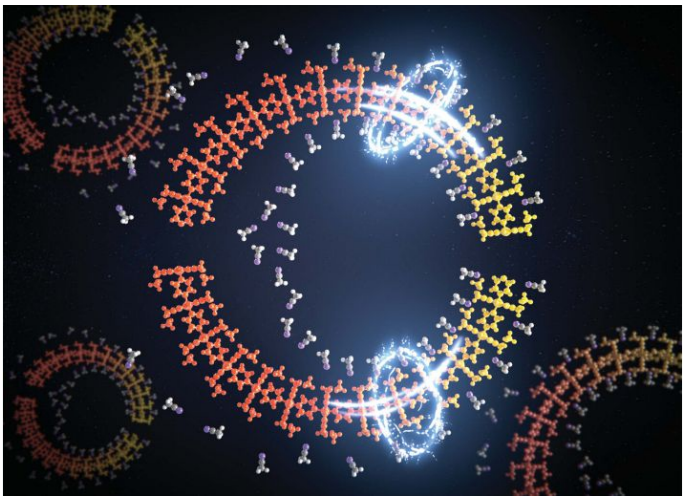

2. Covalent post-synthetic modification of switchable iron-based coordination polymers by volatile organic compounds: a versatile strategy for selective sensor development, Esther Resines-Urien, Lucía Piñeiro-López, Estefania Fernandez-Bartolome, Arturo Gamonal, Mar Garcia-Hernandez and Jose Sanchez Costa*, *Dalton Trans.*, **2020**,*49*, 7315-7318.

3. Patent: EP2020/074768.

4. Sequential single-crystal-to-single-crystal vapochromic inclusion in a nonporous coordination polymer: unravelling dynamic rearrangement for selective pyridine sensing, Estefania Fernandez-Bartolome, Esther Resines-Urien, María Murillo-Vidal, Lucía Piñeiro-Lopez* and Jose Sanchez Costa*, *Inorg. Chem. Front.*, **2021**,*8*, 2426-2432. Back cover.

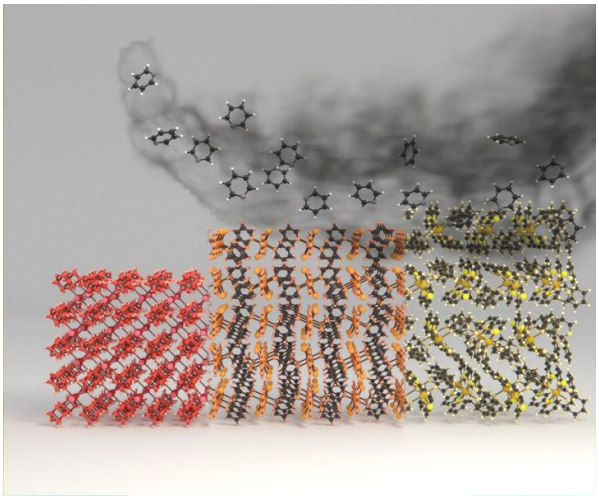

5. Water Soluble Iron-Based Coordination Trimers as Synergistic Adjuvants for Pancreatic Cancer, Marco Cordani, Esther Resines-Urien, Arturo Gamonal, Paula Milán-Rois, Lionel Salmon, Azzedine Bousseksou, Jose Sanchez Costa* and Álvaro Somoza*, *Antioxidants* **2021**, *10*(1), 66.

6. Tunable Proton Conductivity and Color in a Nonporous Coordination Polymer via Lattice Accommodation to Small Molecules, Aysegul Develioglu, Esther Resines-Urien, Roberta Poloni, Lucía Martín-Pérez, Jose Sanchez Costa* and Enrique Burzurí*, *Adv. Sci.*, **2021**,*8*, 2102619.

7. Reversible single-crystal-to-single-crystal transformations in coordination compounds induced by external stimuli, Estefania Fernandez-Bartolome, Ana Martinez-Martinez, Esther Resines-Urien, Lucía Piñeiro-Lopez and Jose Sanchez Costa*, *Coord. Chem. Rev.*, **2022**, *452*, 214281